

---

**Interaction of lipid and polymer films  
with cells:  
A neutron and X-ray reflectometry study**

**Samira Hertrich**

---

Dissertation  
an der Fakultät für Physik  
der Ludwig-Maximilians-Universität  
München

vorgelegt von  
Samira Hertrich

Erstgutachter: Priv. Doz. Dr. Bert Nickel

Zweitgutachter: Prof. Dr. Jan Lipfert

Tag der mündlichen Prüfung: 28.10.2015

# Contents

<b>Zusammenfassung</b>	<b>ix</b>
<b>Summary</b>	<b>xi</b>
<b>1 Introduction</b>	<b>1</b>
<b>2 Study of lipid and polymer films: concepts and methods</b>	<b>5</b>
2.1 Lipid membranes as biological interfaces . . . . .	5
2.1.1 Natural cell membranes . . . . .	5
2.1.2 Supported lipid bilayers . . . . .	7
2.2 Polymers . . . . .	8
2.2.1 Polyethylene glycol (PEG) . . . . .	9
2.3 Immersed surfaces: electrostatic surface potential . . . . .	9
2.4 Diffusion . . . . .	9
2.5 Fluorescence microscopy . . . . .	10
2.5.1 FRAP . . . . .	11
2.6 AFM . . . . .	11
2.7 Neutron and X-ray scattering . . . . .	12
2.7.1 Refractive index . . . . .	12
2.7.2 SLD calculation and contrast variation . . . . .	12
2.7.3 Hydration determination . . . . .	13
2.7.4 Reflectometry . . . . .	13
2.7.5 Reflectometry analysis software: Motofit . . . . .	15
2.8 Reflectometers . . . . .	16
2.8.1 Neutron instruments . . . . .	16
2.8.2 X-ray instruments . . . . .	17

2.9	Fluidic chambers for reflectometry and microscopy . . . . .	18
<b>3</b>	<b>Results: Anionic lipid bilayers</b>	<b>21</b>
3.1	Asymmetric distribution of anionic phospholipids in supported lipid bilayers	22
3.1.1	Sample preparation . . . . .	22
3.1.2	Neutron reflectometry results . . . . .	22
3.2	$\alpha$ -synuclein binding to anionic lipid bilayers . . . . .	24
3.2.1	$\alpha$ -synuclein . . . . .	24
3.2.2	Sample preparation . . . . .	24
3.2.3	Reflectometry results . . . . .	25
3.2.4	Interpretation of $\alpha$ -synuclein data . . . . .	26
3.3	Phase separated bilayer . . . . .	27
3.3.1	DPPC-DOPS neutron reflectivity . . . . .	28
3.3.2	In plane structure of bilayer depending on $\text{Ca}^{2+}$ presence . . . . .	30
<b>4</b>	<b>Results: Tethered lipid bilayers</b>	<b>33</b>
4.1	TLB substrate without bilayer . . . . .	34
4.1.1	Preparation of TLB substrates . . . . .	34
4.1.2	X-ray reflectometry of TLB substrate in air . . . . .	35
4.2	Lipid bilayer on the PEG-tether cushion . . . . .	36
4.2.1	Bilayer deposition . . . . .	36
4.2.2	Diffusion in tethered lipid bilayers . . . . .	37
4.2.3	Neutron and X-ray reflectometry . . . . .	38
4.2.4	AFM . . . . .	41
4.3	Change in thickness of the PEG cushion in carbonate buffer . . . . .	42
<b>5</b>	<b>Results: Surfaces for cell motility and attachment</b>	<b>45</b>
5.1	Fibronectin adsorption to grafted PEG surfaces and cell motility . . . . .	46
5.1.1	PEG surfaces . . . . .	46
5.1.2	Neutron data and fits . . . . .	48
5.1.3	Cellular behavior on the different PEG and FN surfaces . . . . .	52
5.2	Neural cell attachment surfaces . . . . .	55
5.2.1	Film preparation . . . . .	56
5.2.2	X-ray and neutron reflectometry . . . . .	56
5.2.3	Microscopy of cells . . . . .	59

<b>Contents</b>	<b>vii</b>
<b>Conclusion</b>	<b>61</b>
<b>Outlook</b>	<b>63</b>
<b>Bibliography</b>	<b>65</b>
<b>A Publications</b>	<b>75</b>
A.1 Full text of ref. [1]: Asymmetric Distribution of Anionic Phospholipids in Supported Lipid Bilayers	77
A.2 Fulltext of ref. [2]: Highly Hydrated Deformable Polyethylene Glycol-Tethered Lipid Bilayers .	83
A.3 Fulltext of ref. [3]: Cell Motility on Polyethylene Glycol Block Copolymers Correlates to Fibronectin Surface Adsorption. . . . .	91
A.4 Full text of ref. [4]: Neural Stem Cell Spreading on Lipid Based Artificial Cell Surfaces, Characterized by Combined X-ray and Neutron Reflectometry . . . . .	103
A.5 Full text of ref. [5]: Photocatalytic Cleavage of Self-Assembled Organic Monolayers by UV-Induced Charge Transfer from GaN Substrates . . . . .	119
A.6 Full text of ref. [6]: Aperiodic CrSc multilayer mirrors for attosecond water window pulses . .	127
A.7 Full text of ref. [7]: Influence of ibuprofen on phospholipid membranes . . . . .	143



# Zusammenfassung

An Grenzflächen zwischen Festkörpern und biologischen Organismen trifft weiches organisches Material in wässriger Umgebung auf harte Oberflächen. Derartige Grenzflächen spielen eine Rolle bei Modellsystemen zur Untersuchung von biologischen Mechanismen, sowie bei Zellen und biologischem Gewebe in nahem Kontakt mit Festkörpern. Daher gibt es eine Vielzahl von Oberflächenbeschichtungen, die diese Grenzflächen bio-kompatibel machen sollen.

In dieser Arbeit werden verschiedene Oberflächenbeschichtungen aus Lipiden, Proteinen und Polymeren vorgestellt. Mit Neutronenreflektometriemessungen wurde die Ultrastruktur der Schichten in verschiedenen Ebenen bestimmt. Neutronenstreuung hat den grundlegenden Vorteil, dass über die Wahl der Isotope eines Atoms der Kontrast der Probe angepasst werden kann. Ergänzt durch weitere Techniken, wie Röntgenreflektometrie, Fluoreszenzmikroskopie und Atomkraftmikroskopie, konnten Dicke, Zusammensetzung, Wassergehalt und Verformbarkeit der Schichten bestimmt werden.

Eine Mischung von 3:1 neutraler (POPC) und anionischer ( $d_{31}$ -POPS) Lipide wurde durch Vesikelfusion auf Siliziumoxidoberflächen aufgebracht. Diese Vesikel wurden in stark salzhaltigem Puffer präpariert (1,1 M NaCl) und lagerten sich an der Siliziumoxidoberfläche an. Wenn der salzhaltige Puffer durch deionisiertes Wasser ersetzt wurde, platzten die Vesikel durch osmotischen Schock. Die entstehenden Lipiddoppelschichten hatten eine Dicke von 45 Å. Im Bereich der an das Siliziumoxid angrenzenden Lipid-Kopfgruppen befand sich ein dünner Wasserfilm. Innerhalb der Messgenauigkeit fand sich kein POPS in der Membranhälfte, die an das Siliziumoxid grenzte, bedingt durch die elektrostatische Abstoßung. In der dem Siliziumoxid abgewandten Hälfte befanden sich  $(27 \pm 8)\%$  geladene Lipide, was der Zusammensetzung der Vesikel entsprach. Daher war die Stochiometrie der entstandenen Membran nicht durch Flip-Flop der Lipide bedingt, sondern durch den Materialübertrag aus den angelagerten Vesikeln.

Um der Lipidmembran eine natürlichere Umgebung zu bieten, wurde sie mit einem Polymer-Kissen kombiniert. Bei diesen substratgebundenen Lipidmembranen wurden einzelne Lipide über PEG-Ketten an die Oberfläche gebunden. So entstand eine Lipidmembran auf einem 55 Å dicken PEG-Kissen, das einen Wasseranteil von  $(90 \pm 3)\%$  hatte. Trotz der verankerten Lipide war die Membran fluide mit einer Diffusionskonstante von  $(2.1 \pm 0.1) \mu\text{m}^2/\text{s}$ . Durch den hohen Wassergehalt unterhalb der Membran war das komplette System flexibel und konnte mit einer AFM-Spitze um 40 Å verformt werden, bevor die Lipidmembran durchbrochen wurde.

Verschiedenen PEG-beschichteten Oberflächen wurde Fibronectin in Lösung zugesetzt und anschließend das Zellverhalten auf den Oberflächen beobachtet. Im Fall von an hydrophober Grundlage adsorbiertem Pluronic (PPO-PEG) bildete PEG eine dünne Schicht, die nur  $(45 \pm 1)\%$  Wasser enthielt. Darauf konnten sich weder Fibronectin noch Zellen anlagern. Im Gegensatz dazu enthielt PEG unterschiedlicher Länge, das mit PLL angelagert wurde,  $(84 \pm 1)\%$  bis  $(90 \pm 1)\%$  Wasser und bildete dickere Schichten in denen sich 0,4 bis 0,7 mg/m<sup>2</sup> Fibronectin ablagern konnte. Zellen konnten über diese Oberflächen migrieren.

Für die Anlagerung von Nervenzellen auf Oberflächen wurde ein spezielles System untersucht. Eine Lipidmembran bedeckte als unterste Schicht die Siliziumoxidoberfläche. Über Biotinanker wurde darauf eine Streptavidinschicht gesetzt an die wiederum über Biotin ein synthetisches Zelladhäsionsprotein gebunden wurde. Zwischen Lipidmembran und Streptavidin befand sich eine 26 Å dicke Wasserschicht. Beide Proteine bildeten dicht gepackte Monolagen, wobei die 38 Å dicke Streptavidinschicht nahezu wasserfrei war und die 30 Å dicke Schicht des Zelladhäsionsproteins 12% Wasser enthielt. Neuronale Stammzellen breiteten sich auf derartigen Oberflächen aus, während sie auf reinen Lipidmembranen oder Streptavidinoberflächen Kugeln mit wenig Oberflächenkontakt bildeten.

# Summary

At interfaces between solids and biological organisms, soft organic matter in hydrous environment meets hard surfaces. These kind of interfaces play a role in model systems for the study of biological mechanisms, as well as in cells and biological tissue in close contact with solids. Therefore, there are a variety of surface coatings to ensure bio-compatibility of these surfaces.

In this work, different coatings consisting of lipids, proteins and polymers are introduced. Ultra structures of the different layers of the films were determined using neutron reflectometry measurements. Neutron scattering has the fundamental advantage, that the contrast of the sample can be adjusted via choosing the isotope of the atoms. Complemented with further techniques such as X-ray reflectometry, fluorescence microscopy, and atomic force microscopy, thickness, composition, hydration and deformability of the layers could be determined.

A mix of 3:1 neutral (POPC) and anionic ( $d_{31}$ -POPS) lipids was deposited on silicon oxide surfaces via vesicle fusion. The vesicles were prepared in buffer with high salt concentration (1.1 M NaCl) and adsorbed to the silicon oxide surface. By exchanging the buffer for deionized water the vesicles ruptured through osmotic shock. The resulting lipid bilayers had a thickness of 45 Å. In the region of the lipid head groups adjoining the silicon oxide a thin water film was found. Within measurement precision, there was no POPS in the membrane half adjoining the silicon oxide, caused by electrostatic repulsion. In the half turned away from the silicon oxide,  $(27 \pm 8)\%$  anionic lipids were found which conforms to the vesicle composition. Therefore, stoichiometry of the resulting membrane was not caused by lipid flip-flop but by the material transfer from the adsorbed vesicles.

In substrate tethered lipid bilayers, individual lipids were anchored to the surface via PEG-polymer chains. The result was a lipid membrane sitting on a 55 Å PEG cushion with

a hydration of  $(90 \pm 3)\%$ . In spite of the tethered lipids, the membrane was fluid with a diffusion constant of  $(2.1 \pm 0.1) \mu\text{m}^2/\text{s}$ . Because of the high hydration beneath the membrane the whole system was flexible and could be deformed with an AFM tip for  $40 \text{ \AA}$  before the lipid bilayer ruptured.

Fibronectin solution was added to different PEG-coated surfaces and afterwards, cell interaction with those surfaces was analyzed. In case of Pluronic (PPO-PEG) adsorbed to a hydrophobic surface, PEG formed a thin layer containing only  $(45 \pm 1)\%$  water. On that layer, neither fibronectin nor cells could adsorb. On the contrary, PEG of different length adsorbed via a PLL backbone contained  $(84 \pm 1)\%$  to  $(90 \pm 1)\%$  water and established a thicker layer into which  $0.4$  to  $0.7 \text{ mg/m}^2$  of fibronectin could adsorb. Cells were able to migrate across these surfaces.

For attachment of neural cells to surfaces a system of three layers was investigated. A lipid bilayer covered the silicon oxide surface. A streptavidin layer was spread across with biotin anchors, and on top a synthetic cell adhesion protein was bound using biotin anchors again. In between the bilayer and the streptavidin, a  $26 \text{ \AA}$  water layer was found. Both protein layers showed densely packed monolayers, where the  $38 \text{ \AA}$  streptavidin layer was nearly water free and the  $30 \text{ \AA}$  layer of the cell adhesion protein contained  $12\%$  water. Neuronal stem cells spread on these surfaces whereas on lipid membranes or streptavidin surfaces they were round-shaped and had low surface contact.

# Chapter 1

## Introduction

Biophysics is a branch of science concerned with the application of physical principles and methods to biological problems [8]. Since the variety of components of a biological organism is too complex for all-encompassing physical description, the approach is to concentrate on individual aspects or simplified model systems. This study addresses interfaces consisting of lipid bilayers, polymers and proteins as well as cell interaction with such surfaces.

In biological organisms, interfaces play an important role, both as the separation to the outside and to compartmentalize the organisms' inside. Lipid membranes enclose cells at their whole and also many of the organelles inside such as cell nucleus or mitochondria. They are impenetrable for ions and big molecules, and therefore allow concentration gradients between both sides of the membrane. Also the lipid bilayer functions as matrix for proteins [9]. Many functions of the cell are regulated by proteins inserted into or associated to membranes. Some of them function as ion channels or ion pumps to sustain the adequate concentrations [10], while others regulate membrane fusion [11] or signaling [12]. Also, cells produce proteins on the outside of the cell membrane to interact with and adhere to surfaces. On the inside of the cell the cytoskeleton provides an important contribution to the cell's stability. It is built of polymeric filaments: actin filaments, microtubules and intermediate filaments. These filaments stabilize the cell shape and can actively deform the cell [13] or move components inside [14].

The study of interfaces in a biological organism is complicated by their small size, which often makes it impossible to focus on a single interface. One approach to this problem, which was used here, is to place the chosen interface on top of a solid substrate. This

renders the selected interface accessible on a macroscopic area and makes a variety of surface sensitive techniques applicable to study the system. Also, it reduces the complexity of the biological system by its confinement into a plane.

One biological system suitable to study on a substrate is the lipid bilayer [15]. The amphiphilic structure of lipids causes them to self-assemble. In highly hydrous environments they most commonly form into micelles, vesicles and bilayers. On hydrophilic surfaces, often a lipid bilayer will even form spontaneously after addition of lipid vesicles. Many other surfaces can be covered by a lipid bilayer via preparation techniques such as Langmuir-Blodgett [16], or spincoating even when the lipids do not spread on their own. A supported lipid bilayer system can be applied for the study of a solitary bilayer as well as to provide an interface between living and inorganic material.

The drawback of the supported bilayer system is, that the artificial interface might hinder the biological functions of natural cell membranes. This makes a more sophisticated surface covering necessary, as it poses a problem for attachment of living cells to a surface and for the study of membrane proteins [17]. To counteract this problem, the solid surface can be covered with an organic layer, that is tuned to the biological element of the study and places it further removed from the solid surface [18]. Instead of one single bilayer, a multilayer can be manufactured [19].

Hydrated polymers can be used to elevate the biological surface from the solid substrate mimicking the task of the cell filaments. Both the type of polymer and its configuration on the surface influence the adhesion of bilayers [20], proteins [21], and cells [22]. Since cells produce proteins to attach to surfaces, a working point to regulate cell attachment is, to provide the cells with a surface that has the attachment proteins already included [23].

In this work different systems consisting of lipids, proteins, and PEG polymers were studied in hydrous environment on silicon oxide surfaces. Focus is on the interaction between selected components, which can be of electrostatic, hydrophobic or steric nature, as well as specific protein binding. Starting from the surface, crossing to the polymer, lipids, proteins, and finally cells as a whole, the aim is to understand and control the assembly and behavior of these systems. This is a necessity for the use of the model systems in further studies on the way to understanding living organisms, as well as for development of artificial interfaces between inorganic and living matter, i.e. in medical implants.

The technique mainly used in this work is neutron reflectometry [24]. Neutron scattering has several advantages over other techniques used to characterize biological systems: neutrons penetrate into the system and can therefore resolve the inner structure of the layer without destroying it. Also, the exact composition of the sample is quantifiable, as the contrast of several components can be adjusted by using different isotopes of a chemical element. Most commonly that means exchanging hydrogen atoms for deuterium [25]. After a set of several measurements is performed on the same system, the hydration and / or the amount of a chosen component (e.g. lipid composition of the bilayer or amount of protein adsorbed to the interface) can be evaluated. Neutron reflectometry is perfectly suited to the study of thin interfaces. It can resolve thin films on the nanometer scale, i.e. it can provide insight to the substructure of lipids bilayers which have a overall thickness of 4 - 5 nm [26].

Additionally, the samples were characterized with complementary techniques. Scattering with X-ray leads to lower contrast in organic samples but provides even better resolution of thin films than with neutrons [27]. In contrast to the reflectometry techniques which average over the whole of the illuminated surface, atomic force microscopy (AFM) probes a small area, scans the surface, and tests for softness and deformability [28]. Fluorescence microscopy is an established technique to optically observe substances which are marked with a fluorescent dye. The resolution is sufficient to observe single cells or cell organelles. Fluorescence recovery after photo-bleaching is an extension to a standard fluorescence microscope and was employed to measure diffusion in lipid bilayers [29].

This thesis is organized as follows:

- Chapter 2: Concepts and methods
- Chapter 3 - 5: Results, partially published
- Appendix A: Fulltexts of publications



# Chapter 2

## Study of lipid and polymer films: concepts and methods

### 2.1 Lipid membranes as biological interfaces

#### 2.1.1 Natural cell membranes

All cells are surrounded by a cell membrane made up of lipids and proteins. Most defining characteristic of cell membranes is their amphiphilic structure. Both lipids and membrane proteins consist of a hydrophobic and a hydrophilic regions. For this reason they organize into the cell membranes, which separate the cell from its surrounding and also compartmentalize areas inside the cell. Membranes are flexible and vary in their topology. Depending on the form of the lipids (i.e. the relation between the size of the lipid head and that of the lipid chains) and on the associated proteins, they aggregate into planar or highly curved structures.

The lipids of the membranes act as matrix for many of the proteins that regulate the function of the cell, e.g. regulates the ionic gradient on both sides of the membrane [17]. The function of biological organisms is highly dependent on the processes that take place in the lipid bilayer, making understanding cell membranes one of the important tasks for understanding living organisms.

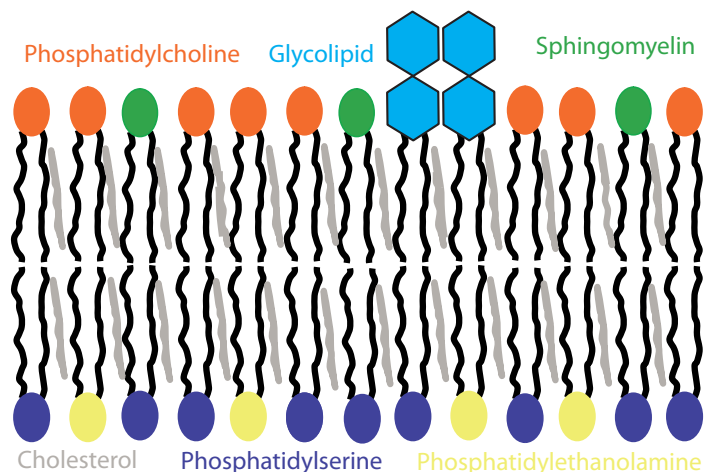


**Figure 2.1:** Lipid composition of an eucariotic plasma membrane: phosphatidylcholine (PC), phosphatidylethanolamine (PE), phosphatidylserine (PS), phosphatidylinositol, glycolipids and cholesterol.

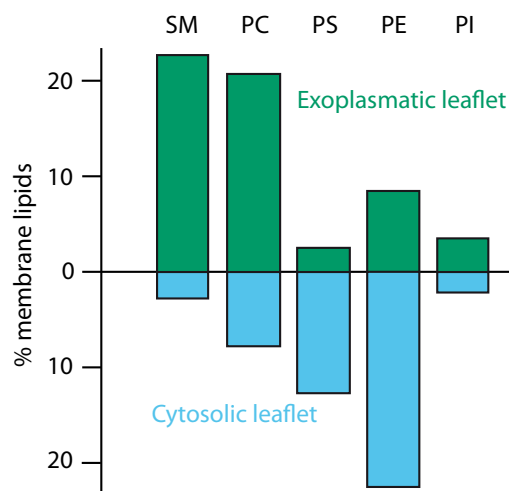


**Figure 2.2:** Natural composition of the lipid bilayer of an eucariotic cell: SM, PC, PS, PE and PI are distributed asymmetrically across the two leaflets.

Natural lipid bilayers are strongly asymmetric and consist of a variety of components, among them different kinds of lipids. A sketch of a natural bilayer is depicted in fig. 2.2. The most common structural lipids in eukaryotic membranes are phosphatidylcholine (PC), phosphatidylethanolamine (PE), phosphatidylserine (PS), phosphatidylinositol and phosphatidic acid [30]. Additionally, there is sphingomyelin (SM) and glycolipids present. These lipids are not distributed equally among both halves of the bilayer (Fig. 2.2).

The asymmetry plays an important role in membrane properties, for cell fusion, activation of the coagulation cascade, and recognition and removal of apoptotic cell corpses by macrophages in case of programmed cell death [31]. Distribution of lipids in the bilayer is organized by the enzymes flippases, floppases and scramblases that sort lipids into their respective leaflet. Spontaneous trans bilayer motion (flip-flop) rates depend on the composition of the bilayer [32]. Natural lipid bilayers consist of mostly PE, PS and CI in the cytosolic leaflet, while the exoplasmatic leaflet is made up of SM, PC and CI with smaller amounts of PE [33].

Many properties of lipid bilayers such as thickness and phase transition temperatures depend on lipid chains. There are lipids with saturated fatty acids such as dipalmitoyl-glycero-phosphatidyl-choline (DPPC), and with unsaturated fatty acids such as dioleoyl-glycero-phospho-choline (DOPC). The lipids palmitoyl-oleoyl-glycero-phosphatidyl-choline (POPC), stearoyl-oleoyl-glycero-phosphatidyl-choline (SOPC), have one of each. In general, the phase transition temperature is lower the more unsaturated the chains are. Charged lipids have different head groups, for example the negatively charged palmitoyl-oleoyl-glycero-phosphatidyl-L-serine (POPS) or dioleoyl-glycero-phosphatidyl-L-serine (DOPS).

### 2.1.2 Supported lipid bilayers

For the study of structure and function of cell membranes and their components, it is practical to have the lipid bilayer seated on a solid surface, as multiple surface sensitive techniques require a planar and defined surface to be employed [15]. There are different methods to deposit lipids onto solid surfaces, such as vesicle fusion [34], spin-coating and transfer of monolayers via Langmuir-Blodgett-technique [16].

Lipids prefer adhesion to hydrophilic surfaces, as the polar outer head-group interacts with the surface. One problem of solid surfaces in close proximity of the bilayer is the possible distortion of natural behavior as the proteins stick to the surface and denature and the lipid bilayer is impeded in its flexibility. Therefore, soft interlayers are employed to cushion the membrane against the support [18]. As a further advancement, in tethered lipid bilayers some lipids are anchored to the surface via polymers [35] or proteins [36].

## 2.2 Polymers

Polymers are macromolecules that consist of a long chain of identical units. There is a great variety of natural and synthetic polymers with a broad range of properties. Polymers are used in combination with biological systems, e.g. to passivate a surface, to cushion against the solid surface, or to tether components to the support. In these systems understanding of polymer behavior and interaction with other components is of importance.

### Polymer coils

The units of the polymer are flexible against each other, allowing the polymer chain to structure into a random coil. The size of the coil depends on the stiffness (persistence length), excluded volume, and ability of the units to rotate against each other. Disregarding excluded volume, the size of an ideal polymer coil in a good solvent can be described by the Flory radius [37]. The Flory radius  $R_F$  depends on the number of units  $N$  and the unit size  $a$ .

$$R_F = N^{3/5}a \quad (2.1)$$

### Grafted polymers

When Polymers are adsorbed to a surface with one end, the conformation and thickness of the polymer layer depends on the size of the polymers and the grafting density as described by de Gennes [38]. For polymers grafted closer to each other, the polymer chains stretch out while their volume stays constant. In that case, the relation of polymer height  $L$  and grafting density  $s$  is:

$$L = Na(a^2s)^{1/3} \quad (2.2)$$

For a low density of grafted points, coils do not overlap. So each polymer forms a half sphere with height  $R_F$ .

### 2.2.1 Polyethylene glycol (PEG)

Polyethylene glycol (PEG), also known as polyethylene oxide (PEO) is a polymer readily available in a range of molecular weights and highly soluble in water. Its monomers consist of two carbon, four hydrogen, and one oxygen atom. Its low toxicity as well as its inertness make PEG the polymer of choice for many occasions.

## 2.3 Immersed surfaces: electrostatic surface potential

When surfaces that can donate or accept protons are immersed in solution, some solid surfaces will carry charges depending on the pH of the solution. SiO<sub>2</sub> has OH-groups on the surface that can be de-protonated, resulting in a charged surface of -0.14 C/m<sup>2</sup> at pH 7.4 [39].

The range of the hydrostatic potential depends highly on the ion concentration in the solution since ions in solution aggregate in proximity to the surface and counteract the surface charge. It is described by the Debye length  $l_D$

$$l_D = \sqrt{\frac{\epsilon_0 \epsilon_r k_B T}{2 N_A e^2 I}} \quad (2.3)$$

The resulting surface potential for SiO<sub>2</sub> at different salt concentrations is illustrated in fig. 2.3.

## 2.4 Diffusion

Lipids in a bilayer or a cell membrane are mobile and diffuse freely in the plane of the bilayer [40]. Generally, diffusion is the uncoordinated and undirected movement induced by Brownian motion. It can be described as the change of a concentration  $c$  over time depending on local differences in concentration.

$$\frac{\partial c(r, t)}{\partial t} = D \nabla^2 c(r, t) \quad (2.4)$$

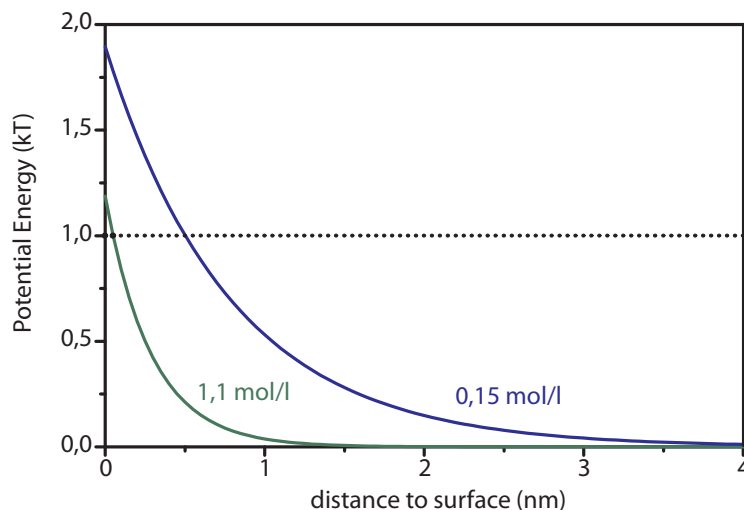


**Figure 2.3:** Surface potential of  $\text{SiO}_2$  at concentrations of 1.1 M and 0.15 M NaCl.

This differential equation can be resolved by the Gaussian function, with diffusion constant  $D$ . For a lipid bilayer confined to two dimensions that is:

$$c(r, t) = \frac{1}{4\pi Dt} \exp\left(-\frac{r^2}{4Dt}\right) \quad (2.5)$$

The squared mean distance the lipid moved, depends on time  $t$  and diffusion constant  $D$ :

$$\langle r^2 \rangle = 4Dt \quad (2.6)$$

## 2.5 Fluorescence microscopy

A fluorescence microscope is a variation of a normal optical microscope. It has additional band pass filters and mirrors in the optical path, that inhibit any direct light from the lamp to reach the ocular or camera. Light with the shorter excitation wavelength can pass from the light source to sample and is used to excite the dye. Only the emitted light with longer wavelength can pass to detection. Therefore, only components marked with fluorescent dye are visible.

In biology, fluorescence microscopy is an established technique to image cells and their components. The fluorescent dye can be either tagged to a small amount of components (i.e. lipids or protein) synthetically or expressed by the biological organism themselves. For the fluorescence expression, genetically modified organisms are used, that had the genetic code of the green fluorescent protein (GFP) transplanted [41].

### 2.5.1 FRAP

Since individual lipids are too small to observe optically via a microscope, a more indirect measurement of the lipid diffusion is necessary. One widely applied method for the determination of mobility in such systems is FRAP (fluorescence recovery after photobleaching) [42]. A FRAP setup consists of a fluorescence microscope with an additional laser.

A spot of a diameter of several  $\mu\text{m}$  is bleached of any fluorescent dye by the laser. The return of fluorescence in the bleached spot is recorded over time. The profile of the bleached spot can be described by a Gaussian function with width  $\sigma(t)$ . From the increase of the width  $\sigma$ , the diffusion constant  $D$  of the fluorescence tagged component can be determined by:

$$\sigma^2(t) = \sigma_0^2 + 2Dt \quad (2.7)$$

## 2.6 AFM

Atomic force microscopy (AFM) is a technique that probes a surface mechanically with a small tip attached to a cantilever. On solids, AFM has a resolution on the atomic scale, the surface is mapped with a scan [43]. This surface mapping even works on lipid bilayers under water [44]. For soft samples, AFM can also be employed to determine softness and deform-ability.

On lipid bilayers, punctuation curves can be recorded with an AFM. When the tip approaches the surface, first the force increases as the lipid bilayer resists. When the lipids give way to the tip, the force decreases abruptly and the tip approaches the rest of the distance up to the support [45].

## 2.7 Neutron and X-ray scattering

Scattering experiments with neutrons and X-rays give insight into the structure of solids and surfaces. Wavelengths of this radiation is in the order of Å, therefore a resolution on the sub-molecular scale is possible.

### 2.7.1 Refractive index

The movement of photons and neutrons in matter can be described by assigning a refractive index to the material [46]. This complex refractive index  $n^*$  can be written as:

$$n^* = 1 - \delta + i\beta \quad (2.8)$$

for energies far from absorption edges. Dispersion  $\delta$  depends on the wavelength  $\lambda$  and the scattering length density (SLD)  $\rho_b$ :

$$\delta = \frac{\lambda^2}{2\pi} \rho_b \quad (2.9)$$

The imaginary part of the refractive index depends on the absorption coefficient  $\mu$ :

$$\beta = \frac{\lambda}{4\pi} \mu \quad (2.10)$$

### 2.7.2 SLD calculation and contrast variation

For X-rays, the SLD can be calculated from the electron density multiplied by the classical electron radius. For neutrons, as they interact with the atomic nuclei, the scattering length density has to be calculated from all the scattering lengths of the atoms. Neutron scattering length of an atom depends on the isotope, e.g. for hydrogen, the scattering length varies between -3.7 fm for hydrogen ( $^1_1H$ ) and 6.7 fm for deuterium ( $^2_1H$ ). Therefore, in neutron scattering there is the possibility to choose contrast of components of the system by using specific isotopes.

### 2.7.3 Hydration determination

From a set of two measurements of the same sample in buffers with different contrast (one in D<sub>2</sub>O, the other in a mix of D<sub>2</sub>O and H<sub>2</sub>O) the hydration  $h$  of the sample can be determined. When a layer has the  $SLD_1$  in the first measurement in buffer 1 and  $SLD_2$  in the second buffer 2, the hydration of that layer can be calculated as:

$$h = \frac{SLD_1 - SLD_2}{SLD_{buffer1} - SLD_{buffer2}} \quad (2.11)$$

For the mix of D<sub>2</sub>O and H<sub>2</sub>O, the percentages can be chosen for a match of SLD on both sides of the bilayer. A mix of 58% D<sub>2</sub>O and 42% H<sub>2</sub>O has a SLD equal to that of SiO<sub>2</sub> and is called contrast matched (cm) in this work.

### 2.7.4 Reflectometry

In reflectometry experiments, intensity is magnified by using a big surface. That means, that there is no lateral resolution of the sample surface, the signal is integrated over all of the surface. The combination of X-ray and neutron reflectometry gives structural information about thickness and composition of the different layers of the film. X-ray reflectometry offers superior resolution whereas neutron reflectivity at different deuteration contrasts helps to distinguish components of the sample.

#### Total reflection

When the incident beam is reflected on a layer with higher SLD, i.e. lower refractive index, for small angles, total reflection will occur. The critical angle for total reflection  $\alpha_c$  can be calculated as:

$$\alpha_c \approx \sqrt{2\delta} = \lambda \sqrt{\frac{\rho_b}{\pi}} \quad (2.12)$$

### Momentum transfer $q$

The momentum transfer  $q = k_f - k_i$  can be written depending on wavelength  $\lambda$  and incident angle  $\theta$  as:

$$q = \frac{4\pi}{\lambda} \sin \theta \quad (2.13)$$

### Fresnelreflexion

The reflected intensity on a smooth surface is described by the Fresnel coefficients for reflection (r) and transmission (t) [47].

$$r = \frac{k_{i,z} - k_{t,z}}{k_{i,z} + k_{t,z}} \quad (2.14)$$

$$t = \frac{2k_{i,z}}{k_{i,z} + k_{t,z}} \quad (2.15)$$

$k_{i,z}$  und  $k_{t,z}$  are z-components of the incident respectively transmitted wave vectors.

For large angles, in case of incident angles  $\alpha_i > 3\alpha_c$  the Fresnel reflectivity can be approximated as:

$$R_F \approx \left(\frac{\alpha_c}{2\alpha_i}\right)^4 \quad (2.16)$$

### Multilayer systems

In multilayer systems, the overall reflectivity is a superposition of reflection on all different layers. Parratt's algorithm to calculate that overall reflectivity works recursively and uses for each layer  $j$  the ratio  $X_j$  between reflected and transmitted intensity.

$$X_j = \frac{R_j}{T_j} \quad (2.17)$$

$X_j$  can be written depending on the next layer  $j + 1$  as:

$$X_j = \frac{R_j}{T_j} = \exp(-2ik_{z,j}z_j) \frac{r_{j,j+1} + X_{j+1} \exp(2ik_{z,j+1}z_j)}{1 + r_{j,j+1}X_{j+1} \exp(2ik_{z,j+1}z_j)} \quad (2.18)$$

where  $r_{j,j+1}$  is the Fresnel coefficient of layer  $j$ .

$$r_{j,j+1} = \frac{k_{z,j} - k_{z,j+1}}{k_{z,j} + k_{z,j+1}} \quad (2.19)$$

### Influence of layer roughness

Especially for larger angles, the reflected X-ray or neutron intensity strongly depends on the surface roughness of the sample's layers. One approach to take the surface roughness into account is the introduction of the Nevot-Croce factor [48]. For the Nevot-Croce factor,  $q^2$  is defined on either side of the interface and thus replaced by the geometric average  $q_1q_2$ . The correction for the reflected intensity of a surface with roughness  $\sigma$  is:

$$R_{NC} = R_F e^{-q_1q_2\sigma^2} \quad (2.20)$$

#### 2.7.5 Reflectometry analysis software: Motofit

For data analysis, the calculated reflectivity of a multilayer model is fitted to the experimental data. In this work, the Motofit-program, which runs on Igor was used [49]. Motofit uses Parrat's algorithm and varies coefficients for layer thickness, SLD, and roughness of the model, as chosen by the user, to reach a least square fit.

## 2.8 Reflectometers

### 2.8.1 Neutron instruments

#### REFSANS

REFSANS [50] is a reflectometer and GISANS machine at FRM II in Garching, operated by HZG (Helmholtz Zentrum Geesthacht). The neutron beam is chopped, so a broad wavelength band can be used. The chopper consists of six blades to ensure that only neutrons of the chosen wavelength can pass, see fig. 2.4. The chopper blades can be moved in position, allowing to chose between high flux and high wavelength resolution.

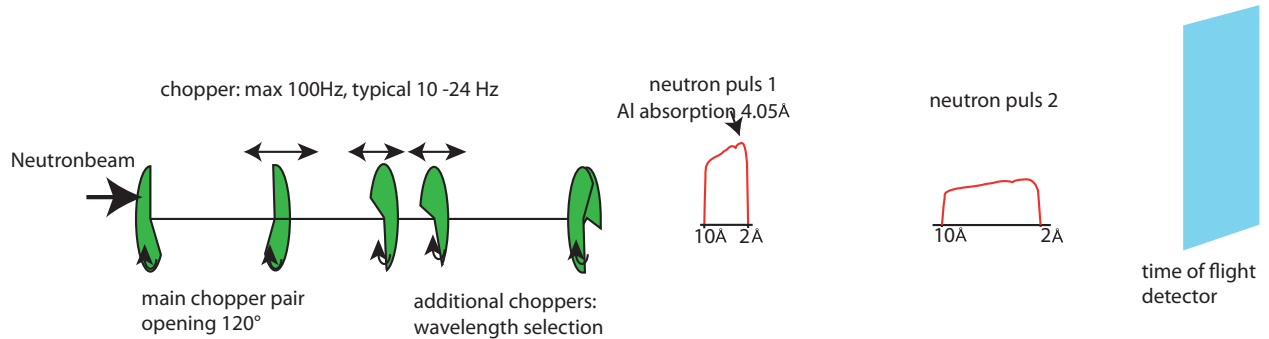


**Figure 2.4:** The white neutron beam coming from the reaktor is pulsed via six chopper blades. The wavelength of each neutron is determined by its time of flight.

While neutrons of all wavelength are at the same position, when they pass the chopper, some time later the neutron pulse is dispersed by the different speed of the neutrons. Each neutron that hits the detector is recorded with both its position on the detector and its time of flight and therefore its wavelength.

Typical values for the wavelength are 2 - 10 Å. The reflectometry measurements were performed at a set of several incident angles with overlapping q-range, e.g. 0.15°, 0.3°, 0.6°, 1.4°, and 2.8°. When the data from all angles is summed up, a continuous data curve up to a q-value of 0.2 Å<sup>-1</sup> can be attained.

## NREX

NREX is a monochromatic reflectometer at FRM II in Garching operated by Max-Planck-Gesellschaft. It uses a monochromator crystal and operates at  $4.3 \text{ \AA}$ . The reflectometry data is measured with a  $\theta - 2\theta$  scan.

### 2.8.2 X-ray instruments

#### X-ray lab setup

In the X-ray lab machine (fig. 2.5) the radiation is produced via a molybdenum X-ray tube. A multilayer mirror aligned to the wavelength of the  $k_\alpha$  line in combination with a set of slits upstream to the sample position ensures a well defined and monochromatic beam of  $17.4 \text{ keV}$ . The sample is mounted into a four-circle goniometer. In the scan, this goniometer tilts the sample as well as moves the detector on a circle around the sample, ensuring the specular beam hits the detector.

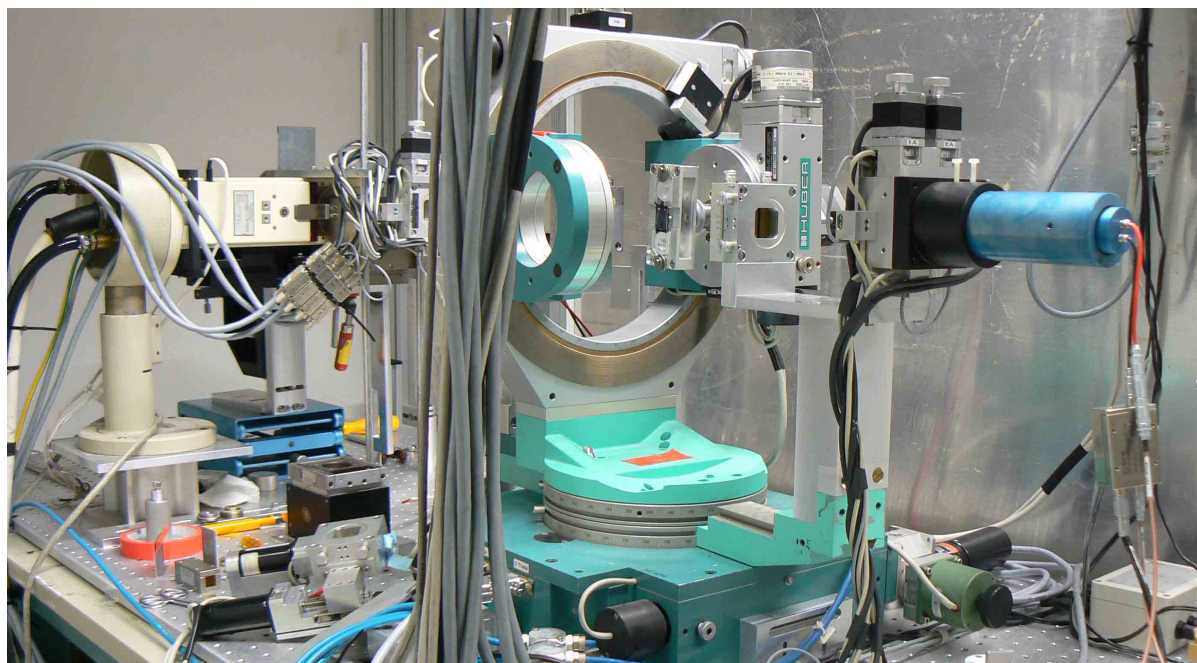


**Figure 2.5:** X-ray lab setup: X-ray tube on the left side, monochromatic mirror, four-circle goniometer, and detector on the right.

The power of the X-ray generator can be tuned. For small reflection angles or high intensity peaks (Bragg peaks) a lower voltage and current is used since the beam would otherwise overload the detector. For larger angles, higher power generates higher intensity and thus a shorter counting time. The X-ray lab setup can run scans up to large angles and the beam width can be varied, making the setup suited for a variety of samples, such as lipid bilayers under water but also highly reflecting multilayer mirrors [6], thin organic films [5], and lipid multilayer systems [7].

### Synchrotron-Beamline D4

In synchrotron X-ray sources, the electrons in the ring are additionally deflected by wigglers or undulators. Both wigglers and undulators are sets of magnets that induce a sinus move of the electrons. These magnets are tuned to the chosen energy for the X-rays, but still emit a broad range of wavelength.

The beamline D4 of HASYLAB / DESY uses a monochromator crystal to filter X-rays with a chosen wavelength via Bragg-reflection. For the measurements on lipid bilayers, the energy of the X-rays was set to 20 keV. Since the intensity of the direct beam or the reflected beam at small angles is too high for the detector, a set of attenuators can be moved in and out of the beam. The reflectivity curve is collected with a  $\theta - 2\theta$  scan of sample and detector angle.

## 2.9 Fluidic chambers for reflectometry and microscopy

All reflectometry measurements were performed in fluidic chambers, that allow for a change of buffer of the sample and for quality control via optical microscopy. For that purpose, the chambers contain reservoirs for the buffer and a glass or foil window separated from the sample surface by a thin channel filled with buffer. The distance between this window and the surface has to be kept small enough to allow a long distance objective microscope to still focus on the surface.

### Chamber for X-ray measurements

For X-ray reflectometry, a silicon wafer of 20 mm x 15 mm was glued into a IBIDI- $\mu$ -slide milled out on the top for the size of the wafer. An assembled X-ray sample chamber is shown in fig. 2.6

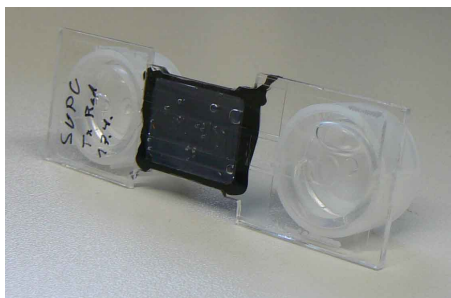


**Figure 2.6:** Fluidic chamber for X-ray measurements and microscopy. Size of the silicon wafer glued into the chamber is 20 mm x 15 mm.

### Chamber for neutron measurements

Neutron measurements were performed on a silicon block of 100 mm x 50 mm x 10 mm inside a chamber built of aluminum, teflon and a quartz window shown in fig. 2.7 When the chamber is assembled, the teflon part is put with the window parallel to the block and screwed close with the aluminum frame.

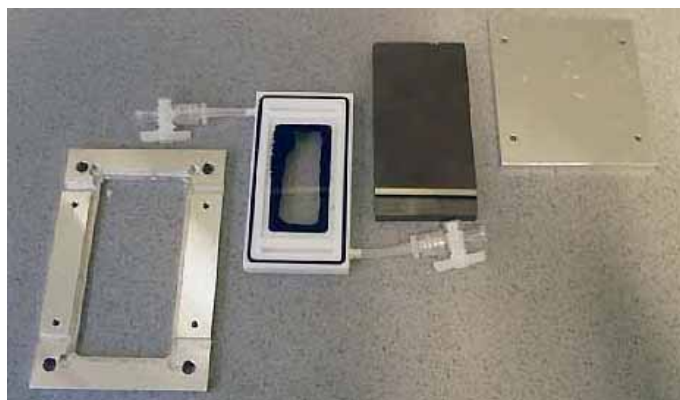


**Figure 2.7:** Components of fluidic chamber for neutron measurements and microscopy. The silicon block size is 100 mm x 50 mm x 10 mm.



# Chapter 3

## Results: Anionic lipid bilayers

Natural lipid bilayers, i.e. cellular membranes, exhibit a high order of asymmetry, as explained in section 2.1. Of special interest is the occurrence of POPS in cell membranes, as its presence in the outer leaflet serves as a marker for apoptosis.

In artificially produced bilayers, lipids can flip from one leaflet to the other on timescales of minutes [51]. Therefore even when the initial leaflet composition is defined, as is possible by depositing the bilayer via the Langmuir-Blottgett technique, the bilayer will restructure. To sustain the asymmetric lipid composition, a force in the system is needed, favoring one kind of lipids in one specific half of the bilayer.

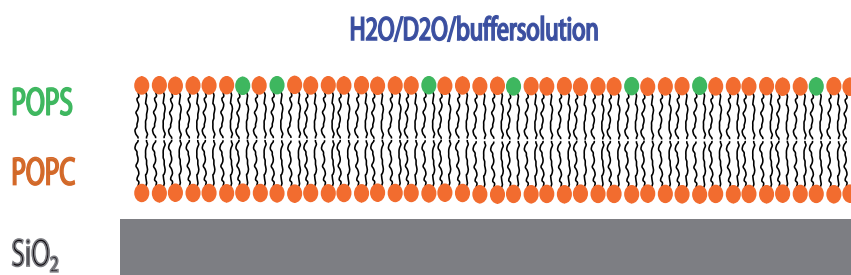


**Figure 3.1:** When a lipid bilayer that consists of neutral and negatively charged lipids is deposited onto negatively charged SiO<sub>2</sub>, the charged lipids are only found in the leaflet adjoining the buffer, not the surface.

Such a force appears, when charged lipids are introduced to the electrostatic surface potential of a charged surface (section 2.3). In this case anionic lipids are repelled from the proximal leaflet by the silicon oxide that also carries negative charge. Such bilayers with

controlled and high contents of anionic lipids in the outer leaflet are versatile platforms for studying the interactions between anionic lipids and proteins that are key elements in the signal transduction pathways in eukaryotic cells [52].

### 3.1 Asymmetric distribution of anionic phospholipids in supported lipid bilayers

The work described in this section has been published [1]. The full article is attached in Appendix A.1.

#### 3.1.1 Sample preparation

POPC/d<sub>31</sub>POPS (3:1) unilamellar vesicles were spread into a bilayer. The vesicles were prepared in high-salt-concentration buffer (1.1 M NaCl). When the buffer was exchanged to DI water, vesicles ruptured and a bilayer formed. Excess lipids were washed away by flushing the fluidic chamber with buffer (salt concentration 0.15 M NaCl) several times, until the lipid bilayer looked homogeneous under the fluorescence microscope. Due to the deuteration of one alkane chain of the anionic POPS, neutron reflectivity on the bilayers could be implemented to reveal the position and the amount of the POPS in the bilayer.

#### 3.1.2 Neutron reflectometry results

A set of two neutron reflectivity measurements were performed at REFSANS (FRMII) (chapter 2.8.1). The first measurement was carried out in D<sub>2</sub>O buffer, the second in contrast matched (cm) buffer, a mix of 58% D<sub>2</sub>O and 42% H<sub>2</sub>O, which has a SLD equal to that of SiO<sub>2</sub>. The data and fit of for these measurements is shown in fig. 3.2, D<sub>2</sub>O data is depicted in blue, cm data and fit in red. The valley in the SLD model (shown in the inset) between 28 Å and 58 Å represents the alkane chains of the bilayer.

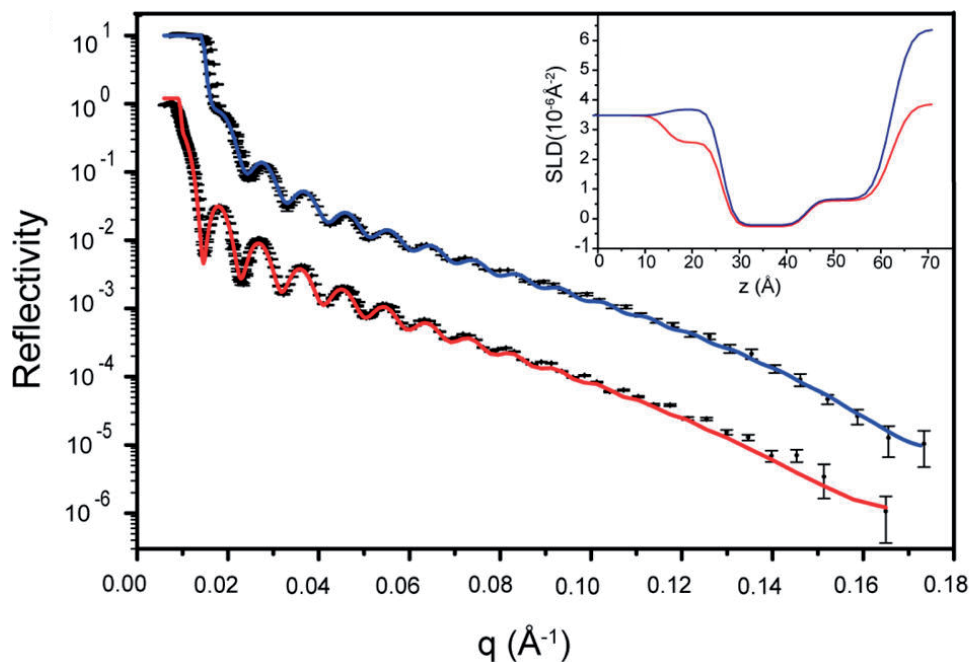


**Figure 3.2:** Reflectivity data and fit of a lipid bilayer spread from vesicles with a lipid mix of 3:1  $d_{31}$ POPS / POPC in  $D_2O$  buffer (blue) and cm buffer (red). The bilayer shows asymmetric leaflets, indicated by the different SLD.

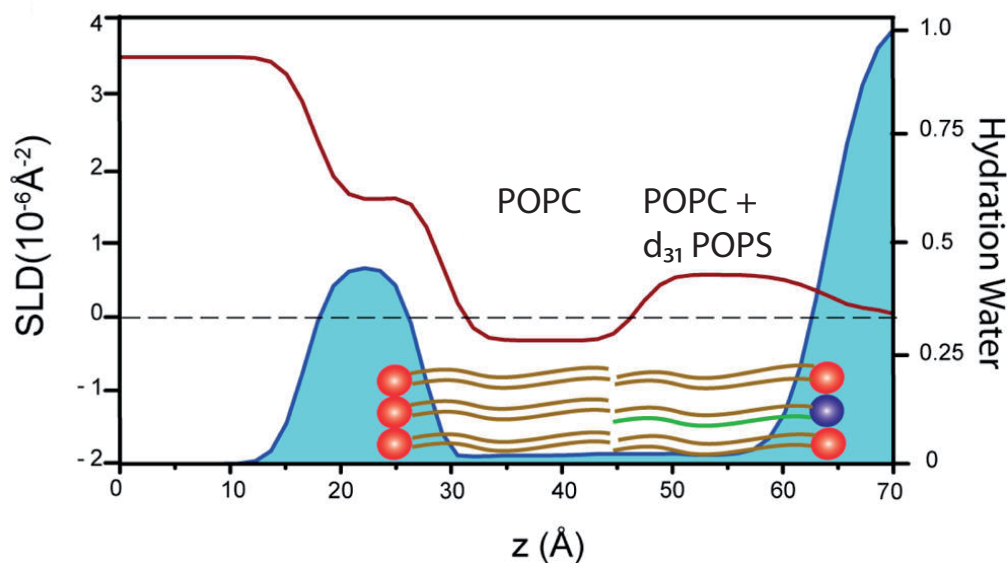


**Figure 3.3:** The head group region of the bilayers are hydrated, as is indicated by the blue area. The brown line pictures the SLD of a 3:1  $d_{31}$ POPS / POPC bilayer without the contribution of the buffer.

Values for the SLD of the lipid's alkane chains (fig. 3.3) were  $(-0.34 \pm 0.20) \times 10^{-6} \text{ \AA}^{-2}$  for the bilayer half facing the substrate and  $(+0.54 \pm 0.23) \times 10^{-6} \text{ \AA}^{-2}$  for the half facing the buffer. The right side showed higher SLD indicating the deuterated lipids were congregated there. Analysis of the exact lipid composition in both leaflets (see fulltext of [1] in appendix A.1) revealed, that no anionic lipids were present in the leaflet adjoining the  $\text{SiO}_2$ , whereas in the leaflet facing the buffer the original composition of 3:1  $\text{d}_{31}\text{POPS} / \text{POPC}$  was preserved.

In fig. 3.3, the SLD, without the contribution of the water, and the hydration (calculated as explained in chapter 2.11) is illustrated. The lipid chain part of the bilayer contained almost no water (1 - 2 %), but there was hydration in the head group region adjoining the  $\text{SiO}_2$ . The head groups facing the buffer were also hydrated, but they were hidden in the transition region between alkane chains and buffer.

The analysis of a 3:1  $\text{d}_{31}\text{POPS} / \text{POPC}$  bilayers showed, that asymmetry in a bilayer could be preserved by electrostatic repulsion of anionic lipids from a charged surface. The lipid composition was not a result of lipid flip-flop, but of material transfer of lipids from vesicles to substrate.

## 3.2 $\alpha$ -synuclein binding to anionic lipid bilayers

### 3.2.1 $\alpha$ -synuclein

$\alpha$ -synuclein is a protein occurring in neural cells where it binds to synaptic membranes. It is medically relevant, since a malfunction of this protein occurs in neural cells of patients suffering from the neuro de-generative Parkinson's disease [53], where  $\alpha$ -synuclein forms big aggregates called Lewy bodies [54]. While  $\alpha$ -synuclein shows a preference for curved bilayer (i.e. small vesicles) it also binds to negatively charged flat bilayers.

### 3.2.2 Sample preparation

The supported lipid bilayer was prepared the same way as in the previous section 3.1.1 with a 3:1  $\text{POPC} / \text{POPS}$  mix without deuterated lipids. A solution of  $1\mu\text{M}$   $\alpha$ -synuclein solution in HEPES buffer was added after the first set of measurements.

### 3.2.3 Reflectometry results

#### X-ray

The X-ray reflectivity data and fit is shown in fig. 3.4, with the SLD model in the inset. A 3 Å thinning of the bilayer and a small loss of contrast between headgroups and lipid chains was noticeable after addition of  $\alpha$ -synuclein. The thinning indicated restructuring of the bilayer. The loss of contrast could hint to either protein insertion or water inclusion in the lipid film.

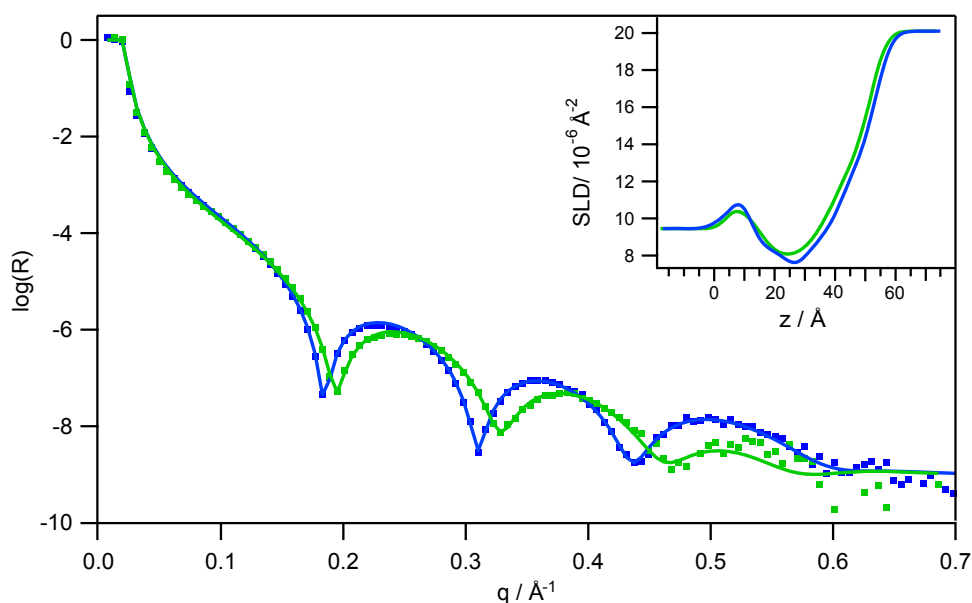


**Figure 3.4:**  $\alpha$ -synuclein interaction to a supported lipid bilayer: X-ray reflectivity data and fit of POPC - POPS (3:1) before (blue) and after (green) addition of  $\alpha$ -synuclein into the bilayer. SLD model for the fit is shown in the inset.

#### Neutron

The neutron data in fig. 3.5 confirms the membrane thinning effect of  $\alpha$ -synuclein. Analysis of the data did not yield significant contribution of the protein to the SLD model within the precision of measurement, even when deuterated protein was used (measurement with deuterated  $\alpha$ -synuclein is not shown).

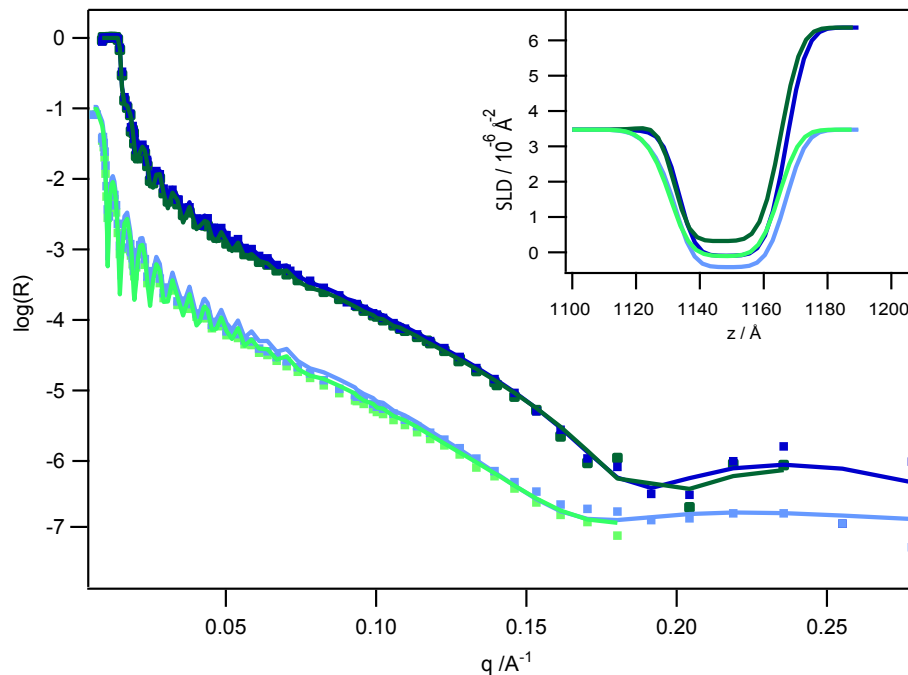


**Figure 3.5:**  $\alpha$ -synuclein interaction to a supported lipid bilayer: Neutron reflectivity data and fit of POPC - POPS (3:1) at two contrasts: Dark colours are measured in  $D_2O$ , light colours in  $cm$ . Data and fit before addition of  $\alpha$ -synuclein (blue) and after (green). The  $cm$  data is shifted by a factor 10. The SLD model for the fit is shown in the inset.

### 3.2.4 Interpretation of $\alpha$ -synuclein data

$\alpha$ -synuclein, especially if deuterated, would provide strong contrast in the lipid chain region. Therefore, the binding of  $\alpha$ -synuclein to the membrane must have been limited to the head group region of the lipid bilayer. The small change of SLD in the chain region represents a slightly increased amount of water in the bilayer. This increase of water did not occur in all measurements and is likely due to the instability of the negatively charged bilayer in the  $\alpha$ -synuclein solution, since the  $\alpha$ -synuclein was added in HEPES buffer without NaCl.

We interpreted these results as, that by wedging in between the lipid bilayer headgroups,  $\alpha$ -synuclein restructured the membrane. In this case, the thinning would have been caused by the change in area per lipid while the lipid chains volume stayed constant.

### 3.3 Phase separated bilayer

As is shown in the section 3.1, both halves of bilayers can be made up of different composition in case of a repelling force to one of the lipid species in the mix. On the other hand, the morphology of bilayers made up of different kind of lipids depends on their phase at the temperature. When one species of lipids is above its phase transition temperature and the other below, a de-mixing of the lipids into domains of different phases will occur.

As DPPC has a phase transition at 41 °C, and DOPS at -11 °C, that phase separation is the case for bilayers composed of DPPC and DOPS at room temperature. When both leaflets of the bilayer initially consisted of lipids in different phases, after some time to equilibrate, both halves of the bilayer are present in the same phase [55]. Additionally, the charged lipids distribute inside the uncharged matrix to minimize free energy [56]. And, since both kinds of lipids exist in different phases at room temperature, domain separation occurs [57].

The question arises, how the bilayer will behave, when the repulsive force from the substrate works to remove one species of lipids from the lower leaflet? In AFM measurements it has been shown, that depending on the  $\text{Ca}^{2+}$  concentration, the bilayer is structured differently. Many small domains are present in buffer with 4mM  $\text{CaCl}_2$ . When there is no  $\text{Ca}^{2+}$  present in the buffer (after flushing with EDTA), the lipids de-mix into large areas as is illustrated in fig. 3.6 [58].

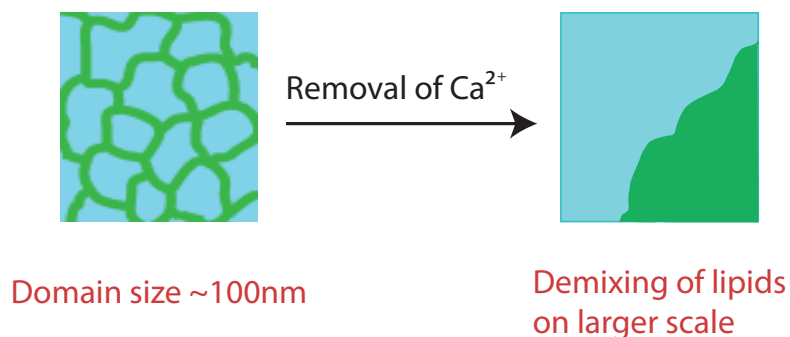


**Figure 3.6:** Domain structure of 4:1  $d_{62}$ DPPC / DOPS in  $\text{Ca}^{2+}$ -buffer (left side) and EDTA buffer (right side). Without the presence of  $\text{Ca}^{2+}$  ions, the small domains are unstable and the phases separate on a larger scale.

### 3.3.1 DPPC-DOPS neutron reflectivity

The reflectometry data and fit of a 4:1  $d_{62}$ DPPC / DOPS bilayer is shown in fig. 3.7. The measurement was performed at two contrasts,  $D_2O$  buffer in red, cm buffer in green. Both buffers contained 4 mM  $CaCl_2$ . The small oscillations in intensity were caused by the oxide layer of the silicon, whereas the signal from the bilayer is represented as the shoulder of the data curve.

In this experiment, DPPC with completely deuterated chains was used. Due to the high content of deuterium, the alkane chains of the bilayer show up with higher SLD in fig. 3.8 compared to the bilayers shown in the previous sections. In the SLD model for the fit of the reflectometry data in fig. 3.8 both halves of the bilayer show significant difference in SLD. The chain region of the bilayer leaflet facing the  $SiO_2$  has a SLD of  $6.6 \times 10^{-6} \text{ \AA}^{-2}$  respectively  $6.3 \times 10^{-6} \text{ \AA}^{-2}$  in  $D_2O$  and cm. In the leaflet adjoining the buffer, the SLD is lower at  $5.6 \times 10^{-6} \text{ \AA}^{-2}$  respectively  $5.3 \times 10^{-6} \text{ \AA}^{-2}$ .

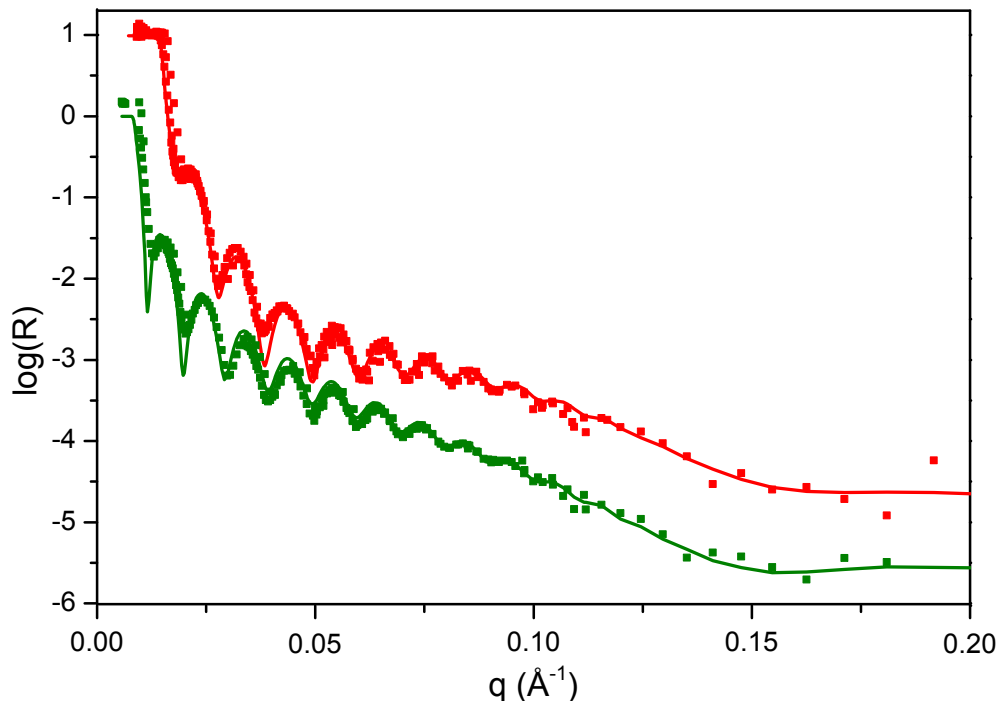


**Figure 3.7:** Reflectometry data and fit of  $d_{62}$ DPPC / DOPS (4:1) in  $D_2O$  buffer (red), cm buffer (green). The green curve is shifted by a factor of 10 for better visibility. Both buffers contained 4 mM  $CaCl_2$ .

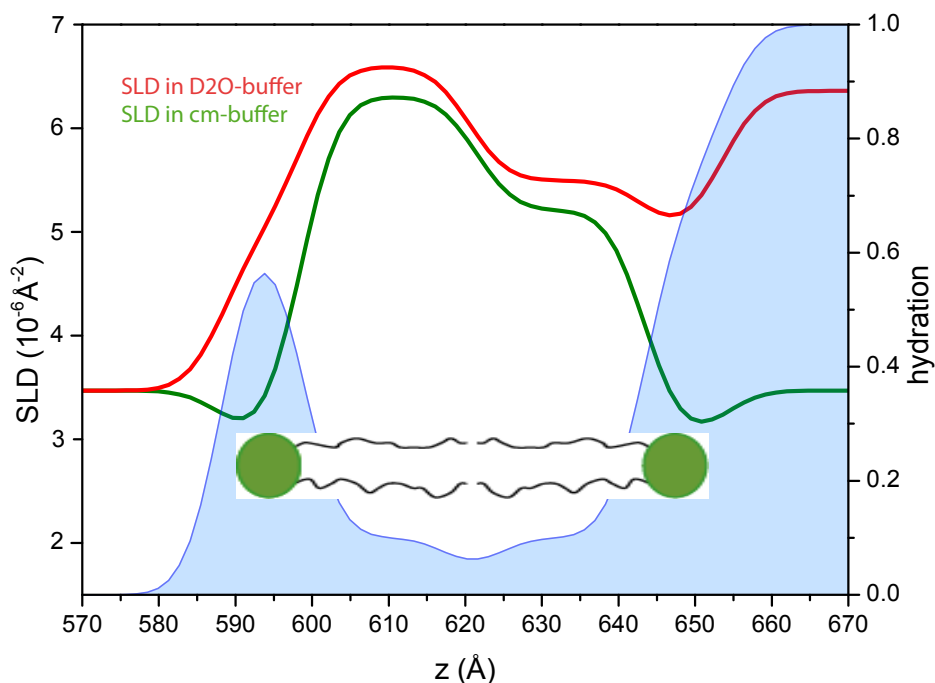


**Figure 3.8:** Hydration and SLD of a 4:1  $d_{62}$  DPPC / DOPS bilayer. The lipid chains of both bilayer halves have different SLD indicating a different lipid composition. As the DOPS is the component not deuterated, it is contained to the leaflet with lower SLD facing the buffer.

The analysis of the exact bilayer composition yields, that the leaflet adjacent to the silicon does not contain any anionic DOPS, whereas the lipid composition of the other leaflet maintains the original 4:1 mix of the vesicles in accordance to the results of chapter 3.1.

The electrostatic forces repulsing the anionic lipids from the surface prevents anionic lipids from flipping into the other leaflet as it would be normally observed for bilayers in mixed phases [55].

### 3.3.2 In plane structure of bilayer depending on $\text{Ca}^{2+}$ presence

Neutron reflectometry suppresses any information not contained in the specular reflection and therefore provides no information about lateral sample structure. In GISANS (grazing incident small angle neutron scattering) the off-specular signal is analyzed [59] and thus the in-plane structure of an interface can be analyzed [60]. GISANS has been successfully employed to study the structure of polymers [61] and porous metallic structures [62].

We employed GISANS to observe the domain structure differences in the  $\text{d}_{62}\text{DPPC}$  / DOPS bilayer with and without the presence of  $\text{Ca}^{2+}$  ions. When the  $\text{Ca}^{2+}$  was removed via flushing the chamber with EDTA buffer, the small domains should disband as a de-mixing of lipids on a larger scale occurs [58]. Since the domains changed significantly in size, the difference in both bilayer conformations should be visible in a GISANS recorded from the sample.

#### GISANS data

The GISANS measurement of the 4:1  $\text{d}_{62}$  DPPC / DOPS was performed at an incident angle of  $0.5^\circ$ . A radial collimator focuses several neutron beams on the sample, that meet up in one spot on the detector to maximize intensity. The intensity of the detector is summed up over a range of wavelength. In fig. 3.9 the GISANS images for wavelengths between 2 Å and 4 Å are shown in  $\text{Ca}^{2+}$ buffer (a) and in EDTA buffer (b).

#### Yoneda peak

The Yoneda peak occurs when either incident angle  $\alpha_i$  or the scattered angle  $\alpha_f$  is at the same value as the critical angle of total reflection  $\alpha_c$ . Since the incident angle for GISANS is fixed and  $\alpha_i > \alpha_c$ , a yoneda peak occurs at:

$$\alpha_f = \alpha_c \quad (3.1)$$

Its intensity depends on scattering contrast in the interface. That contrast can be a result of roughness or, as in the presented case, by domains of different SLD in the interface.

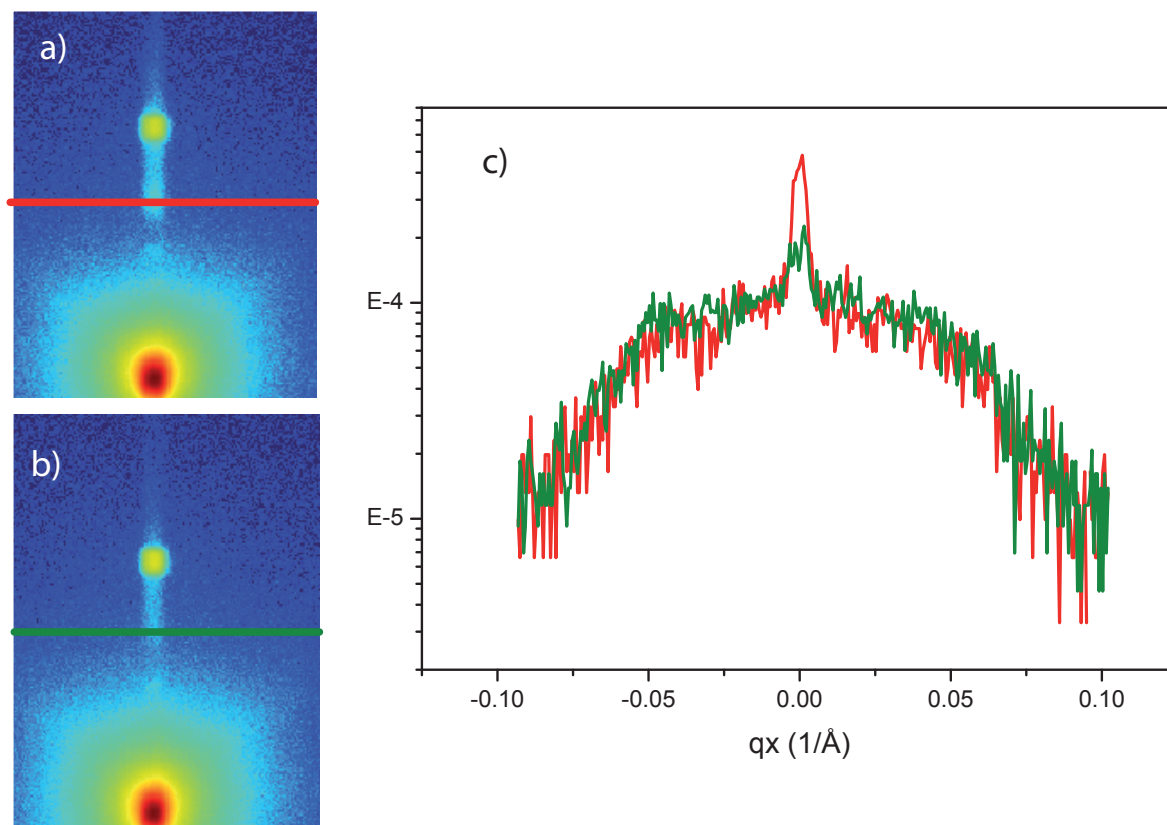


**Figure 3.9:** GISANS maps of 2 - 4 Å of  $d_{62}$  DPPC - DOPS (4:1) in  $Ca^{2+}$ -buffer (a) and in EDTA-buffer (b). Intensity line cuts through the Yoneda peak, indicated by the red and green lines in the maps, are plotted in (c).

There is a significant difference in the intensity at the position of the Yoneda peak in the two images shown in fig. 3.9 a) and fig. 3.9 b): The peak intensity decreases after removal of  $Ca^{2+}$ . The position of the Yoneda peak is indicated with a red line in 3.9 a) ( $Ca^{2+}$ -buffer) and a green line in fig. 3.9 b) (EDTA buffer). In fig. 3.9 c) these linecuts are plotted for direct comparison. When the small domains dissolved, the contrast in the lipid bilayer film was reduced, which diminished the intensity of the Yoneda peak.



# Chapter 4

## Results: Tethered lipid bilayers

Part of the work described in this chapter has been published [2]. The full article is attached in Appendix A.2.

One of the ideas to make an artificial lipid bilayer on a solid surface more natural is to elevate the lipid bilayer via a polymer cushion to preserve the deformability [63] and allow for fluctuations [64]. For stability, the bilayer can be tethered to the surface. There are a variety of systems that use different methods to archive that aim [65]. Some graft the whole lower leaflet [66] or individual lipids [67] to the surface, while others use a tethered trans membrane protein as anchor inside the bilayer [68].

In this work, the chosen system is that of a PEG-tethered lipid bilayer (TLB). PEG coatings are widely used to passivate surfaces against non-specific protein adsorption and are neither charged nor hydrophobic, and therefore not expected to exert significant influence on the bilayer characteristics. On pure PEG surfaces however, lipid bilayers do not spread. This conflict was resolved using PEG functionalized with lipids.

The work presented in this chapter is a continuation of earlier experiments conducted by Christian Daniel, who developed the TLB system [69]. Here, the method of lipid deposition was changed to spin-coating. With spin-coating the amount of lipids deposited to the surface could be regulated, and thus lipid inclusion in the PEG layer, which occurred in the earlier experiments, was prevented.

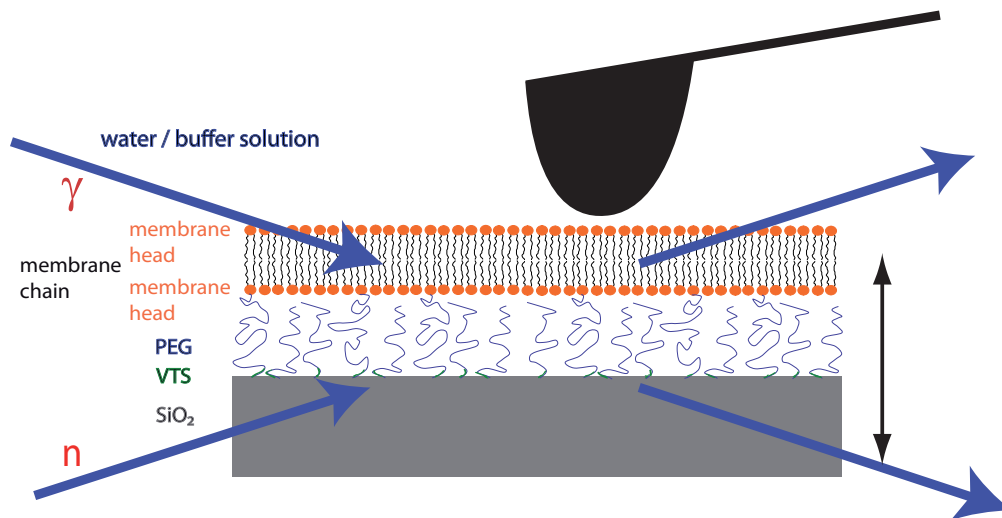


**Figure 4.1:** Sketch of the TLB system. The direction of the incident beam was from the buffer for X-rays and from the silicon for neutrons. The AFM tip compresses the bilayer and the PEG cushion from the top.

The TLB system structure and hydration was fully characterized using a combination of neutron and X-ray reflectometry. Diffusion of fluorescence dye labeled lipids was determined with FRAP. Additionally, the deformability of the system was proven with AFM indentation. This deformability of the system also showed when the neutral buffer of the system was exchanged for carbonate buffer with pH 10 and the PEG cushion decreased in thickness.

## 4.1 TLB substrate without bilayer

### 4.1.1 Preparation of TLB substrates

The preparation of the TLB was a multi-step process [69]: after the surface was cleaned with a RCA cleaning process, the surface was functionalized via silanisation with octenyl-trichlorsilane. The alkane chains of the silane were oxidized in the next step. NHS chemistry was employed to link the PEG lipids to the surface through a peptide bond. Last, the NHS process was repeated with shorter chained PEG to fill the remaining gaps in the existing PEG layer. The chemical structure of the completed SLB substrate is shown in fig. 4.2.

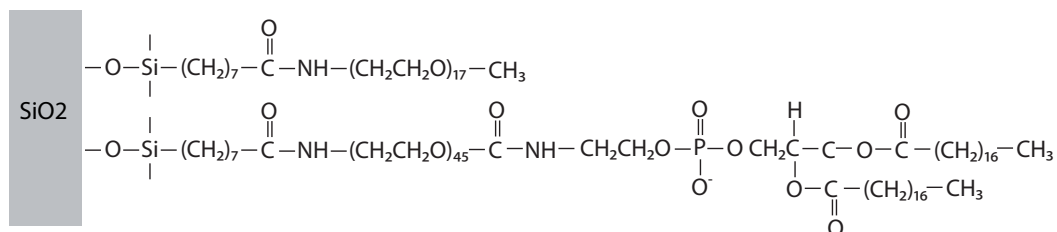


**Figure 4.2:** Chemical structure of the TLB substrate: PEG and PEG lipid grafted to  $\text{SiO}_2$  surface.

#### 4.1.2 X-ray reflectometry of TLB substrate in air

In X-ray reflectometry measurements at the air solid interface, both in in dry and humid air (fig. 4.3), the PEG cushion is visible as a bump in the reflected intensity curve.

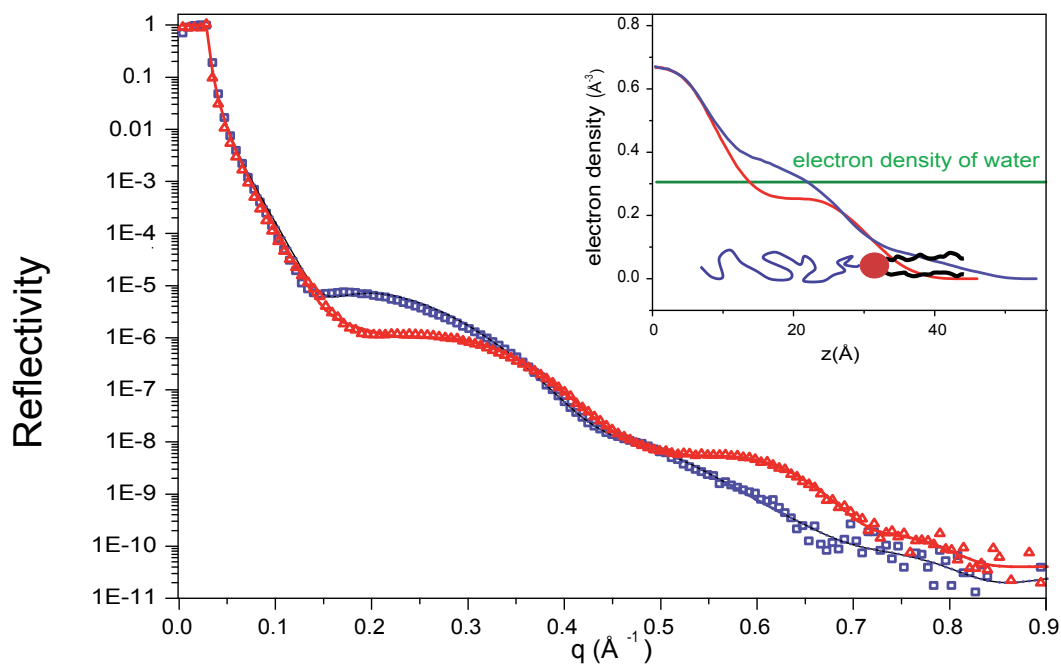


**Figure 4.3:** TLB substrate in air: In red the reflected intensity and fit at RH 30%, in blue at RH 100%. The electron density, calculated from the SLD is shown in the inset. For comparison, the electron density of water is indicated by a green line.

The reflectivity data changed with the hydration of the air, as the film on the surface changed when PEG absorbed water from the surrounding humidity and swelled. In dry air at RH 30% (red curves in fig. 4.3), the electron density of the PEG layer is lower than the theoretical value for PEG of  $0.33 \text{ \AA}^{-3}$  indicating that the PEG layer is slightly porous. When the system was exposed to air saturated with humidity (blue curves in fig. 4.3), water was absorbed into the PEG. This caused the hydrophobic lipid tails to be pushed out of the hydrated PEG. The lipid tails appeared as an extra layer in between the PEG and air.

## 4.2 Lipid bilayer on the PEG-tether cushion

### 4.2.1 Bilayer deposition

The lipids were mixed to contain 0.5% fluorescent lipids (Texas Red - DHPE) overall, dissolved in 2-propanol, and spin-coated on the PEG-lipid substrates.

For X-ray samples, 100  $\mu\text{L}$  solution in 2-propanol (1.5 mg/mL) was spin-coated with a two-step program: 2 s at 2000 rpm followed by 90 s at 3000 rpm. For the neutron samples, spin-coating speed had to be reduced due to the bigger sample size. They were prepared with 2 mL of solution for 5 s at 700 rpm and 90 s at 1000 rpm. Residual solvent was evaporated in vacuum for several hours.

After insertion of the sample into a fluidic chamber and filling of the chamber with buffer or de-ionized water, the samples were flushed several times to remove excess lipids. Before the reflectometry experiments, every sample was controlled with fluorescence microscopy to confirm the homogeneity and the absence of excess material.

### 4.2.2 Diffusion in tethered lipid bilayers

The diffusion constant of Texas Red-labeled lipids was determined using FRAP (see chapter 2.5.1). The FRAP images taken every 340  $\mu\text{s}$  are shown in fig. 4.4. As a reference, a lipid bilayer without PEG cushion or tethered lipids was prepared and measured under the same conditions. Since diffusion constants determined by different methods or under different conditions vary [70], we chose to compare with our reference sample instead of literature values for lipid bilayers.

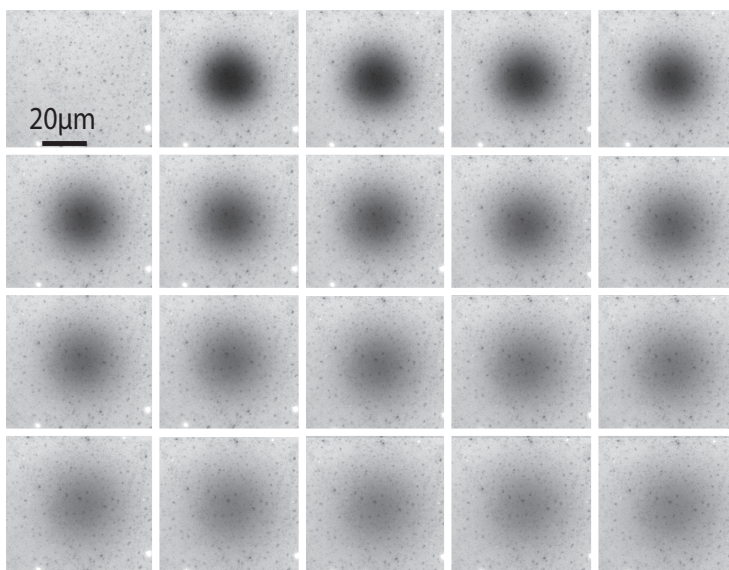


**Figure 4.4:** FRAP pictures of TLB. Time delay between pictures is 340  $\mu\text{s}$ . After the first image, an area is bleached with a laser and back-diffusion of dyed lipid is recorded to determine the diffusivity.

The POPC reference bilayer on silicon oxide surfaces without tethered lipids shows a diffusion constant of  $(2.4 \pm 0.1) \mu\text{m}^2/\text{s}$ . The TLB shows a diffusion constant of  $(2.1 \pm 0.1) \mu\text{m}^2/\text{s}$ , which is only 12% lower than that of the reference bilayer without any grafted lipids as obstacles.

The lipids grafted to the surface, which make up  $(11.5 \pm 3)\%$  of the total lipids, are not fully immobilized. Thermal energy fluctuations in the end-to-end distance of the PEG chain allow the tethered lipid movement, as illustrated in fig. 4.5. For PEG with a weight of 2kDa, this end-to-end length change can be estimated to about 3  $\text{\AA}$  [71]. Hence, lipids can move about 8  $\text{\AA}$ , which is about twice the distance between the center of two lipids in the bilayer.

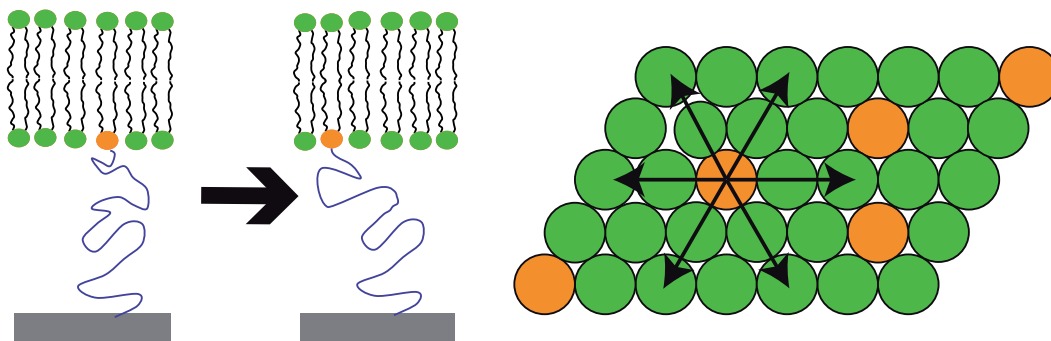


**Figure 4.5:** Sketch of lipid mobility in the bilayer: The tethered lipids can move up to the place of their once removed neighbors.

### 4.2.3 Neutron and X-ray reflectometry

Reflectivity data of the TLBs and least-squares fits to the data of both the neutron and the X-ray experiments are shown in fig. 4.6, the X-ray data in red and neutron measurements in blue (in  $D_2O$ ) and green (in  $D_2O/H_2O$  mix). The associated SLD models is found in the inset.

The five oscillations in the red curve were caused by the TLB. In the neutron data curve, the fast oscillations were caused by the oxide layer, the TLB was visible in the underlying broad shoulder of the blue data curve. The SLD models for all fits are shown in the inset of fig. 4.6. The red SLD model for X-ray data is shown on an inverted z-scale for comparison to the neutron results. This inversion is due to the incident beam being directed through silicon in the neutron measurements and through water in the X-ray measurements.

For X-rays, four layers were distinguishable: the 55 Å hydrated PEG cushion at about the same SLD as water, both head groups with higher SLD and the lipid chains with the lowest SLD. A three-layer model consisting of silicon oxide layer, PEG layer, and lipid chain region was used to fit the neutron measurements. For neutrons, resolution was not good enough to distinguish the hydrated head groups from the bulk buffer or hydrated PEG, they were included in the transition.

The thicknesses for the PEG layer and the lipid bilayer, as determined from the neutron fits, were consistent with those from the X-ray measurements. The lipid bilayer for the neutron measurement was prepared with lipids that have one deuterated alkane chain ( $d_{31}POPC$ ). The SLD of the lipid bilayer region was found at  $(2.5 \pm 0.2) \times 10^{-6} \text{ \AA}^{-2}$  which

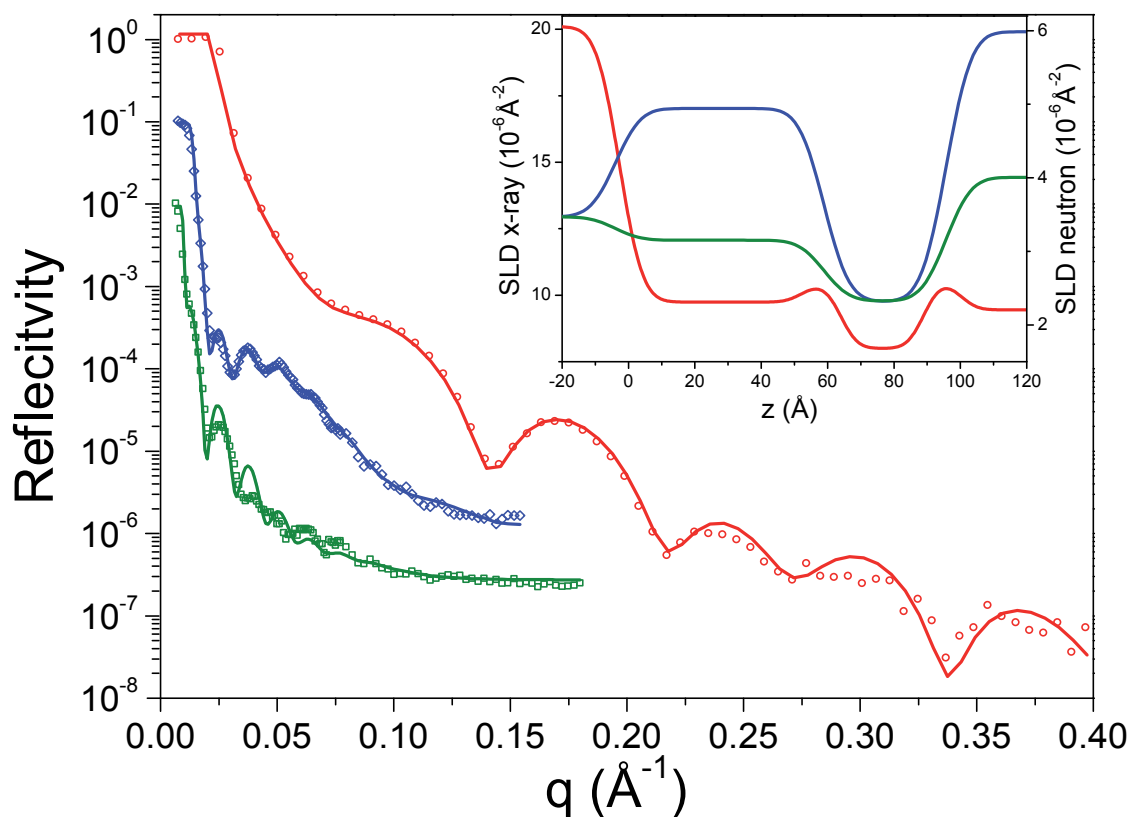


**Figure 4.6:** X-ray (red), neutron in  $D_2O$  (blue) and neutron in  $D_2O/H_2O$  mix (green) reflectometry data of TLBs. The SLD models are shown in the inset, for X-rays, the  $z$ -axis is inverted.

is in compliance to theoretical values for partially deuterated alkane chains. The hydrated PEG had a SLD of  $(4.94 \pm 0.11) \times 10^{-6} \text{ \AA}^{-2}$  in  $D_2O$  and  $(3.15 \pm 0.07) \times 10^{-6} \text{ \AA}^{-2}$  in the  $D_2O/H_2O$  mix.

In fig. 4.7a) the electron density of all layers, calculated from the SLD of the X-ray model, is shown. The contribution of each layer is illustrated by an error function in different colors, grey for the silicon oxide, purple for the PEG, red for the lipid heads, green for the alkane chains and blue for the water.

The hydration for the PEG and the lipid layer was extracted from the neutron measurements and calculated with the formula given in chapter 2.7.3. The profile for the hydration is illustrated in fig. 4.7b).

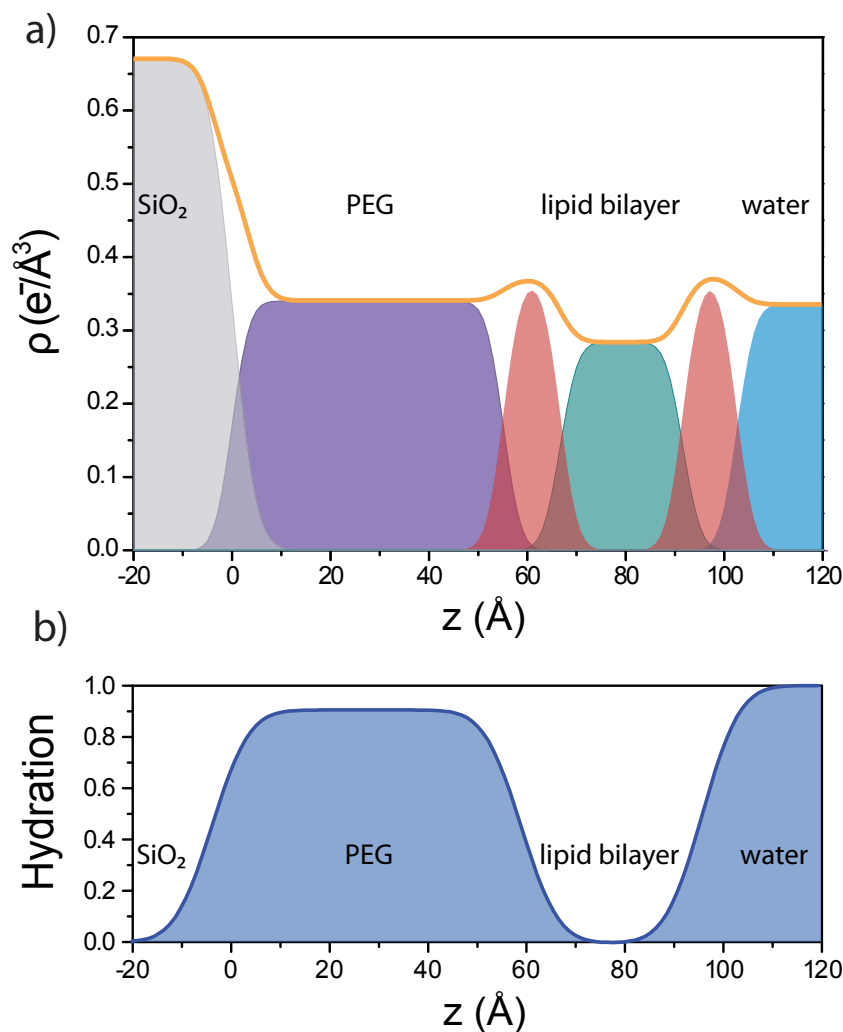


**Figure 4.7:** a) Electron density and contribution to the overall electron density of each layer: grey for the silicon oxide, purple for the PEG, red for the lipid heads, green for the alkane chains and blue for the water. b) Hydration of PEG and lipids, extracted from the models for X-ray and neutron fit.

This difference in SLD of both neutron measurements indicates a hydration of  $(90 \pm 3)\%$  for the PEG region. In contrast, the lipid chain region shows no hydration, its SLD did not change with the change of contrast in the water.

The combination of X-ray and neutron reflectometry confirm the presence of a well-defined bilayer separated from the substrate by a highly hydrated PEG cushion.

#### 4.2.4 AFM

AFM was used on the TLBs confirm thickness measured with reflectometry, and determine deformability and softness with indentation experiments. AFM was performed in a cooperation with Frank Stetter, following his protocol [28]. More than 50 force - distance curves of an AFM tip approaching the surface and puncturing the TLB are superposed in fig. 4.8.

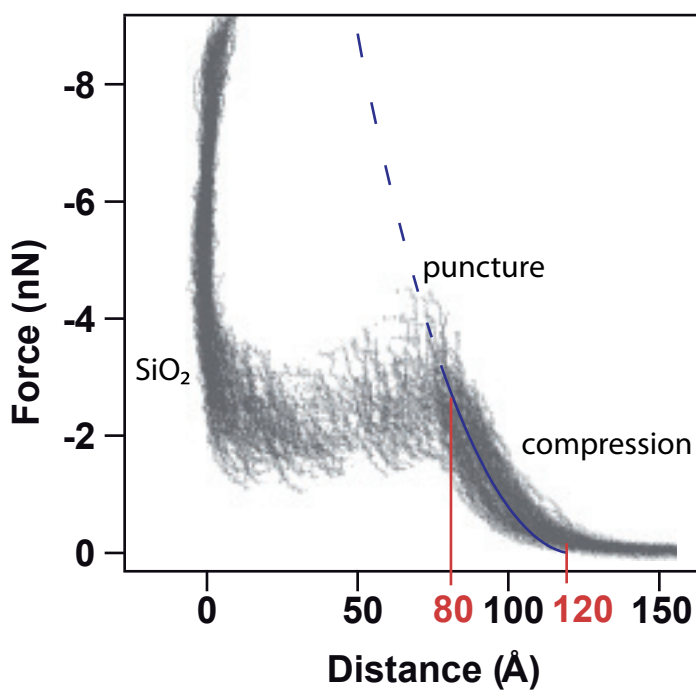


**Figure 4.8:** AFM indentation into the TLB: When the tip approaches the surface, it first deforms the system starting at 120 Å from the surface. At 80 Å the tip breaks through the lipid bilayer.

The tip deformed the bilayer and a repulsive force rose starting at a distance of 120 Å. The force increased up to a distance of about 80 Å as the TLB system was compressed. At that distance, the lipid bilayer ruptured, the underlying PEG gave way, and the AFM tip approaches the rest of the distance to the surface.

For supported lipid bilayers sitting directly on  $\text{SiO}_2$  the repulsive force was observed starting at around 65 Å and the collapse occurred at around 45 Å. The TLB was deformed twice as much before the tip broke through the lipid membrane. The blue compression curve in fig. 4.8 represents an analytical solution for a tip radius of 20 nm, a Poisson ratio of 0.5 and 20 MPa for the Young modulus as parameters for the mechanical Hertz model.

### 4.3 Change in thickness of the PEG cushion in carbonate buffer

The TLBs were stable and their structure unchanged under a variety of different buffer conditions, e.g. PBS-buffer, TRIS-buffer and DI-water. However, when the buffer was exchanged for carbonate buffer with pH 10, a significant change was observed in the system. In fig. 4.9 the reflectivity data and fits for neutral pH (blue) and pH 10 (purple) are plotted together for direct comparison. The cm measurements for this system were also analyzed and confirm the dehydration, but are not shown here.

After change of the buffer to the carbonate buffer with pH 10, the PEG layer was reduced in thickness by 13 Å as can be seen in the inset of fig. 4.9. The reduced thickness went together with a reduced hydration from 90% to 87%, as the amount of PEG on the surface stayed constant. This proves further, that the PEG cushion is flexible and can be compressed. PEG is inert and does not change charge at changed pH. The  $\text{SiO}_2$  surface on the other hand changes charge, which influences the behavior of charged molecules inside the PEG. Additionally, the carbonate molecules might be less solvable in the hydrated PEG due to their size and thus induce osmotic effects.

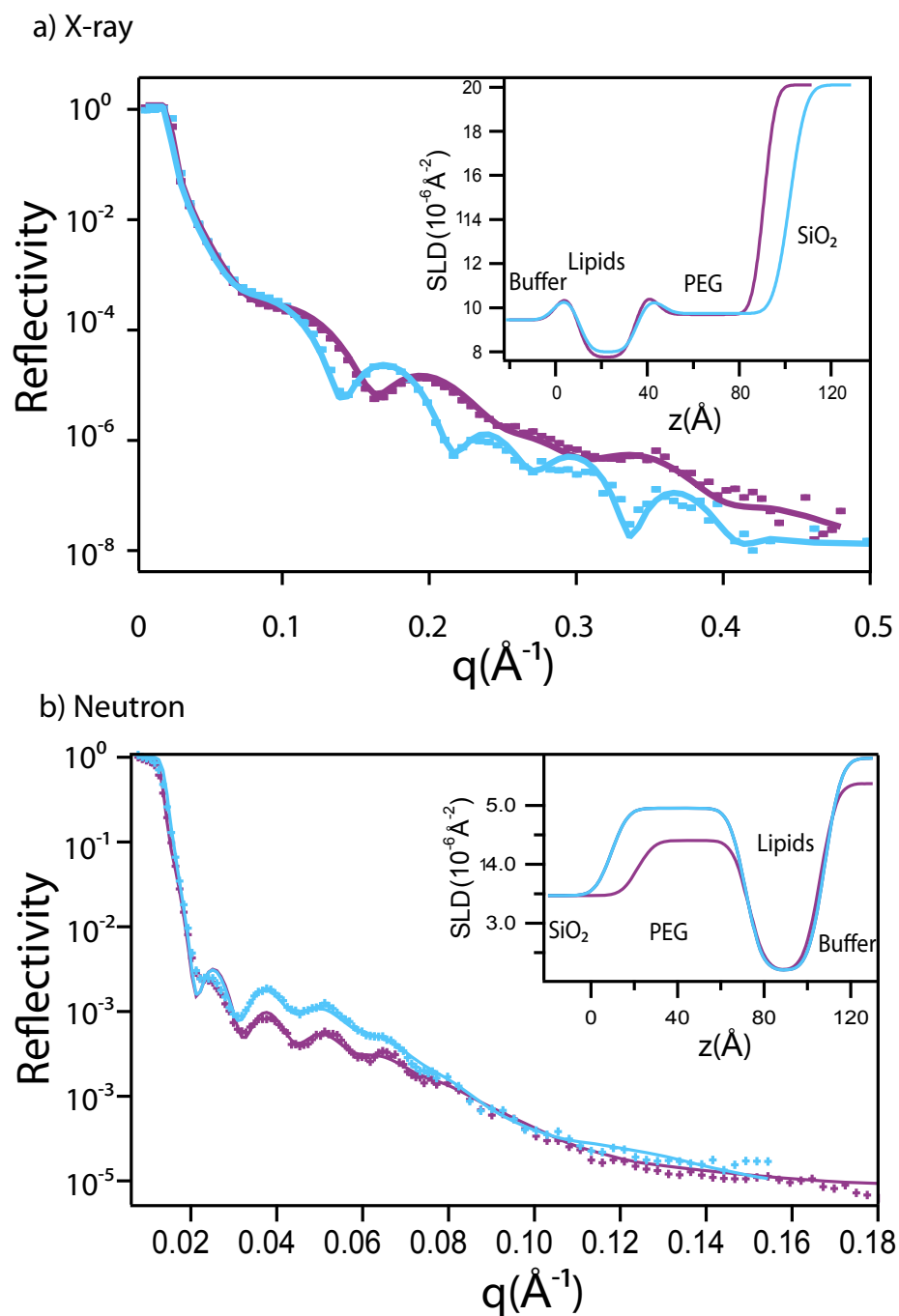


**Figure 4.9:** Comparison of reflectometry at neutral pH and pH 10: Change in thickness of the PEG cushion in carbonate buffer. SLD models for the fits are shown in the inset. a) X-ray reflectivity and fit, blue at neutral pH, purple in carbonate buffer at pH 10. b) Neutron reflectivity in  $D_2O$  and fit.



# Chapter 5

## Results: Surfaces for cell motility and attachment

In the intersection of inorganic surfaces with living matter, occurring i.e. in the development of biomedical devices, artificial organs, and bio-sensors, it is crucial to gain a clear understanding of the interaction of these materials with biological tissues at the cellular level. Cell adhesion to artificial materials is affected by the surface properties such as wettability, roughness, surface charge, and chemical functionalities.

Cells adhere to surfaces via membrane proteins [72]. The effectiveness of cell adhesion and the migration behavior can be controlled by variation of the surface coating. In this chapter the structure of such coatings is associated with cell behavior on these surfaces.

## 5.1 Fibronectin adsorption to grafted PEG surfaces and cell motility

The work described in this section has been published [3]. The full article is attached in Appendix A.3 .

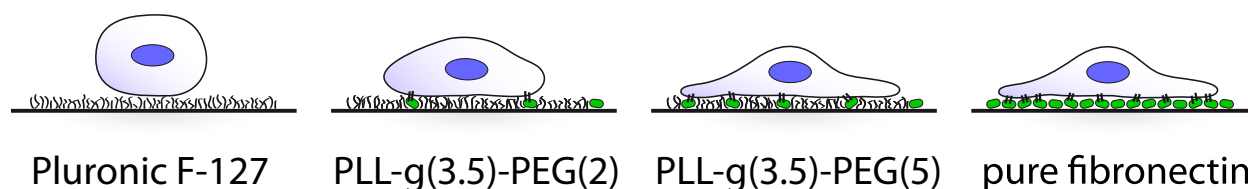


**Figure 5.1:** Sketch of cells on different surfaces.

Cell repellent polymers are often used to passivate surfaces in order to avoid cell adhesion. But the repulsive character of polymer surfaces varies, as protein adsorption and interaction of cells with the surface depends not only on the choice of polymer but also on its conformation. A polymer commonly used for such passivation is PEG. In previous studies, cells were shown to migrate across PEG surfaces [23]. We analyzed the structure and interaction of the cell adhesion protein fibronectin (FN) with three different PEG surfaces with neutron reflectometry. Those results combined with fluorescence microscopy to study the behavior of cells on these surfaces provides an understanding of the mechanisms underlying the different interaction of cells with different PEG surfaces.

### 5.1.1 PEG surfaces

There are a variety of techniques to coat surfaces with PEG polymers. Here, we used two block copolymers, Pluronic (PPO-PEG) and PLL-g-PEG. For both coatings the PEG made up the polymer layer distant to the surface, and PPO respectively the PLL acted as backbone sticking to the surface. The structure of both polymer films is illustrated in fig. 5.2.

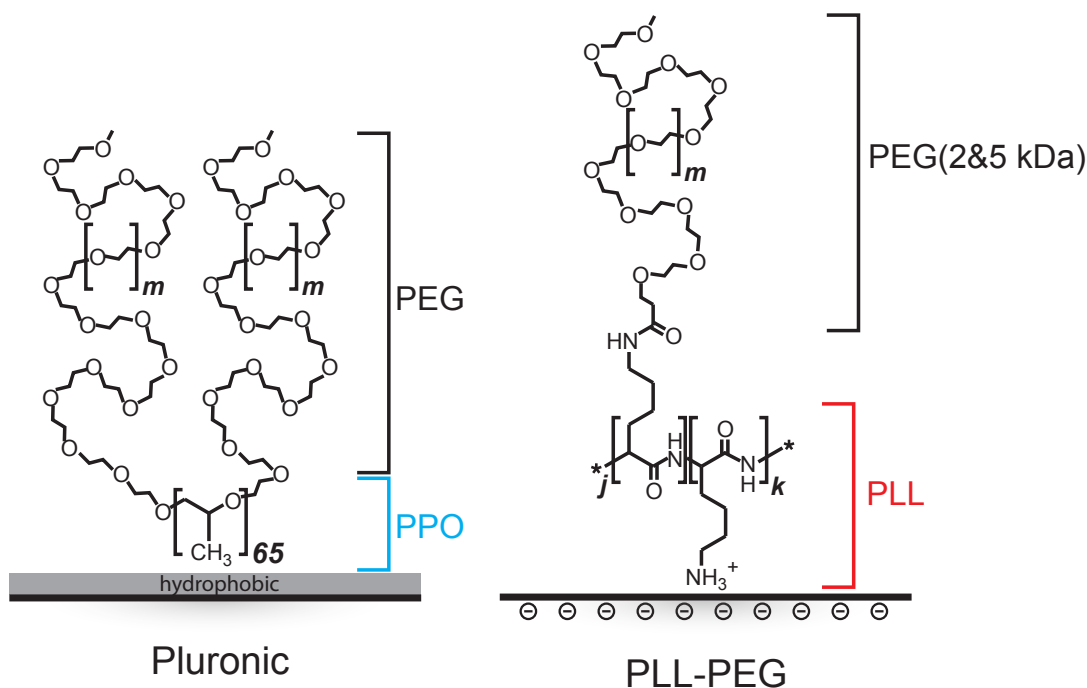


**Figure 5.2:** Structure of Pluronic and PLL-g-PEG: the PPO backbone sticks to hydrophobic surfaces and the PLL backbone anchors the PEG via electrostatic adsorption.

## Pluronic

Pluronic is a block copolymer consisting of PEG and poly-propylene oxide (PPO). It adsorbs to hydrophobic surfaces. The silicon oxide surfaces were treated with hydrophobic silanes before the Pluronic coating is applied.

## PLL-g-PEG

PLL-g-PEG adsorbs to hydrophilic glass surfaces through electrostatic interaction. The substrates were treated in the plasma - cleaner before incubation with PLL-g-PEG. We used two different length of PEG, 2 kDa (PEG(2)) and 5 kDa (PEG(5)), to study the influence of polymer length.

### 5.1.2 Neutron data and fits

Neutron reflectometry at two different contrasts disclosed the differences in structure and hydration of the three PEG surfaces. After the first set of measurements, FN solution with a concentration of 50  $\mu\text{g} / \text{ml}$  was added to the fluidic chambers and the reflectometry measurement repeated after at least 1 h incubation time for the protein.

#### Pluronic

The SLD model for the Pluronic coated surface is shown in fig. 5.3, with the reflectometry data and fit in the inset. The red curve represents the model for the  $\text{D}_2\text{O}$  measurement, the blue curve the one in contrast matched buffer (cm) and the dark red the model for the  $\text{D}_2\text{O}$  measurement after addition of FN.

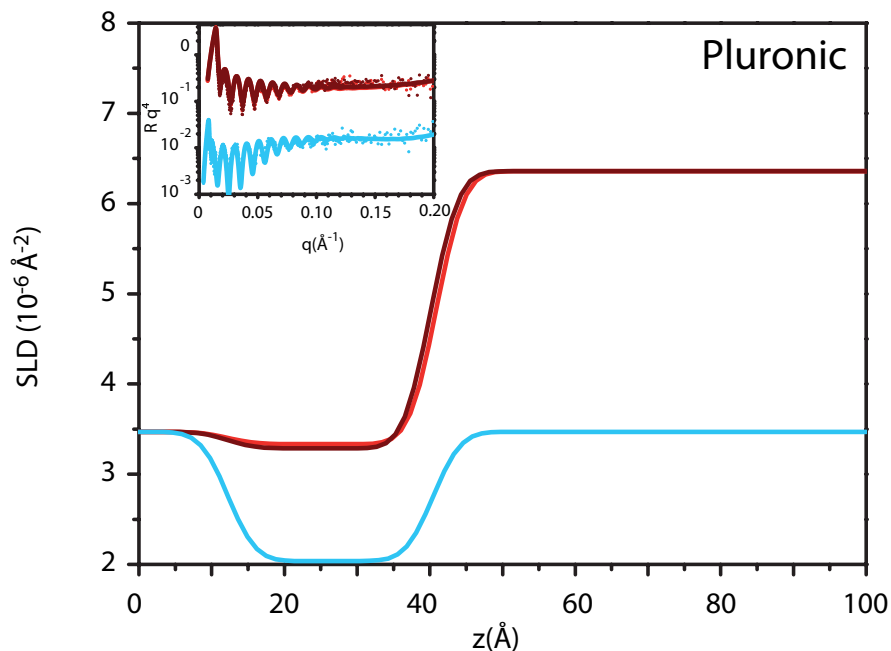


**Figure 5.3:** SLD model for a Pluronic surface in  $\text{D}_2\text{O}$  (red) and cm (blue). The dark red curve is the model for the data recorded after addition of FN, which is the same as before. In all cases the data could be fitted with just one layer. Data and fit is shown in the inset.

The data could be fitted with only one layer on the SiO<sub>2</sub> with  $(45 \pm 1)\%$  hydration and a thickness of  $(28 \pm 1)$  Å. This result indicates that the PEG was laying flat on the surface and coiled back on itself instead of reaching out into the buffer. There was no change in the system after the addition of FN, therefore the protein did not interact with the polymer covered surface.

### PLL-g-PEG

The SLD model for the two PLL-g-PEG coated surfaces is shown in fig. 5.4, with the reflectometry data and fit in the inset. Red colored curves represent the D<sub>2</sub>O, blue colored curves the cm measurement. The dark colored curves were recorded after addition of FN.

The data from the PEG(2) system could be fitted with a two layer model, distinguishing the PLL and the PEG layer. The PLL had a thickness of  $(23 \pm 1)$  Å for PEG(2) and  $(28 \pm 1)$  Å for PEG(5). The PEG(2) layer was  $(51 \pm 1)$  Å thick. The PEG of the PLL-PEG(5) sample thinned out gradually into the buffer after  $(68 \pm 3)$  Å. Therefore, an additional layer with slowly decreasing PEG density had to be added onto the homogeneous PEG layer.

Fits for the data yielded a low hydration for the PLL layer ( $31 \pm 5\%$  for PEG(2) and  $37 \pm 3\%$  for PEG(5)). The PEG was highly hydrated ( $90 \pm 1\%$  for PEG(2) and  $84 \pm 1\%$  for the homogeneous part of PEG(5)) and reached out into the buffer.

When FN was introduced to the PLL-g-PEG covered surfaces, the film changed. The main part of this change occurred in the PLL layer, which seemed to increase in thickness and has an additional mass coverage after addition of FN. It was not possible to separate this layer into two and therefore spacial differentiation between FN and PLL was impossible in our results. Reason for that could be either, that the FN penetrated into the PLL layer or that PLL and FN form two layers with similar SLD on top of each other. The additional mass on the surface attributed to the FN was  $(0.4 \pm 0.2)$  mg/m<sup>2</sup> for PEG(2) and  $(0.7 \pm 0.2)$  mg/m<sup>2</sup> for PEG(5).

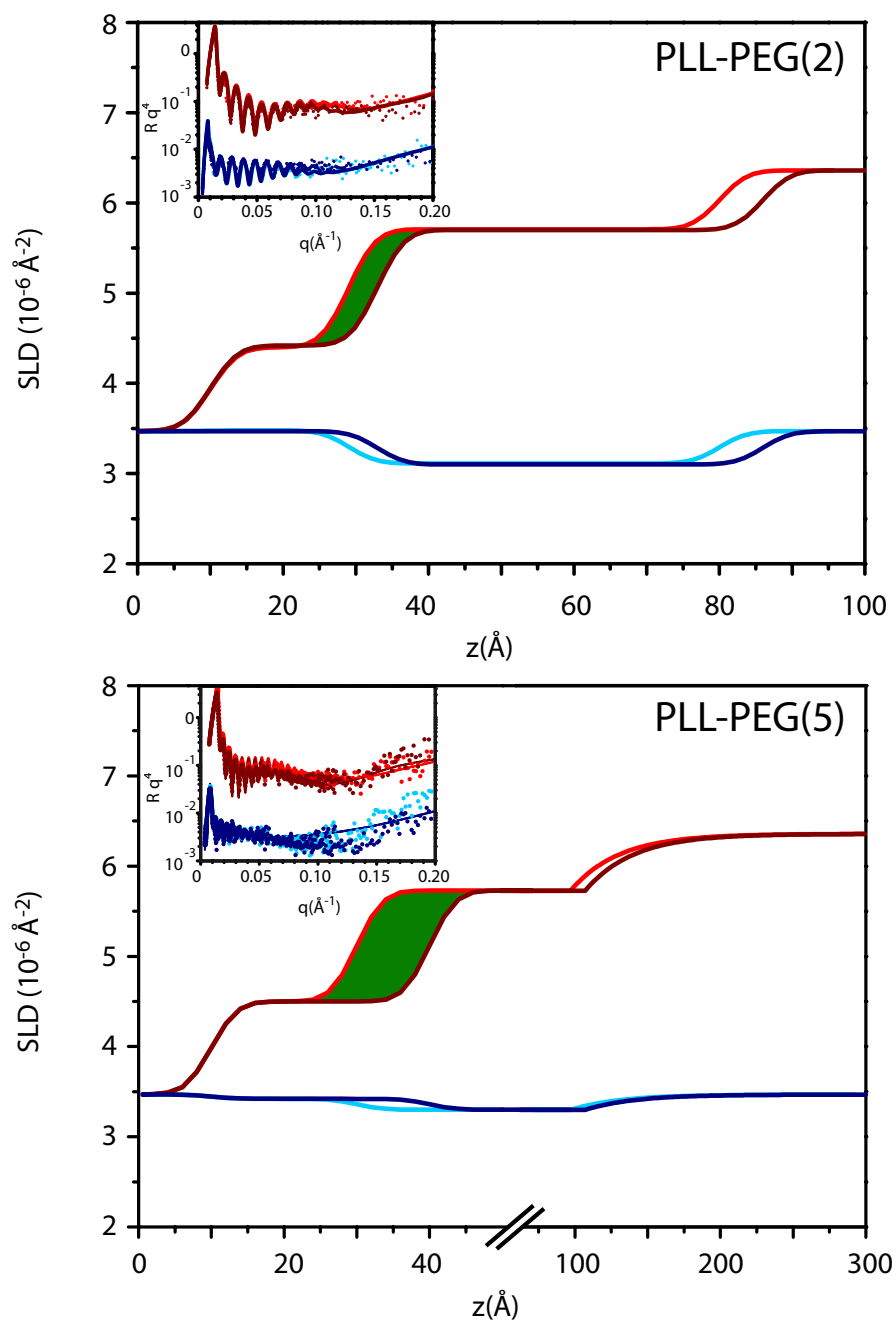


**Figure 5.4:** SLD models for the PLL-g-PEG systems: Red represents the  $D_2O$  measurements, blue the measurements in cm-buffer. Dark red and dark blue colored curves were recorded after addition of FN. The SLD model consists of one layer for the PLL and one for the PEG. For PEG(5) the PEG thinned out gradually whereas for PEG(2) the transition from PEG to buffer was immediate. After addition of FN, the layer adjoining the  $SiO_2$  increased in thickness, indicated by the green area, which represents contribution of the FN. Data and fit is shown in the inset.

### PEG confirmation and FN adsorption

As was shown in the previous section, in case of Pluronic treated surfaces, the PEG was laying flat on the surface and folds back on itself instead of reaching out into the buffer (pancake). Water was repulsed from the PEG layer due to the close proximity to the hydrophobic surface which the PEG shields against. The polymer behavior was caused mostly by hydrophobic effects. No change in the system was observed after the addition of FN, indicating that the protein did not reach the surface through the dense PEG layer, which agrees with results on similar studies [73].

In contrast, the highly hydrated PEG layer of the PLL-g-PEG behaved as a grafted polymer brush. Since the longer PEG(5) chains were more stretched out, the hydration was lower close to the surface. At some distance to the surface, the polymer thinned out, whereas the PEG(2) had homogeneous density lower than the PEG(5) close to the surface. The higher density PEG(5) allows more FN to penetrate and adsorb. This result is in compliance to other studies, where denser, and thus more ordered, PEG proved to be less protein resistant [74].

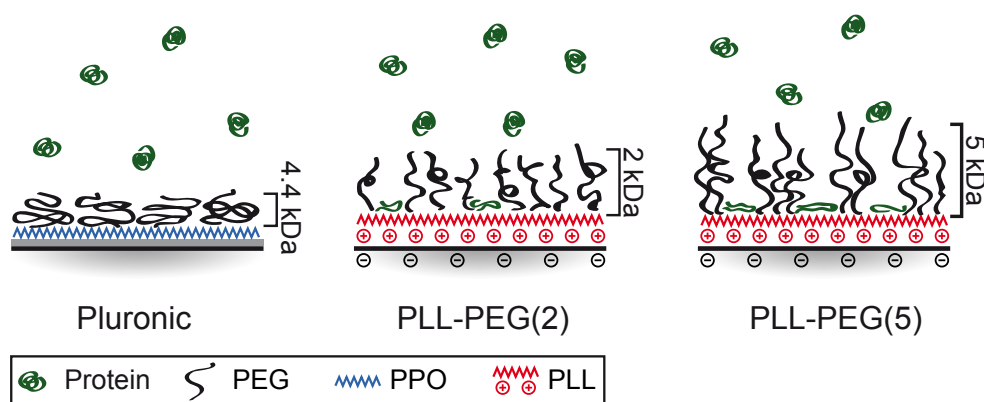


**Figure 5.5:** FN interaction into the polymer: on Pluronic, the FN did not adhere to the surface. On the PLL-PEG systems, FN passed through the PEG layer and adhered to the PLL. The longer chained PEG(5) allowed more FN to adhere than the PEG(2).

After the FN had penetrated through the PEG layer, it could attach to the surface electrostatically. The adsorbed PLL left a net positive charge providing an attractive force for the negatively charged FN. The increase in thickness caused by the FN for both PLL-PEG samples is quite small compared to the diameter of FN, which suggests denaturation and / or a mixing of the FN into the PLL layer.

### 5.1.3 Cellular behavior on the different PEG and FN surfaces

#### Cell morphology and spreading area

For the study of cells, all surfaces were exposed to FN solution. Adeno carcinoma cells A549 with stained plasma membrane were seeded onto the surfaces after washing of the FN solution. The morphology and motility of the cells was studied with a fluorescence microscopy.

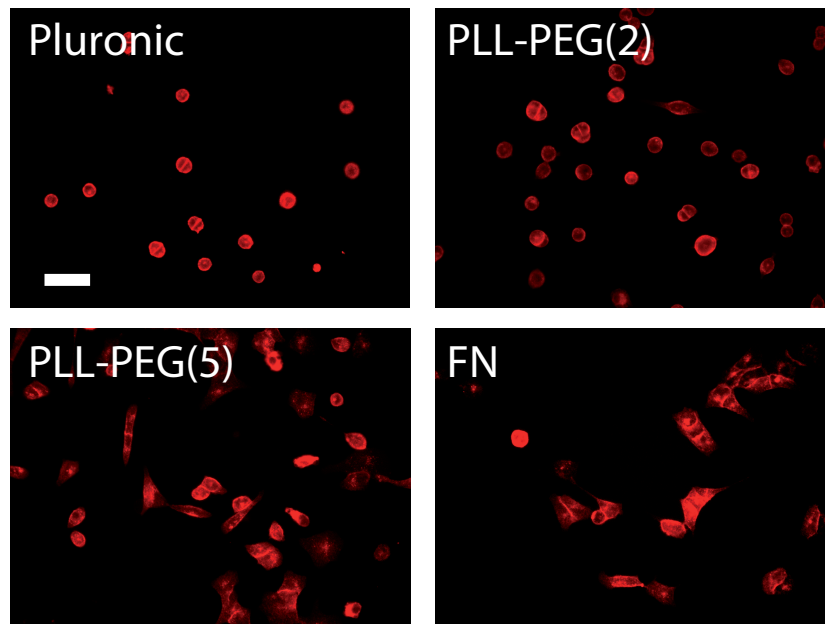


**Figure 5.6:** Microscopy images of adeno carcinoma cells on PEG and FN surfaces. The size and shape of the cells varied with the surface: round and small on Pluronic, more elongated on PLL-PEG(2). On PLL-PEG(5) and FN cells spread the most. The scale bar corresponds to 100  $\mu\text{m}$

The cell morphology is shown in fig. 5.6. On Pluronic, cells covered only a small area and were round shaped. The contact area to the substrate was even smaller than the projection of the cell on the microscopy image. On the PLL surfaces, the cell shapes were elongated, on the PEG(5) even more than on PEG(2). The shape of cells on PEG(5) was similarly spread out as on the reference surface of pure FN.

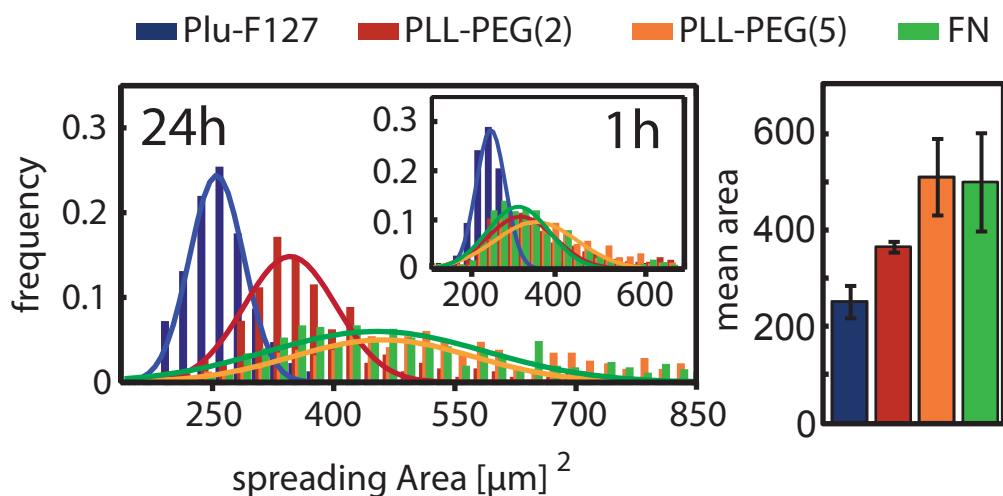


**Figure 5.7:** Comparison of spreading areas per cell: On Pluronic, cells round up and only have minimal contact to the surface. On the PLL-PEG surfaces, cells can spread out, on PEG(5) more than on PEG(2).

In fig. 5.7 the area covered by the cells are compared on the different surfaces. On PLL-PEG(5) cells covered areas of the same size as on FN whereas they covered less on PLL-PEG(2) and had the smallest size on Pluronic. Cells spread on the surfaces via attaching with proteins to adhesion sites on the substrate. In our samples, those adhesion sites were provided by the FN. The adhesion site density of the PLL-PEG(5) surface seems to be enough for the cells to reach full spreading.

### Cell migration

When cells migrate, they have to detach their anchors at the rear and form new ones in the direction of movement. In fig. 5.8 the migration behavior is illustrated via trajectories and mean square displacement curves. On Pluronic, cells did not move. On PLL-PEG(5), cells moved the fastest. Since both attaching to and detaching from the anchor points takes time, the cell speed is highest when there are enough attachment sites to reach full spreading of the cell but not more. That was the case for the PLL-PEG(5). In case of the PLL-PEG(2) and the pure FN, cells were slowed down by too few and too many sites, respectively.

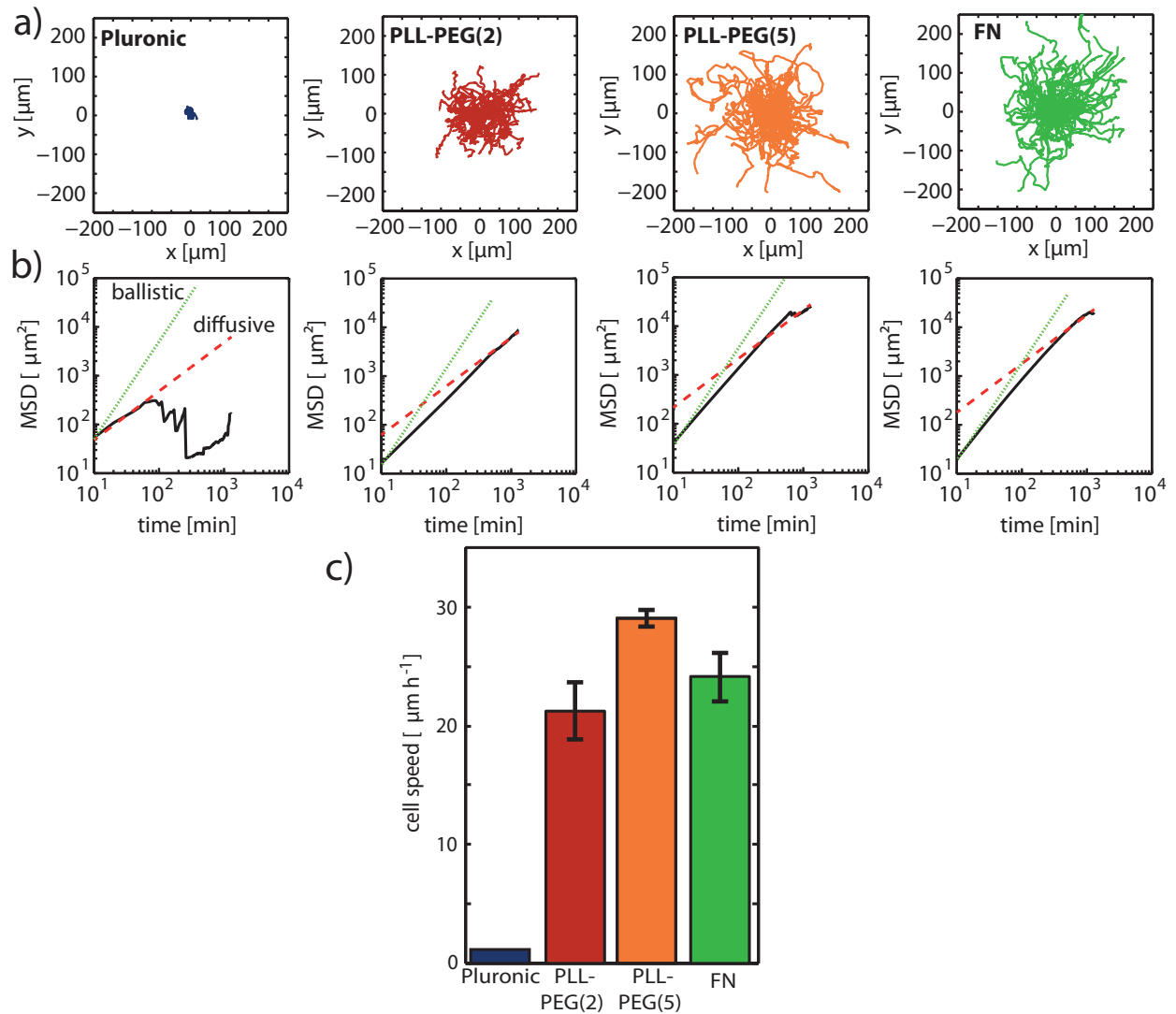


**Figure 5.8:** Trajectories (a) and mean square displacements (b) of cells on different PEG and FN surfaces. The motion of cells resemble ballistic motion for short timescales and diffusive for longer. (c) Cells move the fastest on PLL-PEG(5) and not at all on Pluronic.

## 5.2 Neural cell attachment surfaces

The work described in this section has been published [4]. The full article is attached in Appendix A.4.

Different cell types prefer different surfaces for attachment. These surfaces can be tuned in structure and softness in order to fulfill the the characteristic needs of the cells. Neural cells are sensitive to their surrounding. Therefore, development of a coating adjusted to there needs is a prerequisite for their study. Here, we prepared and analyzed a film consisting of three layers that coated a SiO<sub>2</sub> surface and concluded in a peptide layer specifically synthesized for neural cell attachment.

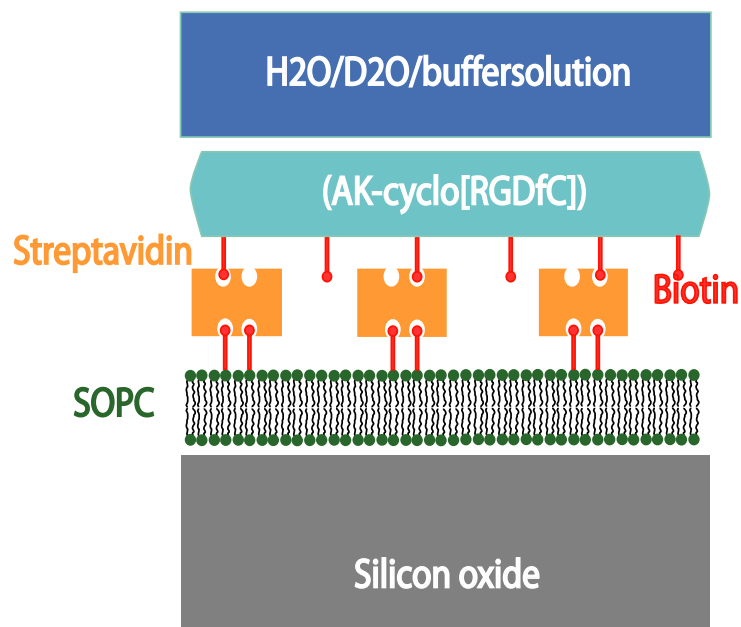


**Figure 5.9:** Structure of the three layer film for neural cell attachment.

### 5.2.1 Film preparation

In order to get a controlled homogeneous surface, the coating was performed in three steps. First, a bilayer of SOPC lipids, that contained 2% biotinylated lipids, was formed via spincoating, hydrating and flushing. Second, streptavidin was added in solution and incubated to bind to the biotin. The attachment of streptavidin to biotin is specific and strong and thus well suited for controlled attachment of molecules. In the final step, AK-cyclo[RGDfC], a synthetic protein that contains a high concentration of RGD-peptides and biotin anchors was added. Neural cells can attach to those RGD-peptide groups. The structure of the complete film is sketched in fig. 5.10.

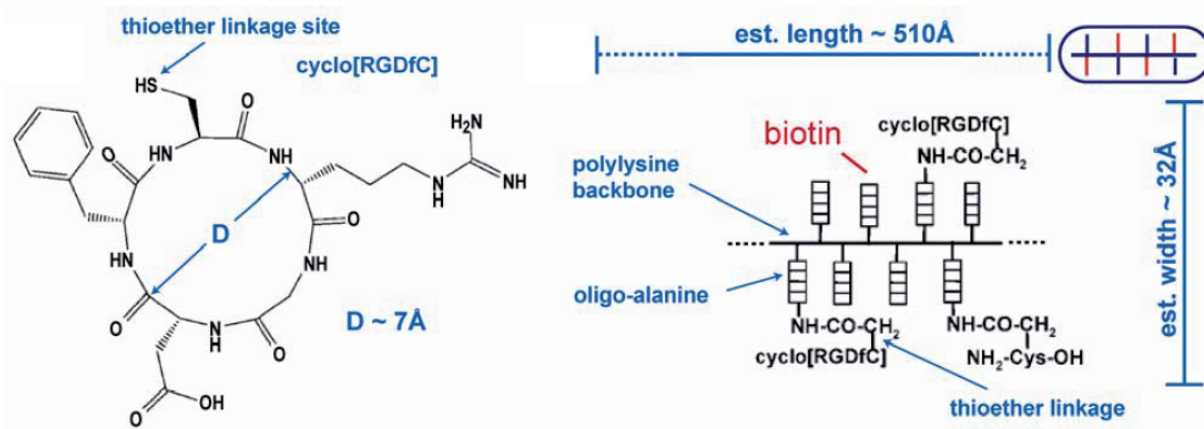


**Figure 5.10:** Molecular structure of the synthetic cell attachment protein AK-cyclo[RGDfC].

### 5.2.2 X-ray and neutron reflectometry

Neutron and X-ray reflectometry measurements of the trilayer system provided information about the inner structure. The data and fit to the data is shown in fig. 5.11. The combination was chosen since X-rays (blue curve) provided higher resolution. Neutron reflectometry was performed at two different contrast to extract hydration, first in D<sub>2</sub>O (green curve), then in contrast matched (cm) buffer, a mix of D<sub>2</sub>O and H<sub>2</sub>O equalized to the SLD of SiO<sub>2</sub> (red curve).

For the X-ray data, the  $q$ -range was up to  $0.7 \text{ \AA}^{-1}$  which allowed us to resolve thin layers such as the lipid head groups, which are only a few  $\text{\AA}$  sized. The four oscillations visible in

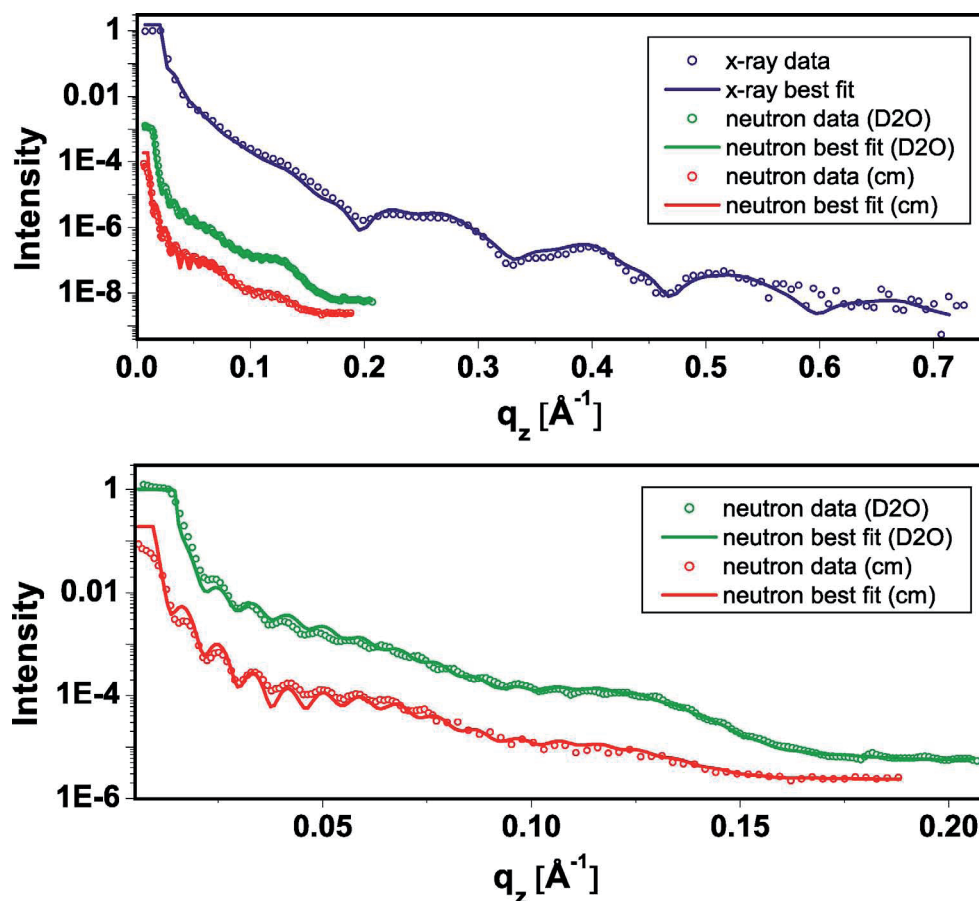


**Figure 5.11:** Neutron and x-ray reflectometry data and fit of the neural cell attachment film: the lower graph shows the same neutron data zoomed in for better visibility.

the X-ray curve mostly represented the lipid bilayer, as it provided the most contrast for the X-rays. The additional protein layers were visible in the substructure of the oscillations.

The rapid oscillations in intensity in the neutron data and fit (lower graph as zoom in) originated from the  $\text{SiO}_2$  layer and are not included in the SLD models shown in fig. 5.12. There were two shoulders visible for both  $\text{D}_2\text{O}$  and cm data, which were less broad than the oscillations in the X-ray curve, as for neutrons there is also strong contrast in the protein layers of the film.

Data of the neutron and X-ray measurement were fitted together using the “global fit” option of Motofit. The SLD models from the fit are shown in fig. 5.12. The whole film was visible from all three data sets, but neutrons provided much higher contrast for the film than X-rays. Especially areas of high and low hydration could be easily distinguished from the differences in the two neutron SLD models.

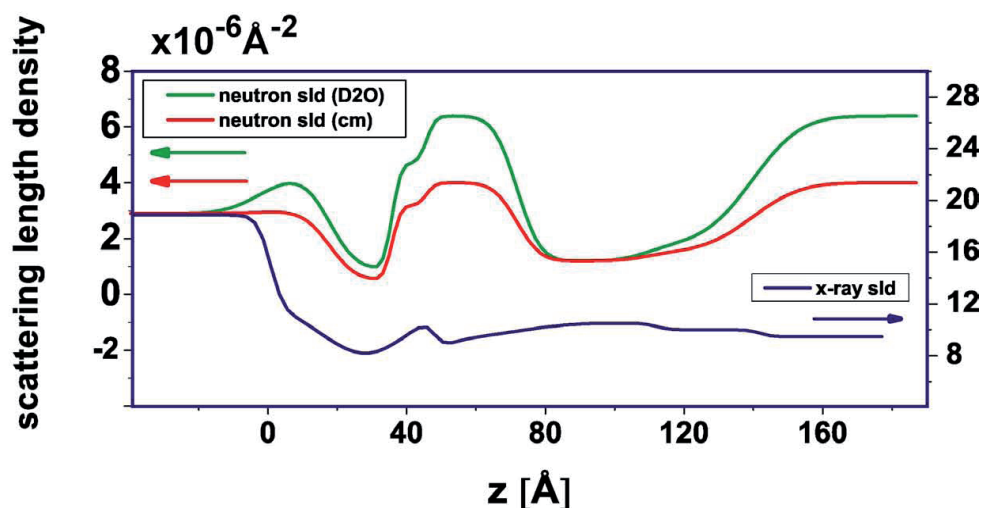


**Figure 5.12:** SLD for the neural cell attachment surface: X-ray SLD in blue, neutron SLD in  $D_2O$  green, and neutron SLD in cm red

Fig. 5.13 shows the hydration of the different layers of the sample, extracted from the SLD models of the neutron fit. Below the hydration curve is a sketch of the components. The area where the biotin linkers in between lipids and streptavidin are located was highly hydrated, since only 2% of lipids contained a biotin anchor. Therefore the surface covering of the biotin layer is low and hydration in that region is high. Both hydrophilic head group layers of the lipids also show a hydration of 55%. In contrast, the lipid chain region and the protein layers, both streptavidin and AK-cyclo[RGDfC], do not contain much water. This indicates a densely packed protein layer and is therefore promising for good neuron attachment.

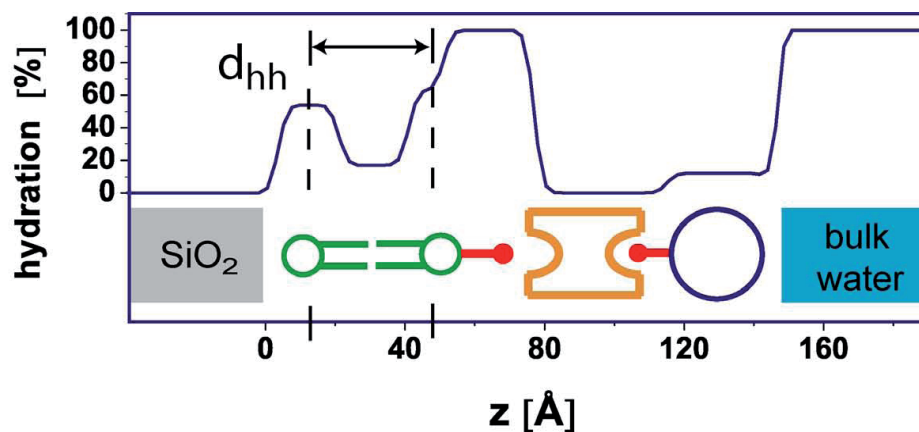


**Figure 5.13:** Hydration of the neural cell attachment system. Below the hydration curve, the components are sketched.

### 5.2.3 Microscopy of cells

The neural cell attachment surfaces were tested by analyzing the spreading behavior of green fluorescent protein (GFP) expressing neural stem cells. The cells were exposed to three different surfaces: a plain lipid bilayer (SOPC), a lipid bilayer covered with streptavidin and the AK-cyclo[RGDfC] system. Microscopy images and sketches of the cell form are shown in fig. 5.14. On both SOPC and streptavidin the cells were spherical shaped and did not spread. On the AK-cyclo[RGDfC] surface on the other hand, rapid spreading of the cells was observed.

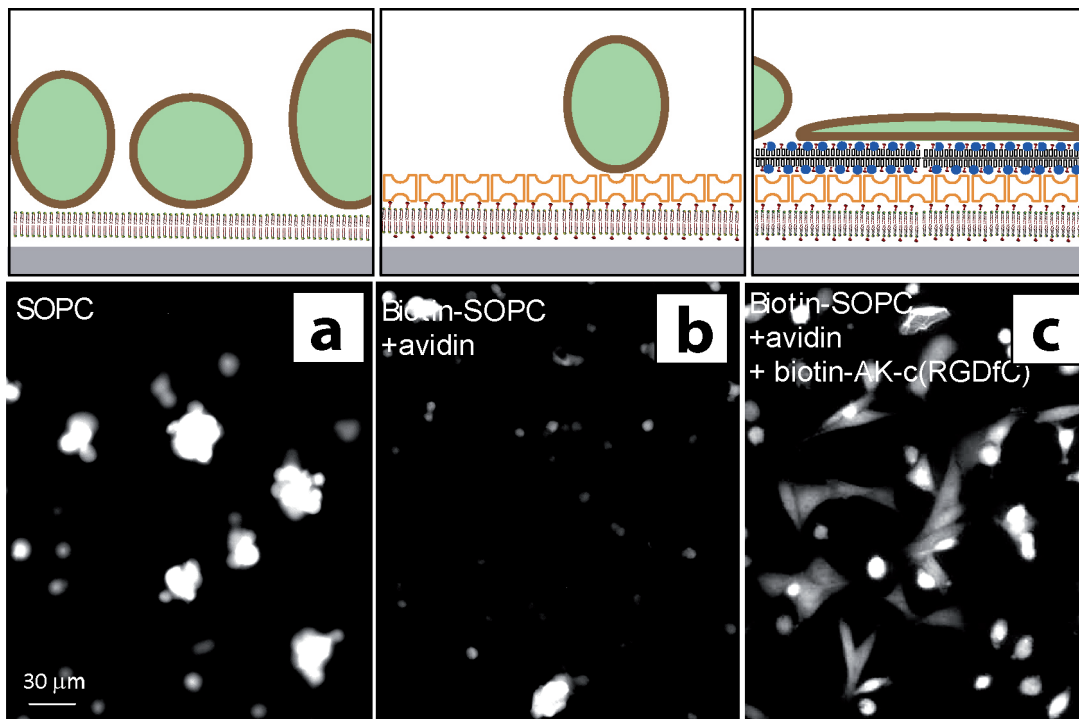


**Figure 5.14:** Microscopy images of GFP expressing neural stem cells: cells round up on a lipid bilayer (a) or a streptavidin layer (b), whereas they spread out and attach to the AK-cyclo[RGDfC] coated surface (c).



# Conclusion

Neutron reflectometry measurements with contrast variation provided insight into the composition of different films on the solid-liquid interface. In this work, this technique was used in combination with X-ray reflectometry, fluorescence microscopy and AFM to characterize films built up of lipids, proteins and polymers on silicon oxide supports under water. For neutrons, there is a big difference in the scattering length of normal hydrogen atoms and deuterium atoms. Therefore, all neutron measurements were performed in D<sub>2</sub>O buffer and in a mix of D<sub>2</sub>O and H<sub>2</sub>O buffer. The difference in the results of those two measurements provided detailed depth information about hydration of the system. The same effect of variation of contrast via deuteration was used when lipid bilayers composed of two kind of lipids were prepared with one species of partially deuterated lipids.

X-ray reflectometry complemented the neutrons measurements and provided higher resolution of thin films, with the drawback of low contrast for hydrated organic samples. With AFM indentation, surfaces were probed mechanically measuring softness and deformability. Whereas with reflectometry the signal is gathered from the whole macroscopic sample surface, AFM investigates locally with a small tip. Fluorescence microscopy was employed both for verification of sample quality before the reflectometry experiments and for observation of cells on surfaces.

Lipid bilayers containing anionic lipids were shown to have asymmetric lipid distribution across the two leaflets. In the half of the bilayer adjacent to the silicon oxide, only neutral lipids were found, as anionic lipids are repulsed electro-statically from the negatively charged surface. This asymmetry was also observed in a second project, where the deuterated lipids were in the liquid ordered phase whereas the other lipids were in the fluid phase.

Lipid bilayers were cushioned on a highly hydrated PEG polymer layer in the next project. In that system, individual lipids of the lower leaflet anchored the bilayer to the substrate. Diffusion of the lipids was only slightly reduced, as measured in a FRAP experiment. The tethered lipid bilayer could be deformed with the tip of an AFM twice as much as a bilayer directly sitting on the solid support before it ruptured. When the system was exposed to carbonate buffer at pH 10, the PEG cushion decreased in thickness. Both those results proved that the highly hydrated PEG cushion makes the bilayer flexible in respect to deformation. This characteristic brings the tethered lipid bilayer closer to a natural membrane as it allows for fluctuations and bending.

For many cell adhesion surfaces a fibronectin (FN) covering is employed. On the contrary, PEG is often used to passivate surfaces and inhibit both protein adsorption and cell adhesion. In this work, we showed that this inhibition depends strongly on the conformation of the PEG: On PLL-PEG covered surfaces treated with FN cells could still attach and migrate whereas on Pluronic cells do not attach. The reason for this, as revealed by neutron reflectometry, was that the pancake conformation of the PEG in the Pluronic repulsed the FN, whereas in the PLL-PEG FN adsorbed to the backbone of the copolymer.

Lipid bilayers were combined with protein layers to obtain more complex systems. The aim was to provide neural cells with a dense mono-layer of a synthetic cell adhesion protein. This was realized via covering the lipid bilayer with a streptavidin layer and settling the cell adhesion protein on top of that. For both interlayer links biotin was used, in the form of biotinylated lipids and biotin anchors attached to the cell adhesion protein. Thus a smooth densely packed mono-layer of the cell adhesion protein was achieved.

# Outlook

This work provides fundamental understanding of several films on the solid-liquid interface. In future, such systems can be employed for a variety of biophysical applications.

Many of the cellular processes take place in the proximity of cell membranes, therefore, artificial membrane systems are a prerequisite as model systems to study these complex mechanisms. The proteins involved are often incorporated into or associated to the membranes [75]. Due to their own amphiphilic nature, they need the lipid bilayers in order to preserve their natural structure. In an artificial system, for transmembrane proteins, hydration beneath the bilayer, as is the case for the TLBs, is essential [76].

For the study of single cells and their functions, a well defined matrix is indispensable [77]. The understanding of polymer, protein, and cell interactions gained in this work can be employed to specially tune systems. As organisms react actively to their surrounding, this tuning is necessary to archive the desired behavior.

Cell adhesion coatings are also employed on interfaces between living tissue and foreign matter, as it is the case for medical implants, where protein adsorption depends on the surface [78]. For longevity and to avoid immune rejection, such surfaces have to be specially engineered [79].

The combination of neutron reflectometry measurements with a variety of other techniques proved successful for many organic films on surfaces in hydrous environments. In future, these techniques can also be applied to films produced by cells themselves in order to observe living systems [80].



# Bibliography

- [1] S. Stanglmaier, S. Hertrich, K. Fritz, J. F. Moulin, M. Haese-Seiller, J. O. Raedler, and B. Nickel. Asymmetric distribution of anionic phospholipids in supported lipid bilayers. *Langmuir*, 28 (29): 10818–10821, 2012.
- [2] S. Hertrich, F. Stetter, A. Rühm, T. Hugel, and B. Nickel. Highly hydrated deformable polyethylene glycol-tethered lipid bilayers. *Langmuir*, 30 (31): 9442–7, 2014.
- [3] P. J. F. Röttgermann, S. Hertrich, I. Berts, M. Albert, F. J. Seegerer, J.-F. Moulin, B. Nickel, and J. O. Rädler. Cell Motility on Polyethylene Glycol Block Copolymers Correlates to Fibronectin Surface Adsorption. *Macromol. Biosci.*, 14 (12): 1755–63, 2014.
- [4] M. Huth, S. Hertrich, G. Mezo, E. Madarasz, and B. Nickel. Neural stem cell spreading on lipid based artificial cell surfaces, characterized by combined x-ray and neutron reflectometry. *Materials*, 3 (11): 4994–5006, 2010.
- [5] J. Howgate, S. J. Schoell, M. Hoeb, W. Steins, B. Baur, S. Hertrich, B. Nickel, I. D. Sharp, M. Stutzmann, and M. Eickhoff. Photocatalytic cleavage of self-assembled organic monolayers by uv-induced charge transfer from gan substrates. *Advanced Materials*, 22 (24): 2632–2636, 2010.
- [6] A. Guggenmos, R. Rauhut, M. Hofstetter, S. Hertrich, B. Nickel, J. Schmidt, E. M. Gullikson, M. Seibald, W. Schnick, and U. Kleineberg. Aperiodic crsc multilayer mirrors for attosecond water window pulses. *Opt. Express*, 21 (19): 21728–21740, 2013.
- [7] S. Jaksch, F. Lipfert, A. Koutsioubas, S. Mattauch, O. Holderer, O. Ivanova, H. Frielinghaus, S. Hertrich, S. F. Fischer, and B. Nickel. Influence of ibuprofen on phospholipid membranes. *Phys. Rev. E*, 91 (2): 022716, 2015.

- [8] <http://www.merriam-webster.com/dictionary/biophysics>.
- [9] G. M. Cooper. *The Cell: A Molecular Approach*. Sunderland (MA): Sinauer Associates, 2000.
- [10] R. W. Tsien, P. Hess, E. W. McCleskey, and R. L. Rosenberg. CALCIUM CHANNELS: Mechanisms of Selectivity, Permeation, and Block. *Ann. Rev. Biophys. Biophys. Chem.*, 16: 265–290, 1987.
- [11] D. Ungar and F. M. Hughson. SNARE protein structure and function. *Annu. Rev. Cell Dev. Biol.*, 19: 493–517, 2003.
- [12] M. A. Lemmon and J. Schlessinger. NIH Public Access. *Cell*, 141 (7): 1117–1134, 2010.
- [13] L. J. F. Jones, R. Carballido-Lopez, and J. Errington. Control of Cell Shape in Bacteria: Helical, Actin-like Filaments in *Bacillus subtilis*. *Cell*, 104 (6): 913–922, 2001.
- [14] M. Welte. Bidirectional transport along microtubules. *Curr. Biol.*, 14 (13): R525–37, 2004.
- [15] E. Sackmann. Supported membranes: scientific and practical applications. *Science*, 271 (5245): 43–48, 1996.
- [16] J. A. Zasadzinski, R. Viswanathan, L. Madsen, J. Garnæs, and D. K. Schwartz. Langmuir-Blodgett Films. *Science*, 263 (5154): 1726–1733, 1994.
- [17] A. G. Lee. How lipids affect the activities of integral membrane proteins. *Biochim. Biophys. Acta*, 1666 (1-2): 62–87, 2004.
- [18] I. P. McCabe and M. B. Forstner. Polymer Supported Lipid Bilayers. *Open J. Biophys.*, 03 (1A): 59–69, 2013.
- [19] T. Charitat, E. Bellet-Amalric, G. Fragneto, and F. Graner. Adsorbed and free lipid bilayers at the solid-liquid interface. *Eur. Phys. J. B*, 8 (4): 583–593, 1999.
- [20] S. Nirasay, A. Badia, G. Leclair, J. P. Claverie, and I. Marcotte. Polydopamine-Supported Lipid Bilayers. *Materials*, 5 (12): 2621–2636, 2012.
- [21] R. Michel, S. Pasche, M. Textor, and D. G. Castner. Influence of PEG architecture on protein adsorption and conformation. *Langmuir*, 21 (26): 12327–32, 2005.

- [22] E. Biazar, M. Heidari, A. Asefnejad, A. Asefnezhad, and N. Montazeri. The relationship between cellular adhesion and surface roughness in polystyrene modified by microwave plasma radiation. *Int. J. Nanomedicine*, 6: 631–9, 2011.
- [23] P. J. F. Röttgermann, A. P. Alberola, and J. O. Rädler. Cellular self-organization on micro-structured surfaces. *Soft Matter*, 10 (14): 2397–404, 2014.
- [24] R. K. Thomas. Neutron reflection from liquid interfaces. *Annu. Rev. Phys. Chem.*, 55 (1): 391–426, 2004.
- [25] B. Jacrot. The study of biological structures by neutron scattering from solution. *Rep. Prog. Phys.*, 39: 911–953, 1976.
- [26] E. B. Watkins, R. J. El-khoury, C. E. Miller, B. G. Seaby, J. Majewski, C. M. Marques, and T. L. Kuhl. Structure and thermodynamics of lipid bilayers on polyethylene glycol cushions: fact and fiction of PEG cushioned membranes. *Langmuir*, 27 (22): 13618–28, 2011.
- [27] E. Novakova, K. Giewekemeyer, and T. Salditt. Structure of two-component lipid membranes on solid support: An X-ray reflectivity study. *Phys. Rev. E*, 74 (5): 051911, 2006.
- [28] F. Stetter and T. Hugel. The nanomechanical properties of lipid membranes are significantly influenced by the presence of ethanol. *Biophysical Journal*, 104 (5): 1049–1055, 2013.
- [29] D. Axelrod, D. E. Koppel, J. Schlessinger, E. Elson, and W. W. Webb. Mobility measurement by analysis of fluorescence photobleaching recovery kinetics. *Biophys. J.*, 16 (9): 1055–1069, 1976.
- [30] G. van Meer, D. R. Voelker, and G. W. Feigenson. Membrane lipids: where they are and how they behave. *Nat. Rev. Mol. Cell Biol.*, 9 (2): 112–24, 2008.
- [31] B. Fadeel and D. Xue. The ins and outs of phospholipid asymmetry in the plasma membrane: roles in health and disease. *Crit. Rev. Biochem. Mol. Biol.*, 44 (5): 264–277, 2010.
- [32] F.-X. Contreras, L. Sánchez-Magraner, A. Alonso, and F. M. Goñi. Transbilayer (flip-flop) lipid motion and lipid scrambling in membranes. *FEBS Lett.*, 584 (9): 1779–86, 2010.

- [33] B. D. Smith and T. N. Lambert. Molecular ferries: membrane carriers that promote phospholipid flip-flop and chloride transport. *Chem. Commun.*, (18): 2261–2268, 2003.
- [34] P. S. Cremer and S. G. Boxer. Formation and spreading of lipid bilayers on planar glass supports. *J. Phys. Chem. B*, 103 (13): 2554–2559, 1999.
- [35] M. L. Wagner and L. K. Tamm. Tethered polymer-supported planar lipid bilayers for reconstitution of integral membrane proteins: silane-polyethyleneglycol-lipid as a cushion and covalent linker. *Biophys. J.*, 79 (3): 1400–14, 2000.
- [36] R. Naumann, E. Schmidt, A. Jonczyk, K. Fendler, B. Kadenbach, T. Liebermann, A. Offenhäusser, and W. Knoll. The peptide-tethered lipid membrane as a biomimetic system to incorporate cytochrome c oxidase in a functionally active form. *Biosens. Bioelectron.*, 14 (7): 651–662, 1999.
- [37] P. Flory. *Principles of Polymer Chemistry*. Cornell University Press, Ithaca, N.Y, 1971.
- [38] P. G. de Gennes. Conformations of Polymers Attached to an Interface. *Macromolecules*, 13: 1069–1075, 1980.
- [39] Y. Duval, J. A. Mielczarski, O. S. Pokrovsky, E. Mielczarski, and J. J. Ehrhardt. Evidence of the existence of three types of species at the quartz-aqueous solution interface at pH 0-10: XPS surface group quantification and surface complexation modeling. *J. Phys. Chem. B*, 106 (11): 2937–2945, 2002.
- [40] P. Almeida and W. Vaz. *Lateral diffusion in membranes*, volume 1A. Amsterdam: Elsevier, 1995.
- [41] M. Chalfie, Y. Tu, G. Euskirchen, W. W. Ward, and D. C. Prasher. Green Fluorescent Protein as a Marker for Gene Expression. *Science*, 263 (5148): 802–805, 1994.
- [42] T. K. L. Meyvis, S. C. De Smedt, P. Van Oostveldt, and J. Demeester. Fluorescence recovery after photobleaching: A versatile tool for mobility and interaction measurements in pharmaceutical research. *Pharmaceutical Research*, 16 (8): 1153–1162, 1999.
- [43] G. K. Binnig. Atomic-Force Microscopy. *Phys. Scr.*, T19: 53–55, 1987.
- [44] J. H. Tong and T. J. McIntosh. Structure of supported bilayers composed of lipopolysaccharides and bacterial phospholipids: Raft formation and implications for bacterial resistance. *Biophys. J.*, 86 (6): 3759–3771, 2004.

- [45] A. Alessandrini, H. M. Seeger, A. Di Cerbo, T. Caramaschi, and P. Facci. What do we really measure in AFM punch-through experiments on supported lipid bilayers? *Soft Matter*, 7 (15): 7054–7064, 2011.
- [46] M. Tolan. *X-Ray Scattering from Soft-Matter Thin Films*. Springer-Verlag Berlin Heidelberg, 1999.
- [47] M. Born and E. Wolf. *Principles of Optics*. Pergamon Press, 1970.
- [48] P. NEVOT L, CROCE. Characterization of surfaces by grazing x-ray reflection - application to study of polishing of some silicate-glasses. *Revue de physique appliquee*, 15 (3): 761–779, 1980.
- [49] A. Nelson. Co-refinement of multiple-contrast neutron/X-ray reflectivity data using MOTOFIT. *J. Appl. Crystallogr.*, 39 (2): 273–276, 2006.
- [50] R. Kampmann, M. Haese-Seiller, V. Kudryashov, B. Nickel, C. Daniel, W. Fenzl, A. Schreyer, E. Sackmann, and J. Rädler. Horizontal ToF-neutron reflectometer REF-SANS at FRM-II Munich/Germany: First tests and status. *Physica B: Condensed Matter*, 385-386: 1161–1163, 2006.
- [51] J. Liu and J. C. Conboy. 1,2-Diacyl-Phosphatidylcholine Flip-Flop Measured Directly By Sum-Frequency Vibrational Spectroscopy. *Biophys. J.*, 89 (4): 2522–32, 2005.
- [52] K. Fritz, G. Fritz, B. Windschiegl, C. Steinem, and B. Nickel. Arrangement of Annexin A2 tetramer and its impact on the structure and diffusivity of supported lipid bilayers. *Soft Matter*, 6 (17): 4084–4094, 2010.
- [53] M. Goedert. Alpha-synuclein and neurodegenerative diseases. *Nat. Rev. Neurosci.*, 2: 492–501, 2001.
- [54] C. B. Lücking and A. Brice. Alpha-synuclein and parkinson’s disease. *Cell. Mol. Life. Sci.*, 57: 1894–1908, 2000.
- [55] E. I. Goksu, J. M. Vanegas, C. D. Blanchette, W.-C. Lin, and M. L. Longo. AFM for structure and dynamics of biomembranes. *Biochim. Biophys. Acta*, 1788 (1): 254–66, 2009.
- [56] Y. Rodríguez, M. Mezei, and R. Osman. Association free energy of dipalmitoylphosphatidylserines in a mixed dipalmitoylphosphatidylcholine membrane. *Biophys. J.*, 92 (9): 3071–80, 2007.

- [57] F. A. Heberle and G. W. Feigenson. Phase Separation in Lipid Membranes. *Cold Spring Harb Perspect Biol*, 3 (a004630): 1–13, 2011.
- [58] I. Reviakine, A. Simon, and A. Brisson. Effect of  $\text{Ca}^{2+}$  on the morphology of mixed DPPC-DOPS supported phospholipid bilayers. *Langmuir*, 16 (4): 1473–1477, 2000.
- [59] J. Daillant, K. Quinn, C. Gourier, and F. Rieutord. Grazing incidence surface scattering of X-rays. *J. Chem. Soc., Faraday Trans*, 92 (4): 505–513, 1996.
- [60] P. Mueller-Buschbaum. Grazing incidence small-angle neutron scattering: challenges and possibilities. *Polym. J.*, 45 (1, SI): 34–42, 2013.
- [61] P. Mueller-Buschbaum, L. Schulz, E. Metwalli, J. F. Moulin, and R. Cubitt. Lateral structures of buried interfaces in ABA-type triblock copolymer films. *Langmuir*, 24 (15): 7639–7644, 2008.
- [62] M. Rawolle, K. Sarkar, M. A. Niedermeier, M. Schindler, P. Lellig, J. S. Gutmann, J.-F. Moulin, M. Haese-Seiller, A. S. Wochnik, C. Scheu, and P. Mueller-Buschbaum. Infiltration of Polymer Hole-Conductor into Mesoporous Titania Structures for Solid-State Dye-Sensitized Solar Cells. *ACS Appl. Mater. Interfaces*, 5 (3): 719–729, 2013.
- [63] J. T. Groves. Bending mechanics and molecular organization in biological membranes. *Annu. Rev. Phys. Chem.*, 58: 697–717, 2007.
- [64] M. C. Watson, E. S. Penev, P. M. Welch, and F. L. H. Brown. Thermal fluctuations in shape, thickness, and molecular orientation in lipid bilayers. *J. Chem. Phys.*, 135 (24): 244701, 2011.
- [65] C. Rossi and J. Chopineau. Biomimetic tethered lipid membranes designed for membrane-protein interaction studies. *Eur. Biophys. J.*, 36 (8): 955–65, 2007.
- [66] S. R. Jadhav, D. Sui, R. M. Garavito, and R. M. Worden. Fabrication of highly insulating tethered bilayer lipid membrane using yeast cell membrane fractions for measuring ion channel activity. *J. Colloid Interface Sci.*, 322 (2): 465–72, 2008.
- [67] R. Budvytyte, G. Valincius, G. Niaura, V. Voiciuk, M. Mickevicius, H. Chapman, H.-Z. Goh, P. Shekhar, F. Heinrich, S. Shenoy, M. Lösche, and D. J. Vanderah. Structure and properties of tethered bilayer lipid membranes with unsaturated anchor molecules. *Langmuir*, 29 (27): 8645–8656, 2013.

- [68] F. Giess, M. G. Friedrich, J. Heberle, R. L. Naumann, and W. Knoll. The protein-tethered lipid bilayer: a novel mimic of the biological membrane. *Biophys. J.*, 87 (5): 3213–20, 2004.
- [69] C. Daniel, K. E. Sohn, T. E. Mates, E. J. Kramer, J. O. Raedler, E. Sackmann, B. Nickel, and L. Andruzzi. Structural characterization of an elevated lipid bilayer obtained by stepwise functionalization of a self-assembled alkenyl silane film. *Biointerphases*, 2 (3): 109–118, 2007.
- [70] L. Guo, J. Y. Har, J. Sankaran, Y. Hong, B. Kannan, and T. Wohland. Molecular diffusion measurement in lipid bilayers over wide concentration ranges: a comparative study. *Chemphyschem*, 9 (5): 721–728, 2008.
- [71] J. F. Marko and E. D. Siggia. Stretching DNA. *Macromolecules*, 28 (26): 8759–8770, 1995.
- [72] B. M. Gumbiner. Cell Adhesion: The Molecular Basis of Tissue Architecture and Morphogenesis. *Cell*, 84 (3): 345–357, 1996.
- [73] T. Mcpherson, A. Kidane, I. Szleifer, and K. Park. Prevention of Protein Adsorption by Tethered Poly(ethylene oxide) Layers: Experiments and Single-Chain Mean-Field Analysis. *Langmuir*, 14 (1): 176–186, 1998.
- [74] S. Pasche, S. M. De Paul, J. Vörös, N. D. Spencer, and M. Textor. Poly (L-lysine)-graft-poly (ethylene glycol) Assembled Monolayers on Niobium Oxide Surfaces: A Quantitative Study of the Influence of Polymer Interfacial Architecture on Resistance to Protein Adsorption by ToF-SIMS and in Situ OWLS. *Langmuir*, 19 (22): 9216–9225, 2003.
- [75] S. Damiati, A. Schrems, E.-K. Sinner, U. B. Sleytr, and B. Schuster. Probing peptide and protein insertion in a biomimetic S-layer supported lipid membrane platform. *Int. J. Mol. Sci.*, 16 (2): 2824–38, 2015.
- [76] H. Basit, V. Gaul, S. Maher, R. J. Forster, and T. E. Keyes. Aqueous-filled polymer microcavity arrays: versatile & stable lipid bilayer platforms offering high lateral mobility to incorporated membrane proteins. *Analyst*, 140 (9): 3012–8, 2015.
- [77] P. Sharma, A. Kim, A. Gill, J. Wang, K. Sheets, B. Behkam, and A. S. Nain. Aligned and suspended fiber force probes for drug testing at single cell resolution. *Biofabrication*, 6 (4): 045006, 2014.

- 
- [78] H. Majd, S. S. Scherer, S. Boo, S. Ramondetti, E. Cambridge, W. Raffoul, M. Friedrich, B. Pittet, D. Pioletti, B. Hinz, and G. Pietramaggiore. Novel micropatterns mechanically control fibrotic reactions at the surface of silicone implants. *Biomaterials*, 54: 136–47, 2015.
- [79] H. Zhang and M. Chiao. Anti-fouling Coatings of Poly(dimethylsiloxane) Devices for Biological and Biomedical Applications. *J. Med. Biol. Eng.*, 35 (2): 143–155, 2015.
- [80] A. Junghans, M. J. Waltman, H. L. Smith, L. Pocivavsek, N. Zebda, K. Birukov, M. Viapiano, and J. Majewski. Understanding dynamic changes in live cell adhesion with neutron reflectometry. *Mod Phys Lett B.*, 28 (30): 1320015, 2015.

# List of Figures

2.1	Lipid composition of an eucariotic plasma membrane . . . . .	6
2.2	Natural composition of the lipid bilayer of an eucariotic lipid membrane . . . . .	6
2.3	Surface potential of SiO <sub>2</sub> at different NaCl concentrations . . . . .	10
2.4	Chopperblades and Neutronpulses . . . . .	16
2.5	X-ray lab setup . . . . .	17
2.6	Fluidic chamber for X-ray measurements and microscopy . . . . .	19
2.7	Components of neutron fluidic chamber . . . . .	19
3.1	Asymmetric supported lipid bilayer . . . . .	21
3.2	Neutron reflectometry on 3:1 d <sub>31</sub> POPS / POPC . . . . .	23
3.3	Hydration and dry SLD of 3:1 d <sub>31</sub> POPS / POPC bilayer. . . . .	23
3.4	X-ray reflectivity measurement of $\alpha$ -synuclein interaction . . . . .	25
3.5	Neutron reflectivity measurement of $\alpha$ -synuclein interaction . . . . .	26
3.6	Sketch of domain structure of 4:1 d <sub>62</sub> DPPC / DOPS . . . . .	27
3.7	Reflectometry data and fit of d <sub>62</sub> DPPC / DOPS (4:1) . . . . .	28
3.8	Hydration and SLD d <sub>62</sub> DPPC / DOPS (4:1) . . . . .	29
3.9	GISANS maps of d <sub>62</sub> DPPC - DOPS . . . . .	31
4.1	Sketch of the TLB system. . . . .	34
4.2	Chemical structure of the TLB substrate . . . . .	35
4.3	TLB substrate, X-ray reflectometry on air . . . . .	35
4.4	FRAP on TLB . . . . .	37
4.5	Diffusion of lipids . . . . .	38
4.6	Neutron and X-ray data and SLD model for TLB . . . . .	39
4.7	Electron density and hydration, extracted from the models . . . . .	40
4.8	AFM indention into the TLB . . . . .	41

---

4.9	Change in thickness of the PEG cushion in carbonate buffer . . . . .	43
5.1	Sketch of cells on different PEG surfaces . . . . .	46
5.2	Structure of PEG surfaces . . . . .	47
5.3	Neutron reflectometry on Pluronic . . . . .	48
5.4	Neutron reflectometry on PLL-g-PEG . . . . .	50
5.5	FN interaction into the polymer . . . . .	51
5.6	Microscopy of cells on PEG and FN surfaces . . . . .	52
5.7	Comparison of spreading areas per cell . . . . .	53
5.8	Trajectories and speed of cells . . . . .	54
5.9	Neural Cell attachment surface structure . . . . .	55
5.10	Cell attachment peptide . . . . .	56
5.11	Neutron and x-ray reflectometry data for lipid protein multilayer . . . . .	57
5.12	Scattering length density . . . . .	58
5.13	Hydration of the neural cell attachment system . . . . .	58
5.14	Microscopy images of neural cells . . . . .	59

# Appendix A

## Publications

Fulltexts of all publications SH contributed to are included here.

Each publication is described in a header page, which includes title, listing of all authors, abstract, and the type of contribution.



## A.1 Full text of ref. [1]:

### Asymmetric Distribution of Anionic Phospholipids in Supported Lipid Bilayers

**Authors:** Stefan Stanglmaier, Samira Hertrich, Kirstin Fritz, Jean-François Moulin, Martin Haese-Seiller, Joachim O. Rädler, and Bert Nickel

**Abstract:** Lipid bilayers with a controlled content of anionic lipids are a prerequisite for the quantitative study of hydrophobicelectrostatic interactions of proteins with lipid bilayers. Here, the asymmetric distribution of zwitterionic and anionic lipids in supported lipid bilayers is studied by neutron reflectometry. We prepare POPC/POPS (3:1) unilamellar vesicles in a high-salt-concentration buffer. Initially, no fusion of the vesicles to a SiO<sub>2</sub> surface is observed over hours and days. Once the isotonic buffer is exchanged with hypotonic buffer, vesicle fusion and bilayer formation occur by osmotic shock. Neutron reflectivity on the bilayers formed this way reveals the presence of anionic lipids (d<sub>31</sub>-POPS) in the outer bilayer leaflet only, and no POPS is observed in the leaflet facing the SiO<sub>2</sub> substrate. We argue that this asymmetric distribution of POPS is induced by the electrostatic repulsion of the phosphatidylserines from the negatively charged hydroxy surface groups of the silicon block. Such bilayers with controlled and high contents of anionic lipids in the outer leaflet are versatile platforms for studying anionic lipid protein interactions that are key elements in signal transduction pathways in the cytoplasmic leaflet of eukaryotic cells.

#### SH contribution:

- Contribution to neutron reflectometry measurement, data analysis and interpretation
- Contribution to writing the paper



# Asymmetric Distribution of Anionic Phospholipids in Supported Lipid Bilayers

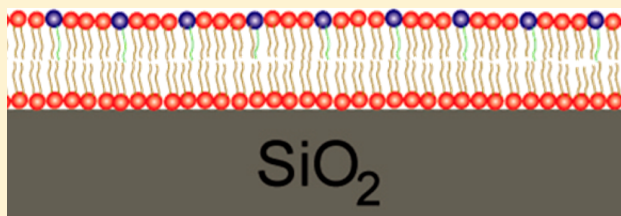
S. Stanglmaier,<sup>†</sup> S. Hertrich,<sup>†</sup> K. Fritz,<sup>†</sup> J.-F. Moulin,<sup>‡</sup> M. Haese-Seiller,<sup>‡</sup> J. O. Rädler,<sup>†</sup> and B. Nickel<sup>\*†</sup>

<sup>†</sup>Ludwig-Maximilians-Universität, Fakultät für Physik & CeNS, Geschwister-Scholl-Platz 1, 80539 Munich, Germany

<sup>‡</sup>Helmholtz Zentrum Geesthacht at FRM-2, Institut für Werkstofforschung, Abteilung WPN, Lichtenbergstr. 1, 85747 Garching

## Supporting Information

**ABSTRACT:** Lipid bilayers with a controlled content of anionic lipids are a prerequisite for the quantitative study of hydrophobic–electrostatic interactions of proteins with lipid bilayers. Here, the asymmetric distribution of zwitterionic and anionic lipids in supported lipid bilayers is studied by neutron reflectometry. We prepare POPC/POPS (3:1) unilamellar vesicles in a high-salt-concentration buffer. Initially, no fusion of the vesicles to a SiO<sub>2</sub> surface is observed over hours and days. Once the isotonic buffer is exchanged with hypotonic buffer, vesicle fusion and bilayer formation occur by osmotic shock. Neutron reflectivity on the bilayers formed this way reveals the presence of anionic lipids (*d*<sub>31</sub>-POPS) in the outer bilayer leaflet only, and no POPS is observed in the leaflet facing the SiO<sub>2</sub> substrate. We argue that this asymmetric distribution of POPS is induced by the electrostatic repulsion of the phosphatidylserines from the negatively charged hydroxy surface groups of the silicon block. Such bilayers with controlled and high contents of anionic lipids in the outer leaflet are versatile platforms for studying anionic lipid protein interactions that are key elements in signal transduction pathways in the cytoplasmic leaflet of eukaryotic cells.



## 1. INTRODUCTION

Anionic lipids play a prominent role in mediating the coupling of proteins to the cytoplasmic membrane. GTPases, for example, interact with the membrane because of a combination of direct electrostatic and hydrophobic forces.<sup>1</sup> For annexins, Ca ions act as a salt bridge binding the negatively charged protein to an anionic membrane.<sup>2</sup> Remarkably, the lipid compositions of the two leaflets of eukaryotic plasma membranes exhibit a high degree of asymmetry.<sup>3</sup> Anionic lipids such as phosphatidylserine (PS) occur only in the cytoplasmic leaflet of eukaryotic plasma membranes under normal conditions. The occurrence of PS lipids in the outer layer of the plasma membrane of blood platelets leads to coagulation, whereas PS in the outer surface of apoptotic cells causes recognition by phagocytes.<sup>4</sup> Therefore, PS-binding proteins such as annexins<sup>2</sup> are used as an apoptosis marker. Anionic phospholipids also trigger the formation of amyloid-type fibers by several proapoptotic, cytotoxic, and antimicrobial proteins and peptides.<sup>5–7</sup>

To study the interaction mechanism of proteins with anionic lipids in supported bilayers,<sup>8,9</sup> precise control of the anionic lipid composition in the protein adjacent leaflet is mandatory. On one hand, one may deposit asymmetric bilayers by Langmuir–Schäfer transfer.<sup>10</sup> On the other hand, one may choose the lipid composition, substrate surface,<sup>11,12</sup> and ionic strength of the buffer accordingly to favor the formation of an asymmetric membrane by self-organization (e.g., by vesicle fusion<sup>13</sup>). In any case, a precise experimental readout is needed to confirm the lipid distribution. Neutron reflectometry (NR) is

a unique interference technique that allows us to quantify the lipid distribution between two leaflets. Here, we show that by NR it is possible to determine the lipid content per leaflet in a bilayer created by osmotic shock.

## 2. MATERIAL AND METHODS

**2.1. Substrate and Sample Preparation for Lipid Bilayer Deposition.** A polished silicon block (100 mm × 50 mm × 10 mm, Crystec, Berlin, Germany) was thermally oxidized; the 100 nm oxide layer allows for fluorescence microscopy. Before the deposition of the SLB, the block was cleaned by sonication in isopropanol and acetone for 10 min each, followed by intensive rinsing with deionized (DI) water. Afterward, a two-step chemical cleaning procedure was applied.<sup>14</sup> First, the substrate was boiled in H<sub>2</sub>O<sub>2</sub>/HCl/H<sub>2</sub>O (1:1:5 by volume) for 60 min and then in H<sub>2</sub>O<sub>2</sub>/NH<sub>4</sub>OH/H<sub>2</sub>O (1:1:5) for another 60 min at 80 °C. After each step, the substrate was rinsed thoroughly with DI water. Afterward, the surface of the silicon substrate was hydrophilic. The block was kept in ethanol until further use.

**2.2. Vesicles and Supported Lipid Bilayer Formation.** POPC, *d*<sub>31</sub>-POPC, and *d*<sub>31</sub>-POPS, dissolved in a chloroform solution, were purchased from Avanti Polar Lipids (Alabaster, AL) and used as received. TR-DHPE was purchased from Invitrogen and dissolved in chloroform. For the preparation of unilamellar vesicles, solutions of first 99.5 mol % *d*<sub>31</sub>-POPC and 0.5 mol % TR-DHPE and second 74.6 mol % POPC, 24.9 mol % *d*<sub>31</sub>-POPS, and 0.5 mol % TR-DHPE were mixed in a glass vial. In the following text, these mixtures are termed

Received: May 15, 2012

Revised: June 22, 2012

Published: July 12, 2012

$d_{31}$ -POPC and POPC/ $d_{31}$ -POPS (3:1), respectively. The chloroform was evaporated in a nitrogen stream followed by evacuation in vacuum. The dry lipid film in the vial was suspended with high-salt-concentration phosphate buffer I (1.1 M NaCl, 2.7 mM KCl, 10 mM  $\text{Na}_2\text{HPO}_4$  and 2 mM  $\text{KH}_2\text{PO}_4$  in  $\text{D}_2\text{O}$ , pH 7.4) to a final concentration of 1 mg/mL and heated to 40–45 °C for 2 h. The lipid suspension was vortex mixed and passed through a polycarbonate filter with 100 nm pores (Avanti Polar Lipids) 11 times.<sup>15</sup> The vesicle solution was injected into the sample chamber, which was previously filled with high-salt-concentration phosphate buffer I, and incubated for 3 h. This allowed the vesicles to adhere to the hydrophilic surface of the  $\text{SiO}_2$  substrate.<sup>16</sup> To rupture the vesicles adhered to the surface, medium-salt-concentration phosphate buffer II (138 mM NaCl, 2.7 mM KCl, 10 mM  $\text{Na}_2\text{HPO}_4$ , and 2 mM  $\text{KH}_2\text{PO}_4$  in  $\text{D}_2\text{O}$ , pH 7.4) was slowly injected into the sample chamber. This buffer change induces osmotic stress in the vesicles, which are now surrounded by hypotonic buffer. The osmotic stress induces vesicle rupture and the formation of a continuous bilayer on the  $\text{SiO}_2$  surface. After rupture, the samples were flushed several times with DI water ( $\text{D}_2\text{O}$ ) to remove excess material in the form of multilayers or aggregates. After being rinsed, the chamber was again filled with medium salt buffer II to stabilize the SLB on the  $\text{SiO}_2$  block against delamination with time. The homogeneity and fluidity of the SLB were verified by fluorescence microscopy.

**2.3. Neutron Reflectivity Measurements.** The measurements were performed at the REFSANS neutron reflectometer at FRM II in Munich. REFSANS is a time-of-flight (ToF) instrument for reflectometry at the solid–liquid interface.<sup>17,18</sup> We make use of isotope labeling (i.e., deuteration of the lipid chains) and contrast variation by exchanging  $\text{D}_2\text{O}$  against a mixture of  $\text{H}_2\text{O}/\text{D}_2\text{O}$ . This allows us to determine the volume fraction of the lipids ( $x_1$ ) and the hydration water fraction ( $x_2$ ) as a function of depth as well as the scattering length density (SLD) profile of the bilayer. The detailed procedure is outlined in the Supporting Information.

### 3. EXPERIMENTS AND DISCUSSION

We start by confirming that the scattering length density profile of a pure  $d_{31}$ -POPC bilayer on  $\text{SiO}_2$  is symmetric. The bilayer is evaluated by neutron reflectometry after equilibration for 24 h at room temperature. The normalized reflected intensity of the  $d_{31}$ -POPC SLB sample in PBS buffer in  $\text{D}_2\text{O}$  is shown in Figure 1a(i). The edge of total reflection occurs at  $q \approx 0.015 \text{ \AA}^{-1}$ , as expected for a  $\text{SiO}_2$  interface in a  $\text{D}_2\text{O}$  contrast. The measurement of the  $d_{31}$ -POPC SLB in a PBS buffer of  $\text{D}_2\text{O}/\text{H}_2\text{O}$  is also shown in Figure 1a(ii). Here, the SLD of the  $\text{D}_2\text{O}/\text{H}_2\text{O}$  solvent is matched to that of  $\text{SiO}_2$ . Because of the reduced contrast between solvent and  $\text{Si}$ , the total reflection edge is further reduced to  $q \approx 0.008 \text{ \AA}^{-1}$ , as expected. The reflectivity data in both measurements show rapid intensity oscillations originating from the thick oxide layer (here  $d_{\text{SiO}_2} \approx 650 \text{ \AA}$ ) on top of the silicon block and a broad shoulder originating from the lipid bilayer. The intensities obtained from the modeling of the experimental data using the Parratt formalism<sup>19,20</sup> and the Motofit program<sup>21</sup> are shown as blue and red curves in Figure 1a(i),(ii). The respective SLD profiles of the two solvent contrasts ( $\text{SLD}_{\text{exp1}}$  and  $\text{SLD}_{\text{exp2}}$ ) are shown in Figure 1a(iii). Because of partial deuteration of the lipid chain, the scattering contrast of the bilayer with respect to the  $\text{Si}/\text{SiO}_2$  substrate is low.

Under the  $\text{D}_2\text{O}$  contrast condition, an increase in SLD between  $z \approx 10$  and 25 Å is observed (cf. Figure 1a(iii), blue curve); we interpret this increase as due to the hydration of the lipid headgroup.<sup>22</sup> The hydration analysis outlined in the Supporting Information indicates a water volume fraction of ca. 30% for the headgroup. As expected, no such increase is observed under the  $\text{D}_2\text{O}/\text{H}_2\text{O}$  contrast condition (cf. Figure

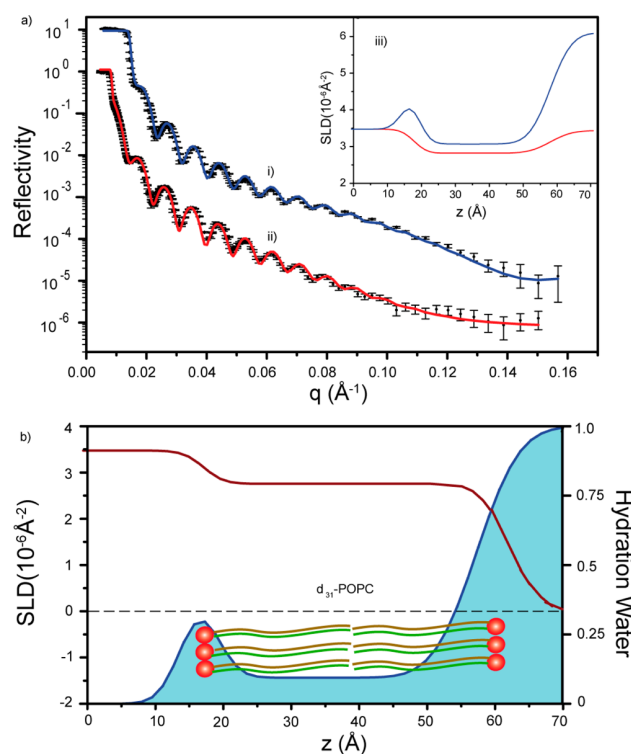


**Figure 1.** Neutron reflectometry and analysis. (a) Reflectivity data from a  $d_{31}$ -POPC SLB. The corresponding modeling function is represented by colored lines: (i)  $\text{D}_2\text{O}$  contrast (blue line); (ii) a  $\text{D}_2\text{O}/\text{H}_2\text{O}$  mixture with SLD equal to  $\text{SiO}_2$  (red line). (iii) an SLD profile as extracted from the modeling. (b) SLD profile without solvent (dark brown line) and hydration fraction (blue area).

1a(iii), red curve). The region of the  $d_{31}$ -POPC chain is clearly visible in the SLD profile in Figure 1b in the range of  $z \approx 25$ –55 Å. The solvent fraction of the hydrophobic chain region observed here is approximately 10% (details in eq 2 in the Supporting Information) and is most likely caused by incomplete coverage of the silicon substrate by the lipid bilayer. Such incomplete coverage has been observed before and is well in the expected range;<sup>23</sup> note that the measurement averages an area of ca. 600  $\text{cm}^2$ . The SLD is distributed symmetrically across the inner and outer leaflets of the membrane (Figure 1b). From the analysis outlined in the experimental section, we obtain  $\text{SLD}_{\text{chain}} = \text{SLD}_{\text{w/o solvent}} = 2.76 \times 10^{-6} \text{ \AA}^{-2}$ . The value for  $\text{SLD}_{\text{chain}}$  estimated from the molecular volume ranges from  $3.3 \times 10^{-6}$  to  $2.6 \times 10^{-6} \text{ \AA}^{-2}$ , equivalent to areal densities of 55  $\text{\AA}^2/\text{lipid}$  and 70  $\text{\AA}^2/\text{lipid}$ , respectively, indicating that the SLB here is in the fluid, low-density state. In summary, the experiment confirms that the two leaflets in a deuterated POPC bilayer are identical in density.

To study the distribution of the anionic lipids in a mixed bilayer, we chose to deuterate the PS lipid this time. A mixture of POPC/ $d_{31}$ -POPS in a ratio of 3:1 is investigated. The reflectivity measurement on this bilayer in  $\text{D}_2\text{O}$  contrast is shown in Figure 2a(i). Then, the solvent in the sample cell was exchanged against the silicon oxide-matched  $\text{D}_2\text{O}/\text{H}_2\text{O}$  contrast (Figure 2a(ii)). The colored lines in Figure 2a are the corresponding intensity fits. The scattering length density profile of the POPC/ $d_{31}$ -POPS (3:1) SLB is shown in Figure 2b (SLD). Again, in  $\text{D}_2\text{O}$  contrast a hydration layer between

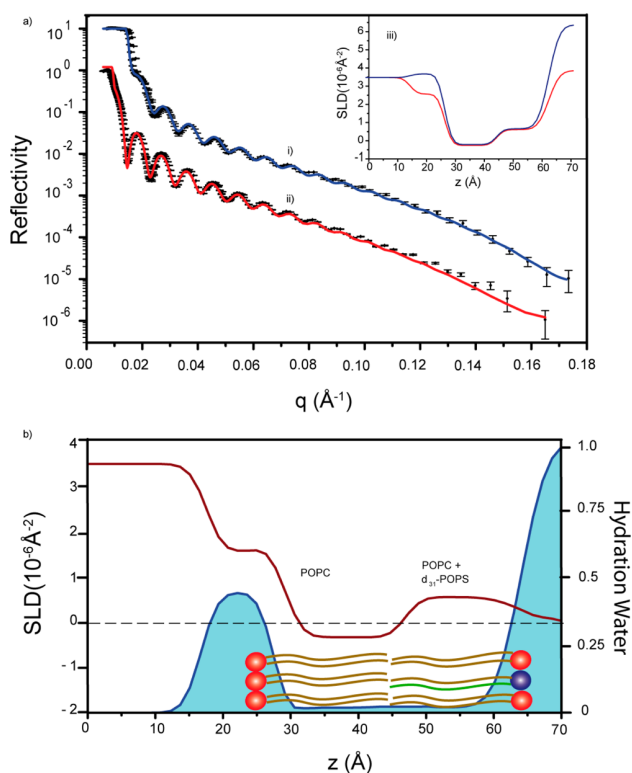


**Figure 2.** Neutron reflectometry data and analysis. (a) Reflectivity data from a mixed (POPC/ $d_{31}$ -POPS 3:1) SLB. The corresponding modeling function is represented by colored lines: (i)  $D_2O$  contrast (blue line); (ii) a  $D_2O/H_2O$  mixture with SLD equal to  $SiO_2$  (red line); and (iii) an SLD profile, as extracted from the modeling. (b) SLD profile without solvent (dark-brown line) and a hydration fraction (blue area).

the  $SiO_2$  substrate and the inner membrane leaflet is indicated by an increase in the SLD profile close to the substrate.

Most remarkably, the region of the lipid chains in Figure 2b exhibits two plateaus in the range between  $z \approx 32\text{--}44$  Å and  $z \approx 48\text{--}60$  Å (i.e., there is clear asymmetry between the inner and outer leaflets). The SLD values clearly indicate an enrichment of deuterated ( $d_{31}$ -POPS) lipids in the outer leaflet of the membrane. The water fraction of 1 to 2% in the hydrophobic chain region observed here indicates a high coverage of the silicon substrate by the lipid bilayer. From the analysis of the experimental SLDs,<sup>24</sup> we obtain  $SLD_{\text{chain}} = SLD_{\text{w/o solvent}} = (-0.34 \pm 0.20) \times 10^{-6} \text{ \AA}^{-2}$  for the inner leaflet and  $(+0.54 \pm 0.23) \times 10^{-6} \text{ \AA}^{-2}$  for the outer leaflet. A comparison to estimated SLDs of a bare  $d_{31}$ -POPS bilayer  $(+2.6 \times 10^{-6} \text{ \AA}^{-2})$ , a bare POPC bilayer  $(-0.23 \times 10^{-6} \text{ \AA}^{-2})$ , and a mixed POPC/ $d_{31}$ -POPS (3:1) bilayer  $(+0.47 \times 10^{-6} \text{ \AA}^{-2})$  allows for a clear-cut interpretation of this result. Namely, using an areal density of  $70 \text{ \AA}^2/\text{lipid}$ , the PS concentration in the outer bilayer leaflet is  $27 \pm 8\%$  (i.e., very close to the stoichiometric ratio of 25%). However, we do not see contributions of PS at the inner, substrate facing leaflet, which is purely POPC within the accuracy of the analysis ( $0 \pm 3\%$ ). The observation that the stoichiometric ratio of the vesicles is conserved in the outer bilayer sheet but that PS is depleted in the leaflet adjacent to the substrate indicates that this asymmetric distribution is apparently not due to a redistribution of lipids between the inner and outer leaflets (e.g., by flip-flop or edge diffusion) but is due to a different

mass-transfer efficiency upon vesicle fusion (i.e., some PS fraction in the vesicles is lost upon transfer to the supported bilayer).

Now we discuss how electrostatic interactions can explain the experimental findings. The density of silanol groups at the silica surface is up to  $4.9 \text{ sites/nm}^2$ .<sup>25</sup> At pH 7.4, about 18% of those are deprotonated,<sup>25</sup> yielding a negative surface charge density ( $\sigma$ ) on the order of  $\sigma = -0.14 \text{ C/m}^2$ . In a high salt buffer (i.e., at 1.1 M monovalent NaCl electrolyte), the Debye screening length ( $\kappa^{-1}$ ) is approximately 3 Å. Therefore, the electrostatic potential originating from the surface charge of the  $SiO_2$  surface falls off rapidly (cf. Supporting Information). Thus, prior to contact, only the anionic lipids facing  $SiO_2$  feel a repulsion. Therefore, we assume that prior to vesicle fusion anionic  $d_{31}$ -POPS lipids in contact with the substrate diffuse out of the contact area. After inducing vesicle rupture by changing from an isotonic to a hypotonic condition, we assume that mainly the upper parts of the ruptured unilamellar vesicles, representing excess material, are removed from the surface. Thus, after rinsing and allowing for self-healing, a uniform, defect-free lipid bilayer is formed that originates mainly from the contact area of the vesicles. After self-healing, the bilayer is stored in 0.15 M (1:1) electrolyte NaCl. Therefore, the depletion of the anionic  $d_{31}$ -POPS lipids in the leaflet facing the silicon substrate is further stabilized, in agreement with the experiments. A similar observation has been made for POPC bilayers on silicon supports, where a gradient in anionic Texas Red DHPE lipids developed between proximal and distal leaflets at low salt concentration (0.075 M).<sup>26</sup> This suggests that the described mechanism may be rather general.

## 4. CONCLUSIONS

We have shown that osmotic shock can be used to deposit mixed SLBs of anionic and zwitterionic lipids on  $SiO_2$ . With this method, asymmetric lipid bilayers may be prepared and quantified using neutron reflectometry and deuterium-labeled lipids. Anionic lipids are depleted in the leaflet facing the substrate, and their fraction in the buffer-facing leaflet is in agreement with the initial stoichiometry of 3:1. The asymmetric distribution can be rationalized by electrostatic effects prior to vesicle fusion. Apparently, electrostatic repulsion suppresses the transfer of PS, especially in the layer proximal to the negatively charged substrate. Supported lipid bilayers with a controlled anionic fraction in the outer membrane are versatile platforms for studying the hydrophobic–electrostatic interaction of proteins with the cytoplasmic leaflet, which is a key element in many cellular signal pathways.

### ■ ASSOCIATED CONTENT

#### 📄 Supporting Information

Neutron reflectivity of bare Si, method of contrast variation, and literature values for the bilayer SLDs. Estimation of the potential of a charged silicon oxide surface. This material is available free of charge via the Internet at <http://pubs.acs.org>.

### ■ AUTHOR INFORMATION

#### Notes

The authors declare no competing financial interest.

### ■ ACKNOWLEDGMENTS

We acknowledge financial support from BMBF-05KN10WM1.

## ABBREVIATIONS

POPC = 1-palmitoyl-2-oleoyl-*sn*-glycero-3-phosphatidylcholine

$d_{31}$ -POPC = 1-palmitoyl( $d_{31}$ )-2-oleoyl-*sn*-glycero-3-phosphatidylcholine

$d_{31}$ -POPS = 1-palmitoyl( $d_{31}$ )-2-oleoyl-*sn*-glycero-3-[phosphatidyl-L-serine]

TR-DHPE = Texas Red-labeled 1,2-dihexadecanoyl-*sn*-glycerol-3-phosphatidylethanolamine

## REFERENCES

- (1) Sackmann, E.; Merkel, R. *Lehrbuch der Biophysik*; Wiley-VCH: Berlin, 2010.
- (2) Fritz, K.; Fritz, G.; Windschiegl, B.; Steinem, C.; Nickel, B. Arrangement of Annexin A2 tetramer and its impact on the structure and diffusivity of supported lipid bilayers. *Soft Matter* **2010**, *6*, 4084–4094.
- (3) Boon, M. J.; Smith, B. D. Chemical control of phospholipid distribution across bilayer membranes. *Med. Res. Rev.* **2002**, *22*, 251–281.
- (4) Zwaal, R.; Comfurius, P.; Bevers, E. Surface exposure of phosphatidylserine in pathological cells. *Cell. Mol. Life Sci.* **2005**, *62*, 971–988.
- (5) Segrest, J. P.; Pownall, H. J.; Jackson, R. L.; Glenner, G. G.; Pollock, P. S. Amyloid A: amphipathic helices and lipid binding. *Biochemistry* **1976**, *15*, 3187–3191.
- (6) Zhao, H.; Tuominen, E. K. J.; Kinnunen, P. K. J. Formation of amyloid fibers triggered by phosphatidylserine-containing membranes. *Biochemistry* **2004**, *43*, 10302–10307.
- (7) Zhao, H.; Jutila, A.; Nurminen, T.; Wickström, S. A.; Keski-Oja, J.; Kinnunen, P. K. J. Binding of endostatin to phosphatidylserine-containing membranes and formation of amyloid-like fibers. *Biochemistry* **2005**, *44*, 2857–2863.
- (8) Sackmann, E. Supported membranes: scientific and practical applications. *Science* **1996**, *271*, 43–48.
- (9) Cremer, P. S.; Boxer, S. G. Formation and spreading of lipid bilayers on planar glass supports. *J. Phys. Chem. B* **1999**, *103*, 2554–2559.
- (10) Langmuir, I.; Schäfer, V. J. Activities of urease and pepsin monolayers. *J. Am. Chem. Soc.* **1938**, *60*, 1351–1360.
- (11) Lenz, P.; Ajo-Franklin, C. M.; Boxer, S. G. Patterned supported lipid bilayers and monolayers on poly(dimethylsiloxane). *Langmuir* **2004**, *20*, 11092–11099.
- (12) Scomparin, C.; Lecuyer, S.; Ferreira, M.; Charitat, T.; Tinland, B. Diffusion in supported lipid bilayers: influence of substrate and preparation technique on the internal dynamics. *Eur. Phys. J. E* **2009**, *28*, 211–220.
- (13) Rossetti, F. F.; Bally, M.; Michel, R.; Textor, M.; Reviakine, I. Interactions between titanium dioxide and phosphatidyl serine containing liposomes: formation and patterning of supported phospholipid bilayers on the surface of a medically relevant material. *Langmuir* **2005**, *21*, 6443–6450.
- (14) Kern, W.; Puitonen, D. A. Cleaning solutions based on hydrogen peroxide for use in silicon semiconductor technology. *RCA Rev.* **1970**, *31*, 187–206.
- (15) MacDonald, R. C.; Mac Donald, R. I.; Menco, B. P. M.; Takeshita, K.; Subbarao, N. K.; Hu, L. Small-volume extrusion apparatus for preparation of large, unilamellar vesicles. *Biochim. Biophys. Acta* **1991**, *1061*, 297–303.
- (16) Gutberlet, T.; Steitz, R.; Fragneto, G.; Klösigen, B. Phospholipid bilayer formation at a bare Si surface: a time-resolved neutron reflectivity study. *J. Phys.: Condens. Matter* **2004**, *16*, 2469–2476.
- (17) Kampmann, R.; Haese-Seiller, M.; Kudryashov, V.; Deriglazov, V.; Tristl, M.; Daniel, Ch.; Toperverg, B.; Schreyer, A.; Sackmann, E. The potential of the horizontal reflectometer REFSANS/FRM-II for measuring low reflectivity and diffuse surface scattering. *Physica B* **2004**, *350*, e763–e766.
- (18) Kampmann, R.; Haese-Seiller, M.; Marmotti, M.; Burmester, J.; Deriglazov, V.; Syromiatnikov, V.; Okorokov, A.; Frisius, F.; Tristl, M.; Sackmann, E. The novel reflectometer REFSANS for analyses of liquid and soft surfaces at the new research reactor FRM-II in Munich, Germany. *Appl. Phys. A: Mater. Sci. Process.* **2002**, *74*, S249–S251.
- (19) Parratt, L. G. Surface studies of solids by total reflection of X-rays. *Phys. Rev.* **1954**, *95*, 359.
- (20) Nevot, L.; Croce, P. Characterization of surfaces by grazing X-ray reflection – application to study of polishing of some silicate glasses. *Rev. Phys. Appl.* **1980**, *15*, 761–779.
- (21) Nelson, A. Co-refinement of multiple contrast neutron/X-ray reflectivity data using MOTOFIT. *J. Appl. Crystallogr.* **2006**, *39*, 273–276.
- (22) Wacklin, H. P.; Tiberg, F.; Thomas, R. K. Formation of supported phospholipid bilayers via co-adsorption with  $\beta$ -D-dodecyl maltoside. *Biochim. Biophys. Acta* **2005**, *1668*, 17–24.
- (23) Wacklin, H. P.; Tiberg, F.; Fragneto, G.; Thomas, R. K. Distribution of reaction products in phospholipase A(2) hydrolysis. *Biochim. Biophys. Acta, Biomembr.* **2007**, *1768*, 1036–1049.
- (24) Armen, R. S.; Uitto, O. D.; Feller, S. E. Phospholipid component volumes: determination and application to bilayer structure calculations. *Biophys. J.* **1998**, *75*, 734–744.
- (25) Duval, Y.; Mielczarski, J. A.; Pokrovsky, O. S.; Mielczarski, E.; Ehrhardt, J. J. Evidence of the existence of three types of species at the quartz-aqueous solution interface at pH 0–10: XPS surface group quantification and surface complexation modeling. *J. Phys. Chem. B* **2002**, *106*, 2937–2945.
- (26) Shreve, A. P.; Howland, M. C.; Sapuri-Butti, A. R.; Allen, T. W.; Parikh, A. N. Evidence for leaflet-dependent redistribution of charged molecules in fluid supported phospholipid bilayers. *Langmuir* **2008**, *24*, 13250–13253.

## A.2 Fulltext of ref. [2]:

### Highly Hydrated Deformable Polyethylene Glycol-Tethered Lipid Bilayers

**Authors:** Samira Hertrich, Frank Stetter, Adrian Rühm, Thorsten Hugel, and Bert Nickel

**Abstract:** The realization of a solid-supported lipid bilayer acting as a workbench for the study of membrane processes is a difficult task. For robustness, the bilayer has to be tethered to the substrate. At the same time, diffusion of the lipids and plastic deformations of the membrane should not be obstructed. Furthermore, a highly hydrated surrounding is mandatory. Here, we show that grafting of a polyethylene glycol lipid construct (PEG2000-DSPE) to a silicon oxide surface via multiple-step silane chemistry and subsequent deposition of lipids by spin-coating result in a cushioned membrane that has the desired properties. Neutron and X-ray reflectometry measurements are combined to access thickness, density, and hydration of the bilayer and the PEG cushion. We observe a spacer of  $55 \text{ \AA}$  thickness between lipid bilayer and silicon-oxide surface with a rather high hydration of up to  $90 \pm 3\%$  water. While  $11.5 \pm 3\%$  of the lipids are grafted to the surface, as determined from the neutron data, the diffusion constant of the lipids, as probed by diffusion of  $0.5\%$  Texas Red labeled lipids, remains rather large ( $D = 2.1 \pm 0.1 \mu\text{m}^2/\text{s}$ ), which is a reduction of only  $12\%$  compared to a supported lipid bilayer reference without immobilized lipids. Finally, AFM indentation confirms the plastic behavior of the membrane against deformation. We show that rupture of the bilayer does not occur before the deformation exceeds  $40 \text{ \AA}$ . Altogether, the presented PEG-tethered lipid bilayer mimics the deformability of natural cell membranes much better than standard solid-supported lipid bilayers.

#### SH contribution:

- Performing the neutron, X-ray, and FRAP measurements
- Data analysis of neutron and X-ray reflectometry and FRAP data
- writing the paper



# Highly Hydrated Deformable Polyethylene Glycol-Tethered Lipid Bilayers

Samira Hertrich,<sup>†</sup> Frank Stetter,<sup>‡</sup> Adrian Rühm,<sup>||,⊥</sup> Thorsten Hugel,<sup>‡,§</sup> and Bert Nickel<sup>\*,†,§</sup>

<sup>†</sup>Fakultät für Physik & CeNS, Ludwig-Maximilians-Universität, Geschwister-Scholl-Platz 1, 80539 Munich, Germany

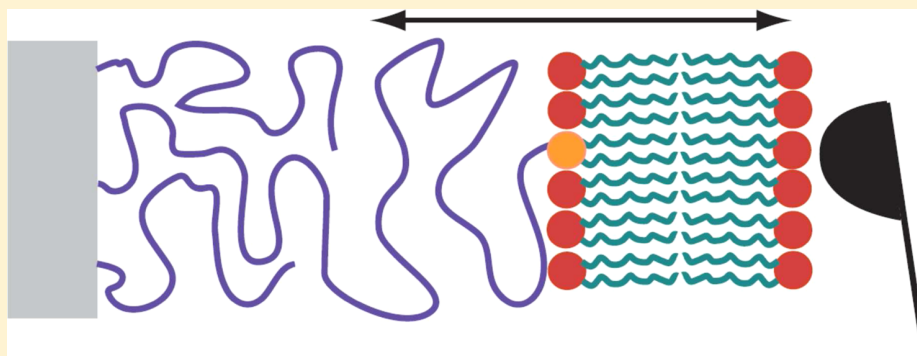
<sup>‡</sup>IMETUM, Physik-Department, E22a, Technische Universität München, James Franck Strasse 1, 85748 Garching, Germany

<sup>§</sup>Nanosystems Initiative Munich, Schellingstrasse 4, 80539 Munich, Germany

<sup>||</sup>Max-Planck-Institut für Intelligente Systeme, Heisenbergstrasse 3, 70569 Stuttgart, Germany

<sup>⊥</sup>Forschungsneutronenquelle Heinz Maier-Leibnitz (FRM II), Lichtenbergstrasse 1, 85748 Garching, Germany

## Supporting Information



**ABSTRACT:** The realization of a solid-supported lipid bilayer acting as a workbench for the study of membrane processes is a difficult task. For robustness, the bilayer has to be tethered to the substrate. At the same time, diffusion of the lipids and plastic deformations of the membrane should not be obstructed. Furthermore, a highly hydrated surrounding is mandatory. Here, we show that grafting of a polyethylene glycol–lipid construct (PEG2000–DSPE) to a silicon oxide surface via multiple-step silane chemistry and subsequent deposition of lipids by spin-coating result in a cushioned membrane that has the desired properties. Neutron and X-ray reflectometry measurements are combined to access thickness, density, and hydration of the bilayer and the PEG cushion. We observe a spacer of 55 Å thickness between lipid bilayer and silicon-oxide surface with a rather high hydration of up to  $90 \pm 3\%$  water. While  $11.5 \pm 3\%$  of the lipids are grafted to the surface, as determined from the neutron data, the diffusion constant of the lipids, as probed by diffusion of 0.5% Texas Red labeled lipids, remains rather large ( $D = 2.1 \pm 0.1 \mu\text{m}^2/\text{s}$ ), which is a reduction of only 12% compared to a supported lipid bilayer reference without immobilized lipids. Finally, AFM indentation confirms the plastic behavior of the membrane against deformation. We show that rupture of the bilayer does not occur before the deformation exceeds 40 Å. Altogether, the presented PEG-tethered lipid bilayer mimics the deformability of natural cell membranes much better than standard solid-supported lipid bilayers.

## INTRODUCTION

The realization of biomimetic lipid membranes is a long-standing task for facilitating the difficult study of processes which involve membranes.<sup>1,2</sup> Planar supported lipid bilayers are well-known systems extensively used to mimic cell surfaces and to develop biosensors.<sup>3,4</sup> For solid-supported lipid bilayers, the solid interface in close contact with the lipids proves disadvantageous, as it does not reproduce the deformability or natural fluctuation of the membrane,<sup>5,6</sup> and incorporation of transmembrane proteins without direct contact with the surface is not possible in such systems.<sup>7</sup> To achieve a more natural and cell-like surrounding, a variety of interlayers separating the lipids from the solid interface have been introduced.<sup>8</sup> Lipids can be deposited on these surfaces by different methods; the most

common are vesicle fusion and Langmuir–Blodgett.<sup>9</sup> Examples include covering the solid surface with a polymer layer,<sup>10</sup> inclusion of a low percentage of polymer functionalized lipids when preparing the bilayer,<sup>11</sup> and placing a lipid bilayer on top of another one.<sup>12</sup> While those surface coatings were successfully implemented in supported and tethered lipid bilayer systems, many of the interlayers are very thick (100–1000 Å) promoting uneven height when hydrated.<sup>13</sup> On the other hand, if individual lipids are tethered by short polymers (~10 Å), the bilayer elevation is not high enough to form a hydrous and

**Received:** November 27, 2013

**Revised:** June 6, 2014

**Published:** July 21, 2014

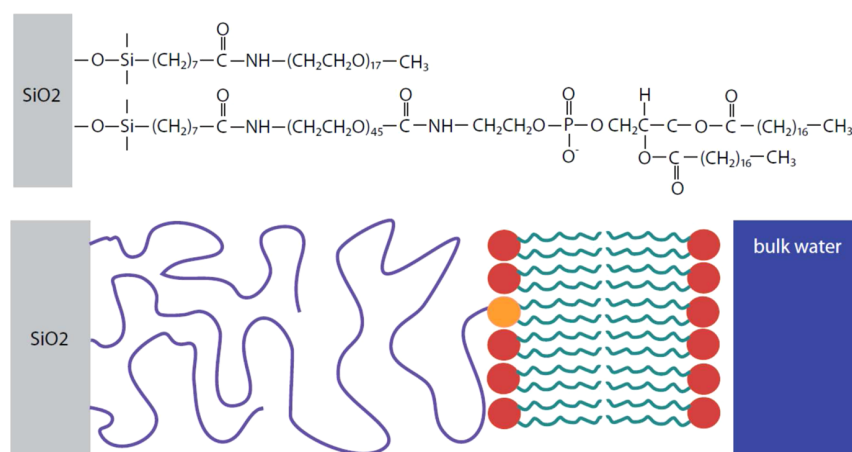


**Figure 1.** Structure of the tethered lipid bilayer (TLB): (a) Chemical composition of the silane and PEG–lipid cushion. (b) Cartoon of the structure of the TLB consisting of the silicon oxide surface, the PEG cushion, one tethered lipid (yellow head), and several lipids in the bilayer (red heads). On the right side, the bulk water is represented in blue.

deformable support.<sup>14,15</sup> Here, we aim for a cushion thickness comparable to the bilayer dimension. Note that on bare silicon oxide, lipid bilayers show rather high diffusion rates,<sup>2</sup> slowed down only by about a factor of 2 with respect to lipids in vesicles.<sup>16</sup> In contrast, some polymer cushions, e.g., poly-(allylamine hydrochloride), reduce the diffusion constant drastically by 2 orders of magnitude, indicating a sticky interaction of the amino groups of the polymer with the lipids.<sup>17</sup> A weakly interacting cushion material such as polyethylene glycol (PEG), which is neither charged nor hydrophobic, is more promising. However, on bare PEG, a lipid bilayer does not form. The way out of this dilemma is to make use of lipo-PEG, i.e., PEG molecules that have a lipid attached at one end. If the PEG end is grafted to the surface, the lipid end can anchor a lipid bilayer.<sup>18</sup> Such tethered bilayers (TBL) exhibit diffusion constants which are similar to those of lipid bilayers on glass.<sup>18</sup> However, if the lipo-PEG density is too high, i.e., if more than 4–5% of the lipids are grafted to the surface, a large immobile fraction develops.<sup>18</sup> Here, we present an improved tethered lipid bilayer protocol, which extends our previous work substantially.<sup>19</sup> A multistep chemical process is used to modify the surface of silicon substrates covered with an oxide layer. First, short alkanes are grafted and their free ends are oxidized to carboxylic acid groups, and PEG2000 lipids (45 ethylene oxide units) are attached via a peptide bond. As the last step of the grafting, the PEG layer is back-filled with PEG750 to close remaining cavities in the cushion; see Figure 1. On this surface, the bilayer was formed via vesicle fusion, which resulted in excess lipids included in the cushion and on the surface of the bilayer. Now, instead, the lipids are spin-coated in solvent and the tethered lipid bilayer (TLB) self-assembles when the surface is hydrated. For noncharged lipids such as 1-stearoyl-2-oleoyl-*sn*-glycero-3-phosphatidylcholine (SOPC) and 1-palmitoyl-*d*<sub>31</sub>-2-oleoyl-*sn*-glycero-3-phosphocholine (D31-POPC) used in this study, the spin-coating technique provided very nice results as outlined below, while previous work using vesicle fusion produced lipid aggregates inserted into the PEG layer.<sup>19</sup>

The structure of the TLBs is resolved by neutron and X-ray reflectometry measurements. These techniques complement each other, as neutrons offer the possibility to tune the scattering length density (SLD) via deuteration of components<sup>20</sup> and X-rays provide high resolution to resolve the

individual layers of the sample.<sup>21</sup> Additionally, fluorescence-dyed lipids are mixed in to verify the homogeneity and fluidity of the bilayer before the scattering experiments are performed. The diffusion constants of the TLB are determined via fluorescence recovery after photobleaching (FRAP).

To test the deformability of the TLB system, we used atomic force microscopy (AFM). While free-standing lipid bilayers, e.g., pore-spanning membranes, can be deformed for several hundred nanometers,<sup>22</sup> supported lipid bilayers rupture at deformations beyond 2 nm.<sup>23,24</sup> The softness of the supported bilayer before rupture can be quantified by the Young's modulus, which was determined to be 20 MPa by us and others;<sup>23,25</sup> some authors also reported somewhat higher values, e.g., 80 MPa.<sup>26</sup> For polymer-supported or tethered lipid bilayers, such indentation measurements were not done yet.

## ■ MATERIALS AND METHODS

**Materials.** Silicon wafers from SiMat with a thermally grown oxide layer of 1000 Å and a size of  $15 \times 20 \times 0.7 \text{ mm}^3$  were used for the X-ray, fluorescence, and AFM experiments. For the neutron experiment a thermally oxidized polished silicon block of size  $100 \times 50 \times 10 \text{ mm}^3$  from Crystec was used. Lipids and PEG–lipids were purchased from Avanti Polar Lipids. PEG750 was purchased from Polymer Rapp. Fluorescently labeled lipid, Texas Red–1,2-dihexadecanoyl-*sn*-glycero-3-phosphoethanolamine (Texas Red–DHPE), was purchased from Invitrogen.

**Substrate Preparation and Lipid Deposition.** The preparation of PEG2000–lipid surface on a silicon oxide surface was done according to the literature procedure.<sup>19</sup> The lipids were deposited on the surface via spin-coating. For X-ray samples prepared on the  $20 \times 15 \text{ mm}^2$  silicon wafers,  $100 \mu\text{L}$  of a SOPC solution in 2-propanol ( $1.5 \text{ mg mL}^{-1}$ ) containing 0.5% fluorescent lipids (Texas Red–DHPE) was spin-coated with a two-step program, i.e., 2 s at 2000 rpm with the following 90 s at 3000 rpm. For the neutron sample, spin-coating speed had to be reduced due to the bigger sample size (silicon block,  $100 \times 50 \times 10 \text{ mm}^3$ ). They were prepared with a 2 mL solution in 2-propanol ( $1.5 \text{ mg mL}^{-1}$ ). Spin-coating was done in a two-step program, i.e., 5 s at 700 rpm followed by 90 s at 1000 rpm. Residual solvent was evaporated in vacuum for several hours. Afterward, the wafers and the silicon block were inserted in specially designed fluidic chambers.<sup>21</sup> Each sample was flushed several times to remove excess lipids. Before the reflectometry experiments, every sample was checked with fluorescence microscopy for homogeneity and absence of excess material.

**Fluorescence Microscopy.** Fluorescence microscopy and FRAP were used to verify the homogeneity and diffusivity of the lipid bilayers.<sup>27</sup> The FRAP setup consists of an inverted Zeiss Axiovert 100M microscope combined with a Toptica Photonics iPulse 488 laser. A spot of  $\sim 10 \mu\text{m}$  diameter was bleached. The reappearance of fluorescence in the bleached spot was analyzed to determine the diffusion constant of lipids in the TLB using a diode with 530 nm light (Thorlabs).<sup>28</sup>

**X-ray Reflectivity Measurements.** X-ray reflectivity measurements were performed at the beamline D4 at HASYLAB/DESY in Hamburg. At a photon energy of 19.9 keV, the reflectivity of the TLB was recorded as a  $\theta$ - $2\theta$  scan of sample and detector angle. These were converted to momentum transfer according to  $q = 4\pi/\lambda \sin(\theta)$ . The background was determined by a second scan with an offset for the  $\theta$  angle by  $0.05^\circ$  and corrected for by subtraction. The effective sample size due to overillumination at different angles was accounted for according to simple geometric corrections. Finally, the intensity was normalized to 1 at the critical edge. Fits for the SLD of the bilayer and PEG cushion were performed with the Motofit program running on IGOR.<sup>29</sup>

**Neutron Reflectivity Measurements.** Neutron reflectivity measurements were performed at the N-REX<sup>+</sup> instrument at FRM2 (Munich, Germany), a monochromatic reflectometer, with a wavelength of 4.3 Å. The same sample was measured twice, once in D<sub>2</sub>O, and once in a mix of 75% D<sub>2</sub>O and 25% H<sub>2</sub>O. In contrast to the X-ray measurement, the neutron beam is incident through the silicon. As with the X-ray data, the neutron data were normalized and fitted with Motofit. The neutron data of both contrasts were fitted simultaneously with the same model applying the same analysis as described in detail before.<sup>20</sup>

**AFM.** AFM indentation was performed using an MFP-3D AFM (Asylum Research, Santa Barbara, CA) with triangular silicon nitride cantilevers (DNP-S, Bruker, Santa Barbara, CA) with a nominal tip radius of 10 nm. The small radius was chosen to prevent bilayer formation on the tip. Indentation measurements were performed by vertically moving the AFM tip toward the TLB. When the tip is close to the bilayer, it starts to interact with the surface, resulting in an upward deflection of the cantilever. As the force rises, the TLB is compressed by steric interaction between the tip and the bilayer until the bilayer yields (breakthrough). For the next indentation curve, the tip was retracted by about 500 nm, moved to a slightly different location, and moved again toward the TLB. The tip was moved with a vertical velocity of 500 nm/s. Plotting the force on the cantilever versus its distance from the surface results in so-called force–distance curves (see Figure 4). A detailed description of the method can be found elsewhere.<sup>23</sup>

## RESULTS

**Diffusion of Lipids in the TLB.** Initially, FRAP was used to determine the diffusion constant of the Texas Red-labeled lipids in the tethered bilayer sample. A solid-supported membrane sample prepared and measured under the same conditions acted as reference. The POPC reference bilayer on silicon oxide surfaces without tethered lipids shows a diffusion constant of  $2.4 \pm 0.1 \mu\text{m}^2/\text{s}$ . The TLB shows a diffusion constant of  $2.1 \pm 0.1 \mu\text{m}^2/\text{s}$ , which is only 12% lower than that of the reference bilayer without any grafted lipids as obstacles.

**X-ray and Neutron Reflectivity.** To access the structural details, X-ray and neutron reflectometry measurements were performed. In general, X-ray reflectometry offers superior spatial resolution, but due to the low scattering contrast of organic samples, it does not offer sufficient information about the sample compositions. For example, PEG and water are not distinguishable due to the resemblance of their electron densities. For this reason, it is advantageous to combine X-ray with neutron reflectivity measurements at different deuteration contrasts. This combination proved successful as

the results of both neutron and X-ray reflectivity measurements complement each other, which provided detailed information on the TLB structure. Reflectivity data of the membrane and least-squares fits to the data of both the neutron and the X-ray experiment are shown in Figure 2a. The X-ray data (red curve)

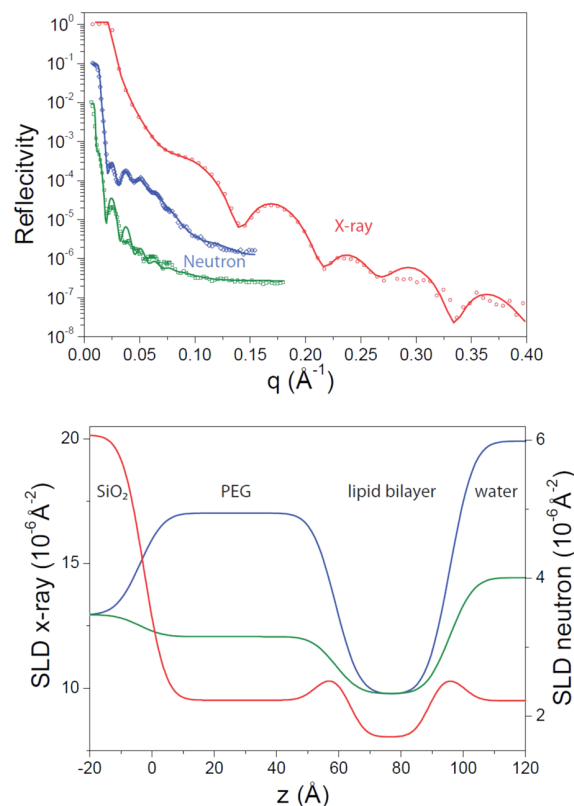


**Figure 2.** (a) Normalized neutron and X-ray reflectivity data and fit. Neutron data in D<sub>2</sub>O are shown in blue, in D<sub>2</sub>O/H<sub>2</sub>O mix in green, and X-ray data in red. Neutron data are scaled with a factor 0.1 and 0.01 for clarity. (b) SLD model for the fit of X-ray (red) and neutron data at both contrasts (blue, green). Silicon oxide is on the left side of the model, adjacent to the PEG layer, then the lipid bilayer, and on the right side of the model the water.

ranges up to  $q = 0.4 \text{ \AA}^{-1}$ . The data show five oscillations in intensity originating from the TLB on the silicon oxide substrate. The data from the neutron measurements are shown in blue and green (measurement in D<sub>2</sub>O and in D<sub>2</sub>O/H<sub>2</sub>O, respectively). Here, the  $q$ -range is limited to  $q = 0.15 \text{ \AA}^{-1}$  due to the weaker intensity of the neutron instrument. Both sets of neutron data show rapid oscillations caused by the 500 Å silicon oxide layer covering the block. In contrast, the broad shoulder in the D<sub>2</sub>O data is caused by the TLB, as confirmed by the modeling of the intensity. In Figure 2b the models for the SLD for all three reflectivities are shown. Since the incident beam is directed through the silicon in the neutron measurements and through the water in the X-ray measurements, the SLD for the X-ray data fit in Figure 2b is shown on an inverted  $z$ -scale for reasons of comparison to the neutron results. Due to the higher  $q$ -range, the X-ray measurement provides higher resolution and allows differentiating the sample structure into four layers for the fit. The PEG cushion of 55 Å thickness is located directly on the silicon oxide and has a SLD of  $(9.5 \pm 0.2) \times 10^{-6} \text{ \AA}^{-2}$ . Note that, for X-rays, this SLD matches both

the density of PEG and water; thus, it is not possible to extract the hydration at this point from the X-ray data alone. The lipid head groups of both halves of the bilayer show up in X-ray measurements with a higher SLD of  $(10.5 \pm 0.15) \times 10^{-6} \text{ \AA}^{-2}$  due to the phosphate. The fit determines the head thickness to be  $11 \pm 0.5 \text{ \AA}$ . The chain region in between is represented by a thickness of  $25.5 \pm 0.5 \text{ \AA}$  and a lower SLD of  $(8.0 \pm 0.2) \times 10^{-6} \text{ \AA}^{-2}$ , in agreement with the expected values for alkane chains. Thus, the whole bilayer thickness is about  $47 \text{ \AA}$  and matches the structure of lipid bilayers cited in the literature.<sup>30</sup> The silicon oxide layer of  $1000 \text{ \AA}$  was not included in the model, since its oscillations are too narrow to be resolved by the step size. In Figure 3a the electron density of all layers, calculated from the SLD of the X-ray model, is illustrated.

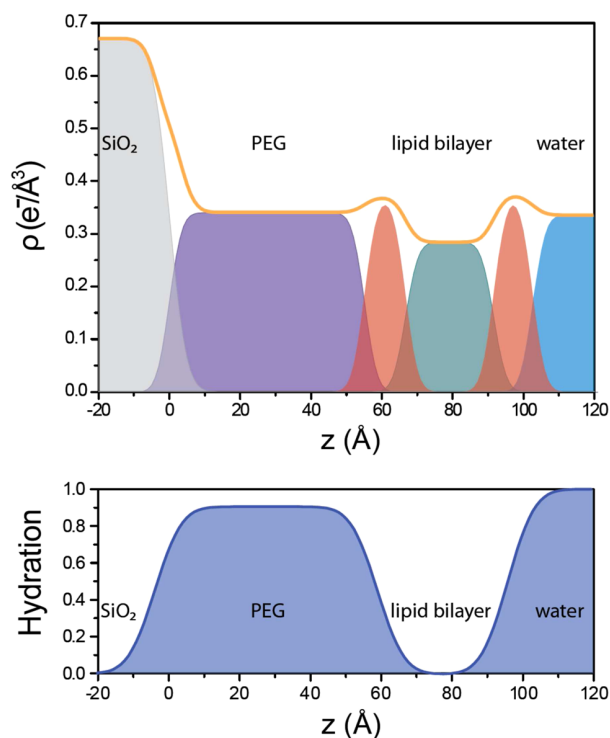


**Figure 3.** (a) Electron density of the different layers of the system, extracted from the X-ray measurement. The silicon substrate is on the left side (gray) and the bulk water on the right (blue). PEG has the same electron density as water (purple), and the lipid headgroups show up with higher  $e^-$  density (red) and the lipid chains with lower (green). (b) Hydration (volume water fraction) of lipid bilayer and PEG cushion extracted from the difference of the neutron models at different contrasts ( $D_2O$  and  $D_2O/H_2O$  mix with SLD  $4.0 \times 10^{-6} \text{ \AA}^{-2}$ ).

A three-layer model consisting of silicon oxide layer, PEG layer, and lipid chain region is used to fit the neutron measurements. The thicknesses for the PEG layer and the lipid bilayer, as determined from the neutron fits, are consistent with those from the X-ray measurements. Since the silicon oxide layer of  $500 \text{ \AA}$  gives rise to small oscillations of the signal, it is included in the fit. The lipid bilayer for the neutron measurement was prepared with lipids that have one deuterated alkane chain (D31-POPC). Therefore, the SLD of the lipid bilayer region is found at  $(2.5 \pm 0.2) \times 10^{-6} \text{ \AA}^{-2}$ , which is the expected value for the mix of deuterated and hydrogenated alkane chains, when taking into account the nondeuterated

tethered lipids.<sup>20</sup> The headgroups are not distinguishable from the adjoining layers in the neutron data fit. Due to their small size, the headgroups do not give rise to a separate SLD layer. They are included in the roughness of the chain and water interface. The hydrated PEG has a SLD of  $(4.94 \pm 0.11) \times 10^{-6} \text{ \AA}^{-2}$  in  $D_2O$  and  $(3.15 \pm 0.07) \times 10^{-6} \text{ \AA}^{-2}$  in the  $D_2O/H_2O$  mix. This difference in SLD indicates a hydration of  $90 \pm 3\%$  of this region. In contrast, the lipid chain region shows no hydration; i.e., the SLD did not change with the change of contrast in the water. In Figure 3b the hydration of the sample as calculated from the two models for the neutron fits is shown. Altogether, the X-ray and neutron measurements confirm the presence of a well-defined bilayer separated by a highly hydrated cushion from the substrate.

**AFM Indentation.** To investigate the nanomechanical response of the TLBs, we performed indentation experiments. More than 50 force–distance curves of an AFM tip indenting and eventually puncturing the TLB are superposed in Figure 4.

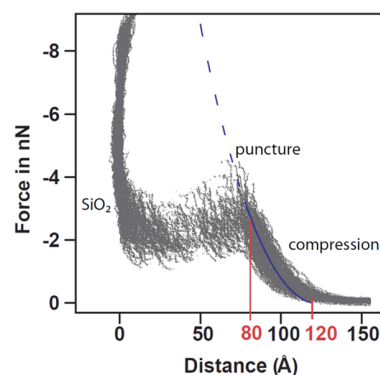


**Figure 4.** AFM measurements: Superposition of indentation curves of an AFM tip into the TLB. Upon approach to the surface, first the TLB is deformed (compressed) from about  $120 \text{ \AA}$  until at  $\sim 80 \text{ \AA}$  from the silicon surface the tip breaks through the lipid bilayer (puncture). The Hertz model curve with a Young modulus of  $20 \text{ MPa}$  is shown in blue.

When the tip approaches the bilayer, a repulsive force is observed starting at a distance of  $120 \text{ \AA}$  from the silicon surface. The repulsive force increases up to a distance of about  $80 \text{ \AA}$ . After that point, the resistive force collapses and the tip approaches the silicon surface. This can be compared to puncture experiments on solid-supported membranes, which lack the cushion.<sup>23</sup> There, a repulsive force was observed starting at around  $65 \text{ \AA}$ , and the collapse occurred at around  $45 \text{ \AA}$ . In other words, for TLBs, the membrane can be deformed by  $40 \text{ \AA}$ , i.e., twice as much as the supported lipid bilayer (SLB) before puncture. For comparison, the blue compression curve in Fig 4 represents the analytical solution to the mechanical Hertz model assuming a tip radius of  $20 \text{ nm}$ , a Poisson ratio of  $0.5$ , and  $20 \text{ MPa}$  for the Young modulus.

## DISCUSSION

**Layer Thickness and Hydration.** From the neutron data, we can directly extract the hydration and film thickness of the PEG layer. Since pure PEG2000 has a density of  $1.1 \text{ g cm}^{-3}$  and thus a molecular volume of  $3020 \text{ \AA}^3$ , a hydration of  $90 \pm 3\%$  implies that the volume per PEG2000 group is  $30\,200 \pm 7000 \text{ \AA}^3$ . This value is in good agreement with the volume of hydrated, weakly overlapping PEG2000 chains.<sup>31</sup> Indeed, the thickness of the PEG layer ( $55 \text{ \AA}$ ) is already larger than the

Flory radius (35 Å),<sup>31</sup> indicating the onset of brush formation.<sup>32</sup> A typical area per lipid molecule for SOPC and POPC bilayers is 63 Å.<sup>2,33</sup> From this value and the hydrated PEG density, the fraction of lipids in the lower bilayer leaflet, which are tethered to the surface, can be estimated to be 11.5 ± 3%; the actual number of grafted lipids may be less, since we neglect the contribution of PEG750, which is only a minor fraction of the grafting layer filling in the voids not accessible to PEG2000.

**Diffusion of TLBs.** In previous work, using lipo-PEG molecules with 77 EO subunits in TLBs gave rise to a large immobile fraction of up to 50% once the PEG layer reached the brush state.<sup>18</sup> In our work, the diffusion constant of the Texas Red-labeled lipids in the bilayer is only slightly reduced compared to that in a supported lipid bilayer, from 2.4 ± 0.1 to 2.1 ± 0.1 μm<sup>2</sup>/s. The SLB was chosen as a reference,<sup>21</sup> since diffusion constants determined by different methods or under different conditions vary.<sup>34</sup> In the obstructed diffusion model, a reduction of the diffusion rate as observed here (ca. 12%) is expected for an immobile obstacle density of 4–5%.<sup>35,36</sup> Here, we estimate from the structural analysis that 11.5 ± 3% of the lipids are grafted; however, these lipids are not fully immobilized, as the PEG chain allows for restricted movement of the lipid bound to the end of the polymer in the lipid bilayer plane. Roughly speaking, a tethered lipid can still perform restricted movements, since thermal energy fluctuations change the end-to-end distance of the PEG chain. For PEG2000, this end-to-end length change can be estimated to about 3 Å,<sup>37</sup> which allows for lateral displacements of more than the diameter of lipids in a bilayer (ca. 8 Å). Thus, it is plausible that the grafted lipids behave not as fully immobilized obstacles. Note that due to electrostatic repulsion of the anionic dye from the DSPE-PEG lipids, we expect that the Texas Red probes mainly the distal, water-facing leaflet. Although the tethered lipids are only present in the lower half of the bilayer, a reduction of diffusion in one leaflet applies to both halves, as their mobility is strongly coupled.<sup>38,39</sup>

**AFM Indentation.** Once an AFM tip pushes on a SLB, the membrane has to restructure, initially by thinning and finally by rupturing.<sup>40</sup> In case of a TLB, one may expect that part of the overall deformation can be attributed to a deformation of the PEG layer. Indeed, the TLB ruptures only after a deformation of about 40 Å compared to 20 Å for a SLB. This indicates that the PEG cushion underneath the lipid bilayer is compressible, and external deformations are distributed among the cushion and the membrane. Furthermore, our AFM data are in agreement with a net Young modulus of ~20 MPa, which is similar to values reported by us and others for SLBs using the same analysis,<sup>23,25</sup> while some authors found somewhat larger values (80 MPa).<sup>26</sup> This confirms that the elastic properties of the PEG layer match the SLB properties quite well.

## CONCLUSION

In this work, we have employed several techniques to characterize a new TLB system in detail. We have shown that it is possible to prepare a tethered lipid bilayer on silicon oxide with a soft interlayer, cushioning the lipids against the solid surface. The PEG interlayer of the TLB is highly hydrated, with a water content of 90 ± 3%, as determined by neutron reflectometry. Diffusion in the system was reduced by only 12%. The AFM indentation measurements prove the softness of the PEG layer perpendicular to the surface. Possible applications of such elevated lipid bilayers are, for example,

the study of membrane-perforating proteins or binding studies of membrane-associated proteins. Here the PEG layer is expected to behave as a mattress, allowing for membrane deformation, which is a prerequisite for functional binding of many membrane-associated proteins.<sup>41,42</sup> Furthermore, we expect the PEG to suppress unspecific protein adsorption to the Si wafer. Additionally, the application of TLBs as a surface for cell growth and attachment is perceivable, as they provide a more natural and cell-like surrounding than solid surfaces.

## ASSOCIATED CONTENT

### Supporting Information

FRAP micrographs of (a) tethered lipid bilayer and (b) supported lipid bilayer. This material is available free of charge via the Internet at <http://pubs.acs.org>.

## AUTHOR INFORMATION

### Corresponding Author

\*E-mail: [nickel@lmu.de](mailto:nickel@lmu.de).

### Notes

The authors declare no competing financial interest.

## ACKNOWLEDGMENTS

This work was supported by the DFG Excellence Cluster Nanosystems Initiative Munich (NIM). It is based upon experiments performed at the N-REX<sup>+</sup> instrument operated by the MPG at the Heinz Maier-Leibnitz Zentrum (MLZ), Garching, Germany. We acknowledge financial support from BMBF-05KN10WM1 and 05KN13WM1. F.S. and T.H. thank the Hanns-Seidel-Stiftung and the ESF EuroMEMBRANE CRP OXPL (Hu 997/7-1) for financial support.

## REFERENCES

- (1) Sackmann, E. Supported Membranes: Scientific and Practical Applications. *Science* **1996**, *271*, 43–48.
- (2) Tamm, L. K.; McConnell, H. M. Supported Phospholipid Bilayers. *Biophys. J.* **1985**, *47*, 105–113.
- (3) Lee, D.-C.; Chang, B.-J.; Yu, L.; Frey, S. L.; Lee, K. Y. C.; Patchipulusu, S.; Hall, C. Polymer Cushions Functionalized with Lipid Molecules. *Langmuir* **2004**, *20*, 11297–11300.
- (4) Castellana, E. T.; Cremer, P. S. Solid Supported Lipid Bilayers: From Biophysical Studies to Sensor Design. *Surf. Sci. Rep.* **2006**, *61*, 429–444.
- (5) Groves, J. T. Bending Mechanics and Molecular Organization in Biological Membranes. *Annu. Rev. Phys. Chem.* **2007**, *58*, 697–717.
- (6) Watson, M. C.; Penev, E. S.; Welch, P. M.; Brown, F. L. H. Thermal Fluctuations in Shape, Thickness, and Molecular Orientation in Lipid Bilayers. *J. Chem. Phys.* **2011**, *135*, 24470101–24470122.
- (7) Salafsky, J.; Groves, J. T.; Boxer, S. G. Architecture and Function of Membrane Proteins in Planar Supported Bilayers: A Study with Photosynthetic Reaction Centers. *Biochemistry* **1996**, *35*, 14773–14781.
- (8) McCabe, I. P.; Forstner, M. B. Polymer Supported Lipid Bilayers. *Open J. Biophys.* **2013**, *03*, 59–69.
- (9) Wacklin, H. P. Composition and Asymmetry in Supported Membranes Formed by Vesicle Fusion. *Langmuir* **2011**, *27*, 7698–7707.
- (10) Nirasay, S.; Badia, A.; Leclair, G.; Claverie, J. P.; Marcotte, I. Polydopamine-Supported Lipid Bilayers. *Materials (Basel)* **2012**, *5*, 2621–2636.
- (11) Watkins, E. B.; El-khoury, R. J.; Miller, C. E.; Seaby, B. G.; Majewski, J.; Marques, C. M.; Kuhl, T. L. Structure and Thermodynamics of Lipid Bilayers on Polyethylene Glycol Cushions: Fact and Fiction of PEG Cushioned Membranes. *Langmuir* **2011**, *27*, 13618–28.

- (12) Fragneto, G.; Charitat, T.; Daillant, J. Floating Lipid Bilayers: Models for Physics and Biology. *Eur. Biophys. J.* **2012**, *41*, 863–74.
- (13) Smith, H. L.; Jablin, M. S.; Vidyasagar, A.; Saiz, J.; Watkins, E.; Toomey, R.; Hurd, A. J.; Majewski, J. Model Lipid Membranes on a Tunable Polymer Cushion. *Phys. Rev. Lett.* **2009**, *102*, 2281021–2281024.
- (14) Atanasov, V.; Knorr, N.; Duran, R. S.; Ingebrandt, S.; Offenhäusser, A.; Knoll, W.; Köper, I. Membrane on a Chip: A Functional Tethered Lipid Bilayer Membrane on Silicon Oxide Surfaces. *Biophys. J.* **2005**, *89*, 1780–1788.
- (15) Budvytyte, R.; Valincius, G.; Niaura, G.; Voiciuc, V.; Mickevicius, M.; Chapman, H.; Goh, H.-Z.; Shekhar, P.; Heinrich, F.; Shenoy, S.; et al. Structure and Properties of Tethered Bilayer Lipid Membranes with Unsaturated Anchor Molecules. *Langmuir* **2013**, *29*, 8645–8656.
- (16) Przybylo, M.; Sýkora, J.; Humpolickova, J.; Benda, A.; Zan, A.; Hof, M. Lipid Diffusion in Giant Unilamellar Vesicles Is More than 2 Times Faster than in Supported Phospholipid Bilayers under Identical Conditions. *Langmuir* **2006**, *22*, 9096–9.
- (17) Fischlechner, M.; Zaulig, M.; Meyer, S.; Estrela-Lopis, I.; Cuéllar, L.; Irigoyen, J.; Pescador, P.; Brumen, M.; Messner, P.; Moya, S.; et al. Lipid Layers on Polyelectrolyte Multilayer Supports. *Soft Matter* **2008**, *4*, 2245–2258.
- (18) Wagner, M. L.; Tamm, L. K. Tethered Polymer-Supported Planar Lipid Bilayers for Reconstitution of Integral Membrane Proteins: Silane–Polyethyleneglycol–Lipid as a Cushion and Covalent Linker. *Biophys. J.* **2000**, *79*, 1400–14.
- (19) Daniel, C.; Sohn, K. E.; Mates, T. E.; Kramer, E. J.; Rädler, J. O.; Sackmann, E.; Nickel, B.; Andruzzi, L. Structural Characterization of an Elevated Lipid Bilayer Obtained by Stepwise Functionalization of a Self-Assembled Alkenyl Silane Film. *Biointerphases* **2007**, *2*, 109–118.
- (20) Stanglmaier, S.; Hertrich, S.; Fritz, K.; Moulin, J.-F.; Haese-Seiller, M.; Rädler, J. O.; Nickel, B. Asymmetric Distribution of Anionic Phospholipids in Supported Lipid Bilayers. *Langmuir* **2012**, *28*, 10818–10821.
- (21) Reich, C.; Hochrein, M. B.; Krause, B.; Nickel, B. A Microfluidic Setup for Studies of Solid–Liquid Interfaces Using X-Ray Reflectivity and Fluorescence Microscopy. *Rev. Sci. Instrum.* **2005**, *76*, 0951031–0951037.
- (22) Steltenkamp, S.; Müller, M. M.; Deserno, M.; Hennesthal, C.; Steinem, C.; Janshoff, A. Mechanical Properties of Pore-Spanning Lipid Bilayers Probed by Atomic Force Microscopy. *Biophys. J.* **2006**, *91*, 217–26.
- (23) Stetter, F. W. S.; Hugel, T. The Nanomechanical Properties of Lipid Membranes Are Significantly Influenced by the Presence of Ethanol. *Biophys. J.* **2013**, *104*, 1049–1055.
- (24) Franz, V.; Loi, S.; Müller, H.; Bamberg, E.; Butt, H.-J. Tip Penetration through Lipid Bilayers in Atomic Force Microscopy. *Colloids Surf. B. Biointerfaces* **2002**, *23*, 191–200.
- (25) Picas, L.; Rico, F.; Scheuring, S. Direct Measurement of the Mechanical Properties of Lipid Phases in Supported Bilayers. *Biophys. J.* **2012**, *102*, L01–3.
- (26) Sullan, R. M. A.; Li, J. K.; Zou, S. Direct Correlation of Structures and Nanomechanical Properties of Multicomponent Lipid Bilayers. *Langmuir* **2009**, *25*, 7471–7477.
- (27) Axelrod, D.; Koppel, D. E.; Schlessinger, J.; Elson, E.; Webb, W. W. Mobility Measurement by Analysis of Fluorescence Photobleaching Recovery Kinetics. *Biophys. J.* **1976**, *16*, 1055–1069.
- (28) Hennig, M.; Wolff, M.; Neumann, J.; Wixforth, A.; Schneider, M. F.; Rädler, J. O. DNA Concentration Modulation on Supported Lipid Bilayers Switched by Surface Acoustic Waves. *Langmuir* **2011**, *27*, 14721–14725.
- (29) Nelson, A. Co-Refinement of Multiple-Contrast neutron/X-ray Reflectivity Data Using MOTOFIT. *J. Appl. Crystallogr.* **2006**, *39*, 273–276.
- (30) Kucerka, N.; Tristram-Nagle, S.; Nagle, J. F. Structure of Fully Hydrated Fluid Phase Lipid Bilayers with Monounsaturated Chains. *J. Membr. Biol.* **2006**, *208*, 193–202.
- (31) Kuhl, T. L.; Leckband, D. E.; Lasic, D. D.; Israelachvili, J. N. Modulation of Interaction Forces between Bilayers Exposing Short-Chained Ethylene Oxide Headgroups. *Biophys. J.* **1994**, *66*, 1479–88.
- (32) Allen, C.; Dos Santos, N.; Gallagher, R.; Chiu, G. N. C.; Shu, Y.; Li, W. M.; Johnstone, S. a.; Janoff, A. S.; Mayer, L. D.; Webb, M. S.; et al. Controlling the Physical Behavior and Biological Performance of Liposome Formulations through Use of Surface Grafted Poly(ethylene Glycol). *Biosci. Rep.* **2002**, *22*, 225–250.
- (33) Kučerka, N.; Nieh, M.-P.; Katsaras, J. Fluid Phase Lipid Areas and Bilayer Thicknesses of Commonly Used Phosphatidylcholines as a Function of Temperature. *Biochim. Biophys. Acta* **2011**, *1808*, 2761–2771.
- (34) Guo, L.; Har, J. Y.; Sankaran, J.; Hong, Y.; Kannan, B.; Wohland, T. Molecular Diffusion Measurement in Lipid Bilayers over Wide Concentration Ranges: A Comparative Study. *ChemPhysChem* **2008**, *9*, 721–728.
- (35) Deverall, M. A.; Gindl, E.; Sinner, E.-K.; Besir, H.; Ruehe, J.; Saxton, M. J.; Naumann, C. A. Membrane Lateral Mobility Obstructed by Polymer-Tethered Lipids Studied at the Single Molecule Level. *Biophys. J.* **2005**, *88*, 1875–1886.
- (36) Schram, V.; Tocanne, J. F.; Lopez, a. Influence of Obstacles on Lipid Lateral Diffusion: Computer Simulation of FRAP Experiments and Application to Proteoliposomes and Biomembranes. *Eur. Biophys. J.* **1994**, *23*, 337–48.
- (37) Marko, J. F.; Siggia, E. D. Stretching DNA. *Macromolecules* **1995**, *28*, 8759–8770.
- (38) Merkel, R.; Sackmann, E.; Evans, E. Molecular Friction and in Supported Bilayers Epitactic Coupling Monolayers. *J. Phys. (Paris)* **1989**, *50*, 1535–1555.
- (39) Machán, R.; Hof, M. Lipid Diffusion in Planar Membranes Investigated by Fluorescence Correlation Spectroscopy. *Biochim. Biophys. Acta* **2010**, *1798*, 1377–91.
- (40) Alessandrini, A.; Seeger, H. M.; Di Cerbo, A.; Caramaschi, T.; Facci, P. What Do We Really Measure in AFM Punch-through Experiments on Supported Lipid Bilayers? *Soft Matter* **2011**, *7*, 7054–7064.
- (41) Chen, Z.; Mao, Y.; Yang, J.; Zhang, T.; Zhao, L.; Yu, K.; Zheng, M.; Jiang, H.; Yang, H. Characterizing the Binding of Annexin V to a Lipid Bilayer Using Molecular Dynamics Simulations. *Proteins* **2014**, *82*, 312–22.
- (42) Kirchhausen, T. Bending Membranes. *Nat. Cell Biol.* **2012**, *14*, 906–8.

### A.3 Fulltext of ref. [3]:

## Cell Motility on Polyethylene Glycol Block Copolymers Correlates to Fibronectin Surface Adsorption.

**Authors:** Peter J. F. Röttgermann\*, Samira Hertrich\*, Ida Berts, Max Albert, Felix J. Segerer, Jean-François Moulin, Bert Nickel, Joachim O. Rädler

\* PR and SH contributed equally to this work

**Abstract:** Adhesion and motility of cells on polyethylene glycol (PEG) engineered surfaces are of fundamental interest for the development of biotechnological devices. Here, the structure of PEG block copolymers physisorbed to surfaces by poly-L-lysine (PLL) or polypropylene oxide (PPO) is studied. Cell behavior on such surfaces incubated with fibronectin (FN) is analyzed via time-lapse microscopy, the amount and the location of FN is determined via neutron reflectivity. While FN does not adsorb onto PPO-PEG, 0.4 - 0.7 mg / m<sup>2</sup> of FN is found in the vicinity of the PLL moiety of PLL-PEG. Cells exhibit 21% increased motility on PLL-PEG (5 kDa PEG chains) compared to pure FN layers, and 12% decreased motility for PLL-PEG (2 kDa PEG chains). These findings suggest that by design of PEGylated surfaces cell migration can be controlled.

#### SH contribution:

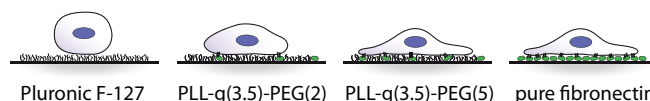
- Neutron reflectometry measurements
- Analysis and interpretation of neutron data
- writing the neutron parts of the paper
- writing the paper together with PR and IB



# Cell Motility on Polyethylene Glycol Block Copolymers Correlates to Fibronectin Surface Adsorption

Peter J. F. Röttgermann,<sup>a</sup> Samira Hertrich,<sup>a</sup> Ida Berts, Max Albert, Felix J. Segerer, Jean-François Moulin, Bert Nickel, Joachim O. Rädler\*

Adhesion and motility of cells on polyethylene glycol (PEG) engineered surfaces are of fundamental interest for the development of biotechnological devices. Here, the structure of PEG block copolymers physisorbed to surfaces by polylysine (PLL) or polypropylene oxide (PPO) is studied. Cell behavior on such surfaces incubated with fibronectin (FN) is analyzed via time-lapse microscopy, the amount and the location of FN is determined via neutron reflectivity. While FN does not adsorb onto PPOPEG, 0.4–0.7 mg m<sup>-2</sup> of FN is found in the vicinity of the PLL moiety of PLLPEG. Cells exhibit 21% increased motility on PLLPEG (5 kDa PEG chains) compared to pure FN layers, and 12% decreased motility for PLLPEG (2 kDa PEG chains). These findings suggest that by design of PEGylated surfaces cell migration can be controlled.



## 1. Introduction

In biomedical engineering and biotechnology, cell adhesion and motility on artificially engineered surfaces are of great importance. In a natural environment, cells interact with the extracellular matrix which determines cell shape and collective motion.<sup>[1]</sup> On artificial substrates, cells are solely confronted with the mechanical and chemical properties of the underlying surface. For example, stiffness as well as roughness of surfaces increases the spreading of cells.<sup>[2–4]</sup> Over the past few years, the functionalization of engineered

polymer surfaces has advanced significantly. Lithographic techniques have been developed to generate micropatterned surfaces for protein immobilization and controlled cellular growth.<sup>[5–7]</sup> In these approaches, the attachment and movement of cells is controlled by patterning the surface with cell adhesion promoting proteins on the one hand and cell repellent polymers on the other hand. In particular, the protein fibronectin (FN) and the polymer polyethylene glycol (PEG) are commonly used.<sup>[8–10]</sup> FN is an adhesive glycoprotein of the extracellular matrix<sup>[11]</sup> and its primary function is to mediate cell attachment.<sup>[12–14]</sup> PEG is a multifaceted neutral polymer, soluble both in water and many organic solvents. It is well known for its non-adhesive properties with regard to protein adsorption as well as attachment of microorganisms. This protein repellence of surface grafted PEG has been the subject of many studies investigating the influence of chain length, grafting density, and chain mobility.<sup>[15–18]</sup> Grafting of PEG to solid surfaces can be achieved by various chemical linkages, e.g., thiols or silanes for gold and oxide surfaces, yielding highly stable and well defined monolayers.<sup>[19,20]</sup> Alternatively, PEG block copolymers are used to form stable monolayers by physisorption from solution.<sup>[21]</sup> In particular, electrostatic

P. J. F. Röttgermann, S. Hertrich, Dr. I. Berts, M. Albert, F. J. Segerer, Dr. B. Nickel, Prof. J. O. Rädler  
Faculty of Physics and Center for NanoScience (CeNS), Ludwig-Maximilians-University, Geschwister-Scholl-Platz 1, 80539 Munich, Germany  
E-mail: raedler@lmu.de  
Dr. J.-F. Moulin  
Helmholtz Zentrum Geesthacht, Institut für Werkstofforschung, FRM II, Lichtenbergstr. 1, 85747 Garching, Germany

\*Peter J. F. Röttgermann and Samira Hertrich contributed equally to this work.

surface anchoring via poly-L-lysine-grafted PEG (PLL-PEG) has found widespread application in cell patterning.<sup>[7,22]</sup>

There is a remarkable difference in protein resistance between differently designed PEG polymers both for grafted and self-assembled monolayers.<sup>[19,20,23,24]</sup> For example, for PEG covalently and densely bound on silicon, both proteins and cells are found to be strongly repelled.<sup>[25]</sup> In contrast, we have showed in previous work that cells are capable of migrating from PLL-PEG passivated areas to adhesion sites coated with FN and thus self-organize into ordered arrays.<sup>[7]</sup> In this case, however, the last step in the surface preparation involves the incubation of the PLL-PEG with FN. It is hypothesized that the exposure of the PLL-PEG layer to FN renders the PLL-PEG coating partially cell adhesive.

It is therefore important to probe whether FN adsorbs to PLL-PEG coatings and if so, where it is located. Experimental access to localize FN within the PEG is difficult. Thus, we employ neutron reflectometry<sup>[26]</sup> to analyze the structure of different PEG layers and to determine the amount and distribution of FN in these PEG layers. We focus our study on two polymer constructs: first, the PEG grafted to a hydrophobic polymer anchor PPO and second, the PLL-PEG with PEG chains of both 2 and 5 kDa length. The structural information is then correlated with cell morphology and cell motility on these surfaces.

## 2. Results

### 2.1. Surface Passivation

Cellular adhesion and motility properties are studied on three different PEG surfaces and on an unpassivated surface as reference. The PEG layers are formed using two different polymer coatings, Pluronic, and PLL-PEG. Pluronic (F-127) is a PEG-PPO-PEG triblock-copolymer, consisting of two end-attached PEG (4.4 kDa) polymers on a 65-mer PPO. The PPO chain is hydrophobic; thus in water it physisorbs readily on hydrophobic surfaces. In contrast, the PLL chain of the PLL-PEG construct is positively charged, which results in a spontaneous adsorption on clean silicon oxide surfaces. In summary, both surface passivations are based on a physisorbed polymer coating. All experiments were performed at physiological salt concentration and pH. Figure 1 illustrates the chemical structure of the samples. Two different

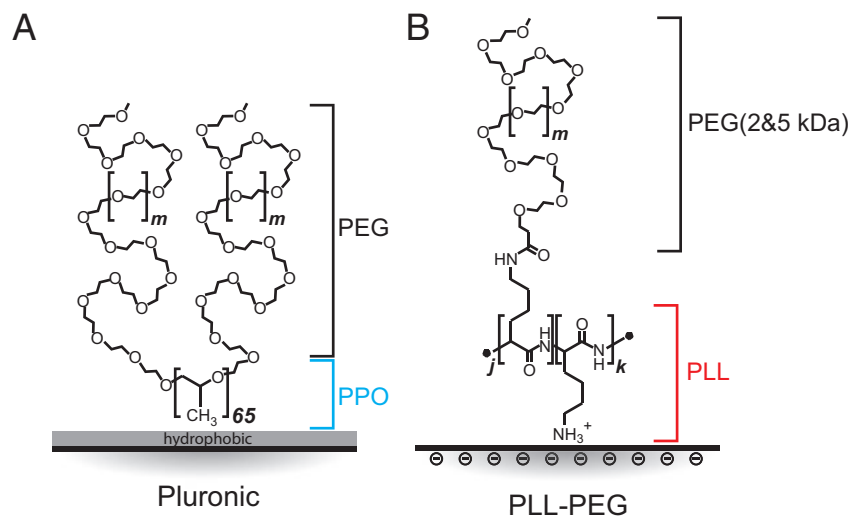


**Figure 1.** Schematics of the polymer architecture of Pluronic and PLL-PEG. A) Two PEG chains of 4.4 kDa ( $m = 99$ ) are linked to a 65-mer of polypropylene oxide. B) On a PLL chain of 20 kDa, PEG chains of various lengths (2 and 5 kDa,  $m = 45$  and 114) are linked in a grafting ratio of  $k/j = 3.5$  (lysine units/PEG chain).

chain lengths of PEG (2 and 5 kDa) on PLL are compared, herein denoted as PLL-PEG (2) and PLL-PEG (5). Finally, all substrates are incubated with FN.

### 2.2. Cell Morphology on Different Polymer Layers

To evaluate the morphology and spreading behavior on the different surfaces, cell contour areas were analyzed. Note that the microscopy images only show the projection areas of the cells, however, the cell contact area might be even smaller. Cell morphology and area give a first indication of how cells attach to the underlying surface, i.e., strong adhesion is commonly identified by flat cell shape while round cells indicate weak or no adhesion. Figure 2A shows fluorescence micrographs of plasma membrane stained adeno carcinoma cells (A549) on the different surfaces after 24 h. On Pluronic, all cells occupy a small area and are round shaped, i.e., cells do not spread. On PLL-PEG (2), cells partially adhere as their shape is more elongated. For PLL-PEG (5) and for FN (on the unpassivated culture dish), the spread out cell shape is even more distinct. Here, hardly any round shaped cells can be observed except for dividing cells. Furthermore, cells form filopodia on both substrates, and also start to proliferate during the first 24 h. This proliferation can be identified by cell junctions of several neighboring cells (Figure 2A).

In Figure 2B, the distributions of the contour area per cell for the different surfaces are plotted. One hour after seeding, the distributions are already distinguishable from each other. On Pluronic, the mean contour area is  $225 \mu\text{m}^2$  with a relatively small standard deviation of  $50 \mu\text{m}^2$ . On the other coatings, the contour area is higher. This observation

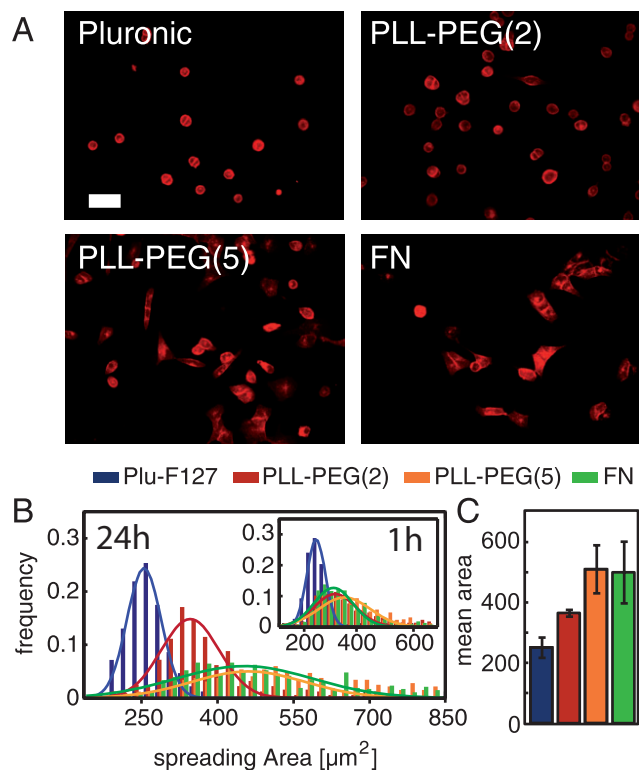


**Figure 2.** A) Fluorescence micrographs of plasma membrane stained A549 cells on Pluronic, PLL-PEG (2), PLL-PEG (5), and unpassivated surface, all incubated with FN, after 24 h. Scale bar 100  $\mu\text{m}$ . B) Distribution of the cell contour area for Pluronic (blue), PLL-PEG (2) (red), PLL-PEG (5) (orange), and FN (green) at 24 and 1 h (inset) after seeding. C) Mean contour area per cell of A549 cells after 24 h. Error bars represent the standard deviation of three experiments.

becomes more obvious after 24 h. The contour area per cell reaches values of  $365 \pm 100 \mu\text{m}^2$  (mean  $\pm$  standard deviation) for PLL-PEG (2),  $510 \pm 200 \mu\text{m}^2$  for PLL-PEG (5), and  $500 \pm 240 \mu\text{m}^2$  for FN (see Figure 2C). Only on Pluronic, the contour area stays low with  $250 \pm 65 \mu\text{m}^2$  indicating that cells are still not adherent.

### 2.3. Cell Motility

To access cell motility on the different surfaces, cell trajectories were extracted from fluorescence time-lapse microscopy images. Figure 3A shows several exemplary cell trajectories on Pluronic, on both PLL-PEG, and on pure FN surfaces over a period of 24 h. No cell migration was observed on the Pluronic surface, while on all other surfaces cells did migrate. Different populations of resting and persistently migrating cells were not observed, as cells were moving continuously. One way to quantify migration is to evaluate the mean squared displacement (MSD) with respect to the initial position. On PLL-PEG (2), the MSD is 125  $\mu\text{m}$ , i.e., less than the 200  $\mu\text{m}$  on PLL-PEG (5) after 1 d. The displacement on FN is similar, but slightly lower than on PLL-PEG (5).

To assess motility in a quantitative way the time evolution of the MSD is calculated by taking the ensemble average over all cells, as illustrated in Figure 3B. Typical cell migration can be described by a persistent random walk.<sup>[27]</sup> Initially, cells on PLL-PEG (2 and 5) and FN show indications of directed motion (shown with green dotted lines). On the longer time scale, the MSD data in Figure 3B approach a diffusive migration (random walk), shown with red dashed lines. A common way to determine cell speed is to calculate the contour length of the trajectory for all cells and divide this by the overall tracking

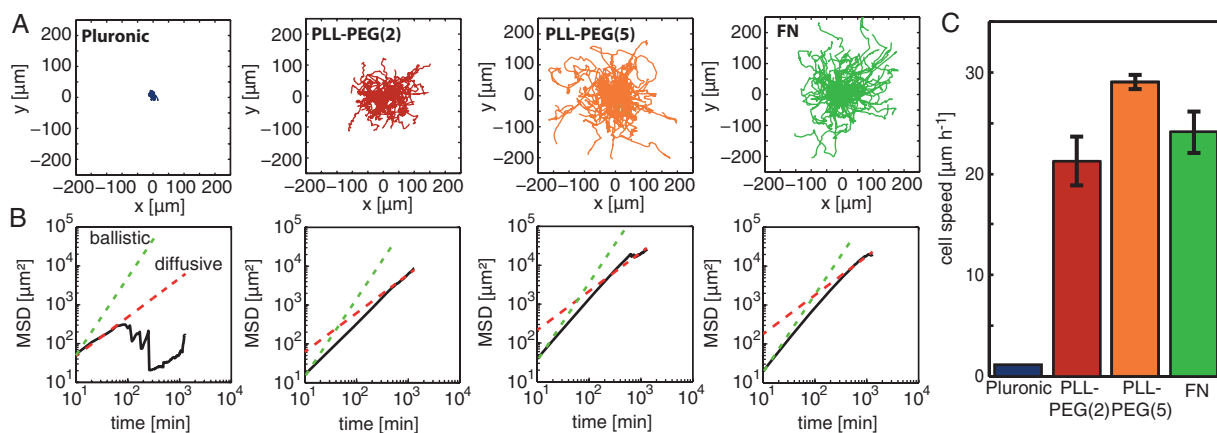


**Figure 3.** A) Representative cell trajectories on the four different substrates over a period of 24 h: Pluronic (blue), PLL-PEG (2) (red), PLL-PEG (5) (orange), and FN (green). B) Mean square displacements (black curves) are plotted against time for the various substrates. As a guide to the eye, the MSD dependence for directed motion (dotted green curve, slope 2) and diffusive motion (dashed red curve, slope 1) are indicated. C) Bar plot of single cell speed for the various substrates. Error bars represent the standard deviation of three experiments.

time, see Figure 3C. Using this procedure, the lowest cell speed of  $1.2 \mu\text{m h}^{-1}$  is obtained for Pluronic surface; this is at the detection limit of our setup. For the other surfaces, cell velocities are  $21.2 \pm 2.5 \mu\text{m h}^{-1}$  for PLL-PEG (2),  $29.1 \pm 0.7 \mu\text{m h}^{-1}$  for PLL-PEG (5), and  $24.1 \pm 2 \mu\text{m h}^{-1}$  for FN.

#### 2.4. Neutron Reflectivity on Polymer Layers

Neutron reflectometry measurements provide detailed information regarding the amount and distribution of protein in the different polymer layers. Two sets of measurements were performed on each system, first in  $\text{D}_2\text{O}$  and second in a mix of  $\text{D}_2\text{O}$  and  $\text{H}_2\text{O}$  with the scattering length density (SLD) matched to that of  $\text{SiO}_2$ . From the combination of these two measurements, we obtain hydration and composition of the films. Experiments were carried out on  $\text{SiO}_2$  film to enhance contrast. Fresnel corrected neutron reflectivity  $R(q)q^4$  are shown in the inset of Figure 4A–C. All reflectivity curves show oscillations in the intensity caused by the oxide layer on the silicon block. Silicon substrate with an oxide layer thickness of  $d = 580 \pm 4 \text{ \AA}$  was used for both the Pluronic and the PLL-PEG (2) samples. The oscillations of the intensity are narrower for samples containing PLL-PEG (5) due to the much thicker  $\text{SiO}_2$  layer ( $1090 \pm 5 \text{ \AA}$ ). The signal caused by the film is visible as the broad fringe at about  $q = 0.1 \text{ \AA}^{-1}$ .

The neutron data are fitted using different models. Starting from a one-layer model, the number of layers is increased plus their thickness and roughness adjusted until the calculated reflectivity of the models fits best the measured data. The minimum model necessary to reproduce the data is always chosen. The Pluronic data, could be fitted with one  $28 \text{ \AA}$  layer and a SLD of  $3.3 \times 10^{-6} \text{ \AA}^{-2}$  in  $\text{D}_2\text{O}$  and  $2.0 \times 10^{-6} \text{ \AA}^{-2}$  in the  $\text{D}_2\text{O}/\text{H}_2\text{O}$  mix, indicating a hydration of 45%. The dry SLD for the Pluronic layer is at the expected value of  $\sim 0.45 \times 10^{-6} \text{ \AA}^{-2}$ , the theoretical values for pure PEG and PPO are  $0.6 \times 10^{-6}$  and  $0.35 \times 10^{-6} \text{ \AA}^{-2}$ , respectively. After incubation with FN, no significant change was observed for the neutron reflectivity data of the Pluronic sample measured in  $\text{D}_2\text{O}$ , see Figure 4A. Therefore, the protein causes no change for the Pluronic surface.

A two-layer model is needed for the interpretation of the PLL-PEG samples. Here, the layer adjacent to the  $\text{SiO}_2$  has a SLD of  $4.4 \times 10^{-6} \text{ \AA}^{-2}$  (in  $\text{D}_2\text{O}$ ) and  $3.5 \times 10^{-6} \text{ \AA}^{-2}$  ( $\text{D}_2\text{O}/\text{H}_2\text{O}$  mix) for PLL-PEG (2), and  $4.5 \times 10^{-6}$  and  $3.42 \times 10^{-6} \text{ \AA}^{-2}$  for PLL-PEG (5). This layer represents the PLL and increases in thickness after addition of FN. The hydrated PEG layer on top has a SLD of  $5.7 \times 10^{-6}$  and  $3.1 \times 10^{-6} \text{ \AA}^{-2}$  for PLL-PEG (2), and  $5.73 \times 10^{-6}$  and  $3.3 \times 10^{-6} \text{ \AA}^{-2}$  for PLL-PEG (5). The PLL-PEG (2) system shows a highly hydrated PEG layer with 90% water and a thickness of about  $50 \text{ \AA}$ ,

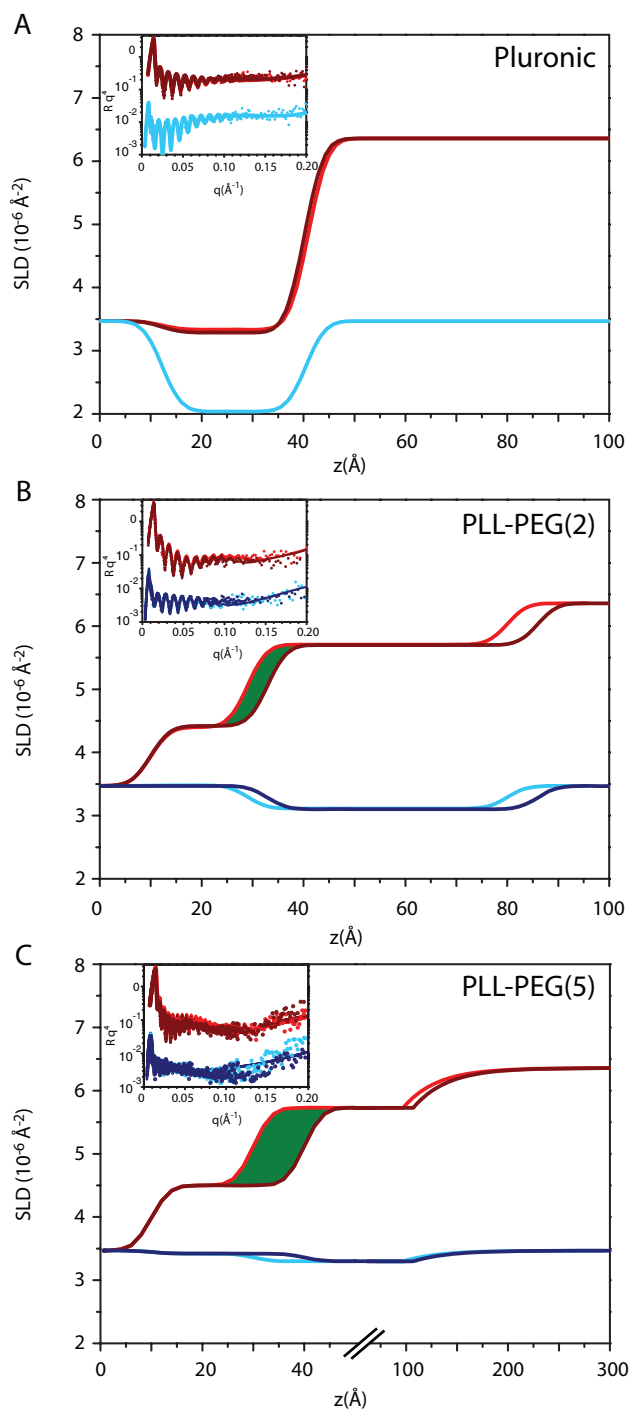


**Figure 4.** SLD profiles with the corresponding reflectivity data and fits (insets) for Pluronic A), PLL-PEG (2) B), and PLL-PEG (5) C). The samples before the addition of FN are shown in light red for the  $\text{D}_2\text{O}$  contrast and light blue for the  $\text{D}_2\text{O}/\text{H}_2\text{O}$  mix contrast. After the addition of FN, the data are shown in dark red for the  $\text{D}_2\text{O}$  contrast and dark blue for the  $\text{D}_2\text{O}/\text{H}_2\text{O}$  mix contrast. The measurements in the  $\text{D}_2\text{O}/\text{H}_2\text{O}$  mix buffer are offset by a factor 0.1 for clarity. The effect of the FN is visible in the change in thickness indicated by the green area shown in B) and C). The x-axis in C) is differently scaled for improved visualization. The much longer PEG chains decay exponentially towards the bulk.

and underneath a PLL layer with hydration of 31% and a thickness of about 20 Å. The PLL-PEG (5) also shows a hydrated PEG layer (84% water) with the polymer density that can be fitted with an exponentially decreasing profile towards the bulk. The homogeneous part of the layer has a thickness of 68 Å, above, the PEG density decreases with a decay length of 33 Å. Its total length is almost double the thickness of PLL-PEG (2). The underlying PLL layer is 20 Å thick and contains 37% water, i.e., the layer is slightly less dense compared to PLL-PEG (2). After the incubation with FN, the reflectivity signal deviates for PLL-PEG (2) (Figure 4B dark red and dark blue) between  $q = 0.08 \text{ \AA}^{-1}$  and  $q = 0.15 \text{ \AA}^{-1}$  from the signal before (Figure 4B light red and light blue), indicating that FN changed the overall system. The same trend was observed for PLL-PEG (5), see Figure 4C.

Table 1 shows thickness, hydration and surface coverage extracted from the SLD model. While the SLD of both PLL and PEG layers remained unchanged, the underlying PLL layer increases in thickness by 4 Å for the shorter PEG. We conclude that the amount of material adsorbed to the surface increased after addition of FN. We evaluated the change in thickness to determine the

amount of FN to be  $0.4 \text{ mg m}^{-2}$ . FN is affecting the PLL layer by an increase of 8 Å in layer thickness for the PLL-PEG (5). The amount of FN in this case is  $0.7 \text{ mg m}^{-2}$ .

### 3. Discussion

#### 3.1. Description of Grafted PEG Layers

In our neutron reflectivity study, we showed that we can measure thickness, mass coverage, and thus PEG grafting density. Those values can be compared with theoretical descriptions. The relation of polymer height  $L$  and grafting density  $\sigma$  is  $L = Na(a^2\sigma)^{1/3}$  with monomer size  $a = 0.35 \text{ nm}$ <sup>[28]</sup> for PEG, and the polymerization degree  $N$  as described by Alexander and de Gennes (AdG).<sup>[29,30]</sup> The AdG theory is valid for polymers in a brush conformation, i.e., the product of the grafting density and the squared Flory radius  $R_F = aN^{3/5}$  is less than 1. The values predicted by this model are compared to our data in Table 2. Both PLL-PEG copolymers are clearly in the brush regime ( $\sigma^{-1} (R_F)^{-2} = 0.55$  and  $0.14$ ). In case of the PLL-PEG (2), the thickness of the PEG layer is 16% higher than predicted by the model. Nevertheless, the thickness of PEG is

**Table 1.** Fit parameters of Pluronic and PLL-PEG with calculated surface coverage from the neutron reflectivity experiment.

Sample	Layer description	Thickness [Å]	% Water in layer	Surface coverage [mg · m <sup>-2</sup> ]
Pluronic	PPO + PEG	28 ± 1	45 ± 1	1.8 ± 0.1
	After FN incubation	PPO + PEG	28 ± 1	45 ± 1
PLL-PEG (2)	PLL	19 ± 1	31 ± 2	1.8 ± 0.1
	PEG	51 ± 1	90 ± 1	0.51 ± 0.02
	After FN incubation	PLL + FN	23 ± 1	31 ± 5
	PEG	53 ± 1	90 ± 3	0.53 ± 0.03
	PLL-PEG (5)	PLL	20 ± 1	37 ± 3
After FN incubation	PEG	68 ± 3	84 ± 1	1.65 ± 0.04
	PLL + FN	28 ± 1	37 ± 2	2.47 ± 0.1
	PEG	68 ± 3	84 ± 1	1.65 ± 0.04

**Table 2.** Comparison of AdG theory and neutron data with  $N$  monomer units, measured surface density  $\sigma_{\text{exp}}$ , measured and calculated PEG layer thickness  $L_{\text{exp}}$  and  $L_{\text{theory}}$ , Flory radius  $R_F$ , relation of  $\sigma^{-1} (R_F)^{-2}$ , and type of conformation.

Surface	$N$	$\sigma_{\text{exp}} \cdot 10^{-3} [\text{Å}^{-2}]$	$L_{\text{exp}} [\text{Å}]$	$L_{\text{theory}} [\text{Å}]$	$R_F [\text{Å}]$	$\sigma^{-1} (R_F)^{-2}$	Conformation
PLL-g (3.5)-PEG (2)	45	1.54	51	42	34	0.55	Brush
PLL-g (3.5)-PEG (5)	114	1.99	68 + 33	116	60	0.14	Brush
PPO-g (32.5)-PEG (4.4)	99	1.72	<28	96	55	0.19	Pancake

consistent with previous measurements of PEG cushions<sup>[31]</sup> and PEG-tethered lipid bilayers.<sup>[32]</sup> In case of the PLL-PEG (5), the theoretical thickness of 116 Å is also in good agreement with the data fit, that produced a homogeneous layer of 68 Å and on top an exponential layer with a decay length of 33 Å. For the Pluronic film, the AdG model is not valid, as in that case the polymer extension is ruled by hydrophobic interaction with the surface. Thus, PEG adopts a much thinner pancake structure and shields the hydrophobic surface from the water.<sup>[33]</sup>

### 3.2. Surface Passivation and Protein Interaction

The anchor polymers, PLL and PPO, as well as the PEG chain length and density affect the degree of surface passivation. The Pluronic coating consists of 4.4 kDa PEG chains while the PLL-PEG film consists of 2 and 5 kDa PEG chains, respectively. Despite the long PEG chains of the Pluronic coating, the overall polymer layer is thinner and less hydrated (45% water), shown by the reflectivity data in Figure 4. The low water content and high PEG density in the Pluronic film does not allow for FN intercalation within the sensitivity of the neutron reflectometry experiment. This is in line with the above-described shielding effect of the PEG for the underlying hydrophobic PPO layer, blocking the adsorption sites to the protein. Similar behavior was also observed experimentally by O'Connor<sup>[17]</sup> and McPherson.<sup>[33]</sup>

On the contrary, the PEG layers of both PLL-PEG films contain more than 80% water and are not dense enough for complete protein repellence. In our work, we can specify both the location and the amount of protein by neutron reflectometry: FN was found in small amounts in the vicinity of the PLL layer. This indicates primary adsorption, which is the adsorption of proteins at the substrate surface of a polymer brush. The SLD of FN, with the majority of the exchangeable protons replaced with the ones from the solvent, is very close to the one of PLL (FN fully exchanged in D<sub>2</sub>O is  $3.12 \times 10^{-6} \text{ \AA}^{-2}$  compared to  $3.4 \times 10^{-6} \text{ \AA}^{-2}$  for PLL in D<sub>2</sub>O). Due to this fact, it is not possible to distinguish between the PLL and the FN in the layer. Adsorption of FN in the PLL region is driven by electrostatics, in contrast to the theoretical prediction of protein adsorption into polymers by Halperin.<sup>[34]</sup> The adsorbed PLL on the silicon oxide leaves a net positive charge<sup>[35]</sup> and FN is negatively charged in physiological solution (isoelectric point 5.2).<sup>[36]</sup> Despite the big protein size, FN in the unfolded state is flexible and rod-like with a diameter (20 Å) comparable to a small protein.<sup>[37]</sup>

Hence, it can penetrate the brushes and absorb primarily to a surface. Comparable results were presented by Pasche et al.<sup>[38]</sup> where the incubation of serum in a systematic series of PLL-PEG coatings with varying PEG molecular weights and grafting ratios revealed protein adsorption. Moreover, a study of the adsorption of myoglobin (diameter of 40 Å) onto PEG brushes using neutron scattering revealed similar behavior.<sup>[39]</sup> The protein layer closest to the polymer surface has a low thickness compared to the protein dimensions, which is interpreted as denaturation of the protein. In our case, we suggest that this effect is combined with a mixing of the FN with the PLL, thus resulting in the small layer thickness assigned to the FN.

Figure 5 illustrates the surfaces and their respective interaction with FN. Longer PEG chains of 5 kDa did not form a uniform layer but were rather stretched out. A disordered configuration may offer less protection compared to well ordered chains allowing more FN to diffuse through to the PLL.<sup>[38]</sup> This may be the reason why the 2 kDa PEG chains show better FN repellence compared to 5 kDa chains.

### 3.3. PEG Interface and Cell Behavior

In the following, we compare the surface properties with cell behavior. Firstly, cells do not adhere to Pluronic, as indicated by the round shape of the cells. This is caused by the absence or insufficient accessibility of FN binding sites in the Pluronic film. In contrast, cells spread on PLL-PEG where FN adsorption was observed. Thus, small amounts of surface bound FN seem to be essential for cell spreading. Indeed, Massia and Hubbell<sup>[40]</sup> showed that  $1 \text{ fmol cm}^{-2}$  is already sufficient for complete spreading of cells on a bare surface, which corresponds to a ligand spacing of 440 nm. Our data for the FN underneath a PEG moiety reveal amounts of  $72 \text{ fmol cm}^{-2}$  for PLL-PEG (2),  $127 \text{ fmol cm}^{-2}$  for PLL-PEG (5) and none for Pluronic (detection limit of

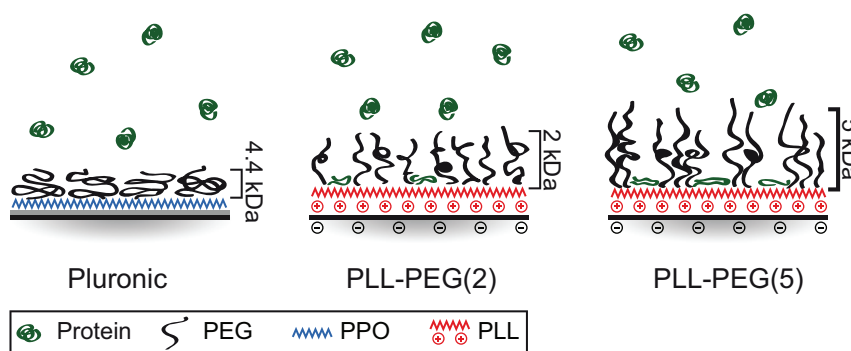


**Figure 5.** Interpretation based on the neutron SLD profiles of the adsorption of FN in the three different polymer coatings Pluronic, PLL-PEG (2), and PLL-PEG (5). In the first case, FN is not adsorbed on the pancake-like Pluronic layer, while on the PLL-PEG samples small amounts of FN penetrate the extended brushed PEG layers to attach to underlying PLL. The higher PEG density leads to non-ordered chains and therefore to higher protein adsorption.

18 fmol cm<sup>-2</sup>). All these values are considerably above the predicted minimal ligand density most likely due to the fact that FN is bound primarily to the PLL and shielded by the PEG layer. Cells have to form protrusions through the PEG layer to bind to the FN. In addition, the conformation of FN in our system plays a role as it exists probably in the unfolded rod-like state which minimizes the accessibility of the RGD binding site.<sup>[41]</sup> Aggregates might further increase the average spacing of two binding sites for cells and also favor the formation of focal adhesions.

Apart from the different spreading, also cell migration correlates with the different surface properties. The longest persistence time is observed for the pure FN surface whereas the highest velocity is observed on PLL-PEG (5). As cells polarize in one direction (mostly random in absence of a chemo-attractant) they have a higher probability to move forward in the same direction instead of turning towards any other direction.<sup>[42–44]</sup> The protein on the pure FN surface is isotropically distributed and the process of the directed motion is only interrupted by intracellular processes resulting in the highest persistent time of motion. PLL-PEG (5) exhibits fewer adhesion points which leads on the one hand to more frequent interruption in the migration and on the other hand to faster movement, possibly due to faster detachment.<sup>[45]</sup> PLL-PEG (2) exhibits even fewer anchor points, the amount of FN is further decreased, and the cell movement cannot be sustained at such high speed. It seems the cells have to repolarize more often, which is time consuming and results in a much slower movement. A similar behavior with a maximum in the velocity distribution has been observed before.<sup>[43,46]</sup>

These findings indicate that there is an optimal FN density with regard to the maximal covered distance. This is best met by the PLL-PEG (5) layer. If the density is lower, e.g., on PLL-PEG (2), cells may not find anchor points to advance as fast. On the other hand, a too high anchor point density as for the pure FN surface slows the cells due to detachment time. It is likely that cell attachment to PEG could alter the underlying brush structure. The average distance of cell membrane and solid substrate is also likely to be tuned by FN and the PEG molecular weight and could be measured by neutron reflectivity.<sup>[47]</sup>

## 4. Conclusion

In this work, we have correlated the amount of FN adsorption into different PEG layers with cell adhesion and motility. PEG grafted to a hydrophobic PPO anchor suppresses cell adhesion and migration almost completely and shows no FN adsorption. This is most likely due to the shielding effect of the PEG from the hydrophobic moiety. For PLL-PEG layers, we find that the brush-like structure of the PEG layer still allows for adsorption of FN underneath

the PEG layer, i.e., in close proximity to the PLL anchor. Cells exhibit faster speed on the PLL-PEG (5) compared to that of pure FN surface. These findings suggest that the combination of partial adsorption of cell adhesive proteins and the cell repellent properties of PEG are suited to elevate cell motility. Thus, artificially designed surfaces of PEG block copolymers and proteins could fine-tune cell motility properties.

## 5. Experimental Section

### 5.1. Sample Preparation

For the reflectometry measurements, silicon blocks were cleaned in an ultrasonic bath for 10 min in ethanol, 10 min in purified water (MiliQ, Millipore Corporation), and dried with nitrogen. The silicon blocks and the topas substrate ( $\mu$ -dishes ibidi GmbH) for the cell experiments were then exposed to O<sub>2</sub> plasma (3 min at 40 W, Femto Diener). The samples were passivated with PLL (20 kDa)-g (3.5)-PEG (2 or 5 kDa) (SuSoS AG) at a 1 mg ml<sup>-1</sup> aqueous buffer solution (10 mM HEPES and 150 mM NaCl at pH 7.4) for 30 min at room temperature (RT). For Pluronic-F127 (Sigma-Aldrich), the silicon blocks were pre-coated with octadecyltrichlorosilane (Sigma-Aldrich) and/or untreated  $\mu$ -dishes were taken, and passivated with 10 mg ml<sup>-1</sup> buffer aqueous solution for 1 h at RT. The samples were washed thrice with phosphate buffered saline (PBS). Subsequently, all samples were exposed to a 50  $\mu$ g ml<sup>-1</sup> solution of FN (YoProteins) for at least 1 h. The pure protein coating was adsorbed on unpassivated  $\mu$ -dishes for 1 h.

### 5.2. Neutron Reflectivity Measurements

Neutron reflectivity measurements were performed at the REFSANS horizontal time of flight reflectometer operated by the Helmholtz Zentrum Geesthacht at the Heinz Maier-Leibnitz Zentrum in Munich.<sup>[48]</sup> For this experiment, the relative  $q$  resolution was set to  $dq/q = 0.06$  and the incident wavelength spectrum ranged from  $\lambda = 2\text{--}10$  Å. By combining the reflected intensities measured for five incident angles ( $\theta = 0.15^\circ, 0.3^\circ, 0.6^\circ, 1.4^\circ, \text{ and } 2.8^\circ$ ) the reflectivity  $R(q) = I(\lambda, \theta)/I_0(\lambda)$  was obtained up to a scattering vector  $q = 4\pi/\lambda \sin(\theta) = 0.2$  Å<sup>-1</sup> where  $I_0$  denotes the primary beam intensity, and  $I$  the reflected intensity.

In neutron measurements, the SLD can be adjusted by choosing different isotopes. Here, contrast variation of PBS buffer solution was used to determine the hydration of the film. Therefore, two reflectivity measurements on each sample were performed: one in D<sub>2</sub>O buffer, then the second in a mixture of 61% D<sub>2</sub>O and 39% H<sub>2</sub>O, i.e., matched to the SLD of silicon oxide. From the difference in the SLD profile, the hydration and the SLD without the contribution of D<sub>2</sub>O or H<sub>2</sub>O (SLD dry) were calculated.<sup>[49]</sup> Finally, the protein was added to both the D<sub>2</sub>O buffer and the contrast matched buffer for a second set of measurements. Two measurements at different contrasts for each system ensure that changes in conformation or hydration can be differentiated from adsorption of new material on the surface.

The data for Pluronic and PLL-PEG (2) were analyzed with the MOTOFIT program.<sup>[50]</sup> The program allows us to define thin layers

on top of the substrate, which add up to the film. By matching the theoretical and measured reflectivity, the layer thickness and SLD can be determined. The data from PLL-PEG (5) were analyzed using CPROF.<sup>[51]</sup> This program fits multiple contrasts of data for a single sample in a similar way as the MOTOFIT program. In addition, it uses a model with smoothly varying density profiles appropriate for polymers and gels at interfaces.<sup>[52]</sup> The PEG layer of PLL-PEG (2) could also be fitted with a parabolic profile<sup>[53,54]</sup> without altering the agreement using a simpler box model with a low roughness. Parabolic and linear profiles were tested for the PLL-PEG (5) data but the agreement was not as good as for the exponential profile. This is due to either lower grafting density or higher polydispersity.<sup>[52,55]</sup> For the graphical representation of the data, the reflectivity was multiplied by  $q^4$  to correct for the Fresnel decay at higher  $q$  values. This allows for a better visualization of the small changes to the reflected intensity by ultrathin layers.

### 5.3. Cell Culture

The A549 cell line (ATCC) was cultured in modified Eagle's medium with Earle's salts (c-c-pro), 2 mM L-glutamine, and 10% fetal calf serum. Cells were grown to 70–80% confluence, trypsinized and centrifuged at 1 000 rpm for 3 min. Cell pellets were resuspended in either cell medium or, for the experiments in Leibovitz's L15 medium with GlutaMAX (Gibco) and 10% fetal calf serum. Equal cell densities were seeded on each surface. Cells were stained with CellMask Orange Plasma membrane Stain (Life Technologies) by adding 5  $\mu$ M dye for 5 min to highlight the contour of the cells or with the permeable fluorescent dye Hoechst 33342 (Life Technologies) by adding 25 nM dye to the suspension (incubation at 37 °C for 20 min) to track the nuclei. Samples were not washed to avoid an influence on weakly adherent cells.

### 5.4. Time-Resolved Fluorescence Microscopy

Images were taken with an iMIC digital microscope with phase contrast (TILL Photonics) and an oligochrome fluorescent light source (TILL Photonics) in combination with a single-band long-pass DAPI HC filter set and a dualband GFP/mCherry ET filter set (AHF Analysetechnik). Samples were kept at a constant temperature of 37 °C with an ibidi heating system (ibidi GmbH).

### 5.5. Image and Data Analysis

Raw images were preprocessed in ImageJ: the background was subtracted with a built-in function. To highlight the nuclei or the contour of the cells, a band-pass filter was applied (colliding cells were excluded from analysis). Images were binarized by setting a global threshold. Binarized images were clustered and tracked with Cell Evaluator.<sup>[56]</sup> Coordinates of the center of mass and the area of the nuclei were extracted and analyzed in MATLAB.

### 5.6. Cell Motility and Morphology Analysis

The mean square displacement was calculated as  $MSD(t) = \langle \langle (X_i(t+t_0) - X_i(t_0))^2 \rangle \rangle_{t_0, i}$  where  $X_i(t)$  denotes the center of cell

nucleus  $i$  at time  $t$ .  $\langle \cdot \rangle_{t_0}$  designates the average over all times  $t$  with starting time  $t_0$ .  $\langle \cdot \rangle_i$  is the average over all tracked cells. Dead cells, as well as nuclei exceeding a maximal area (indication of two fused cells), were excluded from analysis. At least 200 tracks were analyzed for each experiment. All experiments have been repeated thrice. The MSD data were fitted on the short time scale for the first 40 min with the function  $MSD(t) = 4Dt^2$  and for the long-term behavior with  $MSD(t) = 4Dt$ .

For the evaluation of the spreading area, only single cells have been taken into account. The frequency distributions of the spreading area have been fitted to Gaussian functions.

The single cell speed was calculated by dividing the contour length by the tracking time for a single cell and then averaging over all tracked cells. The contour length is determined by summing the nucleus displacement for each frame.

**Acknowledgments:** Financial support by the Deutsche Forschungsgemeinschaft (DFG) via project B1 and A7 within the SFB 1032, the Excellence Cluster "Nanosystems Initiative Munich (NIM)", FP7 EU grants NanoTransKinetics and NanoMILE, and by BMBF 05K13WM1 is gratefully acknowledged.

Received: May 19, 2014; Revised: August 13, 2014; Published online: September 10, 2014; DOI: 10.1002/mabi.201400246

**Keywords:** cell motility; cell morphology; fibronectin adsorption; neutron reflectivity; polyethylene glycol

- [1] T. E. Angelini, E. Hannezo, X. Trepat, J. J. Fredberg, D. A. Weitz, *Phys. Rev. Lett.* **2010**, 104.
- [2] B. C. Isenberg, P. A. DiMilla, M. Walker, S. Kim, J. Y. Wong, *Biophys. J.* **2009**, 97, 1313.
- [3] A. Zemel, F. Rehfeldt, A. E. X. Brown, D. E. Discher, S. A. Safran, *Nat. Phys.* **2010**, 6, 468.
- [4] E. Biazar, M. Heidari, A. Asefnejad, N. Montazeri, *Int. J. Nanomed.* **2011**, 6, 631.
- [5] R. S. Kane, S. Takayama, E. Ostuni, D. E. Ingber, G. M. Whitesides, *Biomaterials* **1999**, 20, 2363.
- [6] A. S. Blawas, W. M. Reichert, *Biomaterials* **1998**, 19, 595.
- [7] P. J. F. Röttgermann, A. Piera Alberola, J. O. Rädler, *Soft Matter* **2014**, 10, 2397.
- [8] G. Csucs, R. Michel, J. W. Lussi, M. Textor, G. Danuser, *Biomaterials* **2003**, 24, 1713.
- [9] M. Théry, *J. Cell. Sci.* **2010**, 123, 4201.
- [10] A. Azioune, M. Storch, M. Bornens, M. Théry, M. Piel, *Lab Chip* **2009**, 9, 1640.
- [11] S. Stenman, A. Vaheri, *J. Exp. Med.* **1978**, 147, 1054.
- [12] D. L. Elbert, J. A. Hubbell, *Annu. Rev. Mater. Sci.* **1996**, 26, 365.
- [13] K. Sekiguchi, S. Hakomori, *Proc. Natl. Acad. Sci. USA* **1980**, 77, 2661.
- [14] R. Hynes, *Annu. Rev. Cell Biol.* **1985**, 1, 67.
- [15] R. Michel, S. Pasche, M. Textor, D. G. Castner, *Langmuir* **2005**, 21, 12327.
- [16] A. Seehuber, D. Schmidt, R. Dahint, *Langmuir* **2012**, 28, 8700.
- [17] S. M. O'Connor, A. P. Deanglis, S. H. Gehrke, G. S. Retzinger, *Biotechnol. Appl. Biochem.* **2000**, 31, 185.

- [18] A. Halperin, G. Fragneto, A. Schollier, M. Sferrazza, *Langmuir* **2007**, *23*, 10603.
- [19] J. Jung, K. Na, B. Shin, O. Kim, J. Lee, K. Yun, J. Hyun, *J. Biomater. Sci. Polym. Ed.* **2008**, *19*, 161.
- [20] M. Gabi, A. Larmagnac, P. Schulte, J. Vörös, *Colloids Surf. B* **2010**, *79*, 365.
- [21] N.-P. Huang, J. Vörös, S. M. De Paul, M. Textor, N. D. Spencer, *Langmuir* **2001**, *18*, 220.
- [22] J. Fink, M. Théry, A. Azioune, R. Dupont, F. Chatelain, M. Bornens, M. Piel, *Lab Chip* **2007**, *7*, 672.
- [23] T. A. Desai, *Med. Eng. Phys.* **2000**, *22*, 595.
- [24] B. Zhu, T. Eurell, R. Gunawan, D. Leckband, *J. Biomed. Mater. Res.* **2001**, *56*, 406.
- [25] S. Sharma, R. W. Johnson, T. A. Desai, *Langmuir* **2003**, *20*, 348.
- [26] G. Fragneto-Cusani, *J. Phys.: Condens. Matter* **2001**, *13*, 4973.
- [27] E. Méhes, E. Mones, V. Németh, T. Vicsek, *PLoS ONE* **2012**, *7*, e31711.
- [28] N. V. Efremova, S. R. Sheth, D. E. Leckband, *Langmuir* **2001**, *17*, 7628.
- [29] P. G. de Gennes, *J. Phys. France* **1976**, *37*, 1445.
- [30] S. Alexander, *J. Phys. France* **1977**, *38*, 983.
- [31] T. L. Kuhl, D. E. Leckband, D. D. Lasic, J. N. Israelachvili, *Biophys. J.* **1994**, *66*, 1479.
- [32] S. Hertrich, F. Stetter, A. Ruhm, T. Hugel, B. Nickel, *Langmuir* **2014**.
- [33] T. McPherson, A. Kidane, I. Szleifer, K. Park, *Langmuir* **1998**, *14*, 176.
- [34] A. Halperin, *Langmuir* **1999**, *15*, 2525.
- [35] Y. Duval, J. A. Mielczarski, O. S. Pokrovsky, E. Mielczarski, J. J. Ehrhardt, *J. Phys. Chem. B* **2002**, *106*, 2937.
- [36] N. M. Tooney, M. W. Mosesson, D. L. Amrani, J. F. Hainfeld, J. S. Wall, *J. Cell. Biol.* **1983**, *97*, 1686.
- [37] H. P. Erickson, N. Carrell, J. McDonagh, *J. Cell. Biol.* **1981**, *91*, 673.
- [38] S. Pasche, S. M. De Paul, J. Vörös, N. D. Spencer, M. Textor, *Langmuir* **2003**, *19*, 9216.
- [39] E. Schneck, A. Schollier, A. Halperin, M. Moulin, M. Haertlein, M. Sferrazza, G. Fragneto, *Langmuir* **2013**, *29*, 14178.
- [40] S. P. Massia, J. A. Hubbell, *J. Cell. Biol.* **1991**, *114*, 1089.
- [41] E. Klotzsch, I. Schoen, J. Ries, A. Renn, V. Sandoghdar, V. Vogel, *Biomater. Sci.* **2014**, *2*, 883.
- [42] L. Li, S. F. Nørrelykke, E. C. Cox, *PLoS ONE* **2008**, *3*, e2093.
- [43] R. Sambeth, A. Baumgaertner, *Phys. Rev. Lett.* **2001**, *86*, 5196.
- [44] P. J. M. Van Haastert, *PLoS Comput. Biol.* **2010**, *6*, e1000874.
- [45] G. Maheshwari, A. Wells, L. G. Griffith, D. A. Lauffenburger, *Biophys. J.* **1999**, *76*, 2814.
- [46] S. Wu, A. Wells, L. G. Griffith, D. A. Lauffenburger, *Biomaterials* **2011**, *32*, 7524.
- [47] L. Pocivavsek, A. Junghans, N. Zebda, K. Birukov, J. Majewski, *Am. J. Physiol. Lung Cell Mol. Physiol.* **2014**, *306*, L1.
- [48] R. Kampmann, M. Haese-Seiller, V. Kudryashov, B. Nickel, C. Daniel, W. Fenzl, A. Schreyer, E. Sackmann, J. Rädler, *Physica B* **2006**, *385-386*, Part 2, 1161.
- [49] S. Stanglmaier, S. Hertrich, K. Fritz, J. F. Moulin, M. Haese-Seiller, J. O. Rädler, B. Nickel, *Langmuir* **2012**, *28*, 10818.
- [50] A. Nelson, *J. Appl. Cryst.* **2006**, *39*, 273.
- [51] A. R. Rennie, "http://material.fysik.uu.se/Group\_members/adrian/cprof.htm", accessed: August, **2014**.
- [52] I. Berts, G. Fragneto, J. Hilborn, A. Rennie, *Eur. Phys. J. E* **2013**, *36*, 1.
- [53] S. T. Milner, T. A. Witten, M. E. Cates, *Macromolecules* **1989**, *22*, 853.
- [54] W. M. de Vos, F. A. M. Leermakers, *Polymer* **2009**, *50*, 305.
- [55] E. P. K. Currie, M. Wagemaker, M. A. C. Stuart, A. A. van Well, *Physica B* **2000**, *283*, 17.
- [56] S. Youssef, S. Gude, J. O. Rädler, *Integr. Biol.* **2011**, *3*, 1095.



#### A.4 Full text of ref. [4]:

### Neural Stem Cell Spreading on Lipid Based Artificial Cell Surfaces, Characterized by Combined X-ray and Neutron Reflectometry

**Authors:** Martin Huth, Samira Hertrich, Gabor Mezo, Emilia Madarasz, and Bert Nickel

**Abstract:** We developed a bioadhesive coating based on a synthetic peptide-conjugate (AK-cyclo[RGDfC]) which contains multiples of the arginyl-glycyl-aspartic acid (RGD) amino acid sequence. Biotinylated AK-cyclo[RGDfC] is bound to a supported lipid bilayer via a streptavidin interlayer. Layering, hydration and packing of the coating is quantified by X-ray and neutron reflectometry experiments. AK-cyclo[RGDfC] binds to the streptavidin interlayer in a stretched-out on edge configuration. The highly packed configuration with only 12% water content maximizes the number of accessible adhesion sites. Enhanced cell spreading of neural stem cells was observed for AK-cyclo[RGDfC] functionalized bilayers. Due to the large variety of surfaces which can be coated by physisorption of lipid bilayers, this approach is of general interest for the fabrication of biocompatible surfaces.

#### SH contribution:

- Performing the neutron reflectometry measurements
- Analysis of reflectometry data together with MH
- Proofreading the paper



Article

## Neural Stem Cell Spreading on Lipid Based Artificial Cell Surfaces, Characterized by Combined X-ray and Neutron Reflectometry

Martin Huth<sup>1</sup>, Samira Hertrich<sup>1</sup>, Gabor Mezo<sup>2</sup>, Emilia Madarasz<sup>3</sup> and Bert Nickel<sup>1,\*</sup>

<sup>1</sup> Ludwig-Maximilians-Universität, Department für Physik and CeNS, Geschwister-Scholl-Platz 1, 80539 Munich, Germany; E-Mails: m.huth@lmu.de (M.H.); Samira.Hertrich@physik.lmu.de (S.H.)

<sup>2</sup> Research Group of Peptide Chemistry, Hungarian Academy of Science, Eötvös L. University, Pazmany P. stny. 1/A, 1117 Budapest, Hungary; E-Mail: gmezo@elte.hu (G.M.)

<sup>3</sup> Laboratory of Cellular and Developmental Neurobiology, Institute of Experimental Medicine of Hungarian Academy of Science, Szigony u. 43, Budapest, H-1083, Hungary; E-Mail: madarasz.emilia@koki.hu (E.M.)

\* Author to whom correspondence should be addressed; E-Mail: nickel@lmu.de (B.N.); Tel.: +49-89-2180-1460; Fax: +49-89-2180-3281.

Received: 25 October 2010 / Accepted: 9 November 2010 / Published: 22 November 2010

---

**Abstract:** We developed a bioadhesive coating based on a synthetic peptide-conjugate (AK-cyclo[RGDfC]) which contains multiples of the arginyl-glycyl-aspartic acid (RGD) amino acid sequence. Biotinylated AK-cyclo[RGDfC] is bound to a supported lipid bilayer via a streptavidin interlayer. Layering, hydration and packing of the coating is quantified by X-ray and neutron reflectometry experiments. AK-cyclo[RGDfC] binds to the streptavidin interlayer in a stretched-out on edge configuration. The highly packed configuration with only 12% water content maximizes the number of accessible adhesion sites. Enhanced cell spreading of neural stem cells was observed for AK-cyclo[RGDfC] functionalized bilayers. Due to the large variety of surfaces which can be coated by physisorption of lipid bilayers, this approach is of general interest for the fabrication of biocompatible surfaces.

**Keywords:** supported lipid bilayers; biomimetics; bionanotechnology; functional coatings; self-assembly

---

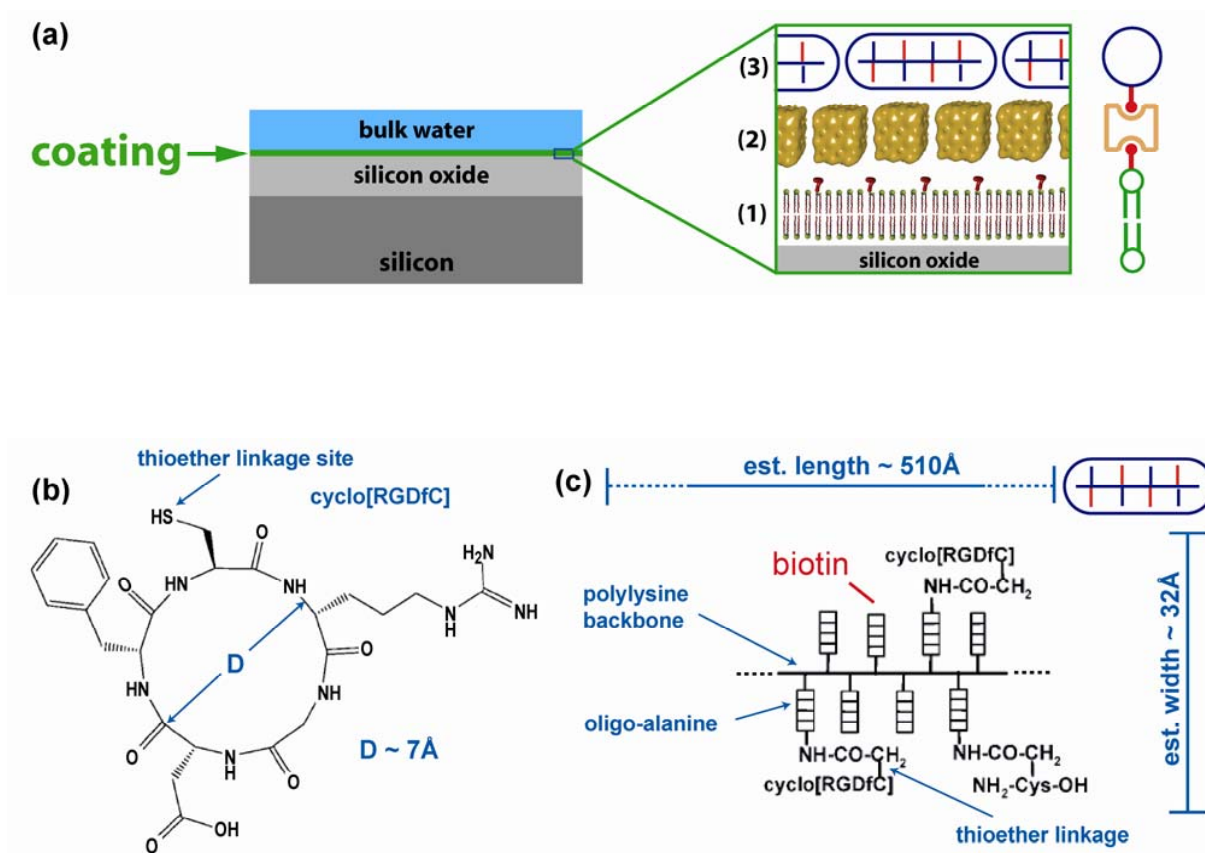
## 1. Introduction

Control of cell attachment on surfaces is a fundamental requirement in biophysical situations where close contact between cells and a technical surface is required, such as in sensing applications or tissue engineering. The natural environment of a cell is composed of extracellular matrix (ECM) and the surfaces of other cells; therefore, an artificial surface coating has to mimic these conditions. Without proper attachment, cells sustain a special apoptotic fate called anoikis [1].

Here, cell attachment is promoted by a synthetic peptide-conjugate AK-cyclo[RGDfC]. AK-cyclo[RGDfC] is a novel, synthetic cell-adhesive peptide [2] comprising a poly-L-lysine backbone with oligo-D/L alanine side chains (AK, see Figure 1c) composed of both D- and L-enantiomers of alanine and carrying the adhesive end-motif cyclo[RGDfC] at the N-termini. As it was shown previously by CD analyses [3,4], the spacer built from raceme alanine residues results in non-structured peptide side-chains with increased sterical flexibility for the adhesive end-motif and improves the solubility of the carrier [5]. As a biologically active, cell adhesive moiety, the cyclo[RGDfC] cyclic pentapeptide (see Figure 1b) was chosen due to the strong affinity of cyclic RGD pentapeptides to selected types of cell surface integrins [6]. The Cys residue provided sites for conjugation and the introduction of a D-enantiomer phenylalanine into the peptide ring was thought to result in a rigid RGD motif [7] easily recognized by  $\alpha_v\beta_3/\alpha_v\beta_5/\alpha_5\beta_1$  integrins known to be present on the surface of a number of neural [8,9] and non-neural stem-like cells [2]. The resulting adhesive peptide conjugate was shown to support adhesion-based selection and serum-free propagation of neural stem cells [10]. This selectivity for adhering neural stem-like cells prompted us to functionalize lipid bilayers with AK-c(RGDfC) rather than peptides carrying linear RGD sequences [11] or laminin-motifs [12]. The cyclic RGD peptide was conjugated to a branched chain polypeptide AK through thioether linkage, which is an efficient tool for the preparation of polypeptide conjugates [13,14]. The RGD sequence is present in many extracellular matrix proteins (fibronectin, vitronectin, tenascin-C, *etc.*). It is responsible for the binding of ECM proteins to their receptors on cell surfaces. Previous studies of cells grown on AK-cyclo[RGDfC] adsorbed on SiO<sub>2</sub> used biotinylated AK-cyclo[RGDfC] (see Figure 1c and Experimental), which is bound to streptavidin template on a biotinylated lipid bilayer (Figure 1a) [15]. Supported lipid bilayers (SLB) have proven to be an excellent experimental platform [16] to mimic functions of cell membranes. Since bare phospholipid bilayers are resistant to cell attachment in the first place, they are very well suited to study the amplification of cell attachment by functionalization with an adhesion promoter [12]. Using microscopy techniques, diffusion and protein binding can be studied [17]. For the characterization of the composition and layering of native or artificial membranes, a variety of surface techniques are available [18]. Structural properties can be accessed using reflection techniques [19-21]. Recently, X-ray experiments have revealed the structure of biotinylated phospholipid bilayers [15] decorated with streptavidin. This two-dimensional lipid-protein template is of special interest because of its biotin-binding properties, since biotin (vitamin B6, a cofactor of many enzymes) can be covalently bound to many proteins. The possibility to coat various surfaces with SLB [15,22-26] by physisorption, *i.e.*, without the need for surface chemistry, is a strong point of this concept. Phospholipid membranes exist in different conformations, *i.e.*, as monolayer, bilayer [22], and on some substrates as interdigitated bilayers [23]. Proteins can be embedded into the membrane or associated

externally [15,27]. Note that SLBs can also be patterned by surface treatments [28-30], stamping [31] and optical post procession [32]. Dynamic patterning of SLB has been achieved using surface acoustic waves [33]. A sensor array coated with lipid bilayers was recently envisioned by Kumar *et al.* [34] and patterned attachment of human epithelial cells to SLB as a function of lipid composition was recently reported by Oliver *et al.* [35]. Here we study neural stem cell attaching to a synthetic cell surface based on a trilayer structure of adhesion protein, streptavidin interlayer and lipid bilayer. The nanostructure of this bioselective surface was investigated with X-ray and neutron diffraction experiments.

**Figure 1.** Schematics. (a) Sample structure. The lipid bilayer containing 2% of biotinylated lipids (1) is covered by a layer of streptavidin (2) which is bound to the lipid membrane by biotin anchors. A biotinylated adhesion peptide (AK-cyclo[RGDfC]) is bound on top of the streptavidin layer (3); (b) Chemical structure of the cyclic RGD-containing binding residue; (c) Architecture of the adhesion peptide. (b) and (c) are adapted from [2].



## 2. Results

### 2.1. Coating structure and arrangement

The structural analysis combines X-ray and neutron reflectometry. The resolution  $\sigma[\text{Å}]$  in a reflectometry experiment can be estimated by  $\pi/q_z$  and is therefore limited by the maximum momentum transfer  $q_z$  that still yields a reflectometry signal. The momentum transfer  $q_z$  is given by  $q_z = 4\pi/\lambda \cdot \sin(2\theta/2)$ . Here,  $2\theta$  is the diffraction angle and  $\lambda$  is the wavelength. For X-ray, we achieve a

$q_z = 0.7 \text{ \AA}^{-1}$  (Figure 2a), thus the internal structure of the layers can be determined with a resolution of  $\sigma = 5 \text{ \AA}$ . The intrinsic weak scattering contrast of proteins and water for X-rays can be improved using neutron beams [36]. For neutrons, the scattering length density (sld) of the solvent can be adjusted from  $-0.5 \cdot 10^{-6} \text{ \AA}^{-2}$  [100% H<sub>2</sub>O] [37] to  $6.36 \cdot 10^{-6} \text{ \AA}^{-2}$  [100% D<sub>2</sub>O] [37] by using a mixture of water and heavy water. The sld of biomolecules are typically in between. The total sld of a layer is a combination of the sld of the molecules in the layer and the sld from hydration water. Thus, measuring in two different water mixtures allows separating the molecular density and layer hydration:

$$sld[\text{layer}] = (1 - h) \cdot sld[\text{molecule}] + h \cdot sld[D_2O / (H_2O + D_2O)] \quad (1)$$

Here  $h$  is the hydration of a layer in [%]. Therefore, in addition to the X-ray reflectometry experiment, we performed neutron reflectometry measurements in two different contrasts. One measurement was performed in 100% D<sub>2</sub>O [D<sub>2</sub>O], and one using a mixture which was contrast matched to the sld of SiO<sub>2</sub> [57% D<sub>2</sub>O + 43% H<sub>2</sub>O, *cm*] (Figure 2). The value for the sld of the contrast matched medium was allowed to change between  $3.3 \cdot 10^{-6} \text{ \AA}^{-2}$  and  $4 \cdot 10^{-6} \text{ \AA}^{-2}$  to allow for small deviations in the mixing ratio in case that the previous medium might not have been exchanged completely. The fit yielded for the mixture a sld value of  $3.9 \cdot 10^{-6} \text{ \AA}^{-2}$ , indicating a 7.5% higher D<sub>2</sub>O fraction in the mixture. Combined fitting was performed using the Motofit [38] package in Igor®. A single set of structural parameters reproduces the neutron and X-ray reflectometry data.

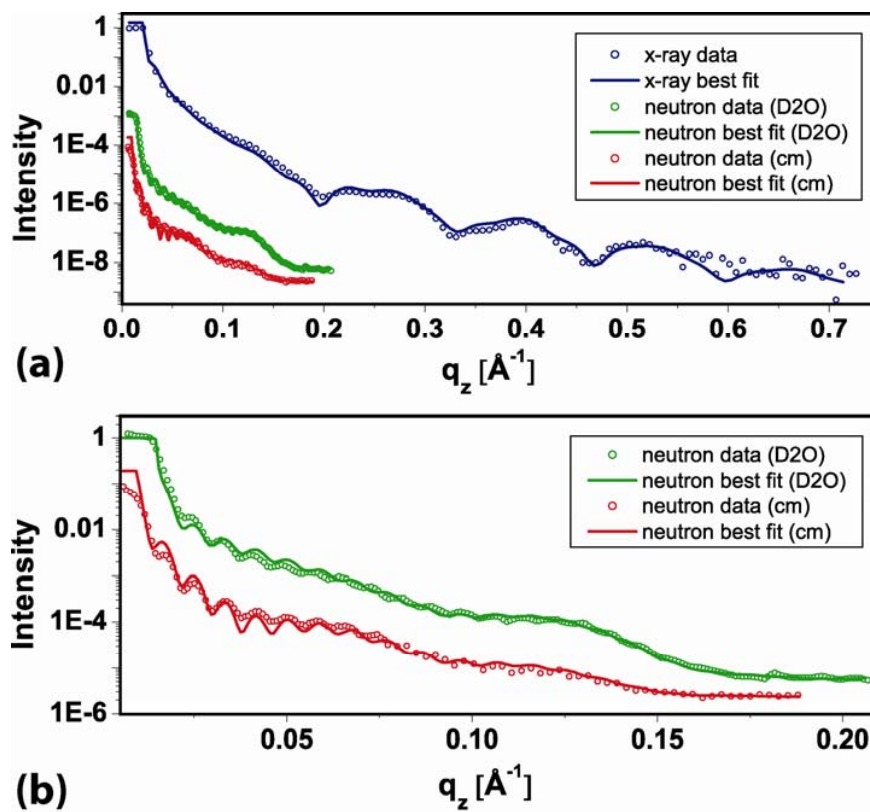
In detail, first the thickness of the layers was determined from the X-ray data. The second step was to evaluate the hydration of the layers from the two neutron measurements. To estimate the hydration level, the molecular slds of lipids and streptavidin have been fixed according to the literature values [37,39] (Table 1). The neutron scattering length density of the AK-cyclo[RGDfC] was also fixed to the value of streptavidin. In an iterative process, the hydration values from the neutron measurements were used to refine the X-ray measurement. The X-ray sld of the AK-cyclo[RGDfC] was allowed to vary by 5% around the sld of streptavidin. The data (open circles) and final best fits (lines) are shown in (Figure 2). The scattering length density profiles are summarized in (Figure 3b). The hydration (Equation 1) of the layered system and a sketch of the constituents are illustrated in (Figure 3a). The parameters of the slab model are summarized in (Table 1).

**Table 1.** Parameters obtained from neutron and X-ray reflectometry data. The values describe the slab model of the sld and hydration profiles depicted in Figure 3.

	Neutron sld [10 <sup>-6</sup> Å <sup>-2</sup> ] [f]	X-ray sld [10 <sup>-6</sup> Å <sup>-2</sup> ] [f]	Thickness [Å]	hydration [%]
lipid heads	1.78	13.8	11	54 (lower) / 63 (upper)
lipid chains	-0.2	8	18	17
hydrated region	6.36 [a] / 3.9 [b]	9.45	26	100
streptavidin	1.2	10.5	38	0
AK-cyclo[RGDfC]	1.2	10.2 [b]	30	12

[a] D<sub>2</sub>O [b] fitted value, see text [f] fixed values

**Figure 2.** Reflectometry data and best fits of the SLB/streptavidin /AK-cyclo[RGD] trilayer in liquid environment (Figure 1a). (a) The reflected intensity is plotted against the momentum transfer  $q_z$ . Intensity scale is logarithmic and normalized to a total reflection signal of 1. The reflectometry data are represented by open symbols, curves represent best fits. The neutron measurements are shown in green [ $D_2O$ ] and red [cm], the X-ray measurement is shown in blue; (b) Expanded view of the neutron data and best fits. Colors and symbols are as in (a).

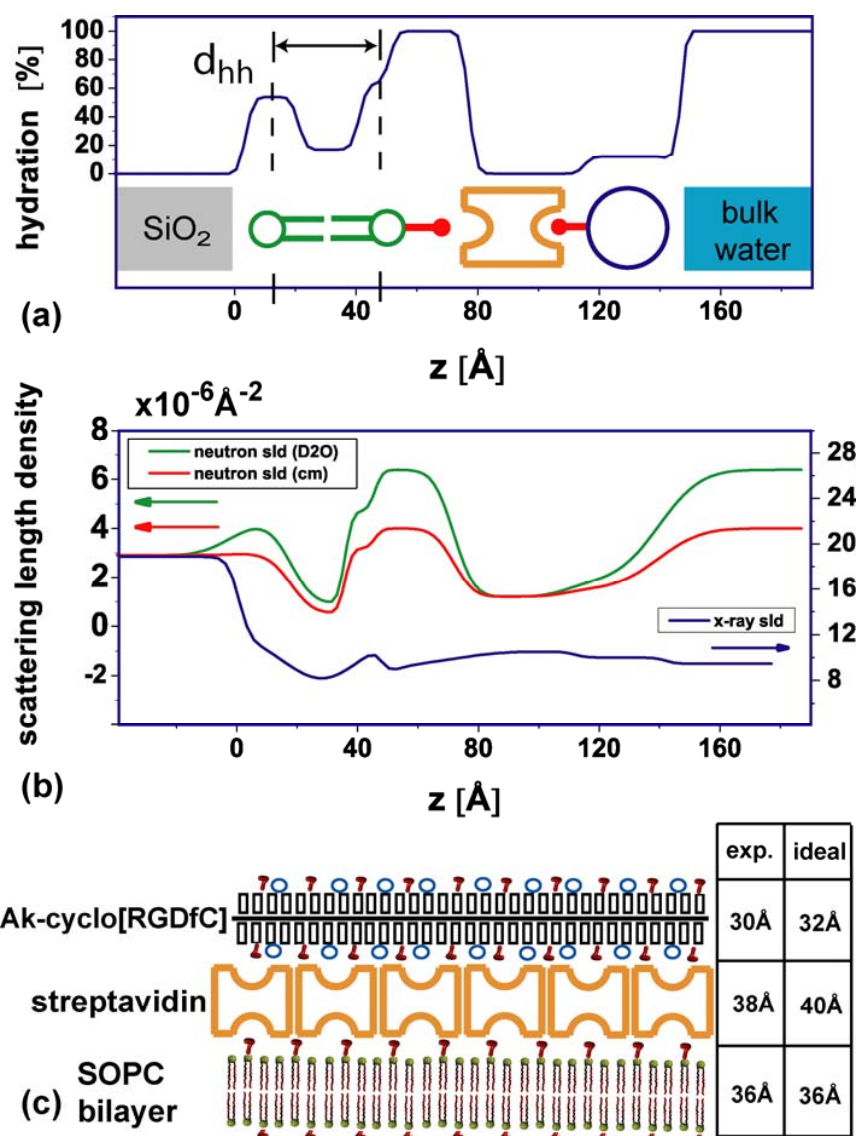


The head to head distance  $d_{hh}$  of the membrane of 36  $\text{\AA}$  (Figure 3a) is in agreement with values previously published [23]. A highly hydrated interlayer of 26  $\text{\AA}$  between the membrane and the streptavidin layer is observed. It contains the biotin anchor of the lipids (2% are biotinylated). Orthorhombic crystals of biotin yielded a unit cell with a long axis of 21  $\text{\AA}$  [40]. Structure determination of crystallized streptavidin-biotin complexes indicates that biotin can extend the dimension of streptavidin by 20% [41] which is in the order of 10  $\text{\AA}$ . The thickness of the close packed streptavidin layer (38  $\text{\AA}$ , no hydration) is in good agreement with the thickness of 40  $\text{\AA}$  found by Horton *et al.* [15].

For the AK-cyclo[RGDfC] layer, we obtain a thickness of 30  $\text{\AA}$  and a water content of 12%. In order to address the packing and configuration of the AK-cyclo[RGDfC] peptide on the streptavidin interlayer, we first estimated the length of the molecule in stretched conformation to 510  $\text{\AA}$  (Figure 1c) by multiplying the length of a lysine compartment (8.5  $\text{\AA}$ ) [42] with the degree of polymerization  $DP_n = 60$  [2]. The width of the molecule is estimated to 32  $\text{\AA}$  by adding the length of two side chains, *i.e.*, twice the sum of oligo-alanine (7  $\text{\AA}$ ), the thioether linkage (2  $\text{\AA}$ ) and the diameter of the

cyclo[RGDfC] compound (7 Å). A schematic of the dimensions is given in Figure 1(c). From the comparison of the observed thickness of 30 Å with the estimated width of 32 Å, and the observation that the hydration of the layer is only 12%, we infer a configuration where the AK-cyclo[RGDfC] molecule is bound in an on edge configuration to the streptavidin surface. This implies an AK-cyclo[RGDfC] packing efficiency of 88%. Because of its length of 510 Å, the AK-cyclo[RGDfC] molecule in on edge configuration binds to several streptavidin molecules. A simplified 2D sketch of the arrangement is shown in Figure 3(c).

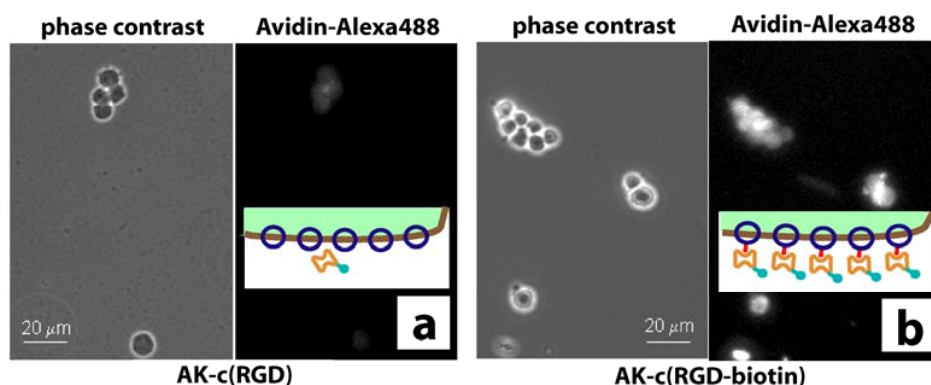
**Figure 3.** Scattering length density and hydration profile. (a) Hydration profile of the layers including a schematic of the layer components.  $d_{hh}$  indicates the head to head distance of the lipid bilayer; (b) Sld profiles of layers. Colored arrows indicate the respective y-axis; (c) Schematic of the synthetic peptide on top of the streptavidin interlayer. Red hooks depict the biotin residues, blue circles indicate the positions of a cyclo(RGDfC) residue. The bilayer-streptavidin interlayer is omitted. The table compares experimental findings and literature values.



## 2.2. Stem cell growth experiments

Neural stem cells carry a high density of integrins able to bind to the cyclo[RGDfC] domain of the synthetic adhesion molecule. In turn, the binding properties of the AK-cyclo[RGDfC] were evaluated by the binding of avidin to biotinylated and not-biotinylated AK-cyclo[RGDfC] (offered as cell surface receptors; Figure 4). Decoration of the stem cells with biotinylated or not-biotinylated AK-cyclo[RGDfC] was verified by subsequent binding of fluorescently labeled avidin to the cells after exposure to AK-cyclo[RGDfC]. In detail, the cells were suspended in artificial liquor solution (ACSF) and were incubated with AK-cyclo[RGDfC] (biotinylated or not-biotinylated) for 30 min at 37 °C, in suspension. After removing the excess peptides by three washes in ACSF, avidin-coupled fluorochrome (Alexa488-Avidin; Molecular Probes) was added to both preparations for 20 min. After rinsing, the binding of avidin to the biotinylated peptide was verified by fluorescence microscopic observations (Figure 4).

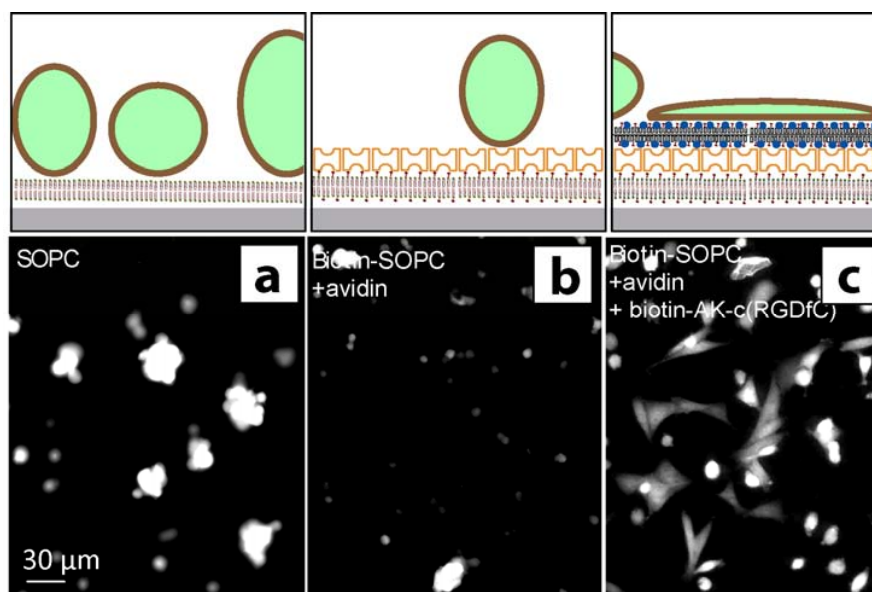
**Figure 4.** Phase-contrast and fluorescence microscopy (FM). (a) Neural stem cells are imaged by phase-contrast microscopy. Cells are first exposed to non-biotinylated AK-cyclo[RGDfC] peptides, and secondly to fluorescently labeled avidin, and finally imaged by FM. (b) Cell exposure to biotinylated AK-cyclo[RGDfC] enhances avidin absorption to cells. The insets illustrate the surface of a cell decorated with AK-cyclo[RGDfC] (shown in blue) or the biotinylated AK-cyclo[RGDfC] (shown in blue with red bars) and the binding to fluorescently labeled avidin (shown in orange, label shown in turquoise).



The spreading of green fluorescent protein (GFP) expressing neural stem cells upon exposure to different surface-coatings was investigated by fluorescence microscopy (Figure 5). For the plain SOPC membrane, a non-spreading, spheroid cell morphology and enhanced formation of cell aggregates indicated poor attachment of the cells to the surface (Figure 5a). Also, the lipid layers functionalized with avidin only did not support the attachment of neural stem cells (Figure 5b). Control experiments using non-biotinylated AK-cyclo[RGDfC], or biotinylated AK-cyclo[RGDfC] without an avidin interlayer, indicated some enhancement of cell attachment. Previous studies showed that AK-cyclo[RGDfC] adsorbs on SiO<sub>2</sub> in loose-packed films [2], therefore we refer this enhancement to unspecific adsorption of AK-cyclo[RGDfC] to membrane defects or bare surface parts. For the

biotinylated AK-cyclo[RGDfC], templated by an avidin-SLB support, improved and rapid spreading of the cells was observed (Figure 5c). The cell morphology indicates cell attachment to the RGD motives.

**Figure 5.** Fluorescence microscopy (FM) images of GFP expressing (fluorescent) radial glial cells. The FM images were recorded 4 h after cell seeding. (a) Radial glial cells attached to SOPC coated surfaces show a spheroid shape; (b) Cell attachment to an avidin functionalized biotinylated membrane is largely suppressed; (c) Rapid spreading of glial cells is observed for the biotin-AK-c[RGDfC] functionalized membrane. Schematics illustrate the conformation of the cells on the surface.



### 3. Discussion

Combining neutron and x-ray reflectometry allowed us to resolve the trilayer structure of the SLB/streptavidin/AK-cyclo[RGDfC] system with a resolution of *ca.* 5 Å. The thickness of the individual layers is within the range expected from the molecular dimensions of the respective layers. In this sense, Figure 3c is a structure model rather than a cartoon. The analysis of the hydration level of the individual layers is a strong point of this approach. The hydration of the lipid bilayer chain part (17%) indicates that the bilayers contain some defects, which may be the origin of the stem cells attaching, but not spreading, to the SLB, cf. Figure 5a. Apparently, the subsequent avidin functionalization closes these defects, since attachment to this layer is largely reduced compared to the bare SLB. Here, the reflectometry measurements indicate a rather tight and homogeneous layer without water, in line with the observation that under these conditions a dense crystalline layer forms [15]. In this context, one should note that contrast variation allows only to measure excess water which can be exchanged by changing the buffer. Furthermore, the water in contact with the lipid headgroups has been separated from the streptavidin layer.

The most interesting finding is the low hydration (12%) and close packing of the cyclo-RGD containing layer, which matches typical values for lipid bilayer chains determined by neutron

reflectometry. This value suggests that the hydrophobic character of the peptide backbone and side chains, in combination with the specific binding to streptavidin and the hydrophilic binding motif exposed to the buffer solution, results in a dense and oriented packing, (see Figure 5c). This could be an advantage compared to e.g., direct binding of the RGD motif to a hydrophilic high energy surface such as SiO<sub>2</sub>. In agreement with high structural homogeneity, we have observed cells spreading on this surface, indicating a proper attachment to the exposed RGD motifs.

#### 4. Experimental Section

Commercially available silicon wafers with a thermally grown oxide layer of 100 nm thickness, purchased from SiMat, Germany, were used as substrates for the X-ray reflectometry and the cell adhesion experiments. The neutron reflectometry measurement was performed using a polished silicon block (10 × 5 × 1 cm) with a 60 nm thermally grown oxide layer. Substrates were cleaned by standard solvents and wet chemistry steps. In detail, wafer pieces were immersed in acetone and isopropanol, followed by sonication in deionized water (DI), followed by an alkaline step (NH<sub>4</sub>OH:H<sub>2</sub>O<sub>2</sub>:DI mixed 1:1:5 at 80 °C, 20 min), an acidic step (HCl:H<sub>2</sub>O<sub>2</sub>:DI mixed 1:1:5 at 80 °C, 15 min), and again the alkaline step. Lipid solutions were produced by mixing SOPC (1-stearoyl-2-oleoyl-sn-glycero-3-phosphocholine) lipids with 0.5 mol% of DHPE (1,2-dihexadecanoyl-sn-glycero-3-phosphoethanolamine) lipids labeled with a fluorescent dye (Oregon Green) and alternatively adding 2 mol% biotin-X-DHPE (N-((6-(biotinoyl)amino)hexanoyl)-DHPE, triethylammonium salt). The lipids were mixed in chloroform and dried with nitrogen. The supported lipid bilayers were produced by spincoating. The appropriate lipid solution was dissolved in isopropanol (1.5 mg/mL) and spincoated on the bare substrate with a BLE delta spincoater, using maximum acceleration and a ramp with 3 sec at 2,000 rpm followed by 60 sec at 3,000 rpm. To minimize solvent residues, the samples were kept in vacuum at room temperature for at least 4 h. Sterile tissue culture plates were used for transport and storage of the samples to prevent bacterial contamination. Mounting of the samples in the microfluidic chamber [43], as well as the change of buffer-solutions or DI water was done in a sterile environment. To form the supported lipid bilayer, the fluidic chamber embedding the lipid coated wafer was filled with deionized water and kept in the dark overnight at ambient temperature. After extensive rinsing, excess lipids in solution and multilayers forming on the surface were removed, using fluorescence microscopy to control. The DI water was first replaced by PBS buffer (pH = 7.4). Then 200 µL of streptavidin (Sigma-Aldrich) dissolved in PBS buffer (40 µg/ml) was injected into the fluidic chamber, which was stored in the dark overnight at ambient temperature. Finally, the Streptavidin solution was replaced by DI water and extensively rinsed. The AK-cyclo[RGDfC] peptide-conjugate was synthesized according to [2] (Research Group of Peptide Chemistry, HAS, Budapest) using the following protocol (see [2, 13,14] for details). The peptides (1 µg/µL) were biotinylated by overnight incubation with SNHS-biotin (2 µg/µL; Sigma) in 1 M phosphate buffer (pH = 7.6). The excess biotin and salts were removed by 24-hour dialyzation (3500 kDa dialyzing membrane; Serva) against distilled water with three fluid changes. After dialyzation, the protein content was determined and the preparation was occasionally concentrated by vacuum dialyzation. Biotinylated AK-cyclo[RGDfC] molecules (10 µg/mL in DI water) were injected into the microfluidic chamber and were let to bind overnight in the dark. After incubation, the chamber was rinsed with DI water to remove excess AK-cyclo[RGDfC]

molecules, which were not bound to the streptavidin layer. Samples were freshly prepared for each experiment.

The X-ray scattering experiments have been carried out at the Hamburger Synchrotronstrahlungslabor (HASYLAB) in Hamburg, Germany (beamline D4). The wavelength was  $\lambda = 0.62 \text{ \AA}$  and measurements on samples representing subsequent steps of the sample preparation series were carried out at different positions of the sample surface to avoid beam damage effects. Neutron experiments were performed at the NREX experiment at the FRM II in Garching, Munich, Germany. The neutron wavelength used was  $\lambda = 4.26 \text{ \AA}$ .

GFP-expressing sub-clone of NE-4C embryonic neuroectodermal stem cells [44] (GFP-4C; ATCC CRL-2926) were propagated on poly-L-lysine coated culture dishes in Minimum Essential Medium (MEM, Sigma, Hungary) supplemented with 5% fetal calf serum, while radial glia-like (RG-1) cells cloned from GFP-expressing fetal mouse forebrain [10] were cultivated on AK-c(RGDfC)-coated dishes in DMEM/F12 (1:1; Sigma Hungary) supplemented with B-27 (Invitrogen, Hungary) and 10 ng/ml EGF. After harvesting by trypsinization, the cells were suspended in artificial cerebrospinal fluid (ACSF). After 20 min recovery at 37 °C in a gas atmosphere containing 5% CO<sub>2</sub>, the cells (at a density of 10<sup>5</sup> cells/mL) were introduced into lipid-coated chambers or were treated with plain or biotinylated AK-cyclo[RGDfC] (0.25 µg/mL) for 30 min, in suspension at mild agitation in a CO<sub>2</sub>-incubator.[44]

#### 4. Conclusions

The combination of x-ray and neutron reflectometry experiments allows quantifying the layered structure of the AK-cyclo[RGDfC]/streptavidin/SLB system in terms of layer thickness, hydration, and packing. AK-cyclo[RGDfC] binds to the streptavidin template in a stretched on edge orientation. The high molecular packing efficiency of 88% provides a dense layer containing the RGD adhesion motive. Neural stem cells readily spread on such surfaces, while the bare SLB does not support the attachment of neural stem-like cells. A large variety of surfaces can be coated by lipid bilayers using physisorption and various techniques for bilayer patterning are available. Using this approach, the preparation of highly effective coatings for stem cells growth on various chemically inert surfaces is possible.

#### Acknowledgements

This work was supported by the EU-STREP 0032352 BIODOT, BMBF 05KN7WMA and by the National Development Program, Hungary BIO\_SURF. The Nanosystems Initiative Munich (NIM) is gratefully acknowledged.

#### References

1. Howe, A.K.; Aplin, A.E.; Juliano, R.L. Anchorage-dependent ERK signaling—mechanisms and consequences. *Curr. Opin. Genet. Dev.* **2002**, *12*, 30-35.

2. Marko, K.; Ligeti, M.; Mezo, G.; Mihala, N.; Kutnyanszky, E.; Kiss, E.; Hudecz, F.; Madarasz, E. A novel synthetic peptide polymer with cyclic RGD motifs supports serum-free attachment of anchorage-dependent cells. *Bioconjugate Chem.* **2008**, *19*, 1757-1766.
3. Votavova, H.; Hudecz, F.; Kajtar, J.; Szekerke, M.; Sponar, J.; Blaha, K. Conformation of Branched Polypeptides Based On Poly(L-Lysine)—Circular-Dichroism Study. *Collect. Czech. Chem. Commun.* **1980**, *45*, 941-949.
4. Mezo, G.; Hudecz, F.; Kajtar, J.; Szekerke, M. Synthesis and Chiroptical Properties of Model Peptides Suitable for The Immunological Characterization of Branched Polypeptides With The General Formula Poly[Lys (Xi-Dl-Alam)]. *Acta Chim. Hung.* **1990**, *127*, 803-812.
5. Szokan, G.; Mezo, G.; Hudecz, F.; Majer, Z.; Schon, I.; Nyeki, O.; Szirtes, T.; Dolling, R. Racemization Analyses of Peptides and Amino-Acid Derivatives by Chromatography With Pre-Column Derivatization. *J. Liq. Chromatogr.* **1989**, *12*, 2855-2875.
6. Aumailley, M.; Gurrath, M.; Muller, G.; Calvete, J.; Timpl, R.; Kessler, H. Arg-Gly-Asp Constrained Within Cyclic Pentapeptides—Strong and Selective Inhibitors of Cell-Adhesion To Vitronectin and Laminin Fragment-P1. *FEBS Lett.* **1991**, *291*, 50-54.
7. Pfaff, M.; Tangemann, K.; Muller, B.; Gurrath, M.; Muller, G.; Kessler, H.; Timpl, R.; Engel, J. Selective Recognition of Cyclic Rgd Peptides of Nmr Defined Conformation by Alpha-Ii-Beta-3, Alpha-V-Beta-3, And Alpha-5-Beta-1 Integrins. *J. Biol. Chem.* **1994**, *269*, 20233-20238.
8. Anton, E.S.; Kreidberg, J.A.; Rakic, P. Distinct functions of alpha(3) and alpha(v) integrin receptors in neuronal migration and laminar organization of the cerebral cortex. *Neuron* **1999**, *22*, 277-289.
9. Hirsch, E.; Gullberg, D.; Balzac, F.; Altruda, F.; Silengo, L.; Tarone, G. Alpha(V) Integrin Subunit Is Predominantly Located in Nervous-Tissue and Skeletal-Muscle During Mouse Development. *Dev. Dyn.* **1994**, *201*, 108-120.
10. Marko, K.; Gocza, E.; Apati, A.; Kohidi, T.; Madarasz, E. Synthetic adhesive peptide conjugate supports xeno-free culturing of embryonic and neural stem cells. *Eur. Cell. Mater.* **2010**, *20*, 166.
11. Ananthanarayanan, B.; Little, L.; Schaffer, D.V.; Healy, K.E.; Tirrell, M. Neural stem cell adhesion and proliferation on phospholipid bilayers functionalized with RGD peptides. *Biomaterials* **2010**, *31*, 8706-15.
12. Thid, D.; Holm, K.; Eriksson, P.S.; Ekeroth, J.; Kasemo, B.; Gold, J. Supported phospholipid bilayers as a platform for neural progenitor cell culture. *J. Biomed. Mater. Res. Part A* **2008**, *84A*, 940-953.
13. Mezo, G.; de Oliveira, E.; Krikorian, D.; Fejlbrieff, M.; Jakab, A.; Tsikaris, V.; Sakarellos, C.; Welling-Wester, S.; Andreu, D.; Hudecz, F. Synthesis and comparison of antibody recognition of conjugates containing herpes simplex virus type 1 glycoprotein D epitope VII. *Bioconjugate Chem.* **2003**, *14*, 1260-1269.
14. Manea, M.; Mezo, G.; Hudecz, F.; Przybylski, M. Polypeptide conjugates comprising a beta-amyloid plaque-specific epitope as new vaccine structures against Alzheimer's disease. *Biopolymers* **2004**, *76*, 503-511.
15. Horton, M.R.; Reich, C.; Gast, A.P.; Radler, J.O.; Nickel, B. Structure and dynamics of crystalline protein layers bound to supported lipid bilayers. *Langmuir* **2007**, *23*, 6263-6269.

16. Castellana, E.T.; Cremer, P. S. Solid supported lipid bilayers: From biophysical studies to sensor design. *Surf. Sci. Rep.* **2006**, *61*, 429-444.
17. Faiss, S.; Kastl, K.; Janshoff, A.; Steinem, C. Formation of irreversibly bound annexin A1 protein domains on POPC/POPS solid supported membranes. *Biochim. Biophys. Acta-Biomembr.* **2008**, *1778*, 1601-1610.
18. Lee, C.; Wacklin, H.; Bain, C.D. Changes in molecular composition and packing during lipid membrane reconstitution from phospholipid-surfactant micelles. *Soft Matter* **2009**, *5*, 568-575.
19. Miller, C.E.; Majewski, J.; Watkins, E.B.; Mulder, D.J.; Gog, T.; Kuhl, T.L. Probing the local order of single phospholipid membranes using grazing incidence x-ray diffraction. *Phys. Rev. Lett.* **2008**, *100*, 058103-058107.
20. Watkins, E.B.; Miller, C.E.; Mulder, D.J.; Kuhl, T.L.; Majewski, J. Structure and Orientational Texture of Self-Organizing Lipid Bilayers. *Phys. Rev. Lett.* **2009**, *102*, 238101:1-238101:4.
21. Smith, H.L.; Howland, M.C.; Szmodis, A.W.; Li, Q.J.; Daemen, L.L.; Parikh, A.N.; Majewski, J. Early Stages of Oxidative Stress-Induced Membrane Permeabilization: A Neutron Reflectometry Study. *J. Am. Chem. Soc.* **2009**, *131*, 3631-3638.
22. Wang, S.T.; Fukuto, M.; Yang, L. *In situ* x-ray reflectivity studies on the formation of substrate-supported phospholipid bilayers and monolayers. *Phys. Rev. E* **2008**, *77*, 031909:1-031909:7.
23. Hochrein, M.B.; Reich, C.; Krause, B.; Radler, J.O.; Nickel, B. Structure and mobility of lipid membranes on a thermoplastic substrate. *Langmuir* **2006**, *22*, 538-545.
24. Sackmann, E. Supported membranes: Scientific and practical applications. *Science* **1996**, *271*, 43-48.
25. Burgess, I.; Li, M.; Horswell, S.L.; Szymanski, G.; Lipkowski, J.; Majewski, J.; Satija, S. Electric field-driven transformations of a supported model biological membrane—An electrochemical and neutron reflectivity study. *Biophys. J.* **2004**, *86*, 1763-1776.
26. Ang, P.K.; Loh, K.P.; Wohland, T.; Nesladek, M.; Van Hove, E. Supported Lipid Bilayer on Nanocrystalline Diamond: Dual Optical and Field-Effect Sensor for Membrane Disruption. *Adv. Funct. Mater.* **2009**, *19*, 109-116.
27. Yamazaki, V.; Sirenko, O.; Schafer, R.J.; Groves, J.T. Lipid mobility and molecular binding in fluid lipid membranes. *J. Am. Chem. Soc.* **2005**, *127*, 2826-2827.
28. Parikh, A.N. Membrane-substrate interface: Phospholipid bilayers at chemically and topographically structured surfaces. *Biointerphases* **2008**, *3*, FA22-FA32.
29. Kim, P.; Lee, S.E.; Jung, H.S.; Lee, H.Y.; Kawai, T.; Suh, K.Y. Soft lithographic patterning of supported lipid bilayers onto a surface and inside microfluidic channels. *Lab Chip* **2006**, *6*, 54-59.
30. Groves, J.T.; Ulman, N.; Boxer, S.G. Micropatterning fluid lipid bilayers on solid supports. *Science* **1997**, *275*, 651-653.
31. Hovis, J.S.; Boxer, S.G. Patterning barriers to lateral diffusion in supported lipid bilayer membranes by blotting and stamping. *Langmuir* **2000**, *16*, 894-897.
32. Yu, C.H.; Parikh, A.N.; Groves, J.T. Direct patterning of membrane-derivatized colloids using *in-situ* UV-ozone photolithography. *Adv. Mater.* **2005**, *17*, 1477-1480.
33. Hennig, M.; Neumann, J.; Wixforth, A.; Radler, J.O.; Schneider, M.F. Dynamic patterns in a supported lipid bilayer driven by standing surface acoustic waves. *Lab Chip* **2009**, *9*, 3050-3053.

34. Kumar, K.; Tang, C.S.; Rossetti, F.F.; Textor, M.; Keller, B.; Voros, J.; Reimhult, E. Formation of supported lipid bilayers on indium tin oxide for dynamically- patterned membrane-functionalized microelectrode arrays. *Lab Chip* **2009**, *9*, 718-725.
35. Oliver, A.E.; Ngassam, V.; Dang, P.; Sanii, B.; Wu, H.W.; Yee, C.K.; Yeh, Y.; Parikh, A.N. Cell Attachment Behavior on Solid and Fluid Substrates Exhibiting Spatial Patterns of Physical Properties. *Langmuir* **2009**, *25*, 6992-6996.
36. Smith, H.L.; Hickey, J.; Jablin, M.S.; Trujillo, A.; Freyer, J.P.; Majewski, J. Mouse Fibroblast Cell Adhesion Studied by Neutron Reflectometry. *Biophys. J.* **2010**, *98*, 793-799.
37. Pencer, J.; Mills, T.; Anghel, V.; Krueger, S.; Epanand, R.M.; Katsaras, J. Detection of submicron-sized raft-like domains in membranes by small-angle neutron scattering. *Eur. Phys. J. E* **2005**, *18*, 447-458.
38. Nelson, A. Co-refinement of multiple-contrast neutron/X-ray reflectivity data using MOTOFIT. *J. Appl. Crystallogr.* **2006**, *39*, 273-276.
39. Schmidt, A.; Spinke, J.; Bayerl, T.; Sackmann, E.; Knoll, W. Streptavidin binding to biotinylated lipid layers on solid supports: A neutron reflection and surface plasmon optical study. *Biophys. J.* **1992**, *63*, 1185-1192.
40. Traub, W. Crystal Structure of Biotin. *Nature* **1956**, *178*, 649-650.
41. Weber, P.C.; Ohlendorf, D.H.; Wendoloski, J.J.; Salemme, F.R. Structural Origins of High-Affinity Biotin Binding To Streptavidin. *Science* **1989**, *243*, 85-88.
42. Salunke, D.M.; Vijayan, M. X-Ray Studies On Crystalline Complexes Involving Amino-Acids and Peptides.11. Crystal-Structure of The Amino-Acid Vitamin Complex Lysine Pantothenate. *Biochim. Biophys. Acta* **1984**, *798*, 175-179.
43. Reich, C.; Hochrein, M.B.; Krause, B.; Nickel, B. A microfluidic setup for studies of solid-liquid interfaces using x-ray reflectivity and fluorescence microscopy. *Rev. Sci. Instrum.* **2005**, *76*, 095103:1-095103:7.
44. Schlett, K.; Madarasz, E. Retinoic acid induced neural differentiation in a neuroectodermal cell line immortalized by p53 deficiency. *J. Neurosci. Res.* **1997**, *47*, 405-415.



## A.5 Full text of ref. [5]:

### Photocatalytic Cleavage of Self-Assembled Organic Monolayers by UV-Induced Charge Transfer from GaN Substrates

**Authors:** John Howgate, Sebastian J. Schoell, Marco Hoeb, Wiebke Steins, Barbara Baur, Samira Hertrich, Bert Nickel, Ian D. Sharp, Martin Stutzmann, and Martin Eickhoff

**Abstract:** Charge transfer between GaN and organic self-assembled monolayers is demonstrated. Alignment of charge-transfer levels allows for photocatalytic cleavage of aliphatic chains on the semiconductor surface. By variation of the Fermi level within GaN and by comparison to SiC, it is shown that charge transfer can be suppressed and the stability of molecular monolayers can be enhanced in the absence of the appropriate energetic alignment.

#### SH contribution:

- Assistance for the X-ray reflectivity measurements



# Photocatalytic Cleavage of Self-Assembled Organic Monolayers by UV-Induced Charge Transfer from GaN Substrates

By John Howgate, Sebastian J. Schoell, Marco Hoeb, Wiebke Steins, Barbara Baur, Samira Hertrich, Bert Nickel, Ian D. Sharp, Martin Stutzmann, and Martin Eickhoff\*

Wide-bandgap semiconductors such as gallium nitride (GaN) and silicon carbide (SiC) have received increasing attention as potential components in advanced organic/inorganic hybrid systems. In both of these materials, the Fermi level can be varied over a wide energy range by controlled impurity incorporation. Moreover, they exhibit excellent characteristics for bio-electronic applications; they are categorized as biocompatible,<sup>[1,2]</sup> they have possibilities for bandgap engineering,<sup>[3,4]</sup> and they can be used both for chemical sensors<sup>[5]</sup> and to analyze biochemical systems on their surfaces.<sup>[6]</sup> So far, such semiconductors have largely been used as passive bio-electronic elements.<sup>[6]</sup> However, many organic systems possess energetic levels whose occupations can be altered by direct electronic charge transfer to or from a semiconductor substrate. Detailed understanding of such charge-transfer mechanisms between inorganic semiconductors and organic molecules is of fundamental importance in the emerging field of molecular and biomolecular electronics. Here, we study the impact of illumination on n- and p-type GaN and SiC with covalently bound self-assembled monolayers (SAMs) formed from octadecyltrimethoxysilane (ODTMS). The use of simple aliphatic chains provides a model system for study of charge-transfer processes which can be extended to complex biological and hybrid systems in the future. For n-type GaN we demonstrate the occurrence of low energy photo-induced charge-transfer ionization of the alkyl chains well below the energy normally required for molecular cleavage. By exploiting the large energetic window spanned by the valence and conduction bands of n- and

p-type GaN and SiC, we determine the alignment required to accommodate such a transfer and assess the stability of SAMs in the presence and absence of such photocatalytic states.

There exist various proven routes to covalently immobilize self assembled monolayers on semiconductor surfaces. One of the best studied is the silanization process, in which organosilane molecules react with hydroxyl-terminated surfaces in the presence of water to yield organic monolayers bound over a crosslinked Si–O–Si network.<sup>[7]</sup> Although these reactions are typically performed on thin hydroxyl-terminated silica films on Si, both GaN and SiC surfaces can be readily hydroxyl-activated. The covalent functionalization of both materials with silane monolayers has recently been demonstrated<sup>[8,9]</sup> and has been exploited for applications in enzyme-modified AlGaIn/GaN field-effect transistors.<sup>[6]</sup> In the present work, silanization was performed using ODTMS to create self-assembled monolayers of octadecylsilane (ODS) on OH-terminated n- and p-type GaN as well as n- and p-type 6H-SiC. Although alkyl chain molecules radically decompose when subjected to high energy UV irradiation,<sup>[10]</sup> they remain stable when the wavelength is well below the molecular ionization energy. However, this stability can be compromised if a level is present to accept an ionization charge transferred under lower energy excitation. For the current investigation, filtered light from a low pressure Hg lamp with a wavelength of 254 nm, corresponding to an energy higher than the bandgap of both GaN and 6H-SiC but below the threshold required for direct ionization or generation of ozone, atomic oxygen, and hydroxyl radicals from air,<sup>[11,12]</sup> was used. The effect of UV irradiation, and the resulting UV-generated charge carriers in the substrates, on the structural and chemical properties of self-assembled ODS monolayers is comparatively analyzed using static water contact angle measurements (SWCA), contact potential difference/surface photovoltage (CPD/SPV), attenuated total reflection Fourier transform infrared spectroscopy (ATR-FTIR), X-ray reflectivity (XRR), X-ray photoelectron spectroscopy (XPS), and transient UV desorption spectroscopy (TUVDs). We find that significant and rapid photocatalytic degradation of the organic layer occurs only for the case of n-type GaN, while the monolayers are stable on all other investigated substrates. This demonstrates that the charge-transfer processes between semiconductors and organic systems depend on the positions of the conduction and valence band edges and can be tailored by appropriate choice of the semiconductor Fermi level (i.e., the direction of the surface band bending).

[\*] Prof. M. Eickhoff

I. Physikalisches Institut  
Justus-Liebig-Universität Gießen  
Heinrich-Buff-Ring 16, 35392 Gießen (Germany)  
E-mail: martin.eickhoff@exp1.uni-giessen.de

J. Howgate, S. J. Schoell, M. Hoeb, W. Steins, B. Baur, Dr. I. D. Sharp,  
Prof. M. Stutzmann  
Walter Schottky Institut  
Technische Universität München  
Am Coulombwall 3, 85748 Garching (Germany)

S. Hertrich, Dr. B. Nickel  
Department für Physik und CeNS  
Ludwig Maximilians-Universität  
Geschwister-Scholl-Platz 1, 80539 München (Germany)

DOI: 10.1002/adma.200903756

Primary characterization of the self-assembled alkylsilane monolayers was performed by thermal desorption spectroscopy (TDS) and SWCA measurements. TDS confirmed previous analyses performed on ODS functionalized GaN and SiC: the desorption enthalpies of hydrocarbon fragments leaving the surfaces indicated strong covalent attachment of molecules<sup>[8,9]</sup> and essentially no desorption of physisorbed contaminants was observed after moderate heating. Assessment of the hydrophobicity was carried out both before and after functionalization by SWCA measurements. After hydroxylation, all samples exhibit contact angles of less than  $10^\circ$ . Following ODS functionalization, all contact angles exceeded  $100^\circ$ . In comparison, contact angles of up to  $110^\circ$  have been reported for high quality, dense ODS monolayers on oxidized Si surfaces.<sup>[13]</sup>

Following illumination at 254 nm a substantial reduction of the contact angle, from the initial value of  $>100^\circ$  to a saturation value of  $25^\circ$  after 30 min of illumination, was observed on ODS functionalized n-type GaN, whereas no significant changes were observed on the surfaces of p-type GaN, n- or p-type SiC. The illumination time required for the contact angle reduction on n-type GaN could be accelerated to approximately 1 min by illumination through a water droplet covering the sample surface. Wavelength dependent measurements were performed on n-type GaN, and showed that above bandgap illumination (energies larger than  $\sim 3.4$  eV) is sufficient for the contact angle to saturate at  $\sim 25^\circ$  within the aforementioned timeframe. No significant change of the contact angle was observed upon illumination with sub-bandgap light. We note that the presence of low intensity near-UV light from the laboratory ambient, which contains wavelengths shorter than  $\sim 365$  nm, was enough to slightly degrade the contact angle of n-type GaN, saturating at a value of  $90^\circ$ . For practical reasons, the remaining experiments were performed using laboratory light exposed samples.

The hydrophobic/hydrophilic contrast between as-prepared and illuminated surfaces is highlighted in Figure 1, in which an ODS-modified n-type GaN surface was selectively illuminated at 254 nm through a shadow mask and subsequently subjected to water vapor. The retention of the pattern fidelity after illumination demonstrates the potential utility of UV-induced SAM degradation for selective spatial modification of surface properties.<sup>[14]</sup>

To more specifically understand the process of UV-induced changes in the SWCAs, we studied the impact of irradiation on the chemical and structural properties of the organic films.

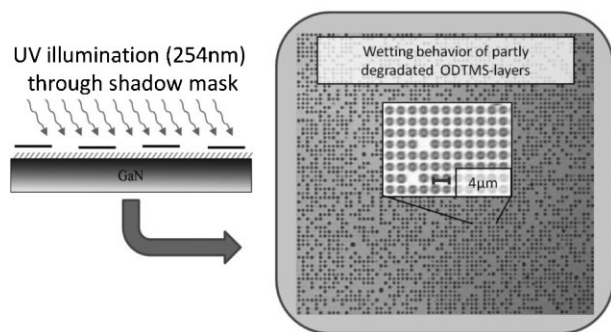


**Figure 1.** UV illumination through a standard shadow mask consisting of  $4 \mu\text{m}$  dots with a pitch of  $3 \mu\text{m}$  produces a hydrophobicity pattern that can be observed by water condensation.

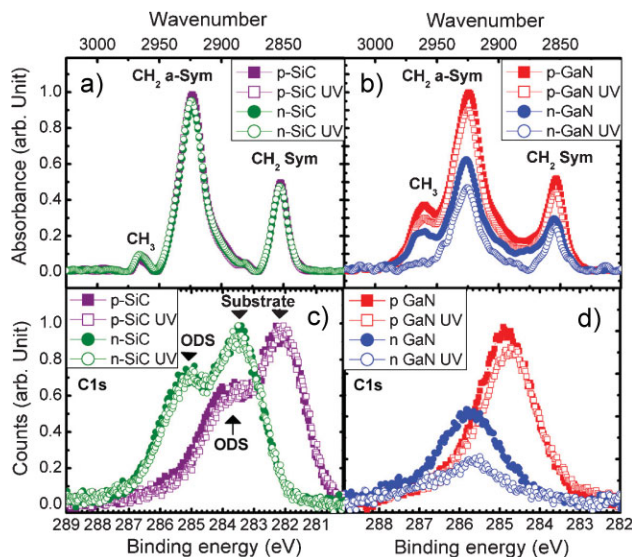


**Figure 2.** ATR-FTIR spectra in the region of hydrocarbon stretching modes from n- and p-type a) SiC and b) GaN before and after UV illumination. XPS spectra of the  $\text{C}_{1\text{s}}$  core level of n- and p-type c) SiC and d) GaN before and after UV irradiation. Both measurement techniques reveal significant degradation of the monolayer following UV illumination for the case of n-type GaN only.

Figure 2a,b show ATR-FTIR spectra from n- and p-type SiC and GaN before and after UV illumination. All of the samples exhibit modes corresponding to symmetric (sym)  $\text{CH}_2$ , anti-symmetric (a-sym)  $\text{CH}_2$ , and anti-symmetric  $\text{CH}_3$  stretching vibrations, as indicated in the figure. The  $\text{CH}_2$  line positions for n- and p-type SiC and p-type GaN samples are red-shifted by  $\sim 2 \text{ cm}^{-1}$  relative to the liquid state, indicating partial ordering of the SAMs, since red-shifts of  $4\text{--}5 \text{ cm}^{-1}$  are typically observed for highly ordered monolayers on Si.<sup>[15]</sup> However, the anti-symmetric and symmetric  $\text{CH}_2$  line positions for monolayers on n-type GaN are not shifted relative to those of liquid alkyl chains, indicating significant disorder within the SAM and in agreement with the relatively low SWCA in ambient light.

Quantitative analysis of the calibrated ATR-FTIR spectral intensities provides a relative measure of the quantities of hydrocarbons remaining on the surfaces after illumination. The largest spectral intensities are observed immediately after functionalization of n- and p-type SiC and p-type GaN and very little change is observed upon illumination. In contrast, the absorbance of the as-prepared ODS SAM on n-type GaN is significantly reduced relative to that of the p-type sample due to stray ambient near-UV light contamination during sample preparation. Following 254 nm UV illumination, a significant reduction of the total hydrocarbon absorption is observed along with an almost complete disappearance of the  $\text{CH}_3$  vibrational mode from the endgroups of the alkyl chain molecules.

Complementary chemical analysis was performed using XPS. The  $\text{C}_{1\text{s}}$  core level signals originating from the organic SAMs on n- and p-type SiC (Fig. 2c) and p-type GaN (Fig. 2d), are unaffected by UV illumination. In contrast, the non-UV-exposed n-type GaN exhibited a reduced signal intensity due to the ambient light effects described above and the UV-exposed sample exhibited

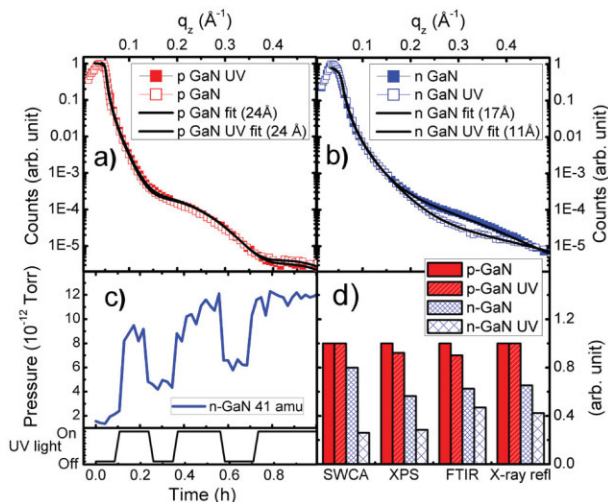


**Figure 3.** X-ray reflectivity spectra of n-type GaN (a) and p-type GaN (b) before and after UV illumination. The obtained fitting parameters for the ODS film thickness are 24, 24, 17, and 11 Å for p-GaN, p-GaN UV, n-GaN, n-GaN UV, respectively. c) TUVDS measurements show the temporal partial pressure mass spectrum (41 amu, corresponding to  $\text{C}_3\text{H}_5$ ) from functionalized n-type GaN along with the on/off times of UV illumination. d) Summary of the normalized changes of SWCA, XPS C 1s core level intensity, ATR-FTIR spectral intensity, and XRR SAM thickness on n- and p-type GaN before and after illumination. Values are normalized to those found on p-type GaN prior to illumination (SWCA:  $101^\circ$ , XRR: 24 Å).

significant additional degradation (Fig. 2d), consistent with the observations from ATR-FTIR measurements. A corresponding increase of the substrate core level intensities is also observed (not shown). We note that, following UV degradation, the  $\text{C}_{1s}$  peak of the n-type GaN sample retains its width despite the significant intensity reduction, indicating that the change is due to hydrocarbons leaving the surface rather than chemical state-induced shifting of the binding energies. The energetic shifts between the n- and p-type samples are due to the changes of the Fermi levels with doping but have reduced magnitudes arising from the oppositely directed surface band bending

Since SWCA, XPS and ATR-FTIR show the fundamental stability of n-, p-type SiC and p-type GaN we chose to focus the remaining measurements on a comparison of n- and p-type GaN. Quantification of the monolayer thicknesses on all GaN samples was achieved by XRR measurements (Fig. 3a,b), which showed monolayer thicknesses of 24 Å on p-type samples both before and after illumination, in excellent agreement with the known molecular length.<sup>[16]</sup>

Immediately following preparation, the SAM thickness on n-type GaN was 17 Å and decreased to 11 Å following UV illumination.

Transient measurements of the partial pressures of specific masses under high vacuum during UV illumination of n-type GaN were performed. The temporal evolution of the partial pressure mass spectrum of the most prominent ODS fragments<sup>[8]</sup> from a functionalized n-type GaN sample upon exposure to UV illumination were recorded; for one of those (41 amu, corresponding to  $\text{C}_3\text{H}_5$ ) the result is shown in Figure 3c. We note that, owing to the pronounced sensitivity of the desorption rate on the presence of residual water on the surface, quantitatively reproducible TUVDS data are currently not available. Nevertheless, the modulation in magnitude of the partial pressure is synchronous with that of the UV source and only occurs in the presence of functionalized n-type GaN samples, proving the direct relationship between UV illumination and degradation of the covalently bound organic monolayer. Furthermore, the sensitivity of the measurement to residual water is consistent with the water acceleration effect observed during SWCA measurements. As summarized in Figure 3d, for all samples there exists a strong correlation between the observations from all measurement techniques. Among the four different ODS functionalized samples, only n-type GaN showed a large degradation of the covalently bound SAM layer upon exposure to above bandgap light.

As depicted in Figure 4a,b the surface-bound and cross-linked ODS molecules possess  $\text{CH}_3$  terminal groups. The combined observations of the  $\text{CH}_2$  degradation and almost complete loss of  $\text{CH}_3$  from ATR-FTIR spectra, the approximate halving of the layer thickness from XRR, and the change of the hydrocarbon intensity from XPS, demonstrate that the remaining (fully degraded) organic film is comprised of the remnants of the ODS molecules

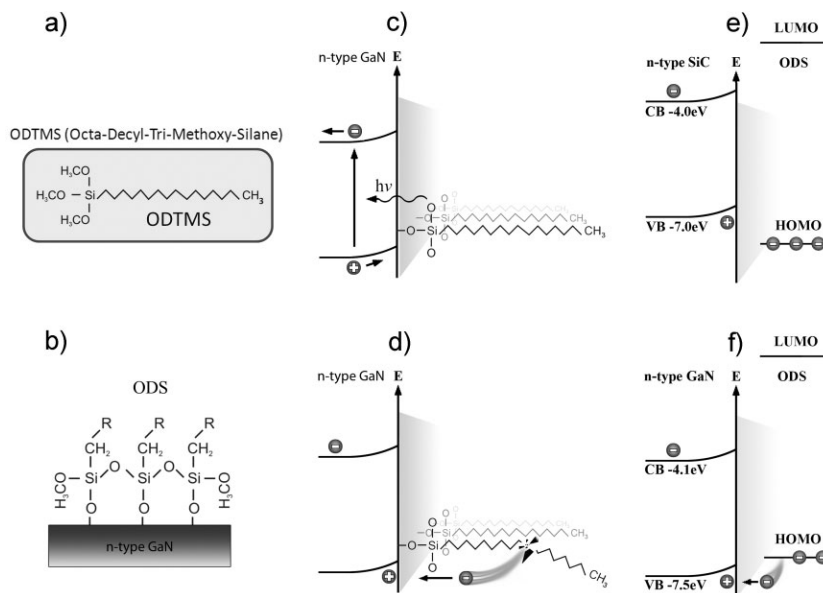


**Figure 4.** a) An ODTMS molecule prior to functionalization. b) The ODTMS is covalently bound to an n-type GaN surface, creating a Si-O-Si network. c) The sample is exposed to above-bandgap light and electron-hole pairs are generated. d) Photo-assisted recombination cleaves the chain of a previously stable molecule. e) n-type SiC band alignment does not allow the transition to take place. f) n-type GaN has the correct band positions to allow the recombination.

after degradation and that UV illumination does not simply reduce the aerial molecular density. Furthermore, the absence of UV-induced degradation on p-type GaN as well as on n- and p-type SiC proves that the observed process is not inherent to the ODS monolayer itself but requires electronic interaction with the underlying substrate material.

Degradation of organic monolayers on solid surfaces under UV illumination has been well studied and widely exploited for patterning of SAMs.<sup>[14]</sup> A range of radiation energies and materials systems have been used. Under UHV conditions, high energy UV illumination originating from HeI and HeII emission introduces defects into monolayers by formation of C=C bonds, but with no pronounced loss of hydrocarbons from the surface.<sup>[17]</sup> Under ambient conditions, vacuum ultraviolet (VUV) radiation at 185 nm (7.2 eV) can be sufficient for generation of highly reactive atomic oxygen or hydroxyl radicals from air which oxidize surface-bound organic molecules.<sup>[11,12]</sup> It has also been demonstrated that VUV radiation is sufficient for ionization or direct cracking of the C–C backbone of molecular monolayers.<sup>[10]</sup> However, the filtered UV source used in the present work, at 254 nm (4.9 eV), intentionally does not have the energy required for either direct generation of oxidizing radicals from air or for direct ionization of aliphatic chains, as evidenced by the stability of monolayers on p-type GaN and n- and p-type SiC. Indeed, we observe that monolayer degradation on n-type GaN occurs under illumination by supra bandgap light with energies as small as 3.4 eV. Degradation of alkanethiol SAMs by near-UV illumination has also been observed and was primarily attributed to photo-oxidation of the thiol headgroup rather than the aliphatic chain;<sup>[18,19]</sup> in the present case the silicate interfacial binding structure is insensitive to similar processes. In the special case of TiO<sub>2</sub>, rapid degradation of SAMs has also been extensively studied and is due to photocatalytic generation of hydroxyl radicals on the surface followed by rapid oxidation of organic monolayers.<sup>[20–22]</sup> However, it has been shown that these radicals are highly mobile on the surface and can yield remote oxidation as far as 20 μm away from the generation site.<sup>[21,22]</sup> As demonstrated in Figure 1 no loss of pattern fidelity is observed following selective illumination through a shadow mask consisting of a dot array with 4 μm feature sizes, proving that an analogous process does not play a significant role in the degradation mechanism.

In light of these observations, we propose a mechanism for photocatalytic degradation of ODS monolayers on n-type GaN based upon charge transfer between the molecular HOMO layer and the semiconductor valence band. Figure 4a–f show schematic diagrams of the ODS molecular binding configuration to the surface of the sample along with the proposed mechanism and corresponding energy level diagrams for n-type 6H-SiC and GaN. CPD/SPV measurements, calibrated using freshly exposed highly oriented pyrolytic graphite (HOPG), reveal the surface valence band positions of GaN and 6H-SiC to be at –7.5 and –7.0 eV below the vacuum level, respectively. The upward surface band bending of n-type GaN and 6H-SiC, which is measured by SPV to be in the range of 0.4–0.5 eV for both materials, results in hole drift to the surface under UV illumination. The GaN valence band position, at –7.5 eV, is much lower than that of 6H-SiC, at –7.0 eV, and is in close alignment with reported values for alkyl chain HOMO levels.<sup>[23,24]</sup> This energetic alignment allows for UV-assisted electron transfer from the alkyl HOMO and

recombination with a surface-accumulated hole in the semiconductor substrate; the loss of a bonding electron from the C–C backbone is analogous to excitation above the ionization energy and causes the molecule to crack or become very reactive, leading to the observed degradation. As a consequence, the energy threshold for this process is reduced to the GaN bandgap energy.<sup>[25]</sup>

It is, however, evident that an alternate model may explain the experimental findings. It has recently been reported that midgap states in n-GaN facilitate water splitting.<sup>[26]</sup> Although a dominant role of these states in the UV-induced charge transfer is considered unlikely due to their comparably low concentration, the acceleration of the degradation process in the presence of water could indicate an indirect involvement that catalyzes the UV-induced degradation.<sup>[27]</sup> The proposed degradation mechanism describes the charge-transfer-induced destabilization of SAMs on n-type GaN; subsequent oxidation of this reactive intermediate state under ambient conditions is reasonable to expect and may be accelerated in the presence of water. A detailed description of such a multistep reaction is beyond the scope of the present work and further experiments will be required to determine the specific contribution of water to the suggested reaction mechanism.

In this work, we have demonstrated UV-induced photocatalytic cleavage of ODS SAMs covalently bound to n-type GaN surfaces and we have identified an energetic window for charge transfer between an organic SAM and an inorganic semiconductor substrate. For the case of aliphatic molecules, such charge transfer leads to photocatalytic degradation of the layer due to removal of bonding orbital electrons. We have proposed a model by which UV illumination of n-type GaN leads to surface accumulation of holes at an energetically favorable position for recombination with an electron abstracted from the HOMO of ODS. Furthermore, we have shown that either an upward shift of the valence band maximum (as is the case for n-type 6H-SiC) or an opposite direction of surface band bending (p-type GaN) leads to a suppression of the charge transfer. This work demonstrates that the charge transfer can significantly reduce the ionization energy threshold for the removal of bonding orbital electrons from organic SAMs. The demonstrated charge transfer and identification of the energetic window within which it is favorable, could allow a selection of organic systems to be actively charged or discharged by direct interaction with the semiconductor substrate. Understanding such charge-transfer phenomena will be vital in the emerging fields of molecular and biomolecular electronics. Furthermore, the demonstrated photocatalytic reduction of molecular ionization levels could be exploited for driving chemical reactions on surfaces.

## Experimental

**Samples:** The GaN samples used were (0001) oriented, 3.5 μm thin films grown by metal organic chemical vapor deposition (MOCVD) on 330 μm thick sapphire substrates (Lumilog, Vallauris, France). The films were silicon-doped with a net carrier concentration of  $n \sim 10^{18} \text{ cm}^{-3}$ . The p-type GaN samples were also grown by MOCVD (TopGaN, Warsaw, Poland) on sapphire substrates and consisted of the following film stack: 1.5 μm undoped GaN, 1.5 μm silicon-doped GaN, 0.5 μm magnesium doped GaN, and 10 nm of adjusted magnesium doped GaN to  $p \sim 10^{18} \text{ cm}^{-3}$ .

The SiC samples used were cut from 350 μm thick single-crystalline, (0001) oriented 6H-SiC wafers. The n-type wafer was nitrogen doped with  $n \sim 10^{18} \text{ cm}^{-3}$  (CrysTec GmbH, Berlin, Germany) and the p-type wafer was

aluminum doped with  $p \sim 10^{18} \text{ cm}^{-3}$  (Cree, Inc. Durham, NC, USA). Prior to use, all SiC wafers were polished to a surface rms roughness of  $\sim 0.3 \text{ nm}$  (NovaSiC, Le Bourget du Lac Cedex, France).

**Sample Preparation:** All samples were prepared according to a standard procedure consisting of room temperature ultrasonic (US) cleaning in DI water (18 M $\Omega$ /cm, Millipore), acetone, and isopropanol room temperature for 10 min each. OH-terminated GaN was achieved by treating the sample for 10 min in hot 3:1 H<sub>2</sub>SO<sub>4</sub>:H<sub>2</sub>O<sub>2</sub> followed by 10 min in an oxygen plasma at 200 W. Confirmation of this process was accomplished by XPS analysis and SWCA, not shown here.

OH-terminated SiC was achieved by 5 min oxygen plasma treatment followed by etching for 5 min in 5% HF, and then repeating the process. This has previously been reported to lead to surface hydroxylation [28–30] and was confirmed by XPS, FTIR and SWCA.

Formation of self-assembled ODS layers on OH-terminated surfaces was performed according to a method presented elsewhere [8,9]. The hydroxylated samples were immersed in a solution of 5% ODTMS in toluene with 0.5% butylamine as catalyst for 150 min at 14 °C, followed by US in toluene and methanol in order to remove any physisorbed molecules.

All samples in a series were treated simultaneously, therefore they were all functionalized under identical conditions. The sample series could often not be measured simultaneously. Several series of the same experiment were, therefore, always performed, each time in a different order.

**Instruments:** Plasma oxidation was performed using a Technics Plasma 100-E, operated at 200 W with an oxygen pressure of 1.4 mbar. SWCA measurements were made using a home-built setup with 1.5  $\mu\text{L}$  drops of ultrapure deionized water ( $>18 \text{ M}\Omega \cdot \text{cm}$ , Millipore). Saturation measurements were performed in 5 min intervals of UV exposure with each interval followed by a SWCA measurement. TDS/UVDS measurements were conducted using a custom built high vacuum system (HV) ( $<10^{-7}$  mbar) consisting of a quartz tube, external heating/UV source, and a Hiden analytical RC IV mass spectrometer (MS) system with a Hal 201 detector. Measurements were always performed after an 800 °C bake-out of the quartz tube and 120 °C bake-out of the HV and MS components. XPS data were collected using custom built UHV system ( $2 \times 10^{-10}$  mbar), equipped with Mg and Al K $\alpha$  X-ray sources operated at 5 kV and 5 mA (Specs, Berlin, Germany). The 120 mm radius hemispherical analyzer was operated at constant pass energy (40 eV) with variable retardation voltage. ATR-FTIR was performed using a Bruker Vertex 70 v spectrometer under vacuum and a Pike Technologies MIRAcle ATR-unit equipped with a single reflection Ge ATR crystal. All spectra were background-referenced to the clean ATR crystal measured against vacuum with a resolution of  $3 \text{ cm}^{-1}$  and with 1200 scans for each measurement. Light mechanical pressure was used to obtain good contact between samples and the Ge ATR crystal. X-ray reflectivity measurements were conducted using a custom-built system consisting of a Mo K $\alpha$  x-ray tube (17.4 keV), at standard temperature and pressure. CPD/SPV measurements were performed using an oscillating Kelvin Probe S Au reference electrode (Besocke Delta Phi, Jülich, Germany) accompanied by Kelvin Control 07 electronics. Illumination was achieved using a 250 W Xe lamp through a range of neutral density filters to ensure saturation of the surface photovoltage.

## Acknowledgements

S.J.S., while listed as second author, shares first authorship on this article. We would like to acknowledge O. Weidemann for his support with XPS. We acknowledge the financial support of German Excellence Initiative via the Nanosystems Initiative Munich (NIM) and the Deutsche Forschungsgemeinschaft (DFG, EI 518/5-1). S.J.S. acknowledges a Ph.D. fellowship from Universität Bayern e.V. and support from the Complint graduate school. I.D.S. acknowledges the support of the Technische Universität München – Institute for Advanced Study, funded by the German Excellence Initiative, and the support of the Alexander von Humboldt Foundation.

Received: November 3, 2009

Revised: January 28, 2010

Published online: May 11, 2010

- [1] G. Steinhoff, O. Purrucker, M. Tanaka, M. Stutzmann, M. Eickhoff, *Adv. Funct. Mater.* **2003**, *13*, 841.
- [2] G. Kotzar, M. Freas, P. Abel, A. Fleischman, S. Roy, C. Zorman, J. M. Moran, J. Melzak, *Biomaterials* **2002**, *23*, 2737.
- [3] M. Stutzmann, J. A. Garrido, M. Eickhoff, M. Brandt, *Phys. Status Solidi A* **2006**, *203*, 3424.
- [4] A. Fissel, *Phys. Rep.* **2003**, *379*, 149.
- [5] G. Steinhoff, M. Hermann, W. J. Schaff, L. F. Eastman, M. Stutzmann, M. Eickhoff, *Appl. Phys. Lett.* **2003**, *83*, 177.
- [6] B. Baur, J. Howgate, H. von Ribbeck, Y. Gawlina, V. Bandalo, G. Steinhoff, M. Stutzmann, M. Eickhoff, *Appl. Phys. Lett.* **2006**, *89*, 183901.
- [7] J. P. Cloarec, J. R. Martin, C. Polychronakos, I. Lawrence, M. F. Lawrence, E. Souteyrand, *Sens. Actuators B* **1999**, *58*, 394.
- [8] B. Baur, G. Steinhoff, J. Hernando, O. Purrucker, M. Tanaka, B. Nickel, M. Stutzmann, M. Eickhoff, *Appl. Phys. Lett.* **2005**, *87*, 263901.
- [9] S. J. Schoell, M. Hoeb, I. D. Sharp, W. Steins, M. Eickhoff, M. Stutzmann, M. S. Brandt, *Appl. Phys. Lett.* **2008**, *92*, 153301.
- [10] H. Sugimura, K. Ushiyama, A. Hozumi, O. Takai, *Langmuir* **2000**, *16*, 885.
- [11] T. Ye, D. Wynn, R. Dudek, E. Borguet, *Langmuir* **2001**, *17*, 4497.
- [12] K. L. Norrod, K. L. Rowlen, *J. Am. Chem. Soc.* **1998**, *120*, 2656.
- [13] S. R. Wasserman, Y. T. Tao, G. M. Whitesides, *Langmuir* **1989**, *5*, 1074.
- [14] R. K. Smith, P. A. Lewis, P. S. Weiss, *Prog. Surf. Sci.* **2004**, *75*, 1.
- [15] J. D. Le Grange, J. L. Markham, C. R. Kurkjian, *Langmuir* **1993**, *9*, 1749.
- [16] C. Boulas, J. V. Davidovits, F. Rondelez, D. Vuillaume, *Phys. Rev. Lett.* **1996**, *76*, 4797.
- [17] F. Amy, C. K. Chan, W. Zhao, J. Hyung, M. Ono, T. Sueyoshi, S. Kera, G. Neshet, A. Salomon, L. Segev, O. Seitz, H. Shpaisman, A. Scholl, M. Haering, T. Bocking, D. Cahen, L. Kronik, N. Ueno, E. Umbach, A. Kahn, *J. Phys. Chem. B* **2006**, *110*, 21826.
- [18] N. Ballav, T. Weidner, M. Zharnikov, *J. Phys. Chem. C* **2007**, *111*, 12002.
- [19] N. J. Brewer, S. Janusz, K. Critchley, S. D. Evans, G. J. Leggett, *J. Phys. Chem. B* **2005**, *109*, 11247.
- [20] J. P. Lee, H. K. Kim, C. R. Park, G. Park, H. T. Kwak, S. M. Koo, M. M. Sung, *J. Phys. Chem. B* **2003**, *107*, 8997.
- [21] H. Haick, Y. Paz, *J. Phys. Chem. B* **2001**, *105*, 3045.
- [22] K. Kawahara, Y. Ohko, T. Tatsuma, A. Fujishima, *Phys. Chem. Chem. Phys.* **2003**, *5*, 4764.
- [23] The typical method for determination of the HOMO level, ultraviolet photoelectron spectroscopy, was not used in the present work since rapid UV-induced degradation would yield spurious results [17]. The value was therefore obtained from Ref. [24].
- [24] A. Salomon, T. Boecking, O. Seitz, T. Markus, F. Amy, C. Chan, W. Zhao, D. Cahen, A. Kahn, *Adv. Mater.* **2007**, *19*, 445.
- [25] In contrast, due to the downward band bending in p-type GaN and SiC, UV illumination results in surface accumulation of electrons instead of holes, independent of energetic alignment. In the absence of recombination sites, the molecular monolayers are stable under UV illumination.
- [26] V. Chakrapani, C. Pendyala, K. Kash, A. B. Anderson, M. K. Sunkara, J. C. Angus, *J. Am. Chem. Soc.* **2008**, *130*, 12944.
- [27] For example, the charge transfer dipole would be significantly reduced due to enhanced screening in the presence of water. Referring to the water splitting mechanism suggested in Ref. [26], electron transfer to the oxygen redox level of the adsorbed water film could enhance electronic transitions from shallow donor states to unoccupied defect states and therefore also the flux of holes drifting to the surface. Direct chemical reactions of hydrogen peroxide or non-radical hydroxide, being two of the possible products of water splitting, appears unlikely as these species are not reactive enough to cause chemical cracking of the alkyl chain.
- [28] M. Hollering, J. Bernhardt, J. Schardt, A. Ziegler, R. Graupner, B. Mattern, A. P. J. Stampfl, U. Starke, K. Heinz, L. Ley, *Phys. Rev. B* **1998**, *58*, 4992.
- [29] N. Sieber, T. Seyller, R. Graupner, L. Ley, R. Mikalo, P. Hoffmann, D. R. Batchelor, D. Schmeisser, *Appl. Surf. Sci.* **2001**, *184*, 278.
- [30] U. Starke, C. Bram, P. Steiner, W. Hartner, L. Hammer, K. Heinz, K. Mueller, *Appl. Surf. Sci.* **1995**, *89*, 175.



## A.6 Full text of ref. [6]:

### Aperiodic CrSc multilayer mirrors for attosecond water window pulses

**Authors:** Alexander Guggenmos, Roman Rauhut, Michael Hofstetter, Samira Hertrich, Bert Nickel, Jrgen Schmidt, Eric M. Gullikson, Markus Seibald, Wolfgang Schnick, and Ulf Kleineberg

**Abstract:** Extending single attosecond pulse technology from currently sub-200 eV to the so called "water window" spectral range may enable for the first time the unique investigation of ultrafast electronic processes within the core states of bio-molecules as proteins or other organic materials. Aperiodic multilayer mirrors serve as key components to shape these attosecond pulses with a high degree of freedom and enable tailored short pulse pump-probe experiments. Here, we report on chirped CrSc multilayer mirrors, fabricated by ion beam deposition with sub-angstrom precision, designed for attosecond pulse shaping in the "water window" spectral range.

#### SH contribution:

- Assistance for the X-ray reflectivity measurements



# Aperiodic CrSc multilayer mirrors for attosecond water window pulses

Alexander Guggenmos,<sup>1,2,\*</sup> Roman Rauhut,<sup>1</sup> Michael Hofstetter,<sup>1,2</sup>  
Samira Hertrich,<sup>1</sup> Bert Nickel,<sup>1</sup> Jürgen Schmidt,<sup>1</sup> Eric M. Gullikson,<sup>3</sup> Markus Seibald,<sup>4</sup>  
Wolfgang Schnick,<sup>4</sup> and Ulf Kleineberg<sup>1,2</sup>

<sup>1</sup>Ludwig-Maximilians-Universität München, Fakultät für Physik, Am Coulombwall 1, D-85748 Garching, Germany

<sup>2</sup>Max-Planck-Institut für Quantenoptik, Hans-Kopfermann-Str. 1, D-85748 Garching, Germany

<sup>3</sup>Center for X-Ray Optics, Lawrence Berkeley National Lab 2-400, 1 Cyclotron Road, Berkeley, CA 94720, USA

<sup>4</sup>Ludwig-Maximilians-Universität München, Department Chemie, Butenandtstr. 5-13, D-81377 München, Germany  
[alexander.guggenmos@physik.uni-muenchen.de](mailto:alexander.guggenmos@physik.uni-muenchen.de)

**Abstract:** Extending single attosecond pulse technology from currently sub-200 eV to the so called ‘water window’ spectral range may enable for the first time the unique investigation of ultrafast electronic processes within the core states of bio-molecules as proteins or other organic materials. Aperiodic multilayer mirrors serve as key components to shape these attosecond pulses with a high degree of freedom and enable tailored short pulse pump-probe experiments. Here, we report on chirped CrSc multilayer mirrors, fabricated by ion beam deposition with sub-angstrom precision, designed for attosecond pulse shaping in the ‘water window’ spectral range.

©2013 Optical Society of America

**OCIS codes:** (320.0320) Ultrafast optics; (320.1590) Chirping; (320.5540) Pulse shaping; (340.7480) X-rays, soft x-rays, extreme ultraviolet (EUV); (310.4165) Multilayer design.

---

## References and links

1. M. Hentschel, R. Kienberger, Ch. Spielmann, G. A. Reider, N. Milosevic, T. Brabec, P. Corkum, U. Heinzmann, M. Drescher, and F. Krausz, “Attosecond metrology,” *Nature* **414**(6863), 509–513 (2001).
2. G. Sansone, F. Kelkensberg, J. F. Pérez-Torres, F. Morales, M. F. Kling, W. Siu, O. Ghafur, P. Johnsson, M. Swoboda, E. Benedetti, F. Ferrari, F. Lépine, J. L. Sanz-Vicario, S. Zherebtsov, I. Znakovskaya, A. L’huillier, M. Yu. Ivanov, M. Nisoli, F. Martín, and M. J. J. Vrakking, “Electron localization following attosecond molecular photoionization,” *Nature* **465**(7299), 763–766 (2010).
3. M. Schultze, M. Fiess, N. Karpowicz, J. Gagnon, M. Korbman, M. Hofstetter, S. Neppl, A. L. Cavalieri, Y. Komninos, Th. Mercouris, C. A. Nicolaides, R. Pazourek, S. Nagele, J. Feist, J. Burgdörfer, A. M. Azzeer, R. Ernstorfer, R. Kienberger, U. Kleineberg, E. Goulielmakis, F. Krausz, and V. S. Yakovlev, “Delay in Photoemission,” *Science* **328**(5986), 1658–1662 (2010).
4. S. Neppl, R. Ernstorfer, E. M. Bothschafter, A. L. Cavalieri, D. Menzel, J. V. Barth, F. Krausz, R. Kienberger, and P. Feulner, “Attosecond Time-Resolved Photoemission from Core and Valence States of Magnesium,” *Phys. Rev. Lett.* **109**(8), 087401 (2012).
5. M. Hofstetter, M. Schultze, M. Fieß, B. Dennhardt, A. Guggenmos, J. Gagnon, V. S. Yakovlev, E. Goulielmakis, R. Kienberger, E. M. Gullikson, F. Krausz, and U. Kleineberg, “Attosecond dispersion control by extreme ultraviolet multilayer mirrors,” *Opt. Express* **19**(3), 1767–1776 (2011).
6. M. Suman, G. Monaco, M.-G. Pelizzo, D. L. Windt, and P. Nicolosi, “Realization and characterization of an XUV multilayer coating for attosecond pulses,” *Opt. Express* **17**(10), 7922–7932 (2009).
7. G. Sansone, L. Poletto, and M. Nisoli, “High-energy attosecond light sources,” *Nat. Photonics* **5**(11), 655–663 (2011).
8. E. Goulielmakis, M. Schultze, M. Hofstetter, V. S. Yakovlev, J. Gagnon, M. Uiberacker, A. L. Aquila, E. M. Gullikson, D. T. Attwood, R. Kienberger, F. Krausz, and U. Kleineberg, “Single-cycle nonlinear optics,” *Science* **320**(5883), 1614–1617 (2008).
9. T. Gorniak, R. Heine, A. P. Mancuso, F. Staier, C. Christophis, M. E. Pettitt, A. Sakdinawat, R. Treusch, N. Guerassimova, J. Feldhaus, C. Gutt, G. Grübel, S. Eisebitt, A. Beyer, A. Götzhäuser, E. Weckert, M. Grunze, I. A. Vartanyants, and A. Rosenhahn, “X-ray holographic microscopy with zone plates applied to biological samples in the water window using 3rd harmonic radiation from the free-electron laser FLASH,” *Opt. Express* **19**(12), 11059–11070 (2011).
10. Ch. Spielmann, N. H. Burnett, S. Sartania, R. Koppitsch, M. Schnürer, C. Kan, M. Lenzner, P. Wobrowschek, and F. Krausz, “Generation of Coherent X-rays in the Water Window Using 5-Femtosecond Laser Pulses,” *Science* **278**(5338), 661–664 (1997).

11. N. N. Salashchenko and E. A. Shamov, "Short-period X-ray multilayers based on Cr/Sc," *Opt. Commun.* **134**(1-6), 7–10 (1997).
12. F. Schäfers, "Multilayers for the EUV/soft X-ray range," *Physica B* **283**(1-3), 119–124 (2000).
13. E. M. Gullikson, F. Salmassi, A. L. Aquila, and F. Dollar, "Progress in short period multilayer coatings for water window applications," <http://www.osti.gov/bridge/servlets/purl/932470-1G3P4J/932470.pdf>.
14. Y. Uspenskii, D. Burenkov, T. Hatano, and M. Yamamoto, "Optimal Design of Multilayer Mirrors for Water-Window Microscope Optics," *Opt. Rev.* **14**(1), 64–73 (2007).
15. T. Tsuru, "Reflection Passband Broadening by Aperiodic Designs of EUV/Soft X-ray Multilayers," *AIP Conf. Proc.* **879**, 1524–1530 (2007).
16. F. Bridou, F. Delmotte, Ph. Troussel, and B. Villette, "Design and fabrication of X-ray non-periodic multilayer mirrors: Apodization and shaping of their spectral response," *Nucl. Instrum. Methods* **680**, 69–74 (2012).
17. C. Bourassin-Bouchet, M. Stephens, S. de Rossi, F. Delmotte, and P. Chavel, "Duration of ultrashort pulses in the presence of spatio-temporal coupling," *Opt. Express* **19**(18), 17357–17371 (2011).
18. A. J. Verhoef, A. V. Mitrofanov, X. T. Nguyen, M. Krikunova, S. Fritzsche, N. M. Kabachnik, M. Drescher, and A. Baltuška, "Time-and-energy-resolved measurement of Auger cascades following Kr 3d excitation by attosecond pulses," *New J. Phys.* **13**(11), 113003 (2011).
19. H. Jiang, J. Zhu, J. Xu, X. Wang, Z. Wang, and M. Watanabe, "Determination of layer-thickness variation in periodic multilayer by X-ray reflectivity," *J. Appl. Phys.* **107**(10), 103523 (2010).
20. F. Eriksson, G. A. Johansson, H. M. Hertz, E. M. Gullikson, U. Kreissig, and J. Birch, "14.5% near-normal incidence reflectance of Cr/Sc x-ray multilayer mirrors for the water window," *Opt. Lett.* **28**(24), 2494–2496 (2003).
21. A. V. Tikhonravov, M. K. Trubetskov, and G. W. DeBell, "Optical coating design approaches based on the needle optimization technique," *Appl. Opt.* **46**(5), 704–710 (2007).
22. H. G. Tompkins and E. A. Irene, in *Handbook of ellipsometry*, William Andrew, ed. (Springer Verlag GmbH, 2005).
23. F. A. Jenkins and H. E. White, in *Fundamentals of Optics*, 4th ed. (McGraw-Hill, Inc. 1981).
24. S. A. Yulin, F. Schaefer, T. Feigl, and N. Kaiser, "High-performance Cr/Sc multilayers for the soft X-ray range," *Proc. SPIE* **5193**, 172–176 (2004).
25. E. M. Gullikson, S. Mrowka, and B. B. Kaufmann, "Recent developments in EUV reflectometry at the Advanced Light Source," *Proc. SPIE* **4343**, 363–373 (2001).
26. L. Nénot and P. Croce, "Caractérisation des surfaces par réflexion rasante de rayons X. Application à l'étude du polissage de quelques verres silicates," *Rev. Phys. Appl. (Paris)* **15**(3), 761–779 (1980).
27. B. L. Henke, E. M. Gullikson, and J. C. Davis, "X-ray interactions: photoabsorption, scattering, transmission, and reflection at E=50-30000 eV, Z=1-92," *At. Data Nucl. Data Tables* **54**(2), 181–342 (1993).
28. E. Spiller, in *Soft X-ray optics*, (SPIE Optical Engineering Press, Bellingham, USA, 1994).
29. D. H. Ko, K. T. Kim, J. Park, J.- Lee, and C. H. Nam, "Attosecond chirp compensation over broadband high-order harmonics to generate near transform-limited 63 as pulses," *New J. Phys.* **12**(6), 063008 (2010).
30. A. L. Cavalieri, E. Goulielmakis, B. Horvath, W. Helml, M. Schultze, M. Fieß, V. Pervak, L. Veisz, V. S. Yakovlev, M. Uiberacker, A. Apolonski, F. Krausz, and R. Kienberger, "Intense 1.5-cycle near infrared laser waveforms and their use for the generation of ultra-broadband soft-x-ray harmonic continua," *New J. Phys.* **9**(7), 242 (2007).
31. P. Heissler, R. Hörlein, J. M. Mikhailova, L. Waldecker, P. Tzallas, A. Buck, K. Schmid, C. M. S. Sears, F. Krausz, L. Veisz, M. Zepf, and G. D. Tsakiris, "Few-Cycle Driven Relativistically Oscillating Plasma Mirrors: A Source of Intense Isolated Attosecond Pulses," *Phys. Rev. Lett.* **108**(23), 235003 (2012).
32. A. Borot, A. Malvache, X. Chen, A. Jullien, J.-P. Geindre, P. Audebert, G. Mourou, F. Quéré, and R. Lopez-Martens, "Attosecond control of collective electron motion in plasmas," *Nat. Phys.* **8**(5), 416–421 (2012).
33. J. A. Wheeler, A. Borot, S. Monchocé, H. Vincenti, A. Ricci, A. Malvache, R. Lopez-Martens, and F. Quéré, "Attosecond lighthouses from plasma mirrors," *Nat. Photonics* **6**(12), 829–833 (2012).
34. E. Gustafsson, T. Ruchon, M. Swoboda, T. Remetter, E. Pourtal, R. López-Martens, Ph. Balcou, and A. L'Huillier, "Broadband attosecond pulse shaping," *Opt. Lett.* **32**(11), 1353–1355 (2007).
35. R. Hörlein, Y. Nomura, P. Tzallas, S. G. Rykovanov, B. Dromey, J. Osterhoff, Zs. Major, S. Karsch, L. Veisz, M. Zepf, D. Charalambidis, F. Krausz, and G. D. Tsakiris, "Temporal characterization of attosecond pulses emitted from solid-density plasmas," *New J. Phys.* **12**(4), 043020 (2010).
36. A.-S. Morlens, P. Balcou, P. Zeitoun, C. Valentin, V. Laude, and S. Kazamias, "Compression of attosecond harmonic pulses by extreme-ultraviolet chirped mirrors," *Opt. Lett.* **30**(12), 1554–1556 (2005).
37. G. Sansone, E. Benedetti, F. Calegari, C. Vozzi, L. Avaldi, R. Flammini, L. Poletto, P. Villorosi, C. Altucci, R. Velotta, S. Stagira, S. De Silvestri, and M. Nisoli, "Isolated Single-Cycle Attosecond Pulses," *Science* **314**(5798), 443–446 (2006).
38. V. Yakovlev and G. Tempea, "Optimization of Chirped Mirrors," *Appl. Opt.* **41**(30), 6514–6520 (2002).
39. A. Aquila, F. Salmassi, and E. Gullikson, "Metrologies for the phase characterization of attosecond extreme ultraviolet optics," *Opt. Lett.* **33**(5), 455–457 (2008).
40. C. Bourassin-Bouchet, S. de Rossi, J. Wang, E. Meltchakov, A. Giglia, N. Mahne, S. Nannarone, and F. Delmotte, "Shaping of single-cycle sub-50-attosecond pulses with multilayer mirrors," *New J. Phys.* **14**(2), 023040 (2012).
41. H. G. Muller, "Reconstruction of attosecond harmonic beating by interference of two-photon transitions," *Appl. Phys. B* **74**(9), s17–s21 (2002).

42. R. López-Martens, K. Varjú, P. Johnsson, J. Mauritsson, Y. Mairesse, P. Salières, M. B. Gaarde, K. J. Schafer, A. Persson, S. Svanberg, C.-G. Wahlström, and A. L’huillier, “Amplitude and Phase Control of Attosecond Light Pulses,” *Phys. Rev. Lett.* **94**(3), 033001 (2005).
  43. Y. Mairesse, A. de Bohan, L. J. Frasinski, H. Merdji, L. C. Dinu, P. Monchicourt, P. Breger, M. Kovačev, R. Taïeb, B. Carré, H. G. Muller, P. Agostini, and P. Salières, “Attosecond Synchronization of High-Harmonic Soft X-rays,” *Science* **302**(5650), 1540–1543 (2003).
- 

## 1. Introduction

Multilayer XUV/soft X-ray mirrors are key components for steering attosecond pulses from high harmonic radiation [1]. These pulses pave the way towards the observation of electron dynamics in atoms, molecules or solid surfaces/nanostructures with an unprecedented temporal precision [2–4]. Aperiodic multilayer mirrors exhibit the required degree of freedom for the tailored shaping of attosecond pulses in the XUV/soft X-ray range [5,6]. Extending the current attosecond technology [7] to the so called ‘water window’ spectral range between the carbon 1s (284 eV) and oxygen 1s (543 eV) states may enable not only the generation of ever shorter isolated pulses [8], but could allow to access deeper electron core levels which may facilitate the investigation of electron dynamics in bio-molecules [9,10]. The material combination of chromium (Cr) and scandium (Sc) is the most appropriate choice for multilayer mirrors in the 250-400 eV photon energy range [11,12], where a maximum normal incidence reflectivity up to 32.1% (in the vicinity of the Sc 2p-edge at 398.7 eV) and a typical interface roughness down to 0.32 nm has been realized for periodic small-bandwidth multilayer by magnetron sputtering technique [13]. Up to now broadband aperiodic CrSc multilayer mirrors have been investigated only theoretically for the ‘water window’ [14,15] or have been realized at grazing angles for the keV range [16]. Previous experiments have shown that aperiodic multilayer mirrors can control the attosecond pulse dispersion around 100 eV [5,6,17] being used for resonant excitation of distinct atomic core states [18]. Extending this control, into the ‘water window’ spectral range, requires multilayer optics of sub-angstrom layer precision as their spectral amplitude and phase are extremely sensitive to even the smallest thickness errors of only a fraction of the nominal layer thickness [19] being typically around 1 nm [20]. Here we present one periodic and two aperiodic chirped CrSc multilayer mirrors, designed via numerical algorithms [21], fabricated by ion beam deposition, and characterized by hard- and soft X-ray reflectometry. We show excellent agreement between the simulated reflectivity (based on the ideal multilayer design) and the measured reflectivity, which allows for a retrieval of the experimentally realized multilayer stack structure. By using the measured reflectivity and calculated spectral phase data (derived from the experimental multilayer structure) the temporal response to a chirped single attosecond pulse at ~320 eV has been calculated.

## 2. Ion beam deposition methodology

### 2.1 Deposition procedure of the multilayer

Periodic small bandwidth CrSc multilayer mirrors, as well as aperiodic broadband multilayer mirrors, have been fabricated using a load-locked dual ion beam deposition machine, utilizing (neutralized) 600 eV krypton ions at a background pressure of  $10^{-7}$  Pa, sketched in Fig. 1.

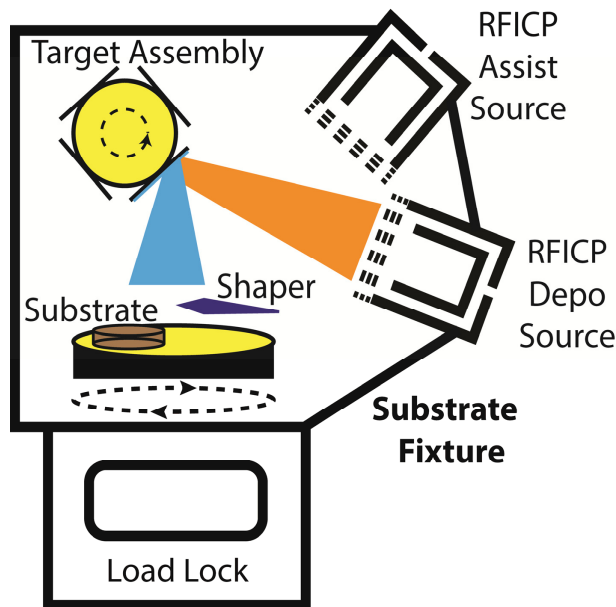


Fig. 1. Schematic setup of the dual ion beam deposition system with load locked sample transfer, four target assemblies, beam shaper and rotating substrate holder.

Each layer thickness has been controlled via its deposition time. Typical sputter rates for both materials are below 0.1 nm per second and have been calibrated using surface profilometry as well as in situ spectral ellipsometry. Sputter time calculations are based on a numerical model, to compensate both for inter-diffusion losses and systematic deposition variations, e.g. shutter response times. The deposition system contains an automatic sample load lock for substrates up to 6 inch, two filament-less radio frequency ion beam sources for target material sputtering (deposition source), as well as ion-assisted deposition (assist source) and four target wheels (400 mm). The substrate holder is spinning during deposition with a spinning frequency of 40 rpm and a R/ $\theta$  shaper is being used for shaping the particle flux laterally for graded multilayer growth or high lateral homogeneity film thickness growth.

### 2.2 Lateral homogeneity and vertical precision

A shaper has been designed to improve the lateral homogeneity as displayed in Fig. 2(a). Deposition rates with and without the shaper have been determined by surface profilometry and XUV reflectivity measurements (comparing the central energy) on a set of molybdenum and silicon (MoSi) multilayer mirrors at various radial positions on the substrate holder. The lateral homogeneity could be improved from about  $\pm 5\%$  to less than  $\pm 0.5\%$  across the full diameter of the substrate holder. For typical 1 inch substrates the maximum homogeneity deviation is less than 0.2%. The shaper is routinely used for the CrSc multilayer deposition results described in the following.

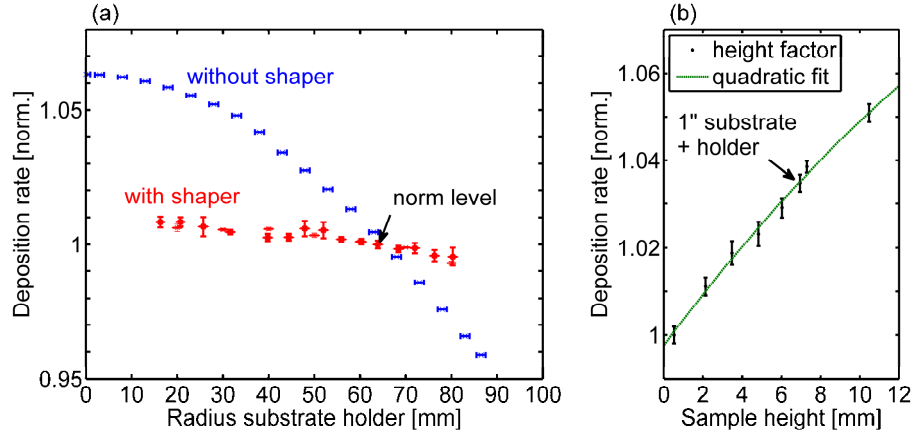


Fig. 2. (a) Lateral (radial) homogeneity of the deposition rates with (red) and without shaper (blue). (b) Rate dependence on the sample height. A quadratic fit coincides quite well with the measured data, since the tapered surface is quadratic dependent on the distance.

Besides lateral homogeneity, the deposition rate depends as well on the sample height and has to be understood and taken into account for a correct mirror design implementation. This pure geometrical dependence can be retrieved analytically from the distance  $D$  between the imaginary target point of divergence and the substrate holder as the tapered surface of the ablated material beam scales quadratic with the distance. The relation of the sputter rate dependent on the sample height reads like:

$$\Gamma = \frac{N}{A \cdot 1s} \Leftrightarrow \frac{\Gamma_2}{\Gamma_1} = \frac{A_1}{A_2} = \left( \frac{d_1}{d_2} \right)^2 = \left( \frac{D-h_1}{D-h_2} \right)^2, \quad (1)$$

where  $\Gamma$  indicates the rate,  $N$  the number of particles,  $A$  the area,  $h$  the sample height and  $d$  is the distance from the sample surface to the extended target focus as imaginary point source (1: reference norm level, 2: various sample heights). The target rates have been calibrated by a lift-off procedure and consecutive surface profilometry. Figure 2(b) shows the measured deposition rate normalized to a  $525 \mu\text{m}$  thick standard silicon wafer. The deposition rate of a standard 1 inch substrate deviates from this silicon wafer by  $\sim 3.5\%$  and would manifest itself in an equal shift in the central energy.

### 3. Multilayer deposition precision

#### 3.1 Study of the top layer oxidation

Detailed analysis of the top layer of a multilayer mirror is essential to correctly model its reflectivity as it influences the superposition of the incident and reflected radiation. Many materials oxidize when being brought to atmosphere, where sputtered material is lost to build the 'natural' oxide layer. We use spectral ellipsometry in situ and ex-situ within a wavelength range of 380-1800 nm to study such oxidation processes [22]. Spectral ellipsometry allows one to retrieve both the optical constants and the layer thicknesses of simple structures from the measured ellipsometry parameters

$$\tan \psi = \left| r_p / r_s \right| \quad \text{and} \quad \Delta = \varphi_p - \varphi_s, \quad (2)$$

where  $r_{p,s}$  are the reflection coefficients and  $\varphi_{p,s}$  indicates the phase of the  $p$  and  $s$  polarization, as a function of the spectral wavelength. An about 8 nm thick single layer of the material (Cr, Sc) was deposited on silicon wafers. The natural  $\text{SiO}_2$ -layer thickness of the wafer was retrieved by ellipsometry before the coating and the grown material thickness was

analyzed directly after the coating process without bringing samples to air. We fitted the measured data with a three layer (Si, SiO<sub>2</sub>, Cr/Sc) model, displayed in Fig. 3.

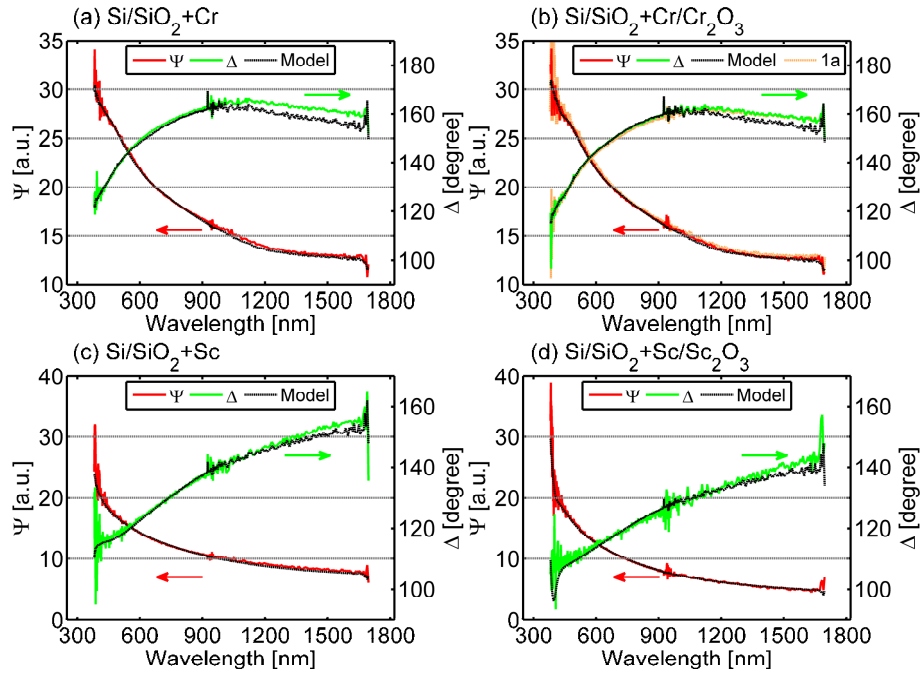


Fig. 3. Ellipsometry parameters psi (red) and delta (green) and the corresponding fitted model (dashed black). Data is taken from samples with pure 8 nm thick layers of (a) chromium and of (c) scandium, and is compared to data measured after 24h oxidation (b) Cr/Cr<sub>2</sub>O<sub>3</sub>, and of (d) Sc/Sc<sub>2</sub>O<sub>3</sub>, respectively. In (b) additional data after one year of oxidation is included, showing no measurable change and indicating that chromium is well suited as passivation layer.

After analysis, the samples have been brought to air for 24 hours, before being analyzed again to study the built up oxide layers and the thickness loss of the material layer from which it is built. The optical constants of chromium and scandium have been measured previously from optically thick bulk samples. The optical constants for chromium oxide were taken from the *Woolam* database whereas scandium oxide was approximated with a Cauchy-layer [23] (with the Cauchy parameters  $A = 1.163$ ,  $B = 0.01493$ ,  $C = 0.0065$ ) since it is impossible to measure the optical constants of such thin dielectric layers directly. As result, we found that a loss of  $0.31 \pm 0.04$  nm of chromium forms a  $1.40 \pm 0.46$  nm thick Cr<sub>2</sub>O<sub>3</sub> layer and  $2.92 \pm 0.29$  nm pure scandium forms a  $6.72 \pm 0.24$  nm thick Sc<sub>2</sub>O<sub>3</sub> layer. This is in full agreement with profilometry which showed a gain of  $1.3 \pm 0.7$  nm for Cr/Cr<sub>2</sub>O<sub>3</sub> and  $3.9 \pm 0.8$  nm for Sc/Sc<sub>2</sub>O<sub>3</sub> compared to a pure 200 nm bulk. Throughout the following chapters reflectivity simulations and designs take into account the built up oxide.

### 3.2 Mirror design implementation

Beside systematic deviations of the sputter machine and analyses of the top layer oxidation, last but not least, detailed knowledge about the interface losses of each distinct material combination is important to ensure a correct simulation and implementation of a multilayer. The interface loss of our CrSc multilayer system has been analyzed in comparative studies of single layer and multilayer stacks using again surface profilometry. Our measurements showed no interface loss for our ion beam sputtered CrSc multilayer system in contrast to magnetron sputtered systems [13].

### 3.3 Characterization by soft/hard X-ray reflectometry

We have evaluated the vertical periodicity accuracy [24] with respect to systematic and random layer thickness deviations inside the CrSc multilayer system, by fabricating a periodic CrSc multilayer mirror with an intended period thickness of  $d = 1.953$  nm and a period number of  $N = 400$  on a Si (100) substrate. The mirror design was chosen according to a near normal incidence (5 degree off normal) peak reflectivity at a photon energy of 320 eV. The total deposition time of this multilayer system was about 5 h. The periodic CrSc multilayer has been analyzed by soft X-ray reflectometry at the reflectometry beamline 6.3.2 at the Advanced Light Source [25]. The results are depicted in Fig. 4(a). Figure 4(b) shows additionally the witness sample, measured now by Mo- $K_{\alpha}$  grazing incidence reflectometry using a laboratory X-ray diffractometer. Both measurements have been evaluated with respect to the period thickness  $d$ , the  $\gamma$ -factor, representing the ratio of the scandium layer thickness to the multilayer period, and the Nevot-Croce [26] interface roughness factor  $\sigma$ . Reflectivity simulations and reflectivity fits have been performed using a self-written multilayer Fresnel code. Throughout this paper, the tabulated values of the atomic scattering factors from Henke and Gullikson [27] for Cr and Sc have been used and bulk layer densities have been assumed.

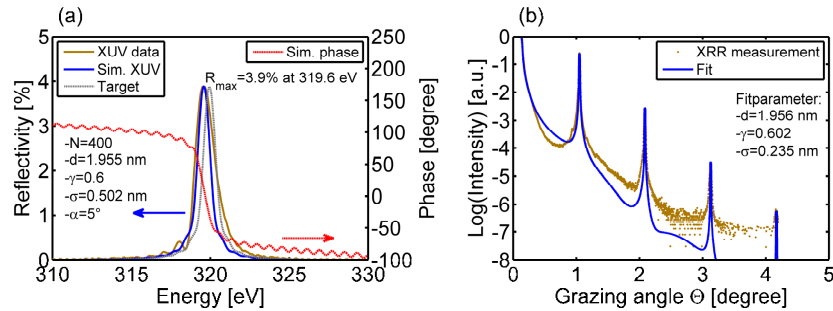


Fig. 4. Characterization of a periodic CrSc multilayer stack, containing 400 periods, by (a) soft X-ray reflectometry and (b) hard X-ray Mo- $K_{\alpha}$  reflectometry. Simulation results are shown for comparison (blue solid lines).

Soft X-ray reflectometry measurement performed at 5 degree off normal reveals a peak photon energy of 319.6 eV and a peak reflectivity of 3.9%. The average period thickness is 1.955 nm and the interface roughness can be estimated to 0.502 nm. The measured reflectivity bandwidth is only slightly larger than expected from the simulation. This indicates a very high vertical periodicity of the deposited multilayer stack with almost negligible random thickness errors. This is confirmed by hard X-ray grazing incidence reflectometry. It reveals a period thickness of 1.956 nm with a multilayer interface roughness of only 0.235 nm, again with very sharp and high contrast Bragg peaks due to the high periodicity of the multilayer stack. While the period thickness and the  $\gamma$ -ratio of both measurements almost perfectly agree, the deviation in the evaluated interface roughness parameter (0.502 nm to 0.235 nm) can be attributed to contamination of the Sc layers. An energy dispersive X-ray spectroscopy measurement indicates  $\sim 13\%$  Cu contamination stemming from the target backing plate, which severely affects the soft X-ray peak reflectivity, while it has only minor influence to the hard X-ray reflectometry measurement. For the aperiodic multilayer results described in chapter 4, we have suppressed the contamination of the Sc layers by mounting a larger Sc sputtering target, which diminishes the spill-out of the ion beam on the backing plate. Furthermore, the different penetration depth of the soft and hard X-ray radiation may reveal different roughness values, because accumulating roughness as well as the interface Power Spectral Density [28] is weighted differently.

### 3.4 Characterization by surface profilometry

As third measurement, the total multilayer stack thickness has been measured by surface profilometry. A set of 24 line scans across different positions of a shadowed deposition edge has been performed. The measured overall thickness together with the mean value and the targeted total stack thickness, based on the calibrated single layer deposition rates of Cr and Sc, is plotted in Fig. 5. The average total stack thickness of 782.959 nm, with a standard deviation of  $SD = 0.703$  nm, differs from the target value (782.3 nm) only by about 0.6 nm (after the deposition of 400 periods).

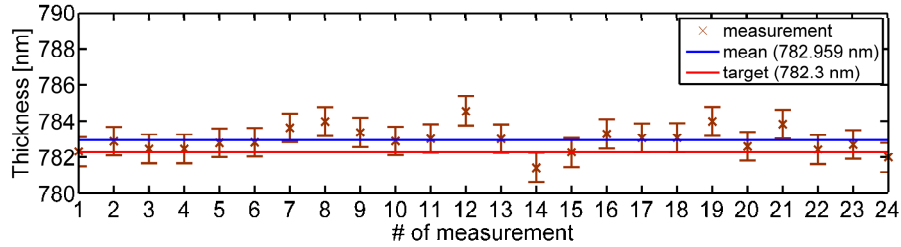


Fig. 5. Total CrSc multilayer stack thickness (same multilayer as in Fig. 4) evaluated from 24 thickness measurements by surface profilometry. Also shown are the mean value and the target stack thickness from calibrated deposition rates.

### 3.5 Comparison of the methods

In summary the retrieved data from different measurement techniques shows a remarkable agreement with the design based on the model in section 3.2, listed in Table 1. The absolute period (layer) deviation is 0.15%. This is the necessary prerequisite for the fabrication of aperiodic chirped multilayer coatings as will be proven in the following. Both the spectral reflectivity amplitude and the phase respond very sensitively to even the smallest layer thickness deviations on an atomic 0.1 nm scale.

**Table 1. Comparison of the evaluated total stack thickness, multilayer period  $d$ , interface roughness  $\sigma$ , thickness ratio  $\gamma$  and the period deviation from the target.**

Method	Total [nm]	$d$ [nm]	$\sigma$ [nm]	$\gamma$	Deviation[%]
Target	782.3	1.953		0.6	
Profilometry	782.959	1.9546			0.08
XRR	783.5	1.956	0.235	0.602	0.15
XUV	783.1	1.955	0.502	0.6	0.10

## 4. Chirped multilayers

Based on the layer accuracy achieved on the periodic CrSc multilayer results, as presented in chapter 3, we have simulated and optimized a set of two different aperiodic broadband CrSc multilayer mirrors aiming for the reflection of single attosecond pulses from the high harmonic plateau in the ‘water window’ spectral range around a photon energy of 326 eV. High Harmonic Generation (HHG) sources producing single isolated attosecond pulses, with pulse durations of 80 as [8] or trains of 63 as pulses [29], are possible based on few cycle intense near-infrared (NIR) laser pulses from carrier envelope phase stabilized Ti:sapphire amplifiers, which are converted into a high harmonic spectrum ranging into the XUV spectral range by non-linear frequency conversion in a rare gas medium (e.g. Ar, Ne, He) [3,30] or solid [31–33]. In the past XUV optics have been used to filter and shape these single attosecond pulses from the almost unmodulated plateau region of the high harmonic spectrum [34,35] and compress these pulses down to its Fourier limit by dispersion correction [36]. While time resolved attosecond experiments have been achieved in the sub 100 eV XUV photon energy range [3,37], very recently, with improved laser sources and multilayer optics,

this time resolution has been extended to the 100-150 eV photon energy range [4]. With ever improving few cycle laser development towards higher pulse energies, this regime will soon be extended into the ‘water window’ soft X-ray spectral range, making new exciting time resolved attosecond experiments on e.g. charge transfer dynamics in bio-molecules possible. Using thin filters for attosecond pulse shaping in this energy regime is limited to fixed opening and absorption edges of the used material and thus restricts the degree of freedom. This leaves multilayer mirrors as the only components for tailor-made spectral filtering and shaping an attosecond ‘water window’ pulse. For that reason, we have developed a chirped aperiodic CrSc multilayer optimized for reflecting sub-70 as pulses from HHG at central photon energy of 326.3 eV (Ar  $L_1$ -edge) with a bandwidth of about 30 eV for future resonant attosecond photo ionization experiments.

#### 4.1 Characteristics of the chirped CrSc multilayer mirrors

The two different aperiodic CrSc multilayer mirrors have been optimized by the thin film program Optilayer, a Fresnel code coupled to a needle optimization algorithm [21,38]. While one multilayer has been designed for introducing an averaged negative chirp (within this paper, the group delay dispersion is the negative second derivative of the spectral phase,  $GDD = -d^2\phi/d\omega^2$ ) of approximately  $-8000 \text{ as}^2$  to compress a possible positive chirp of the high harmonic plateau, a second mirror with similar parameters has been designed to introduce an averaged positive chirp of approximately  $+8000 \text{ as}^2$ . Both mirrors have been designed such that their central energy coincides with the  $L_1$ -edge of Argon (326.3 eV) at an angle of incidence of 45 degree. The optimized stack design for the negatively (a) and positively (b) chirped CrSc multilayer is shown in Fig. 6, each of them containing around 95 individual layers. The design has been chosen according to their robustness of GDD against small layer thickness errors, which will be proven at the end of this section. Typical layer thicknesses are between 1 and 2 nm, with thinnest layers going down to 0.5 nm. For both designs a top layer of 1.4 nm  $\text{Cr}_2\text{O}_3$  out of 0.3 nm Cr has been included in the model. These designs principally prove the large degree of freedom in customizing ‘water window’ attosecond pulses both in space and time using CrSc multilayer mirrors.

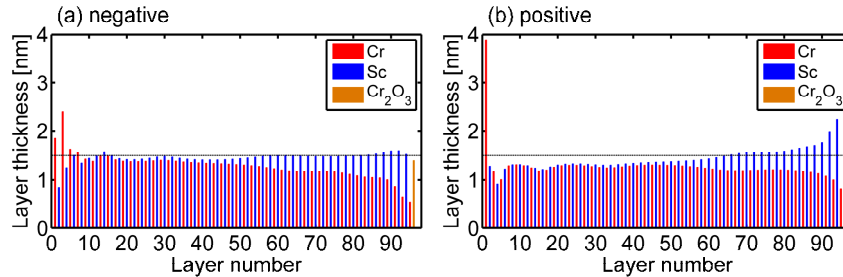


Fig. 6. Multilayer stack designs of the aperiodic CrSc multilayers for the (a) negative and (b) positive chirp. For comparison reasons an arbitrary line with a layer thickness of  $d = 1.5 \text{ nm}$  is depicted (dashed).

After the experimental realization of both designs, we first checked the accuracy by surface profilometry. The total stack height, including the oxide layer, for the negative one was calculated to be 131.2 nm and for the positive one 130.9 nm. Out of the profilometry data we retrieved a measured total stack height of  $(131.4 \pm 0.6) \text{ nm}$  for the negative and  $(131.1 \pm 0.7) \text{ nm}$  for the positive mirror which is in well agreement with the target stack height. The second accuracy check was done by Mo- $K_\alpha$  grazing incidence reflectometry, since this method is well known to be sensitive especially to aperiodic multilayer systems. The measured and fitted data is plotted in Fig. 7.

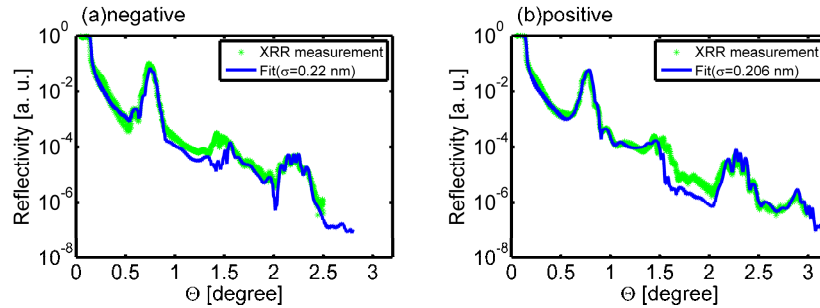


Fig. 7. XRR measurement (green) and the fit (blue) for the negative multilayer mirror in (a) and for the positive one in (b), respectively. The negative mirror has been fitted with a roughness parameter of  $\sigma = 0.22$  nm whereas the positive shows a slightly lower value of  $\sigma = 0.206$  nm. The noise level of the XRR measurement is on the order of approximately  $3.5 \times 10^{-7}$ . Therefore the measurement data for the negative mirror is clipped at around  $\Theta \approx 2.5^\circ$  whereas the positive mirror extends up to  $\Theta \approx 3^\circ$ .

For the fitting procedure, we assumed a perfect implementation of the start design of Fig. 6, thus no thickness errors were included in the fit. The only fitting parameters we have optimized for the agreement with the measurement data were the roughness parameter and the chromium oxide layer thickness (together with the necessary chromium loss) within the error range which has been determined ellipsometrically in section 3.1. Although there are only these fitting parameters allowed, we find a nearly perfect agreement between the simulated aperiodic systems and the XRR measurement. Together with the profilometry data, this is a strong indication of an accurate implementation of the chirped multilayer systems. XUV reflectometry measurements of both chirped multilayer systems are presented and discussed in chapter 4.2.

The introduction of chirp upon reflection can be visualized by standing wave simulations. The electrical field intensity (electrical field squared), normalized to the incoming intensity, has been calculated from the design at the surface and inside both multilayers and is displayed in Fig. 8. It is clearly shown, that the standing wave peak position decreases in photon energy in case of the negatively chirped system shown in Fig. 8(a), while it increases with increasing depth for the positively chirped multilayer in Fig. 8(b). The negatively chirped mirror thus delays the lower energy pulse spectrum with respect to the higher energy pulse spectrum. The second mirror shows the opposite dispersion effect and was designed for comparison.

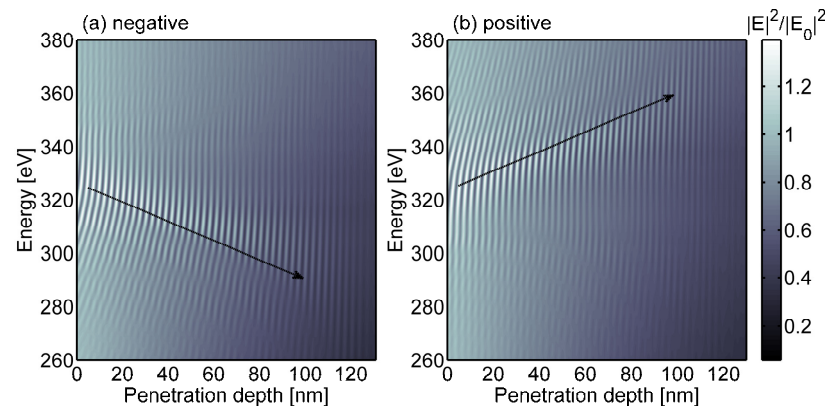


Fig. 8. Calculated field intensity distribution (normalized to incoming intensity) of the standing wave field inside the (a) negatively and (b) positively chirped aperiodic CrSc multilayer. Both multilayer systems have been optimized for an averaged Group Delay Dispersion of approximately  $\pm 8000$   $\text{as}^2$ .

#### 4.2 Soft X-ray reflectometry and layer errors

A comparison of the simulated and measured soft X-ray reflectivity for the negatively and positively chirped multilayer mirror is shown in Fig. 9. The measurements were performed by soft X-ray reflectometry at the beamline 6.3.2 of the Advanced Light Source at an incidence angle of 45 degree [25]. The design simulations were performed using a self-written algorithm and the start designs from Optilayer [21]. An average Nevot-Croce roughness factor of  $\sigma = 0.49$  nm has been retrieved from simulations to account for interfacial imperfections.

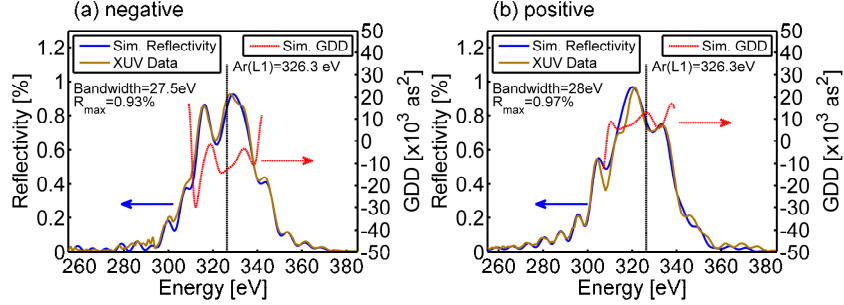


Fig. 9. Soft X-ray reflectivity measurement (brown) and simulation (blue) for the (a) negatively and (b) positively chirped CrSc multilayer together with the corresponding simulated GDD (dashed red).

Both the central energy and the side peaks of the measurements and the designs coincide very well and indicate a nearly perfect experimental implementation of the simulated multilayer stack designs of Fig. 6. Also shown is the calculated evolution of the GDD within the reflectivity bandwidth of both multilayer, indicating an averaged GDD of  $\pm 8000$   $\text{as}^2$ . Both multilayers are very similar in terms of peak energy, spectral bandwidth and peak reflectivity and only differ by the sign of their group delay dispersion. Note that the spectral multilayer phase (and thus the GDD) is not accessible by simple reflectivity measurements. Measurements of the spectral phase in soft X-ray reflectometry have been reported by detecting the standing-wave assisted total electron yield from the multilayer surface as a function of the photon energy around the Bragg peak [39,40]. While this method is very suitable for periodic multilayer systems, its accuracy is limited when applied to aperiodic systems with a weak standing wave. On the other hand one can characterize the spectral phase with two attosecond methods, the RABBITT-technique (Reconstruction of Attosecond harmonic Beating By Interference of Two-photon Transitions) [41,42] or by attosecond photoelectron streaking spectroscopy providing access to a full characterization of the reflected attosecond pulse in amplitude and phase [5,8]. However, for the ‘water window’ spectral range the implementation of both attosecond techniques has not been established yet due to a lack of sufficient photon flux from HHG attosecond sources in this spectral range. Here we analyze and estimate the influence of the layer errors on the reflectivity and the GDD via simulations. The rather perfect match of the designed and the measured reflectivity curves in Fig. 9 proves the correct elimination of systematic deposition errors and leaves only random errors to be analyzed. Here we compare both the simulated reflectivity and the GDD of the original design of the negatively chirped multilayer with that of slightly modified designs. The designs have been chosen randomly by juggling each layer thickness within predefined limits and we have calculated the merit function (MF) of the reflectivity as well as the corresponding averaged GDD value to analyze the quality of reflectivity and GDD simulations:

$$MF = \sqrt{\frac{1}{N} \sum_{i=1}^N (R_{Sim,i} - R_{XUV,i})^2}, \quad (3)$$

where  $N$  is the total number of wavelength sampling with an integer  $i$  representing the position of the sampling equally spaced. 100 designs have been averaged per allowed error and both the reflectivity and the GDD deviations have been calculated. Designs with an overall stack height deviation of more than 0.8% have been left out due to inconsistency with profilometry investigations. From Fig. 10(a) can be deduced, that the average random thickness error is less than 0.5%, corresponding to an average layer thickness error of approximately 0.05 angstrom. Figure 10(b) shows, that the mean GDD value stays nearly constant independently of the layer errors. The upper limit of the layer errors of 0.5% corresponds to a maximum mean GDD error of approximately  $\pm 150 \text{ as}^2$ . To summarize the results, we have a standard deviation of  $\sim 0.024\%$  in the XUV reflectivity and a mean GDD of  $-8090 \pm 150 \text{ as}^2$  for our aperiodic negatively chirped CrSc multilayer mirror.

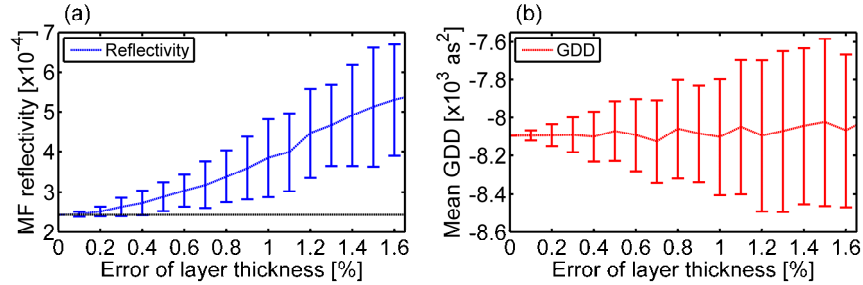


Fig. 10. (a) Merit function for the simulated reflectivity and the XUV measurement for different layer thickness errors. (b) Mean GDD for different layer errors.

#### 4.3 Time domain simulation

An attosecond pulse from the high harmonic plateau regime, with a positive GDD of  $+8000 \text{ as}^2$  in the energy range of the mirror, has been assumed, which is reflected off the negatively chirped mirror. The resulting pulse after reflection is displayed both in the spectral and in the temporal domain in Fig. 11. As a result, the pulse is compressed to a single 69 as pulse with an almost symmetric temporal pulse form and very minor pre and post pulse contributions. The pulse is almost compressed to a Gaussian Fourier limit of 66 as given by the spectral bandwidth of the multilayer of 27.5 eV. Please note, that the assumed positive GDD of  $8000 \text{ as}^2$  of the HHG plateau at 326 eV probably exaggerates the real GDD in the harmonic spectrum in this photon energy range by a factor of four [43]. However, the development, optimization and fabrication of negatively chirped multilayer mirrors with less GDD in the  $-1000 \text{ as}^2$  to  $-2000 \text{ as}^2$  range is even easier to achieve. In this respect, the current results display the high dispersion scenario possible to achieve with a single multilayer reflection.

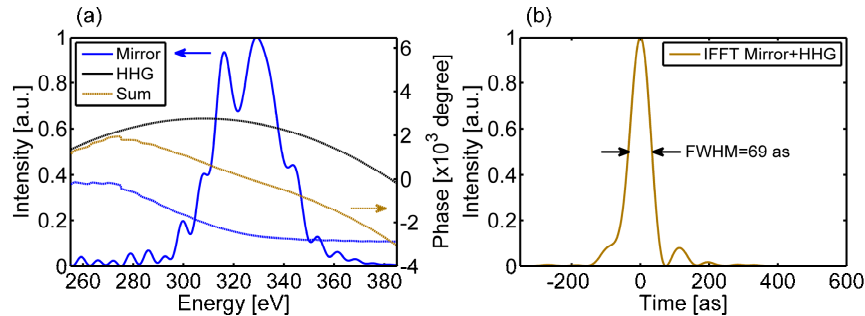


Fig. 11. (a) Intensity of the mirror (blue line) together with the phase for the mirror (dashed blue), HHG (dashed black) and the sum (dashed brown). (b) Simulated temporal pulse response of a positively chirped attosecond pulse from the high harmonic plateau after compression by the negatively chirped CrSc multilayer mirror.

## 5. Conclusion

We have shown the ability to realize multilayer structures by ion beam deposition with sub-angstrom precision, by compensating all systematic errors which arise from the deposition procedure. Based on that, we have realized two chirped CrSc multilayer mirrors for the ‘water window’ photon energy range with an averaged group delay dispersion of approximately  $\pm 8000 \text{ as}^2$ . Such chirped mirrors can be used in the near future to e.g. compress single attosecond pulses from the HHG cutoff region to its Fourier limit below 70 as pulse duration. A good agreement between the targeted and measured reflectivity was found and the desired spectral phase was derived from simulations. Direct temporal attosecond pulse measurements by attosecond electron streaking will be a task for the near future, when HHG sources with sufficient photon flux in the cut-off region, applicable to generate single attosecond pulses, reach up to approximately 350 eV.

## Acknowledgments

We thankfully acknowledge scientific support and valuable discussions by F. Krausz (MPQ, LMU). This work was supported by the DFG Excellence Cluster “Munich-Centre for Advanced Photonics” (MAP).



## A.7 Full text of ref. [7]:

### Influence of ibuprofen on phospholipid membranes

**Authors:** Sebastian Jaksch, Frederik Lipfert, Alexandros Koutsioubas, Stefan Mattauch, Olaf Holderer, Oxana Ivanova, Henrich Frielinghaus, Samira Hertrich, Stefan F. Fischer, and Bert Nickel

**Abstract:** A basic understanding of biological membranes is of paramount importance as these membranes comprise the very building blocks of life itself. Cells depend in their function on a range of properties of the membrane, which are important for the stability and function of the cell, information and nutrient transport, waste disposal, and finally the admission of drugs into the cell and also the deflection of bacteria and viruses. We have investigated the influence of ibuprofen on the structure and dynamics of L- $\alpha$ -phosphatidylcholine (SoyPC) membranes by means of grazing incidence small-angle neutron scattering, neutron reflectometry, and grazing incidence neutron spin echo spectroscopy. From the results of these experiments, we were able to determine that ibuprofen induces a two-step structuring behavior in the SoyPC films, where the structure evolves from the purely lamellar phase for pure SoyPC over a superposition of two hexagonal phases to a purely hexagonal phase at high concentrations. A relaxation, which is visible when no ibuprofen is present in the membrane, vanishes upon addition of ibuprofen. This we attribute to a stiffening of the membrane. This behavior may be instrumental in explaining the toxic behavior of ibuprofen in long-term application.

#### SH contribution:

- Assistance with development of the system
- Assistance for the preliminary X-ray experiments



## Influence of ibuprofen on phospholipid membranes

Sebastian Jaksch,<sup>\*</sup> Frederik Lipfert, Alexandros Koutsioubas, Stefan Mattauch, Olaf Holderer,  
Oxana Ivanova, and Henrich Frielinghaus

*Forschungszentrum Jülich GmbH, JCNS at Heinz Maier-Leibnitz Zentrum, Lichtenbergstraße 1, D-85747 Garching, Germany*

Samira Hertrich, Stefan F. Fischer, and Bert Nickel

*Ludwig-Maximilians-Universität, Department für Physik und CeNS, Geschwister-Scholl-Platz 1, D-80539 München, Germany*

(Received 16 June 2014; revised manuscript received 5 November 2014; published 24 February 2015)

A basic understanding of biological membranes is of paramount importance as these membranes comprise the very building blocks of life itself. Cells depend in their function on a range of properties of the membrane, which are important for the stability and function of the cell, information and nutrient transport, waste disposal, and finally the admission of drugs into the cell and also the deflection of bacteria and viruses. We have investigated the influence of ibuprofen on the structure and dynamics of L- $\alpha$ -phosphatidylcholine (SoyPC) membranes by means of grazing incidence small-angle neutron scattering, neutron reflectometry, and grazing incidence neutron spin echo spectroscopy. From the results of these experiments, we were able to determine that ibuprofen induces a two-step structuring behavior in the SoyPC films, where the structure evolves from the purely lamellar phase for pure SoyPC over a superposition of two hexagonal phases to a purely hexagonal phase at high concentrations. A relaxation, which is visible when no ibuprofen is present in the membrane, vanishes upon addition of ibuprofen. This we attribute to a stiffening of the membrane. This behavior may be instrumental in explaining the toxic behavior of ibuprofen in long-term application.

DOI: [10.1103/PhysRevE.91.022716](https://doi.org/10.1103/PhysRevE.91.022716)

PACS number(s): 87.80.Dj, 61.05.fg

### I. INTRODUCTION

Phospholipid membranes are widely used as model systems for the study of the more complicated biological cell membranes. Via these investigations, information about the structure and behavior of these membranes is gained, which in turn is indispensable in today's medical and biological science. Aeffner *et al.* [1,2] have reported stalk formation in lipid membranes for a variety of phospholipids. In that case, the structural ordering in the membranes was induced by different relative humidities. Another possible way to induce ordering in phospholipid membranes is by electric fields as done by Tronin *et al.* [3]. Here, however, we want to maintain near-physiological conditions while inducing ordering into a lipid membrane. To do so, we use ibuprofen, which is known to decrease the elasticity of phospholipid membranes [4] and is moreover a common nonsteroidal anti-inflammatory (NSAID) drug with a wide range of possible applications, ranging from the treatment of cancer [5], Alzheimer's [6], and inflammations to use as a painkiller. SoyPC is a phospholipid with two hydrocarbon tails that will facilitate the description of the membrane during the data evaluation process, if assumed as a pure hydrocarbon layer.

However, ibuprofen is also reported to be cytotoxic in oral long-term application [7], leading to sometimes-fatal ulcers and other gastrointestinal complications such as stomach bleeding. Investigating the influence of the ibuprofen concentration on structure formation within a phospholipid film may help elucidate the cause of this toxicity. Previous studies found that the increased permeability of the cell membrane and thus the viability of the cell was linked to the NSAID content [8,9].

Studies with chemically similar local anesthetics have been conducted by Malheiros *et al.* [10].

In the present system of ibuprofen and SoyPC, we observe a structural evolution from lamellar over bihexagonal to single hexagonal lattices. A similar hexagonal near-surface structure in soft matter systems has also been reported for  $C_mE_n$  surfactant-water systems [11]. In addition to these structural studies with grazing incidence neutron scattering (GISANS) and neutron reflectometry, we also performed a kinetic study with grazing incidence neutron spin echo spectroscopy (GINSES). With this technique, it is possible to detect kinetics of the film strictly perpendicular to the film surface on the nanometer scale.

### II. EXPERIMENT

#### A. Materials and sample preparation

The SoyPC was obtained in powder form from AvantiLipids (Alabaster/AL, USA), the ibuprofen from Sigma Aldrich (München, Germany), solvent was in all cases isopropanol pA (Roth, Karlsruhe, Germany), and structures are given in Fig. 1. Standard solutions of SoyPC in isopropanol were prepared with a molar ratio of 1.77 mol % between SoyPC and isopropanol. The mixing ratio was chosen in a way to ensure homogeneous mixing and easy handling during the preparation, but it has no discernible impact on the final sample as the sample is dried completely after the preparation. The resulting solutions were stirred for at least 20 min each. Subsequently, the appropriate amounts of ibuprofen were added as given in Table I and stirred again for at least 20 min, which resulted in clear solutions.

The silicon blocks ( $2 \times 5 \times 12$  cm<sup>3</sup>) were prepared for deposition of these solutions by an RCA (Radio Corporation of America) treatment [14] after being cleaned in an ultrasonic

<sup>\*</sup>s.jaksch@fz-juelich.de

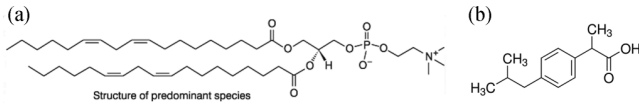


FIG. 1. Structures of (a) SoyPC [12] and (b) ibuprofen [13].

bath until all optical impurities were removed. One side of the blocks was polished to a roughness of less than 5 Å. All solvents were obtained from Roth. The first cleaning bath consisted of 280 mL Millipore filtered and deionized water, 70 mL H<sub>2</sub>O<sub>2</sub> (30%) and 70 mL HCl (37%). Treatment time was 1 h at a temperature of 28 °C. The second bath was 280 mL Millipore filtered and deionized water, 70 mL H<sub>2</sub>O<sub>2</sub> (30%) and 70 mL NH<sub>3</sub> (28%). Treatment time was again 1 h at 33 °C.

After cleaning of the silicon, 12 mL of the prepared solution was deposited on the blocks and dried at room temperature (22 °C) at a pressure of 250 mbar. This pressure had to be maintained, otherwise superheating and bubbling of the film occurred. An o-ring in a custom-made scaffold made sure the solution stayed on top of the silicon block, and the silicon block was adjusted using a spirit level. After 24 h of drying, no remaining isopropanol could be detected either visually or by smell. This resulted in SoyPC layers of macroscopic dimensions (about 2 mm in thickness).

Immediately after preparation, the coated silicon blocks were mounted into the sample cell. The sample cell was then filled with D<sub>2</sub>O (99.8%) and mounted in the respective instrument. In the instruments, the sample cells were kept at 35 °C using a water thermostat. The sample cell allowed for visual inspection after filling and after performing the measurement. During this time, no deterioration of the film coverage on the silicon block was detected.

## B. Sample cell

The sample cell was designed to allow for GISANS, neutron reflectometry, and GINSES consecutively, so the sample could be measured in all experiments in the same sample cell. A sketch of the sample cell is shown in Fig. 2. Neutrons can enter the silicon block at the flat surface on the long side of the block (2 × 5 cm<sup>2</sup>). Due to the low scattering length density (SLD) of silicon, it has a high absorption length, which is of the same order as the length of the block (52.7% transmission at a wavelength of  $\lambda = 7$  Å along the long axis of the block). This geometry allows for a good control of the sample/silicon interface, where the scattering takes place, as opposed to the sample air interface where evaporation or scattering at the cover glass would take place. Also, this setup was designed to achieve a system that is oriented parallel to the surface of the silicon due to the hydrophobicity of the surface. At the same time, neutrons are not unduly blocked by the silicon. Only in

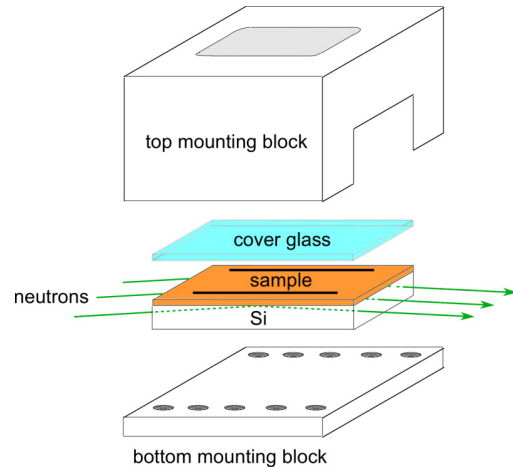


FIG. 2. (Color online) Sketch of the sample cell used to mount the silicon block. The two black stripes on the sample are cadmium spacers to keep the cover glass from touching the sample. Additional o-rings (not shown) ensure that the sample cell does not leak. Various drill holes (not shown) allow for attaching the sample cell to a water thermostat, as well as filling the space between sample and cover glass with D<sub>2</sub>O.

this setup is it possible to provide an initial orientation of the lipid layers along the block surface, so they can be investigated by reflectometry and GISANS. The hydrophilic surface of the silicon block keeps the lamellae aligned. In addition to these reasons, at the solid-liquid interface there is no total external reflection as opposed to the air/liquid interface.

## C. Methods

### 1. GISANS

Grazing incidence small-angle neutron scattering (GISANS) was performed at MARIA at MLZ (Maier-Leibnitz Zentrum), Garching, Germany. The wavelength of the neutrons was set to  $\lambda = 5$  Å at a wavelength spread of  $\Delta\lambda/\lambda = 0.1$ .

GISANS is a technique comparable to conventional small-angle neutron scattering (SANS) as the scattered intensity is the Fourier transform of the irradiated structure [15]. However, instead of the beam impinging on the sample head-on (zero degree incident angle), the sample is irradiated under a shallow angle below the critical angle of total reflection. This way, instead of investigating the directly reflected beam under reflective conditions (incoming angle equal to outgoing angle) as reflectometry, scattered intensity over the complete detector is investigated. In GISANS, measurements are mostly performed below the critical angle of total internal reflection  $\alpha_c = \lambda\sqrt{\Delta\rho/\pi}$ , where  $\Delta\rho = \rho_{\text{film}} - \rho_{\text{substrate}}$  is the scattering length density contrast between the film and the substrate. At these conditions, an evanescent wave with an exponentially decaying penetration depth of  $\Lambda_{\text{eva}} = [\text{Re}\sqrt{4\pi\Delta\rho(1 - \alpha_{\text{in}}^2/\alpha_c^2)}]^{-1}$  is propagating into the sample, so information over the complete surface region down to the depth of the evanescent wave is averaged by the scattering [16]. The geometry is shown in Fig. 3. In our case,  $\Lambda_{\text{eva}}$  can be estimated to  $\Lambda_{\text{eva}} \approx 350$  Å  $\gg D_{\text{lam}} \approx 50$  Å, with  $D_{\text{lam}}$  the thickness

TABLE I. Mixing weights of SoyPC and ibuprofen.

	0	13.6	25.0	34.5	43.1	50.2	53.3
	mol %						
Ibuprofen (mg)	0	138	290	458	658	679	3112
SoyPC (mg)	2610	3229	3189	3189	3189	2479	10030

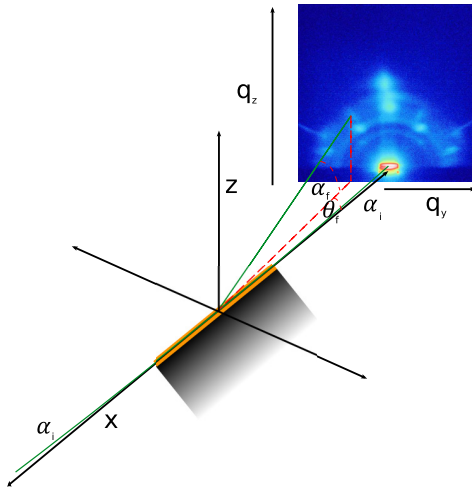


FIG. 3. (Color online) Geometry of a GISANS experiment. In the case of reflectometry, only intensity for  $\alpha_i = \alpha_f$  is evaluated. The path of the neutrons is in green.

of the observed lamellae. The dominant layer signal is thus scattered from  $\approx 7$  layers of the multilamellar system.

In the case investigated here, we find two features we want to analyze: distinct peaks and rings of near uniform intensity. The peaks can be described by classical crystallography and were indexed using TREOR90 [17]. As the primitive tetragonal lattice that was found was not oriented parallel to the surface, the orientation was determined by comparison with simulated scattering images created by XRAYVIEW4.0 [18]. The peaks with a hexagonal symmetry can be explained by a hexagonal symmetry in the sample itself [11].

The rings can be described as diffuse Debye-Scherrer rings around the direct beam and the specular reflected beam [19]. Since the thickness of these layers is already determined by reflectometry, we will concentrate mainly on the relative intensity contribution to calculate the volume fractions of ordered and lamellar phases.

## 2. Neutron reflectometry

Neutron reflectometry was performed at MARIA at MLZ, Garching, Germany. Reflectometry probes the sample composition on the nanometer scale perpendicular to the surface of the sample and is thus an ideal tool for the investigation of layered materials. A wavelength of  $\lambda = 10 \text{ \AA}$  at a wavelength spread of  $\Delta\lambda/\lambda = 0.1$  was used. Data acquisition time for each reflectometry point was 60 s.

To evaluate the data, the Parrat algorithm [20] was used. This algorithm describes the SLD distribution by describing it as a stack of discrete layers. The reflective properties of each layer  $j$  in the multilayer stack can be described by the transition matrix  $M_j$  [21],

$$M_j = \begin{pmatrix} \cos \phi_j & -(1/k_{zj}) \sin \phi_j \\ k_{zj} \sin \phi_j & \cos \phi_j \end{pmatrix}. \quad (1)$$

Here the phase difference  $\phi_j$  is given by the incident angle  $\theta$ , the refractive index  $n$ , the wavelength of the neutrons  $\lambda$ , and

the thickness of the  $j$ th layer  $t_j$  via

$$\phi_j = \frac{2\pi}{\lambda} n_j \sin \theta_j t_j = k_{zj} t_j. \quad (2)$$

The matrix  $M_j$  describes the amplitude of a wave propagating through layer  $j$  to the layer boundary  $(j, j + 1)$  in relation to the behavior at the boundary  $(j - 1, j)$ . As the amplitude and its derivation have to be continuous, it is possible to construct a transition matrix  $M$  for the whole stack of  $N - 1$  layers on the substrate, which is medium  $N$  and infinitely thick (therefore giving boundary conditions of a zero amplitude):

$$M = \begin{pmatrix} m_{11} & m_{12} \\ m_{21} & m_{22} \end{pmatrix} = M_{N-1} M_{N-2} M_{N-3} \cdots M_2 M_1. \quad (3)$$

The reflective coefficient  $R$  of the  $(0,1)$  interface is the given by

$$R = \frac{(k_{z0} k_{zN} m_{12} + m_{21}) - i(k_{zN} m_{11} - k_{z0} m_{22})}{(k_{z0} k_{zN} m_{12} - m_{21}) + i(k_{zN} m_{11} + k_{z0} m_{22})}. \quad (4)$$

A set of matrices is found numerically, which minimizes the difference between the experimental data and the calculated reflected intensity. This allows us to determine the scattering length density  $\rho$  of each layer  $j$  by

$$n = 1 - \frac{\lambda^2 \rho}{2\pi}. \quad (5)$$

These calculations have been implemented in the GENX software [22].

## 3. GINSES

Grazing incidence neutron spin-echo spectroscopy (GINSES) was developed at the J-NSE at the MLZ, Garching, Germany. The same sample cell and geometry as for the reflectometry and GISANS measurements were used. The wavelength was set to  $8 \text{ \AA}$ , while the incoming angle was set to  $0.21^\circ$ . The detector was placed at a  $Q$  value of  $Q = 0.12 \text{ \AA}^{-1}$ . This resulted in counting rates of  $\approx 1$  cps. These low counting rates can be explained by the fact that in contrast to conventional NSE experiments [23,24], the scattering volume only comprises the volume covered by the evanescent wave. However, this is only about  $400 \text{ \AA}$  in thickness. A detailed description of the data analysis for the result can be found in Frielinghaus *et al.* [16]. Due to the low count rates, however, here we limit the analysis to a qualitative interpretation.

## D. Results

In this section, we first present the results of the single GISANS, neutron reflectometry, and GINSES separately. Afterward, the results will be compared and discussed in context among each other.

### 1. GISANS

An overview over the scattering images obtained by the GISANS measurements at all investigated concentrations is shown in Fig. 4. These images show a clear evolution from a lamellar-based scattering over a scattering where several different structures contribute to a hexagonal structure with additional disordered lamellae, as can be seen by the persisting Debye-Scherrer ring.



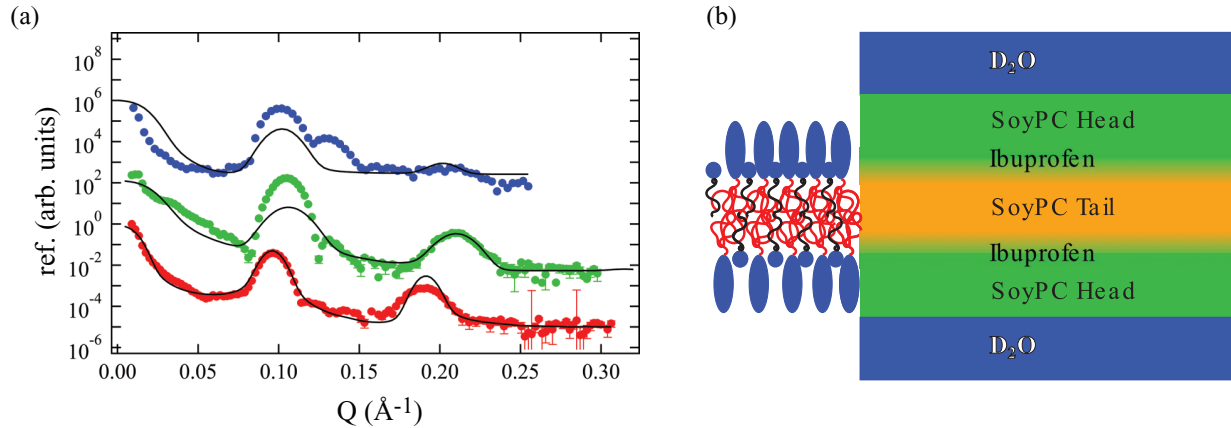


FIG. 6. (Color) (a) Representative reflectometry data with fits. Data sets are shifted for better visibility. Concentrations of ibuprofen (bottom to top) are 0, 13.6, and 25.0 mol %. (b) Depiction of the layer model used by the Parratt algorithm. For better visibility, the hydrophobic parts of SoyPC are in red, and those of ibuprofen are in black.

is always present, but decreasing in volume with increasing ibuprofen content. For pure SoyPC and low concentrations of ibuprofen, nearly the complete volume is made up from lamellae parallel to the surface. The disordered lamellae start appearing at 13.6 mol % of ibuprofen and increase to a relative scattering contribution of about 0.35 at 34.5 mol %. They scatter around this value for all higher concentrations. All three lattices, both hexagonal and the primitive tetragonal lattice, appear simultaneously at 34.5 mol %. After this, at higher ibuprofen concentrations, the volume fraction of the hexagonal lattice standing on edge decreases together with the volume fraction of the primitive tetragonal lattice. This can be understood if you regard the primitive tetragonal lattice as a filler between the two hexagonal lattices, which is necessary wherever these two meet. As the hexagonal lattice standing on edge vanishes, this filler is no longer needed, and the favored hexagonal lattice with a parallel axis to the surface is the only lattice remaining at high concentrations.

## 2. Neutron reflectometry

Representative results with fits according to the Parratt algorithm are shown in Fig. 6(a). All major features of the reflectivity curves could be reproduced. The initially assumed distribution of the layers is depicted in Fig. 6(b). In all systems, about 35–40 repetitions of these layers were found. In addition to these repeating units, a water layer directly on the substrate with a thickness of  $\approx 2$ – $15$   $\text{\AA}$  was found that corresponds with similar systems [26]. The existence of this water layer was corroborated by the fits. The critical angle vanishes in these systems. MARIA uses an elliptically curved focusing guide on the vertical direction, which ensures a vertical beam size of about 1 cm on the sample position. In the horizontal direction, the opening of the two collimation slits (S1,S2), which are 4 m apart, was equal to 1 mm for S1 and 1 mm S2, resulting in a collimated beam of 0.5 mrad ( $\theta = 2 \tan^{-1}([S1 + S2]/2L)$ ).

Discrepancies between the fit, especially in the width of the peaks, and the data can be explained by the fact that at higher concentrations, instead of investigating a purely lamellar system, which is ordered parallel to the substrate surface, additional ordering occurs. If one considers the size of the

footprint of approximately ( $\approx 12 \text{ cm} \times 1.6 \text{ cm} = 19.2 \text{ cm}^2$ ), it becomes apparent that the reflected intensity is comprised of intensity reflected from a lamellar structure as well as the ordered lattice structures. As a perfectly parallel lamellar stack is assumed in the Parratt model, concentrations above 25.0 mol % are not accurately described anymore, and at 25.0 mol % the fit is already challenging. However, we still performed the same analysis of the reflectometry for all concentrations in order to obtain information about the layer structure itself, which is embedded in the sample for all concentrations. To account for the smaller side maxima, which we attribute to the emerging 3D structure, we chose a phenomenological approach and fitted weighted Gaussians to the peaks. The results of these fits reveal the smaller peaks to increase in relative intensity from about  $10^{-3}$  at 13.6 mol % to 0.1 at 43.1 mol %. This is consistent with the idea that the emerging 3D structure is induced by the ibuprofen and thus the relative scattering contribution of the attributed peak increases.

The values for the SLDs of the different layers are given in Table II. Another problem in the accurate description may be that the layers may have an initial disorder already at very low concentrations, and that is not accounted for by our analysis.

Calculated SLD profiles from Eq. (5) are shown in Fig. 7(a). These profiles show that for the pure SoyPC layers, the pure hydrocarbon layer, which was used to model the tail region of SoyPC, is about 40  $\text{\AA}$  wide (for comparison of the respective SLDs used, see Table II). After the introduction of ibuprofen

TABLE II. SLDs used for the fitting of the reflectometry data with the Parratt algorithm. All values except for SoyPC are calculated using tabulated values published by NIST [27]. SLD for SoyPC was determined using contrast variation analysis with  $D_2O/H_2O$  mixtures.

Component	SLD ( $10^{-6} \text{ \AA}^{-2}$ )
Silicon	2.08
$D_2O$	6.38
SoyPC	0.24
Decane	-0.49
Ibuprofen	0.92

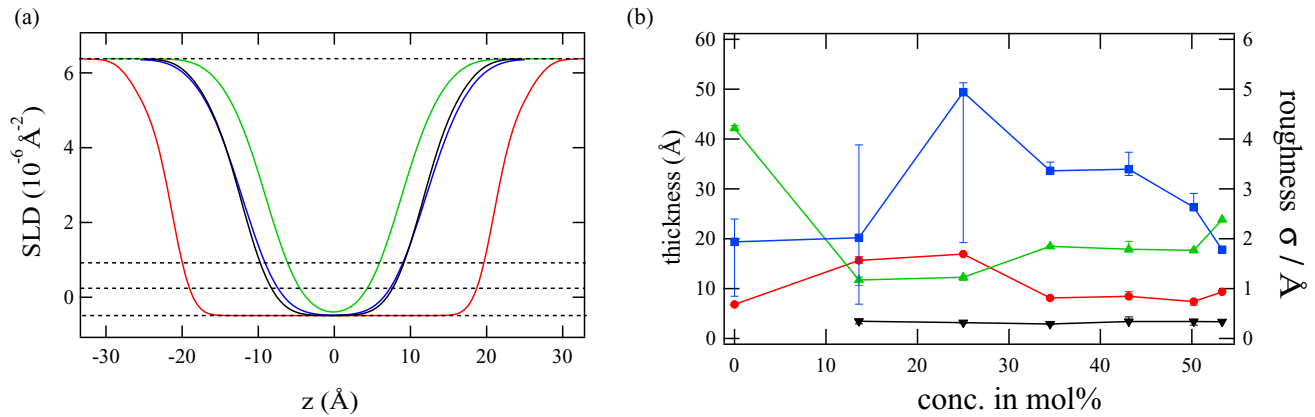


FIG. 7. (Color online) (a) SLD profiles from fits with the Parratt algorithm to reflectometry data for all concentrations. Concentrations are 0 mol % (red), 13.6 mol % (green), 43.1 mol % (blue), and 53.3 mol % (black). Dashed lines indicate the SLD from Table II for decane, SoyPC, ibuprofen, and D<sub>2</sub>O (from bottom to top). (b) Results from modeling the reflectometry curves with the model shown in Fig. 6: Thickness of the D<sub>2</sub>O layer (red circles), thickness of the SoyPC layer (green upright triangles), roughness of the layers (blue squares), and thickness of the ibuprofen layer (black downright triangles).

into the system, this width immediately collapses down to only about 20 Å in thickness. We attribute this apparent collapse to the ibuprofen becoming an interstitial part of the membrane and thus changing the overall SLD profile at the interface. With an increasing amount of ibuprofen, the thickness of the SoyPC layer consecutively increases again, but it does not reach its initial thickness anymore.

The different thicknesses for all layers used in this model can be seen in Fig. 7(b). The sudden decrease that is found in the SLD profiles is reproduced. At first glance it is surprising that the thickness of the ibuprofen layer should be constant for all concentrations, considering the concentration is increased from 13.6 to 53.3 mol %. However, taking into account the increasing thickness of the SoyPC layer, which is primarily the thickness of the hydrocarbon tail, we see a steady increase along with increasing concentration. This can be explained by assuming the ibuprofen is preferentially dissolved by the hydrocarbon tail of the SoyPC and thus inflates this layer.

Another observation from these data is that the modeled roughness of the layers is maximal with about 5 Å at 25.0 mol % ibuprofen. We assume this roughness is correlated to a high strain of the membrane that occurs at the onset of ordering to accommodate different conformations within the layer stack. As the concentration is increased, the ordering is improving again, so the roughness of the layers decreases.

### 3. GINSES

The results from the GINSES measurements are shown in Fig. 8. Due to the long measurement times, only the samples with pure SoyPC and the sample with 34.5 mol % of ibuprofen were investigated. While a relaxation is visible for the pure SoyPC, the sample with additional ibuprofen shows no relaxation. There are too few points to fit a meaningful relaxation time, however this behavior can be qualitatively interpreted as a stiffening of the membranes with increasing ibuprofen content. The measurements were performed for

$Q = 0.12 \text{ \AA}^{-1}$ , which translates to an evanescent wave depth of  $\Lambda_{\text{eva}} \approx 380 \text{ \AA}$ .

The specific choice for the  $Q$ -value can be rationalized by the fact that at correlation peaks, the dynamics get very slow due to the so-called de Gennes narrowing, where the relaxation rate is proportional to the inverse form factor [28,29].

Between Bragg peaks, in a minimum of the static structure factor, the signature of dynamic fluctuations on the form factor of the membranes is more visible; it is therefore an advantage to measure membrane fluctuations between Bragg peaks.

Local fluctuations of membranes, such as the contrast between water and a double layer, or density fluctuations of the scattering length density in the membrane, can result in a relaxation of the intermediate scattering function. This will be visible at high  $Q$ , and preferably not at structure factor peaks.

These local fluctuations of a double layer are visible in the form factor, not the structure factor, which makes the dynamics of different compositions comparable, even if the structure differs.

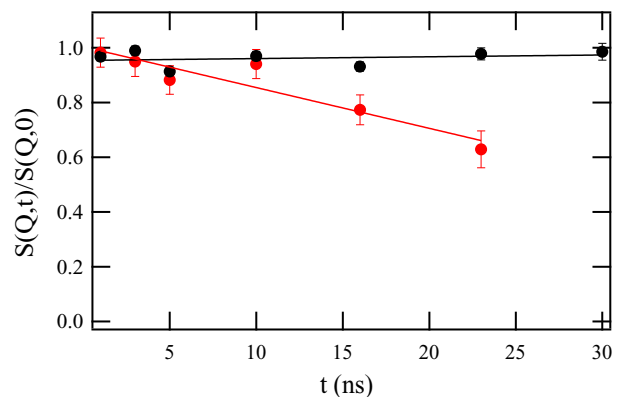


FIG. 8. (Color online) Dynamic structure factors for 0 (red) and 34.5 mol % (black) of ibuprofen in a SoyPC layer. For the pure SoyPC, a distinct relaxation in the investigated time regime is visible, while for 34.5 mol % the sample does not show any relaxations.

### III. DISCUSSION

The introduction of ibuprofen into SoyPC phospholipid films has several effects, which are related to one another. The thinning of the lipid film upon the introduction of ibuprofen, as well as the stiffening, coincide with first a breaking up of the parallel lamellae, then with the emergence of several coexisting lattices, and finally with a single hexagonal lattice at 53.3 mol % ibuprofen in the film.

Following this behavior step by step, it is possible to connect all these behaviors: (i) Evolution of a lamellar powder, (ii) emergence of several lattices, (iii) thinning of the SoyPC layers, and (iv) stiffening of the surface.

Behaviors (iii) and (iv) are connected, assuming that the introduction of ibuprofen is indeed similar to the drying of the lamellae, which is supported by the comparison with data from Aeffner *et al.* [2], where a similar behavior was found for the drying of a phospholipid film. Here we want to stress that the comparison is qualitative, as the membranes in the case of this study were fully hydrated at all times. Thus we only see a relative drying. This drying in turn leads to a strain in the surface, as a dry film becomes less flexible and is less apt to follow the zero curvature of the substrate surface, but it will prefer a curvature that is determined by the packing parameter of the SoyPC. The evolution of a lamellar powder (i) is also a result of this. As the strain on the surface increases and the curvature is more and more determined by a very stiff surface with a high curvature, lattices form (ii) in order to accommodate for this high curvature of the different lamellae. Finally, when the strain is high enough and the lamellae are very stiff, there is only one possible conformation of a lattice that can accommodate for this high strain. This behavior is sketched in Fig. 9. In each of the panels, the newly emerging structure is highlighted, but others, such as the disordered lamellae, may still be present (see Fig. 5). It is striking that in this representation it is not possible to create hexagonal lattices with equal spacings for both orientations, which might be suggested looking at the GISANS images. There are two possible approaches to that: (i) The  $Q$ -space resolution of the GISANS images is not able to resolve this difference in lattice spacing, which amounts to  $4D_{\text{lam}}$  for the hexagonal lattice standing on edge versus  $3D_{\text{lam}} \sin 60^\circ \approx 2.6D_{\text{lam}}$ . This ratio of  $4/2.6 \approx 1.5$  translates into a similar difference in  $Q$ -spacing. Looking at the GISANS images in Fig. 4, it is conceivable that a factor of 1.5 is not visible between the two different hexagonal lattices, as the maxima are quite broad. (ii) It is possible that there are different regions where the lamellar thickness is not constant, and at the same time one or the other hexagonal lattice may be predominant. We also want to stress that we do not attribute this lattice formation to aggregates of ibuprofen, as the enrichment of ibuprofen is supposed to be in plane in the layer as reported by Paloncova *et al.* [30], which does not allow the formation of any kind of lattice of ibuprofen aggregates.

Regarding the inclination of the primitive tetragonal lattice, we could confirm via comparisons of scattering images created with the software XRAYVIEW 4.0 that the lattice is indeed inclined by  $\approx 75^\circ$ . This compares to an inclination of  $\approx 60^\circ$  when regarding the conformation as envisioned in Fig. 9(c). While this deviation is substantial, considering the

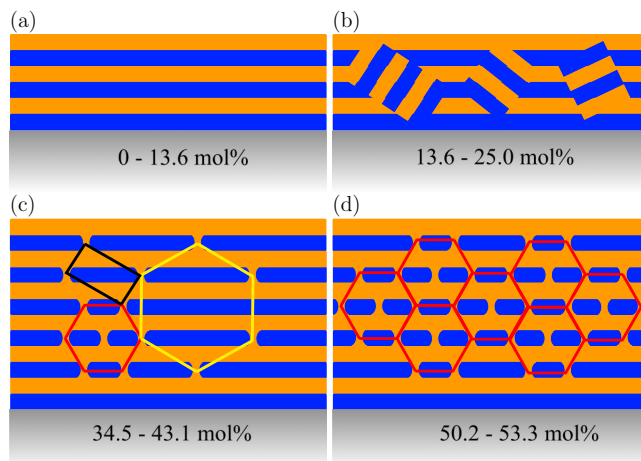


FIG. 9. (Color online) Sketch of the structural evolution of the sample. (a) For low concentrations of ibuprofen, the system is dominated by a lamellar structure while the introduction of more ibuprofen (b) induces disordering of lamellar areas and thus powder scattering of lamellar areas. In an intermediate concentration area (c), there are two different hexagonal lattices that are stabilized against each other by a primitive tetragonal lattice. At very high concentrations (d) only the hexagonal structure with an axis parallel to the substrate is retained. Color coding of the hexagonal structure corresponds to the color coding used in Fig. 4. The lattice forming units in (c) and (d) could be similar to those found by Aeffner *et al.* [1], even though the process of formation is different.

low volume fraction and thus the low intensity scattered from the primitive tetragonal lattice, which accommodates both hexagonal lattices, it still seems a good fit.

To explain this behavior on a molecular level, a consideration of the packing parameter as proposed by Israelachvili [31] is helpful. While SoyPC exhibits a packing parameter close to  $p_{\text{pack}} = v/la_0$ , where  $v$  is the volume of the hydrocarbon chain of the lipid in solution,  $l$  is its length, and  $a_0$  is the surface area in an aggregate occupied by the hydrophilic part, this value decreases strongly as soon as ibuprofen is introduced, as can be seen in Fig. 10. The rationale for the development of the hexagonal structure is that the change in the average packing parameter by introducing ibuprofen into the SoyPC is lowered. This happens as the hydrophobic part of the ibuprofen is much smaller than in the case of SoyPC and thus induces a higher curvature. If the curvature is high

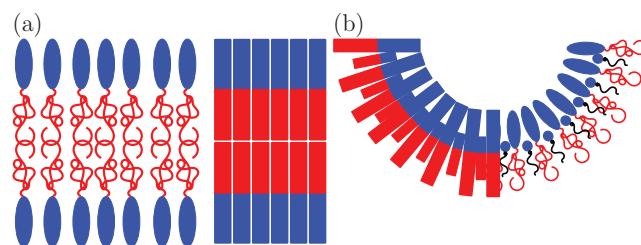


FIG. 10. (Color) Sketches of packing for (a) pure SoyPC layers and (b) SoyPC and ibuprofen. The ibuprofen with the small hydrophilic unit increases the curvature of the multilayer forming SoyPC.

enough, the hexagonal structure emerges, while still parts of the lamellar structure are retained as in the case of the pure SoyPC. This explanation is largely based on the location of the ibuprofen being interstitial between the head and tail groups of the SoyPC. This assumption is corroborated by the reflectometry data as well as by computer simulations [30] and x-ray [32] scattering based electron density found in the literature. Although in these publications smaller molecules were investigated, the physical determining features, namely small size and amphiphilicity, are identical. This seems to hint at a general attraction of small molecule drugs with amphiphilicity to the boundary between the head and tail segment of lipids in a membrane. Geometric considerations such as that of Israelachvili [31] corroborate that in this area the influence of the drugs on the bending modulus and hence the structure of the membrane is most pronounced. This concept is illustrated in Fig. 10.

#### IV. CONCLUSION

We investigated the influence of ibuprofen concentration on the behavior of phospholipid films of SoyPC. We found a correlation between ibuprofen content and the conformation of the lamellae in the film, starting as a film of nearly perfectly parallel lamellae when still a pure SoyPC film, then at low concentrations of ibuprofen exhibiting powder scattering of disordered lamellae. In an intermediate state, there is a coexistence of two hexagonal lattices, one parallel to the substrate surface, one standing on edge, which are both stabilized by a low amount of an inclined primitive tetragonal lattice. At high concentrations, only the hexagonal lattice parallel to

the substrate and the lamellae, both parallel and disordered, are retained. We assume there is a correlation between the ordering of the phospholipid membrane and cytotoxicity, as any imbued structure is a change of the unperturbed configuration of a cell membrane.

Here we have to keep in mind that the ibuprofen concentrations investigated here are beyond any medical applicability, so this same effect cannot be expected in medical practice. It is, however, conceivable that in the case of long-term treatment, where these complications occur, once a *nucleation point* for this damage is created, the damage will start to grow. This initial damage can be due to a local, short-time high concentration immediately after ingestion. Here we want to stress that for the nucleation point, we are strictly speaking in terms of likelihood. This means the individual nucleation point does not need to be stable over a long time, but that during a frequent exposure to high doses of ibuprofen, the probability for the formation of such a nucleation point is strongly increased.

Apart from the structural damage, a structure induced by ibuprofen and the stiffening in itself may alter the mobility of proteins in the membrane before damaging it. However, this change in mobility may inhibit the protein function, thus damaging the cell nonetheless [33].

#### ACKNOWLEDGMENTS

S.H., S.F.F., and B.N. acknowledge financial support by the Deutsche Forschungsgemeinschaft (DFG-SFB1032) and the Bundesministerium für Bildung und Forschung (BMBF-05K13WM1).

- 
- [1] S. Aeffner, T. Reusch, B. Weinhausen, and T. Salditt, *Eur. Phys. J. E* **30**, 205 (2009).
  - [2] S. Aeffner, T. Reusch, B. Weinhausen, and T. Salditt, *Proc. Natl. Acad. Sci. (U.S.A.)* **109**, E1609 (2012).
  - [3] A. Tronin, C.-H. Chen, S. Gupta, D. Worcester, V. Lauter, J. Strzalka, I. Kuzmenko, and J. Blasie, *Chem. Phys.* **422**, 283 (2013), a tribute to Dr. Robin Hochstasser.
  - [4] M. B. Boggara, A. Faraone, and R. Krishnamoorti, *J. Phys. Chem. B* **114**, 8061 (2010).
  - [5] M. J. Thun, S. J. Henley, and C. Patrono, *J. Natl. Cancer Inst.* **94**, 252 (2002).
  - [6] S. Weggen, J. L. Eriksen, P. Das, S. A. Sagi, R. Wang, C. U. Pietrzik, K. A. Findlay, T. E. Smith, M. P. Murphy, T. Bulter, D. E. Kang, N. Marquez-Sterling, T. E. Golde, and E. H. Koo, *Nature (London)* **414**, 212 (2001).
  - [7] L. M. Lichtenberger, Z. M. Wang, J. J. Romero, C. Ulloa, J. C. Perez, M. N. Giraud, and J. C. Barreto, *Nat. Med.* **1**, 154 (1995).
  - [8] M. B. Boggara, M. Mihalescu, and R. Krishnamoorti, *J. Am. Chem. Soc.* **134**, 19669 (2012).
  - [9] W. Tomisato, K. Tanaka, T. Katsu, H. Kakuta, K. Sasaki, S. Tsutsumi, T. Hoshino, M. Aburaya, D. Li, T. Tsuchiya, K. Suzuki, K. Yokomizo, and T. Mizushima, *Biochem. Biophys. Res. Commun.* **323**, 1032 (2004).
  - [10] S. Malheirosa, L. Pintoa, L. Gottardo, D. Yokaichiya, L. Fraceto, N. Meirelles, and E. dePaula, *Biophys. Chem.* **110**, 213 (2004).
  - [11] P. Lang, C. Braun, R. Steitz, G. H. Findenegg, and H. Rhan, *J. Phys. Chem. B* **102**, 7590 (1998).
  - [12] AvantiLipids Co., SoyPC structure (2014), [avantilipids.com/index.php](http://avantilipids.com/index.php).
  - [13] SigmaAldrich Co. LLC, Ibuprofen structure (2014), <http://www.sigmaaldrich.com>.
  - [14] W. Kern and D. A. Puotinen, *RCA Rev.* **31**, 187 (1970).
  - [15] P. Müller-Buschbaum, in *Applications of Synchrotron Light to Scattering and Diffraction in Materials and Life Sciences*, Lecture Notes in Physics Vol. 776, edited by M. Gomez, A. Nogales, M. C. Garcia-Gutierrez, and T. Ezquerra (Springer, Berlin, 2009), pp. 61–89.
  - [16] H. Frielinghaus, M. Kerscher, O. Holderer, M. Monkenbusch, and D. Richter, *Phys. Rev. E* **85**, 041408 (2012).
  - [17] P.-E. Werner, L. Eriksson, and M. Westdahl, *J. Appl. Crystallogr.* **18**, 367 (1985).
  - [18] G. N. Phillips Jr., *Biophys. J.* **69**, 1281 (1995).
  - [19] P. Busch, D. Posselt, D.-M. Smilgies, M. Rauscher, and C. M. Papadakis, *Macromolecules* **40**, 630 (2007).

- [20] L. G. Parratt, *Phys. Rev.* **95**, 359 (1954).
- [21] R. Roe, *Methods of X-ray and Neutron Scattering in Polymer Science* (Oxford University Press, Oxford, 2000).
- [22] M. Björck and G. Andersson, *J. Appl. Crystallogr.* **40**, 1174 (2007).
- [23] M. Monkenbusch, R. Schätzler, and D. Richter, *Nucl. Instrum. Methods Phys. Res. Sect. A* **399**, 301 (1997).
- [24] O. Holderer, M. Monkenbusch, R. Schätzler, H. Kleines, W. Westerhausen, and D. Richter, *Meas. Sci. Technol.* **19**, 034022 (2008).
- [25] S. Jaksch, F. Lipfert, A. Koutsioubas, S. Mattauch, O. Holderer, O. Ivanova, H. Frielinghaus, S. Hertrich, S. F. Fischer, and B. Nickel, See Supplemental Material at <http://link.aps.org/supplemental/10.1103/PhysRevE.91.022716> for representative line cuts.
- [26] S. Krueger, J. F. Ankner, S. K. Satija, C. F. Majkrzak, D. Gurley, and M. Colombini, *Langmuir* **11**, 3218 (1995).
- [27] NIST, NIST SLD tables (2014), <http://www.ncnr.nist.gov/resources/n-lengths/>.
- [28] P.-G. de Gennes, *Physica* **25**, 825 (1959).
- [29] O. Holderer, H. Frielinghaus, M. Monkenbusch, J. Allgaier, D. Richter, and B. Farago, *Eur. Phys. J. E* **22**, 157 (2007).
- [30] M. Paloncova, K. Berka, and M. Otyepka, *J. Phys. Chem. B* **117**, 2403 (2013).
- [31] J. N. Israelachvili, *Intermolecular and Surface Forces* (Academic Press, Oxford, 2011).
- [32] M. A. Barrett, S. Zheng, G. Roshankar, R. J. Alsop, R. K. R. Belanger, C. Huynh, N. Kučerka, and M. C. Rheinstädter, *PLoS ONE* **7**, e34357 (2012).
- [33] M. Saxton, *Biophys. J.* **52**, 989 (1987).